

NQR Data on the Activation Energy of Orientational Defects in Crystal Lattice

A. D. Gordeev, A. N. Osipenko, and G. B. Soifer

Perm State University, ul. Bukireva 15, Perm, 614600 Russia

Received June 6, 2000; in final form, October 24, 2000

Abstract—The nuclear quadrupole spin-lattice relaxation related to the formation of orientational defects in crystals has been analyzed. The defects arise because of thermally activated reorientational motion of molecules and their fragments between the nonequivalent potential wells. These molecular reorientations are considered for double- and triple-well potentials, both periodic and bounded by external side walls. It was shown that, for such potentials, the temperature dependence of the relaxation time provides the data on the activation energy for transitions of molecules in the crystal lattice from the equilibrium ground-state positions to those corresponding to metastable states. We systematized the known NQR data on the activation energies for orientational defects arising in the intracrystal rotations of molecules and atomic groups possessing the imperfect two-, three-, and sixfold axial symmetries. © 2001 MAIK “Nauka/Interperiodica”.

In a molecular crystal with the regular structure, the thermally-activated rotational motion of molecules or atomic groups possessing no axial symmetry gives rise to the formation of orientational defects in the crystal lattice. The formation of these defects forces the reorienting molecules (or their fragments) to occupy the equilibrium positions with unequal potential energies; i.e., the motion occurs between the nonequivalent potential wells. The intracrystal dynamics of axially symmetric molecules associated with their reorientational motion between the equivalent potential wells was studied rather extensively by the nuclear quadrupole resonance (NQR) technique (highly sensitive to the dynamic processes in solids [1]). At the same time, the molecular reorientation occurring between energetically nonequivalent positions in crystals were rarely studied by this technique. Moreover, the interpretation of the NQR data calls for an additional substantiation, especially in the analysis of the relaxation measurements. This paper is aimed at the analysis and generalization of the nuclear quadrupole spin-lattice relaxation data related to the formation of orientational defects in the crystal lattice caused by the motion of the molecules between the nonequivalent potential wells.

It is well known in NQR that the most efficient technique for the investigation of molecular mobility is the analysis of the temperature dependence of the nuclear quadrupole spin-lattice relaxation time T_1 . The corresponding relaxation rate controlled by the thermally activated reorientational motion, is described by the following relationship [1]

$$(T_1^{-1})_{\text{reor}} = b \exp(-E_a/RT), \quad (1)$$

where the parameters b and E_a (activation energy of motion) can be found by conventional data processing.

In the case of the molecular motion in the orienting potential with nonequivalent wells, it is essential to find out which of the parameters determines the activation energy E_a measured. To solve this problem, we analyze in this paper the process of nuclear quadrupole spin-lattice relaxation for the intracrystal orientational motion for potentials with nonequivalent wells. We consider different forms of this potential: double- and triple-well potentials both periodic and bounded by external side walls, which corresponds to the reorientation of molecules or atomic groups possessing imperfect two-, three-, and sixfold axial symmetry, respectively, i.e., to rotations about the C_2' , C_3' , and C_6' axes (see, for example, [2–4]). In the latter situation, characteristic, for example, of benzene derivatives (Table 1), the molecular motion is hindered by intermolecular steric hindrances. As a result, the motion occurs not between all the six nonequivalent equilibrium positions in the crystal, but only in the reduced potential between the stable ground-state positions and the neighboring metastable positions.

The values of the activation energy for intermolecular orientations in the potentials with nonequivalent wells of the aforementioned types determined from the temperature dependence $T_1(T)$ for chlorine-35 nuclei are presented in Table 1 [2, 5–17]. The analysis performed in this paper yields the correlation between the values of the activation energies and the specific transitions between the equilibrium positions of the molecules in the crystal, i.e., the correlation between the activation energy and the dynamics of orientational defects in solids.

The analysis is based on the aforementioned orientational potentials schematically represented in Fig. 1. We choose these simple forms of the potential to reveal

Table 1. Molecular reorientations between the nonequivalent potential wells in crystalline compounds

No.	Compound	Object of reorientation	Motion axis	Form of potential	E_a , kJ/mole	Reference
1	Cl(CN)C-CCl ₂	Molecule	C_2'	P2	37.3	[2]
2	Cl(CN)C=C(C ₆ H ₅) · [N(CH ₂ CH ₂) ₂ O]	Molecule	C_2'	P2	31.8	[5]
3	CClF ₂ COOH	CClF ₂	C_3'	P3	14.0	[6]
4	C(NH ₂) ₃ ⁺ · CClF ₂ COO ⁻	CClF ₂	C_3'	P3	9.2	[6]
5	4-ClC ₆ H ₄ NH · COCClF ₂	CClF ₂	C_3'	P3	13.0	[7]
6	Cl ₃ P=NCCl(CF ₃) ₂	CCl(CF ₃) ₂	C_3'	P3	13.8	[8, 9]
7	Cl ₃ P=NSO ₂ Cl	SO ₂ Cl	C_3'	P3	24.7	[10]
8	(CCl ₃) ₂ CIP=NSO ₂ Cl	SO ₂ Cl	C_3'	P3	46.9	[10]
9	2-NO ₂ C ₆ H ₄ SO ₂ Cl	SO ₂ Cl	C_3'	P3	38.5	[11]
10	4-NO ₂ C ₆ H ₄ SO ₂ Cl*	SO ₂ Cl	C_3'	P3	33.9, 41.8	[12]
11	C ₆ H ₅ Cl	Molecule	C_6'	P3(∞)	39.5	[13]
12	C ₆ H ₅ Cl	Molecule	C_6'	P3(∞)	19.3	[4, 14]
13	C ₆ H ₃ Cl ₃ -1,2,3	Molecule	C_6'	P2(∞)	39.0	[15, 16]
14	C ₆ F ₃ Cl ₃ -1,3,5	Molecule	C_6'	P2(∞)	19.7	[17]

Note: The table contains the following data: the object of the reorientation (molecule, atomic group), the type of the reorientation axis (C_2' , C_3' , and C_6' for the rotational motion for imperfect two-, three-, and sixfold axial symmetry, respectively), the form of orientational potential with nonequivalent potential wells (P2 and P3 are the double- and triple-well periodic potentials, P2(∞) and P3(∞) are the double- and triple-well potentials bounded by external infinitely high walls), activation energy E_a of the reorientation according to the NQR data for chlorine-35.

* Different E_a values are given for two different phases of the compound.

the fundamental features of the nuclear quadrupole spin-lattice relaxation determined by the molecular motion between the nonequivalent potential wells in different structures. The technique used here was reported in [18, 19] for the thermally activated intermolecular reorientations, which are slow in comparison with the NQR frequency, which is usually the case in experiments [1]. The analysis was performed for nuclei with spin 3/2 (for example, for chlorine-35, which is widely used in NQR measurements) in an electric field with an axially symmetric gradient. The imposed constraints do not limit the generality of the consideration.

It should be indicated that molecular reorientational jumps between the potential wells A , B , and C (indicated by arrows in Fig. 1) occur with the probabilities W_n per unit time equal to [20, 21]

$$W_n = W \exp(-E_n/RT), \quad (2)$$

where W is the temperature-independent frequency factor and E_n is the barrier separating the potential wells. In the actual situation for nonequivalent wells (the nonequivalent equilibrium positions of molecules in the crystal lattice), the difference in their depths Δ exceeds

the average thermal energy RT in the whole temperature range of crystal existence.

Molecular jumps between the equilibrium positions A , B , and C cause the changes in the nuclear magnetization associated with the process of spin-lattice relaxation after the action of the radio-frequency onto the spin system of quadrupole nuclei. The behavior of the latter system is determined by the system of kinetic equations corresponding to the molecular motion in the orientational potentials presented in Fig. 1. Despite the model nature of the chosen potentials (see Fig. 1), they describe rather well some situations in actual crystals (see Table 1). The kinetic equations have the form

$$\begin{aligned} \dot{n}_A &= -2W_1n_A + 2W_2P_2n_B, \\ \dot{n}_B &= 2W_1P_2n_A - 2W_2n_B, \end{aligned} \quad (3)$$

where

$$W_1 \equiv W_{AB} = W \exp[-(E + \Delta)/RT]$$

and

$$W_2 \equiv W_{BA} = W \exp(-E/RT)$$

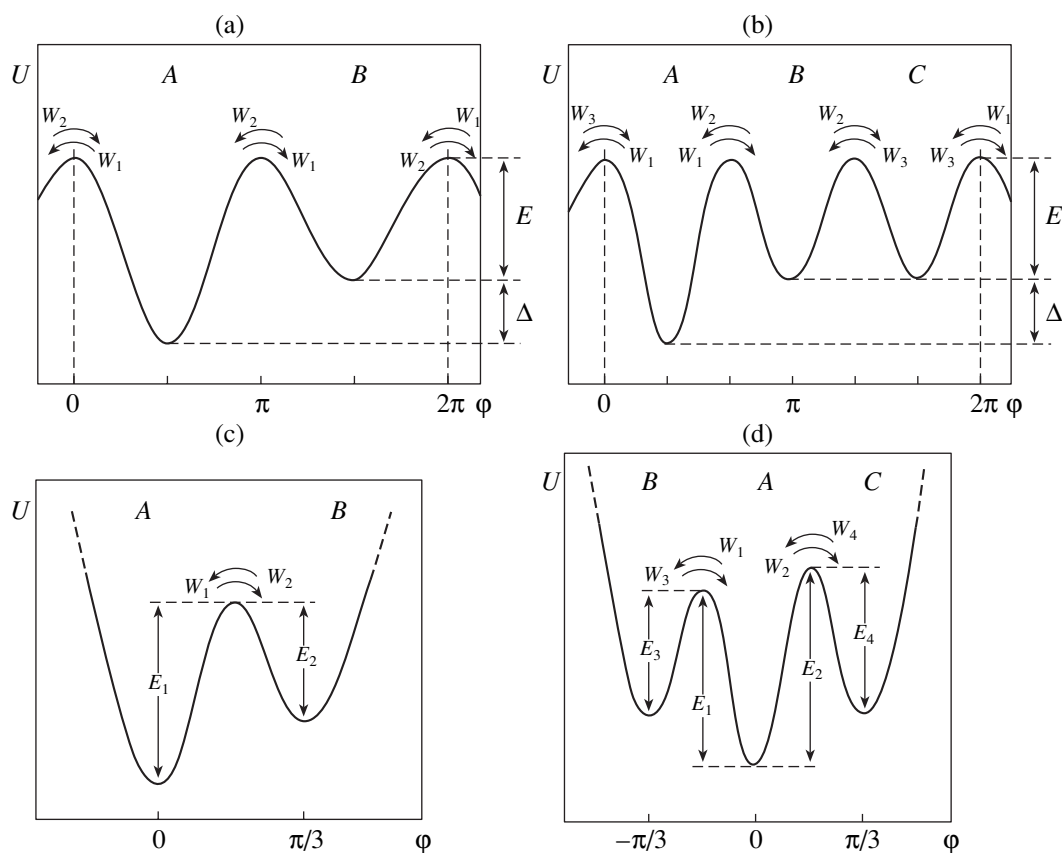


Fig. 1. Double- and triple-well orientational potentials with nonequivalent wells (A, B, and C): (a) and (b) periodic potentials, (c) and (d) potentials bounded by external infinitely high walls; φ is the rotation angle for a molecule or an atomic group during their reorientations; W_n are the probabilities of the reorientational transitions between the potential wells; E , $E + \Delta$, and E_n are the barriers separating the equilibrium molecular orientations.

for the periodic double-well potential (Fig. 1a);

$$\begin{aligned} \dot{n}_A &= -2W_1n_A + W_2P_2n_B + W_3P_2n_C, \\ \dot{n}_B &= W_1P_2n_A - 2W_2n_B + W_3P_2n_C, \\ \dot{n}_C &= W_1P_2n_A + W_2P_2n_B - 2W_3n_C, \end{aligned} \quad (4)$$

where

$$W_1 \equiv W_{AB} = W_{AC} = W \exp[-(E + \Delta)/RT]$$

and

$$\begin{aligned} W_2 &\equiv W_3 \equiv W_{BA} = W_{BC} = W_{CA} \\ &= W_{CB} = W \exp(-E/RT) \end{aligned}$$

for the periodic triple-well potential (Fig. 1b);

$$\begin{aligned} \dot{n}_A &= -W_1n_A + W_2P_2n_B, \\ \dot{n}_B &= W_1P_2n_A - W_2n_B, \end{aligned} \quad (5)$$

where

$$W_1 \equiv W_{AB} = W \exp(-E_1/RT)$$

and

$$W_2 \equiv W_{BA} = W \exp(-E_2/RT)$$

for the double-well potential bounded by external “infinitely high” walls (Fig. 1c);

$$\begin{aligned} \dot{n}_A &= -(W_1 + W_2)n_A + W_3P_2n_B + W_4P_2n_C, \\ \dot{n}_B &= W_1P_2n_A - W_3n_B, \\ \dot{n}_C &= W_2P_2n_A - W_4n_C, \end{aligned} \quad (6)$$

where

$$W_1 \equiv W_{AB}, \quad W_2 \equiv W_{AC}, \quad W_3 \equiv W_{BA}, \quad W_4 \equiv W_{CA},$$

and

$$W_{1-4} = W \exp(-E_{1-4}/RT)$$

for the triple-well potential bounded by external “infinitely high” walls (Fig. 1d).

In Eqs. (3)–(6), the variables n_i , corresponding to the i th well (A, B, or C), are the differences in the spin-state population (proportional to the nuclear magnetization) for quadrupole nuclei with spin 3/2 in the axially symmetric electric-field gradient (EFG). These variables are defined as $n_i(t) = N_i(t) - \bar{N}_i$, where $N_i(t)$ is the population at the moment t , and $\bar{N}_i = N_i(\infty)$ is the equi-

Table 2. Results (7) of the solution of kinetic equations (3)–(6) for nuclear magnetization for the rotational motion of molecules in the orientational potentials

Form of potential	Initial conditions		$(T_1^{-1})_{\text{reor}} = ZW\exp(-E_a/RT)$		Relations between the probabilities of transitions, W_n
	$N_i(0)$	$n_i(0)$	Z	E_a	
P2 (a)	$N_A = 0$ $N_B = \bar{N}_B$	$n_A = -\bar{N}_A$ $n_B = 0$	$2(1 - P_2^2)$	$E + \Delta$	$W_1 \ll W_2$ (at $\beta = 120^\circ$ $P_2 = -1/8$)
P3 (b)	$N_A = 0$ $N_B = \bar{N}_B$ $N_C = \bar{N}_C$	$n_A = -\bar{N}_A$ $n_B = 0$ $n_C = 0$	$\frac{2(2 - P_2 - P_2^2)}{2 - P_2}$	$E + \Delta$	$W_1 \ll (W_2 = W_3)$ (at the tetrahedral β $P_2 = -1/3$)
P2(∞) (c)	$N_A = 0$ $N_B = \bar{N}_B$	$n_A = -\bar{N}_A$ $n_B = 0$	$1 - P_2^2$	E_1	$W_1 \ll W_2$ (at $\beta = 60^\circ$ $P_2 = -1/8$)
P3(∞) (d)	$N_A = 0$ $N_B = \bar{N}_B$ $N_C = \bar{N}_C$	$n_A = -\bar{N}_A$ $n_B = 0$ $n_C = 0$	$1 - P_2^2$	E_1	$W_1 \ll W_3, W_2 \ll W_4, W_1 \gg W_2$ (at $\beta = 60^\circ$ $P_2 = -1/8$)
			$2(1 - P_2^2)^*$	E_1^*	* at $E_2 = E_1, W_1 = W_2$

Note: The potentials are shown in Fig. 1; P2 and P3 are the double- and triple-well periodic potentials, P2(∞) and P3(∞) are the double- and triple-well potentials bounded by external infinitely high walls.

librium population (here, $N_i = N_{(\pm 1/2)_i} - N_{(\pm 3/2)_i}$). The coefficient $P_2 = (3 \cos^2 \beta - 1)/2$ is the second-order Legendre polynomial, where β is the rotation angle for the principal axis of EFG tensor (at the position of the quadrupole nucleus), corresponding to the change in the axis direction induced by the molecular reorientations [19]. For chlorine nuclei, for example, the axis direction corresponding to the maximum EFG value is known [22] to coincide with the direction of the chemical bond for chlorine. This allows us to determine the value of P_2 based on the geometry of the molecules taking part in reorientation.

It has already been mentioned that our consideration relates to the case where the resonating nucleus (chlorine with spin 3/2) is in the axially symmetric EFG. Note that the allowance for deviations from the axial symmetry, i.e., the use in the calculations of a nonzero EFG asymmetry parameter (η), considerably complicates the mathematical treatment of the nuclear quadrupole spin-lattice relaxation process. If the spin equals 3/2, there is no need in such a complication [18], since it is not essential for the problem to be solved. The similar scheme which implies that $\eta = 0$ was also used in the theoretical analysis of the relaxation process associated with molecular reorientations [17, 18]. The expressions for the rate of quadrupole spin-lattice relaxation of the nuclear magnetization T_1^{-1} can be found by solving sets (3)–(6) of kinetic equations with the initial con-

ditions determining the starting deviation from the equilibrium for the system of nuclear spins. It is a characteristic feature of NQR—the excitation of quadrupole nuclei at the resonance frequency and the record of the resonance signal occur only for nuclei of the molecules occupying the equilibrium ground-state position in the crystal lattice, i.e., for nuclei located in the deepest potential well. This is explained by the difference in the resonance conditions for quadrupole nuclei of molecules in crystallographically nonequivalent equilibrium positions [22]. We should also take into account that the overwhelming majority of the molecules are located in the position corresponding to a deeper potential well (the difference in the potential-well depths considerably exceeds the value of RT).

This fact determines the choice of the initial conditions for sets of equations (3)–(6). The corresponding values of $N_i(0)$ and $n_i(0)$ depending on the experimental technique used in the measurements of the relaxation time T_1 are presented in Table 2 (we considered the case of the spin system excited by a resonant radio-frequency 90° pulse). We can use the relations between the probabilities of molecule transitions W_n (see Table 2) with due regard for the fact that the difference in the depths of nonequivalent potential wells considerably exceeds RT . Thus, the solution of sets (3)–(6) found in the usual way leads to the following result [2, 9]:

$$n_A(t) = n_A(0) \exp(-t/T_1). \tag{7}$$

Here, T_1^{-1} is the rate of nuclear quadrupole relaxation related to the quadrupole mechanism for the molecular motion in the potential with nonequivalent wells. This relaxation rate is determined by the probability of reorientational jumps of molecules or atomic groups between the nonequivalent potential wells [2, 9]. This temperature-dependent probability obeys the Arrhenius law [see relationship (2)]. This relaxation parameter for such a relation to the thermally activated reorientational motion of molecules has the physical sense of a relaxation rate $(T_1^{-1})_{\text{reor}}$ from formula (1) and obeys the same law. Hence, it is quite natural to use for it the same notation.

It is clear from relationship (7) that the process of the spin-lattice relaxation has the exponential form for the molecular motion in the potential with the nonequivalent wells. This was confirmed by the results of the experimental tests in crystalline compounds with different forms of the potentials with nonequivalent wells (see, for example, [5, 8]).

For the orientational potentials considered here (see Fig. 1), the temperature dependence of the relaxation rate following from the analysis of the solutions to sets (3)–(6) can be represented by the expression $(T_1^{-1})_{\text{reor}} = ZW_1$. All the versions of this expression are summarized in Table 2. For illustration, the values of corresponding coefficients P_2 for certain specific cases of the motion in the potentials with the nonequivalent wells (shown in Fig. 1) are also indicated in Table 2 [2–4, 15]. The relations between the probabilities W_n of the transitions given in Table 2 illustrate the difference between the depths of nonequivalent potential wells [see Fig. 1 and relationship (2)].

It is clear from Table 2 that for all cases of molecular motion in the potentials with nonequivalent potential wells of different forms considered above, the activation energy E_a of this motion is necessary to overcome the barrier in the molecular transitions from the equilibrium ground-state position to the metastable one. The E_a values were determined from the temperature dependence of the relaxation rate characterizing the nuclear quadrupole spin-lattice relaxation. This conclusion, also formulated in [2, 7, 9], allows one to correct the earlier results [3, 5, 8] obtained for the motion between the nonequivalent potential wells.

Thus, in the thermally activated dynamic process in which the molecules are reoriented between the nonequivalent positions in the crystal lattice, the corresponding activation energy determined by the NQR technique characterizes the formation of the orientational defects in the crystal structure. This information for the reorienting molecules and atomic groups is presented in Table 1. It shows the energy range (15–50 kJ/mol) for activating the formation of the orientational defects in the crystalline compounds under study.

ACKNOWLEDGMENTS

The study was supported by the Russian Foundation for Basic Research, project no. 98-03-32485a.

REFERENCES

1. H. Chihara and N. Nakamura, *Adv. Nucl. Quadrupole Reson.* **4**, 1 (1980).
2. A. D. Gordeev and G. B. Soifer, *Zh. Fiz. Khim.* **72**, 903 (1998).
3. N. E. Aïnbinder, I. A. Kjuntsel, V. A. Mokeeva, *et al.*, *J. Mol. Struct.* **58**, 349 (1980).
4. N. E. Aïnbinder, G. E. Kibrik, A. N. Osipenko, and G. B. Soifer, *Fiz. Tverd. Tela (St. Petersburg)* **39**, 877 (1997) [*Phys. Solid State* **39**, 780 (1997)].
5. Yu. N. Gachegov, A. D. Gordeev, and G. B. Soifer, *Fiz. Tverd. Tela (Leningrad)* **27**, 1659 (1985) [*Sov. Phys. Solid State* **27**, 997 (1985)].
6. R. Basaran, Shi-qi Dou, and A. Weiss, *Z. Naturforsch. A* **47**, 241 (1992).
7. S. Wigand, T. Asaji, R. Ikeda, and D. Nakamura, *Z. Naturforsch. A* **47**, 265 (1992).
8. N. E. Aïnbinder, I. A. Kyuntsel', V. A. Mokeeva, and G. B. Soifer, *Fiz. Tverd. Tela (Leningrad)* **21**, 2498 (1979) [*Sov. Phys. Solid State* **21**, 1441 (1979)].
9. N. E. Aïnbinder, A. N. Osipenko, and G. B. Soifer, *Khim. Fiz.* **17** (4), 30 (1998).
10. I. A. Kyuntsel', V. A. Mokeeva, and G. B. Soifer, *Khim. Fiz.* **5** (9), 1205 (1986).
11. S. C. Perez, R. L. Armstrong, and A. H. Brunetti, *J. Phys.: Condens. Matter* **5**, 4045 (1993).
12. S. C. Perez, R. L. Armstrong, and A. H. Brunetti, *J. Phys.: Condens. Matter* **5**, 4055 (1993).
13. A. D. Gordeev, A. P. Zhukov, and G. B. Soifer, *Fiz. Tverd. Tela (Leningrad)* **32**, 613 (1990) [*Sov. Phys. Solid State* **32**, 359 (1990)].
14. A. P. Zhukov and G. B. Soifer, *Zh. Strukt. Khim.* **32** (4), 170 (1991).
15. I. Tatsuzaki, *J. Phys. Soc. Jpn.* **14** (5), 578 (1959).
16. S. Wigand, N. Weiden, and A. Weiss, *Z. Naturforsch. A* **45**, 490 (1990).
17. N. Nakamura and H. Yoshino, *Bull. Chem. Soc. Jpn.* **63** (1), 21 (1990).
18. S. Alexander and A. Tzalmona, *Phys. Rev.* **138** (3A), 845 (1965).
19. N. E. Aïnbinder, B. F. Amirkhanov, I. V. Izmet'sev, *et al.*, *Fiz. Tverd. Tela (Leningrad)* **13**, 424 (1971) [*Sov. Phys. Solid State* **13**, 344 (1971)].
20. J. E. Anderson, *J. Magn. Reson.* **11**, 398 (1973).
21. L. Latanowicz and Z. Pajak, *Mol. Phys.* **82**, 1187 (1994).
22. G. K. Semin, T. A. Babushkina, and G. G. Yakobson, *Application of Nuclear Quadrupole Resonance in Chemistry* (Khimiya, Leningrad, 1972).

Translated by K. Kugel

REAL STRUCTURE OF CRYSTALS

Partial Dislocations and Stacking Faults in Cubic SiC

U. Kaiser*, I. I. Khodos**, M. N. Kovalchuk**, and W. Richter*

* Institut für Festkörperphysik, Friedrich Schiller Universität, Jena, D-07743 Germany

** Institute of Microelectronic Technology and Ultra-High-Purity Materials,
Russian Academy of Sciences, Chernogolovka, Moscow oblast, 142432 Russia

e-mail: khodos@ipmt-hpm.ac.ru

Received January 9, 2001

Abstract—Numerous stacking faults and dislocations (formed by intersection of stacking faults and dislocations limiting nonintersecting stacking faults) in the 3C-SiC films grown by molecular beam epitaxy on a silicon substrate were studied by electron microscopy with the use of weak beams. A procedure for determining any of possible Burgers vectors of the $(1/6)\langle 11\bar{6} \rangle$ -type glide dislocations and the $(1/6)\langle 110 \rangle$ - and $(1/3)\langle 001 \rangle$ -type sessile partial dislocations (in face-centered cubic lattices) is developed based on the criterion of the contrast value. The sessile dislocations formed by intersections of stacking faults were shown to have the $(1/6)\langle 110 \rangle$ - and $(1/3)\langle 001 \rangle$ -type Burgers vectors. The width of nonintersecting stacking faults corresponds to the stacking-fault energy ranging within 0.1–2 mJ/m². © 2001 MAIK “Nauka/Interperiodica”.

INTRODUCTION

Silicon carbide is a wide band-gap semiconductor existing in the hexagonal and the cubic modifications. There are more than 200 hexagonal nH polytypes with various periodicities n and only one cubic C polytype [1] with the sphalerite-type face-centered cubic (fcc) lattice. It is known that fcc and hexagonal close-packed (hcp) lattices are characterized by the same symmetry of atomic arrangement in the (111) and the (0001) planes but different alternation of their arrangement along the normal to these planes. In the fcc lattice, all three possible positions of the A , B , and C planes (the $ABC\dots$ sequence) are occupied, while, in the hcp lattice ($2H$ polytype), only two positions exist with the $AB\dots$ sequence displaced by $(1/3)\langle 1\bar{1}00 \rangle$ relative to one another. In all the other hexagonal polytypes, the third (C) position is also occupied, and the lattice has a certain “hexagonality.” Thus, the $4H$ -SiC polytype with $ABCB\dots$ packing has 75% of hexagonality, while $6H$ -SiC with the $ABCACB\dots$ packing has only 66% of hexagonality. The difference in the free energies of different polytypes is often quite insignificant [2–4] and, hence, the packing can readily be changed thus producing stacking faults. The lines limiting the change in the packing of the $\{111\}$ planes in fcc crystals are the glide Shockley partial dislocations with the $(1/6)\langle 11\bar{2} \rangle$ -type Burgers vectors \mathbf{b} . In the hcp lattice, the corresponding partial dislocations in (0001) planes are characterized by the $(1/3)\langle 01\bar{1}0 \rangle$ -type Burgers vectors. Stacking faults can arise due to the nucleation and motion of individual partial dislocations or due to splitting of a perfect dislocations into two partial ones. The width of a stacking fault is determined by the balance between the repulsion of the two similarly charged partial dis-

locations and their mutual attraction due to an increase in the free lattice energy due to the presence of a stacking fault [5]. If the difference between the free energies of different polytypes is small, a perfect dislocation is split in such a way that both partial dislocations are resolved in the micrograph as, e.g., in the micrograph of a ZnS crystal [6]. In SiC with the pronounced polytypism, the “widely” split dislocations are observed in both cubic and hexagonal phases [7–10].

According to the transmission electron microscopy (TEM) data, the stacking-fault energy in the basal plane of deformed bulk samples consisting of the $4H$ and the $6H$ SiC hexagonal polytypes are equal to (14.7 ± 2.5) mJ/m² for $4H$ -SiC [9] and 2.5 mJ/m² [7] and (2.9 ± 0.5) mJ/m² [10] for $6H$ -SiC. The 3C-SiC-polytype samples deformed at high temperature showed not only perfect $(1/2)\langle 110 \rangle$ -type dislocations split into Shockley partial dislocations [8] but also individual Shockley dislocations. As far as we know, the structure of as-grown dislocation in the 3C-SiC films has not been studied in detail as yet.

The dislocation parameters (including the Burgers vector and the direction of the dislocation line relative to its Burgers vector) determine the structure of the dislocation core. Although the electrical activity of the dislocations in semiconductors can be explained by different reasons [11], the electrical state of dislocations in semiconductors can depend on the structure of dislocation core [12] and influence the optical and electrical properties of the semiconductors [13, 14]. Our research is aimed at detailed investigation of the types of dislocations in the 3C-SiC films on silicon substrates with pronounced stacking faults which are intersected and form numerous dislocations.

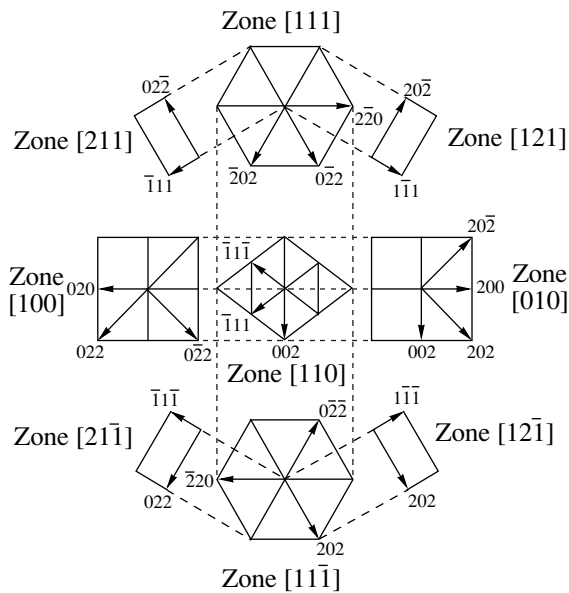


Fig. 1. Schematic location of the crystallographic zones and the diffraction vectors used for determining the Burgers vector.

EXPERIMENTAL

Three-micrometer-thick SiC-3C films were grown by molecular beam epitaxy (MBE) on Si(111) substrates, with the mismatch being 18%. The cross sections of the films with the normal being parallel to [110] direction for TEM studies were prepared by standard techniques including mechanical polishing, thinning, and etching with Ar ions. The samples were examined on a JEM-2000FX electron microscope. Burgers vectors of dislocations were determined from a set of the dark-field images obtained in weak beams, which corresponded to the zone axes whose mutual arrangement is illustrated by Fig. 1. We used the reflections from the planes of the [110] zone, two $\langle 111 \rangle$ zones, four $\langle 112 \rangle$ zones, and two $\langle 100 \rangle$ zones, which were observed in the tilt range of the goniometer ($X = \pm 45^\circ$ and $Y = \pm 36^\circ$).

DETERMINATION OF BURGERS VECTOR

In order to determine Burgers vectors \mathbf{b} and types of partial dislocations in cubic 3C-SiC films we developed a special procedure for unambiguous determination of Burgers vectors in an fcc lattice with the use of the well-known intensity criterion of the image based on the consideration of the scalar product \mathbf{gb} [15], where \mathbf{g} is the diffraction vector. First, it is necessary to distinguish the Shockley and the sessile partial dislocations. This presents no difficulties because Shockley dislocation limits individual stacking faults, while sessile dislocations are formed due to intersections of stacking fault. In order to determine the directions of the Burgers vectors we compared the contrast from dislocations

obtained in weak beams with the calculated $|\mathbf{gb}|$ values, because the $|\mathbf{gb}|^2$ value is proportional to the contrast of the dislocation image [15–17].

The $|\mathbf{gb}|$ values calculated for the twelve possible Burgers vectors \mathbf{b} of Shockley dislocations in the fcc lattice are listed in Table 1. It is evident that the Burgers vector \mathbf{b} of each Shockley dislocation from the twelve $(1/6)\langle 112 \rangle$ Burgers vectors \mathbf{b} can be determined unambiguously. However, in practice the choice of Burgers vectors for dislocations with close \mathbf{gb} values for a number of reflections (e.g., for $\mathbf{gb} = 0$ and $|\mathbf{gb}| = 1/3$) and, hence, with low difference in the image contrast can be somewhat ambiguous. If the stacking-fault plane (one of the four $\{111\}$ planes) is known, the unambiguous determination of the Burgers vector of an individual Shockley dislocation limiting the given stacking fault is substantially simplified, because the number of the possible Burgers vectors of the given Shockley dislocation is reduced from 12 to 3. Then, the true vector can be easily chosen with the aid of a set of reflections from Table 1. The determination of the stacking-fault plane presents no problem. Indeed, two of the four $\{111\}$ planes, $(\bar{1}\bar{1}1)$ and $(\bar{1}1\bar{1})$, parallel to the beam passing along the [110] direction can be determined directly from the electron diffraction pattern. The remaining (111) and $(11\bar{1})$ planes can be distinguished by measuring the change in the width of the image of the stacking fault projection along the displacement direction on the electron diffraction pattern of the [111] or $[11\bar{1}]$ poles for a tilt sample.

In fcc lattice, nine stable sessile partial dislocations are possible (six with the $(1/6)\langle 110 \rangle$ -type Burgers vector and three with the $(1/3)\langle 001 \rangle$ Burgers vectors), which are considered as the result of the reactions between the corresponding Shockley partial dislocations. Table 2 lists all the possible reactions resulting in the formation of these nine sessile dislocations. It is seen that for each pair of the intersecting $\{111\}$ planes, two reactions between Shockley partial dislocations lying in these planes lead to the formation of dislocations with the same $(1/6)\langle 110 \rangle$ Burgers vectors, while the two other reactions, lead to the formation of dislocations with the same $(1/3)\langle 001 \rangle$ Burgers vectors. The two types of Burgers vectors can be distinguished by comparing the experimental contrast with the calculated $|\mathbf{gb}|$ values (Table 3).

RESULTS AND DISCUSSION

The defect structure of the 3C-SiC samples studied consists of stacking faults with 10^8 – 10^9 cm⁻² density, numerous glide partial dislocations limiting the nonintersecting stacking faults, and sessile dislocations formed due to the intersections of stacking faults of different widths and shapes (Figs. 2, 3).

Table 1. Calculated $|\mathbf{gb}|$ values for Shockley partial dislocations

Stacking-fault plane	\mathbf{b}	\mathbf{g}									
		002	200	020	111	$1\bar{1}1$	$2\bar{2}0$	$\bar{2}02$	$02\bar{2}$	202	022
(111)	$\mathbf{b}_{10} = \frac{1}{6}[1\bar{2}1]$	$\frac{1}{3}$	$\frac{1}{3}$	$\frac{2}{3}$	$\frac{1}{3}$	$\frac{2}{3}$	1	0	1	$\frac{2}{3}$	$\frac{1}{3}$
	$\mathbf{b}_{11} = \frac{1}{6}[11\bar{2}]$	$\frac{2}{3}$	$\frac{1}{3}$	$\frac{1}{3}$	$\frac{1}{3}$	$\frac{1}{3}$	0	1	1	$\frac{1}{3}$	$\frac{1}{3}$
	$\mathbf{b}_{12} = \frac{1}{6}[\bar{2}11]$	$\frac{1}{3}$	$\frac{2}{3}$	$\frac{1}{3}$	$\frac{2}{3}$	$\frac{1}{3}$	1	1	0	$\frac{1}{3}$	$\frac{2}{3}$
$(\bar{1}\bar{1}1)$	$\mathbf{b}_7 = \frac{1}{6}[2\bar{1}\bar{1}]$	$\frac{1}{3}$	$\frac{2}{3}$	$\frac{1}{3}$	$\frac{1}{3}$	0	$\frac{1}{3}$	1	$\frac{2}{3}$	$\frac{1}{3}$	0
	$\mathbf{b}_1 = \frac{1}{6}[121]$	$\frac{1}{3}$	$\frac{1}{3}$	$\frac{2}{3}$	$\frac{1}{3}$	0	$\frac{1}{3}$	0	$\frac{1}{3}$	$\frac{2}{3}$	1
	$\mathbf{b}_3 = \frac{1}{6}[\bar{1}12]$	$\frac{2}{3}$	$\frac{1}{3}$	$\frac{1}{3}$	$\frac{2}{3}$	0	$\frac{2}{3}$	1	$\frac{1}{3}$	$\frac{1}{3}$	1
$(11\bar{1})$	$\mathbf{b}_4 = \frac{1}{6}[\bar{1}21]$	$\frac{1}{3}$	$\frac{1}{3}$	$\frac{2}{3}$	$\frac{2}{3}$	$\frac{1}{3}$	1	$\frac{2}{3}$	$\frac{1}{3}$	0	1
	$\mathbf{b}_8 = \frac{1}{6}[2\bar{1}1]$	$\frac{1}{3}$	$\frac{2}{3}$	$\frac{1}{3}$	$\frac{1}{3}$	$\frac{2}{3}$	1	$\frac{1}{3}$	$\frac{2}{3}$	1	0
	$\mathbf{b}_2 = \frac{1}{6}[112]$	$\frac{2}{3}$	$\frac{1}{3}$	$\frac{1}{3}$	$\frac{1}{3}$	$\frac{1}{3}$	0	$\frac{1}{3}$	$\frac{1}{3}$	1	1
$(\bar{1}11)$	$\mathbf{b}_5 = \frac{1}{6}[211]$	$\frac{1}{3}$	$\frac{2}{3}$	$\frac{1}{3}$	0	$\frac{1}{3}$	$\frac{1}{3}$	$\frac{1}{3}$	0	1	$\frac{2}{3}$
	$\mathbf{b}_9 = \frac{1}{6}[1\bar{1}2]$	$\frac{2}{3}$	$\frac{1}{3}$	$\frac{1}{3}$	0	$\frac{2}{3}$	$\frac{2}{3}$	$\frac{1}{3}$	1	1	$\frac{1}{3}$
	$\mathbf{b}_6 = \frac{1}{6}[12\bar{1}]$	$\frac{1}{3}$	$\frac{1}{3}$	$\frac{2}{3}$	0	$\frac{1}{3}$	$\frac{1}{3}$	$\frac{2}{3}$	1	0	$\frac{1}{3}$

Shockley dislocations. The upper part of Fig. 2 shows individual stacking faults 1, 2, and 3 bounded by Shockley partial dislocations. The widths of stacking faults 1 and 2 are nonuniform. The plane of location of these stacking faults, (111), was determined by the technique described above. Now, compare the contrast of the partial dislocations a – d limiting stacking faults 1 and 2 with the products \mathbf{gb} for the three possible $\langle 112 \rangle/6$ -type Burgers vectors of Shockley dislocations in the (111) plane given in Table 1. The high contrast of the a and c dislocations is seen only in Figs. 2d and 2e.

Using Table 1, one can choose the vector $\mathbf{b} = 1/6[\bar{2}11]$ for partial dislocations a and c unambiguously, because these dislocations show high contrast ($|\mathbf{gb}| = 1$) in the $2\bar{2}0$ (Fig. 2d) and the $\bar{2}02$ (Fig. 2e) reflections. At the same time, the image of the stacking fault disappears, which indicates that the product \mathbf{gb} is an integer. This choice is consistent with a pronounced contrast of the a and c dislocations in the 022 and the $\bar{1}11$ reflections

(Figs. 2a–2c), because, in these cases, $|\mathbf{gb}| = 2/3$ (see Table 1). For two other Burgers vectors possible in the (111) plane, the $|\mathbf{gb}|$ value for these reflections is $1/3$, which corresponds to a low contrast or even its complete absence.

The similar analysis showed the Burgers vector of the b and d dislocations is $\mathbf{b} = 1/6[1\bar{2}1]$. As follows from Table 1, only in this case, these dislocations should be invisible in the $\bar{2}02$ reflection ($\mathbf{gb} = 0$), in full accordance with the image in Fig. 2e. The correctness of such a choice of the Burgers vector \mathbf{b} is confirmed by a rather high contrast of the b and d dislocations in the $1\bar{1}1$ reflection (see Fig. 2b) consistent with the value $|\mathbf{gb}| = 2/3$ calculated for this reflection. For two other possible Burgers vectors $|\mathbf{gb}| = 1/3$ (i.e., is rather low). This choice is also supported by the correlation between the images of the b and d dislocations in the 022, $2\bar{2}0$, and $\bar{1}11$ reflections (Figs. 2a, 2c, and 2d)

Table 2. Types and directions of the Burgers vectors of the sessile partial dislocations formed due to the reaction between Shockley partial dislocations at the intersection of the stacking faults lying in the {111} planes of the fcc lattice

Planes of intersection of stacking faults	Reactions between Shockley dislocations	Sessile partial dislocation
1 × 2	$\mathbf{b}_1 - \mathbf{b}_2 = \frac{1}{6} [121] + \frac{1}{6} [\bar{1}\bar{1}\bar{2}]$ $-\mathbf{b}_3 + \mathbf{b}_4 = \frac{1}{6} [1\bar{1}\bar{2}] + \frac{1}{6} [\bar{1}21]$	$\frac{1}{6} [01\bar{1}]$
3 × 1	$\mathbf{b}_5 - \mathbf{b}_1 = \frac{1}{6} [211] + \frac{1}{6} [\bar{1}\bar{2}\bar{1}]$ $-\mathbf{b}_6 + \mathbf{b}_7 = \frac{1}{6} [\bar{1}\bar{2}1] + \frac{1}{6} [12\bar{1}]$	$\frac{1}{6} [1\bar{1}0]$
2 × 3	$\mathbf{b}_2 - \mathbf{b}_5 = \frac{1}{6} [112] + \frac{1}{6} [\bar{2}\bar{1}\bar{1}]$ $-\mathbf{b}_8 + \mathbf{b}_9 = \frac{1}{6} [\bar{2}1\bar{1}] + \frac{1}{6} [1\bar{1}2]$	$\frac{1}{6} [\bar{1}01]$
4 × 3	$-\mathbf{b}_{10} + \mathbf{b}_9 = \frac{1}{6} [\bar{1}2\bar{1}] + \frac{1}{6} [1\bar{1}2]$ $\mathbf{b}_6 - \mathbf{b}_{11} = \frac{1}{6} [12\bar{1}] + \frac{1}{6} [\bar{1}\bar{1}2]$	$\frac{1}{6} [011]$
4 × 2	$-\mathbf{b}_{12} + \mathbf{b}_4 = \frac{1}{6} [2\bar{1}\bar{1}] + \frac{1}{6} [\bar{1}21]$ $-\mathbf{b}_{10} + \mathbf{b}_8 = \frac{1}{6} [\bar{1}2\bar{1}] + \frac{1}{6} [2\bar{1}1]$	$\frac{1}{6} [110]$
1 × 4	$\mathbf{b}_3 - \mathbf{b}_{12} = \frac{1}{6} [\bar{1}12] + \frac{1}{6} [2\bar{1}\bar{1}]$ $\mathbf{b}_7 - \mathbf{b}_{11} = \frac{1}{6} [21\bar{1}] + \frac{1}{6} [\bar{1}\bar{1}2]$	$\frac{1}{6} [101]$
1 × 3	$\mathbf{b}_1 - \mathbf{b}_6 = \frac{1}{6} [121] + \frac{1}{6} [\bar{1}\bar{2}1]$ $\mathbf{b}_5 - \mathbf{b}_7 = \frac{1}{6} [211] + \frac{1}{6} [\bar{2}\bar{1}1]$	$\frac{1}{3} [001]$
2 × 4	$\mathbf{b}_4 + \mathbf{b}_{10} = \frac{1}{6} [\bar{1}21] + \frac{1}{6} [1\bar{2}1]$ $\mathbf{b}_8 + \mathbf{b}_{12} = \frac{1}{6} [2\bar{1}1] + \frac{1}{6} [\bar{2}11]$	
2 × 1	$\mathbf{b}_2 - \mathbf{b}_3 = \frac{1}{6} [112] + \frac{1}{6} [1\bar{1}\bar{2}]$ $\mathbf{b}_1 - \mathbf{b}_4 = \frac{1}{6} [121] + \frac{1}{6} [1\bar{2}\bar{1}]$	$\frac{1}{3} [100]$
3 × 4	$\mathbf{b}_6 + \mathbf{b}_{10} = \frac{1}{6} [12\bar{1}] + \frac{1}{6} [1\bar{2}1]$ $\mathbf{b}_9 + \mathbf{b}_{11} = \frac{1}{6} [1\bar{1}2] + \frac{1}{6} [11\bar{2}]$	

Table 2. (Contd.)

Planes of intersection of stacking faults	Reactions between Shockley dislocations	Sessile partial dislocation
2 × 3	$\mathbf{b}_2 - \mathbf{b}_9 = \frac{1}{6} [112] + \frac{1}{6} [\bar{1} 1 \bar{2}]$ $\mathbf{b}_5 - \mathbf{b}_8 = \frac{1}{6} [211] + \frac{1}{6} [\bar{2} 1 \bar{1}]$	$\frac{1}{3} [010]$
1 × 4	$\mathbf{b}_3 + \mathbf{b}_{11} = \frac{1}{6} [\bar{1} 12] + \frac{1}{6} [11\bar{2}]$ $\mathbf{b}_7 + \mathbf{b}_{12} = \frac{1}{6} [21\bar{1}] + \frac{1}{6} [\bar{2} 11]$	

Plane notation: 1 stands for (1 $\bar{1}$ 1), 2, for (11 $\bar{1}$), 3, for ($\bar{1}$ 11), and 4, for (111).

Table 3. Calculated $|\mathbf{g}\mathbf{b}|$ values for the sessile partial dislocations

b		g									
type	direction	002	200	020	111	1 $\bar{1}$ 1	220	$\bar{2}$ 02	02 $\bar{2}$	202	022
$\frac{1}{6} \langle 011 \rangle$	$\frac{1}{6} [01\bar{1}]$	$\frac{1}{3}$	0	$\frac{1}{3}$	0	$\frac{1}{3}$	$\frac{1}{3}$	$\frac{1}{3}$	$\frac{2}{3}$	$\frac{1}{3}$	0
	$\frac{1}{6} [1\bar{1}0]$	0	$\frac{1}{3}$	$\frac{1}{3}$	$\frac{1}{3}$	$\frac{1}{3}$	$\frac{2}{3}$	$\frac{1}{3}$	$\frac{1}{3}$	$\frac{1}{3}$	$\frac{1}{3}$
	$\frac{1}{6} [\bar{1}01]$	$\frac{1}{3}$	$\frac{1}{3}$	0	$\frac{1}{3}$	0	$\frac{1}{3}$	$\frac{2}{3}$	$\frac{1}{3}$	0	$\frac{1}{3}$
	$\frac{1}{6} [011]$	$\frac{1}{3}$	0	$\frac{1}{3}$	$\frac{1}{3}$	0	$\frac{1}{3}$	$\frac{1}{3}$	0	$\frac{1}{3}$	$\frac{2}{3}$
	$\frac{1}{6} [110]$	0	$\frac{1}{3}$	$\frac{1}{3}$	0	0	0	$\frac{1}{3}$	$\frac{1}{3}$	$\frac{1}{3}$	$\frac{1}{3}$
	$\frac{1}{6} [101]$	$\frac{1}{3}$	$\frac{1}{3}$	0	0	$\frac{1}{3}$	$\frac{1}{3}$	0	$\frac{1}{3}$	$\frac{2}{3}$	$\frac{1}{3}$
$\frac{1}{3} \langle 001 \rangle$	$\frac{1}{3} [001]$	$\frac{2}{3}$	0	0	$\frac{1}{3}$	$\frac{1}{3}$	0	$\frac{2}{3}$	$\frac{2}{3}$	0	$\frac{2}{3}$
	$\frac{1}{3} [010]$	0	0	$\frac{2}{3}$	$\frac{1}{3}$	$\frac{1}{3}$	$\frac{2}{3}$	0	$\frac{2}{3}$	$\frac{2}{3}$	$\frac{2}{3}$
	$\frac{1}{3} [100]$	0	$\frac{2}{3}$	0	$\frac{1}{3}$	$\frac{1}{3}$	$\frac{2}{3}$	$\frac{2}{3}$	0	$\frac{2}{3}$	0

and the calculated $|\mathbf{g}\mathbf{b}|$ values (Table 1): the high contrast in the 022 and $\bar{2}20$ reflections ($|\mathbf{g}\mathbf{b}| = 1$), and weak (or absent) contrast in $\bar{1}11$ reflection ($|\mathbf{g}\mathbf{b}| = 1/3$).

The splitting width of the stacking fault 3 (Fig. 2) bounded by the Shockley dislocations *e* and *f* is more uniform. This stacking fault is located in the (11 $\bar{1}$) plane, as was established by change in the width of its projection at the known tilt. The use of our procedure

for determining Burgers vector gave the value $\mathbf{b} = 1/6[112]$ for the dislocation *e* and $\mathbf{b} = 1/6[\bar{1}21]$ for the dislocation *f*. The width of nonintersecting stacking faults in 3C-SiC can be as high as 2 μm .

Shockley partial dislocations can arise by two ways: first, as a result of the splitting of a perfect dislocation with the Burgers vector $\langle 110 \rangle/2$ (stacking faults 1 and 2 are formed by the reaction $[1\bar{1}0]/2 \rightarrow [\bar{2}11]/6 + [1\bar{2}1]/6$; stacking fault 3, by reaction $[011]/2 \rightarrow 1/6[112] +$

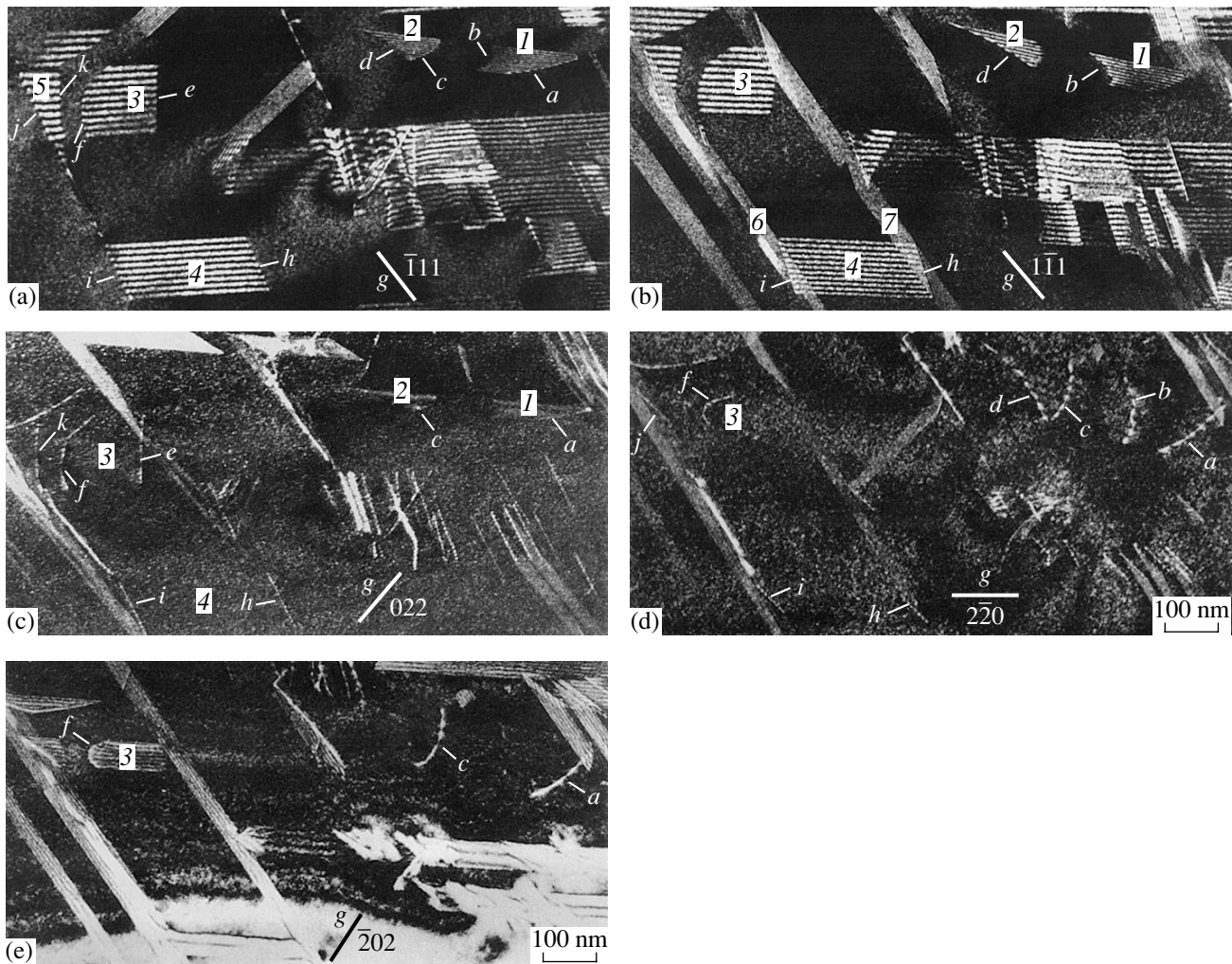


Fig. 2. Weak-beam dark-field images of the Shockley partial dislocations (*a* and *b*) stacking fault 1, (*c* and *d*) stacking fault 2, (*e* and *f*) stacking fault 3, and (*k*) stacking fault 5, (*h* and *i*) the sessile partial dislocations stacking fault 4 and (*j*) stacking fault 5 formed at the intersection of the stacking faults 4 and 5 with the stacking faults 6 and 7. Reflections correspond to the crystallographic zones (a) $[12\bar{1}]$, (b) $[21\bar{1}]$, (c) $[11\bar{1}]$, and (d, e) $[111]$.

$1/6[\bar{1}21]$) and, second, via nucleation of a dislocation at an interface. In the first case, a stacking fault is limited by two partial dislocations; in the second case, only one partial dislocation with the stacking fault bounded by this dislocation can move from the interface. In the above examples, each stacking fault is bounded by two partials and, therefore, one can assume that the Shockley dislocations *a* and *b* (stacking fault 1), *c* and *d* (stacking fault 2), and *e* and *f* (stacking fault 3) are formed due to the splitting of the perfect dislocations.

We estimated the stacking-fault energy γ from the split Δ between two Shockley dislocations formed due to splitting of a perfect glide dislocation, using the well-known relation

$$\gamma = \frac{\mu \mathbf{b}_1 \mathbf{b}_2 (2 - \nu)}{8\pi\Delta(1 - \nu)} \left[1 - \frac{2\nu}{2 - \nu} \cos(2\alpha) \right],$$

where μ is the shear modulus, \mathbf{b}_1 and \mathbf{b}_2 are the Burgers vectors of the partials, α is the angle between the dislocation line and the Burgers vector of the perfect dislocation, and ν is Poisson's ratio. The energy was found to range from 0.1 to 2 mJ/m²; i.e., its value is low in comparison with the γ values for elemental semiconductors and most of the semiconductors with the sphalerite- and wurtzite-type lattices. The wide range of the stacking-fault widths can be attributed to the effect of internal stresses in a growing film. This effect is important if the interaction between partial dislocations is comparable with that of their interaction with the external stress, which can be the case for the pronouncedly split dislocations. Our estimate of the stacking-fault energy is consistent with the value $\gamma \approx 0.2$ mJ/m², determined from the images of split dislocations in cubic SiC [8]. The stacking fault energies obtained in cubic SiC are lower than the energies for

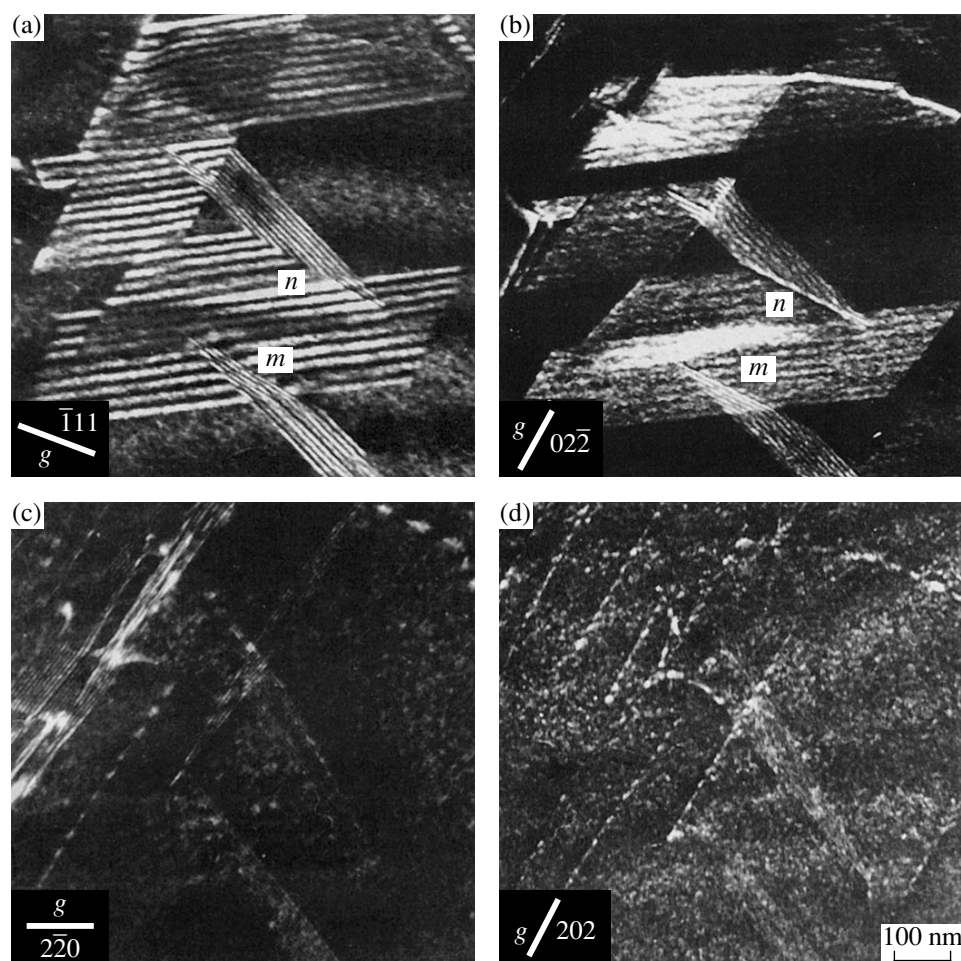


Fig. 3. Weak-beam dark-field images of stacking faults 1–4, whose intersection results in the formation of partial dislocations *m* and *n* in the (a) $\bar{1}11$, (b) $02\bar{2}$, (c) $2\bar{2}0$, and (d) 202 reflections.

6H-SiC and 4H-SiC polytypes [9], which is explained by the lower stability of the cubic polytype (i.e., lower than that of the hexagonal ones) [2–4].

Sessile partial dislocations. Stacking faults often “propagate” up to the intersections with stacking faults from the other $\{111\}$ slip planes (see the intersection of stacking fault 4 with the two parallel stacking faults in Fig. 2 and the intersection of stacking faults 1 and 2 with stacking faults 3 and 4 in Fig. 3), which results in the formation of sessile partial dislocations. There are two types of stable Burgers vectors of the sessile dislocations in an fcc lattice— $\mathbf{b} = \langle 011 \rangle / 6$ and $\mathbf{b} = \langle 001 \rangle / 3$, and both are typical of the 3C-SiC films studied (which will be shown below).

Dislocations with $\mathbf{b} = \langle 011 \rangle / 6$. The images of the stacking faults (obtained in various reflections) that, intersecting, form sessile partial dislocations are shown in Figs. 3a–3d. Consider the *m* and *n* partials formed by intersection of two parallel stacking faults, 1 and 2, lying in the $(1\bar{1}\bar{1})$ plane with the two mutually parallel stacking faults 3 and 4 lying in the $(1\bar{1}1)$ plane (Fig. 4a).

The possible reactions between four Shockley partials in the intersecting planes $(1\bar{1}\bar{1})$ and $(\bar{1}11)$ are indicated in Table 2 (the planes are denoted by 1 and 2). As a result, the sessile dislocations with the shortest $\langle 011 \rangle / 6$ - and $\langle 001 \rangle / 3$ Burgers vectors are formed,

$$\mathbf{b}_1 - \mathbf{b}_2 = \mathbf{b}_4 - \mathbf{b}_3 = [01\bar{1}] / 6,$$

$$\mathbf{b}_2 - \mathbf{b}_3 = \mathbf{b}_1 - \mathbf{b}_4 = [100] / 3.$$

To choose the correct Burgers vector of the above two, for *m* and *n* dislocations, consider the dislocation images. It is seen from Fig. 3b that both dislocations are clearly visible in the $02\bar{2}$ reflection and, therefore (Table 3), their Burgers vector is $\mathbf{b} = [01\bar{1}] / 6$ ($|\mathbf{g}\mathbf{b}| = 2/3$) and not $\mathbf{b} = [100] / 3$ (for which $\mathbf{g}\mathbf{b} = 0$). This conclusion is consistent with their disappearance in the $2\bar{2}0$ and 202 reflections (Figs. 3c, 3d) in full accordance with the calculated value $|\mathbf{g}\mathbf{b}| = 1/3$ (Table 3). The vector $\mathbf{b} = [100] / 3$ corresponds to a higher value, $|\mathbf{g}\mathbf{b}| = 2/3$, at which the contrast of *m* and *n* dislocations should be noticeable.

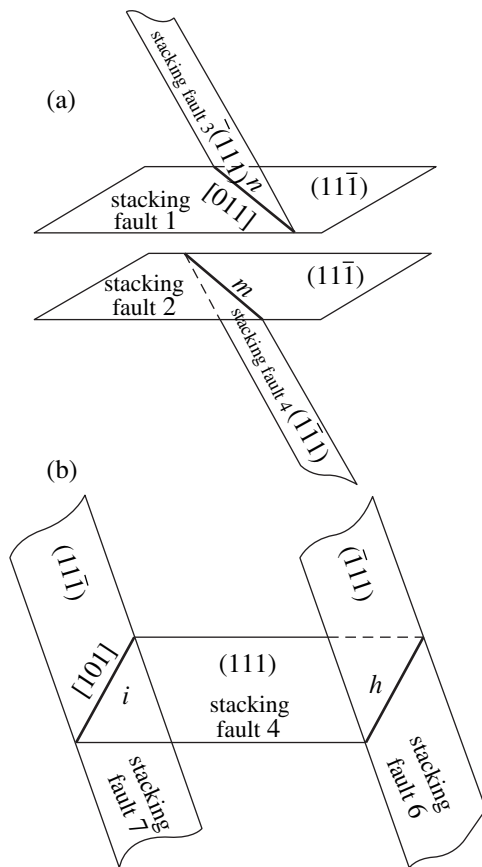


Fig. 4. Schematic location of (a) stacking faults 1–4 shown in Fig. 3 intersecting to form sessile partial dislocations m and n with the $\langle 110 \rangle/6$ -type Burgers vector and (b) stacking faults 4, 6, and 7 shown in Fig. 2 intersecting to form sessile partial dislocations i and h with the $\langle 100 \rangle/3$ Burgers vector.

Dislocations with $\mathbf{b} = \langle 001 \rangle/3$. Now, determine Burgers vector of i and h dislocations (Fig. 2) formed by intersecting stacking fault 4 in the $(\bar{1}\bar{1}1)$ plane and mutually parallel stacking faults 6 and 7 in the $(1\bar{1}\bar{1})$ plane (Fig. 4b). According to Table 2, the following reactions between the dislocations with the \mathbf{b}_2 , \mathbf{b}_4 , and \mathbf{b}_8 Burgers vectors in the $(11\bar{1})$ plane and \mathbf{b}_5 , \mathbf{b}_6 , and \mathbf{b}_9 Burgers vectors in the $(1\bar{1}\bar{1})$ plane should be considered:

$$\mathbf{b}_2 - \mathbf{b}_5 = \mathbf{b}_9 - \mathbf{b}_8 = [\bar{1}01]/6,$$

$$\mathbf{b}_2 - \mathbf{b}_9 = \mathbf{b}_5 - \mathbf{b}_8 = [010]/3.$$

As both i and h dislocations are invisible in the $\bar{2}02$ reflection (Fig. 2e), the $\mathbf{b} = [010]/3$ Burgers vector ($\mathbf{g}\mathbf{b} = 0$, Table 3) and not $\mathbf{b} = [\bar{1}01]/6$ ($|\mathbf{g}\mathbf{b}| = 2/3$) should be chosen, which agrees with the high contrast in the 002 and $2\bar{2}0$ reflections in Figs. 2c and 2d ($|\mathbf{g}\mathbf{b}| = 2/3$ for $\mathbf{b} = [010]/3$, while for $\mathbf{b} = [\bar{1}01]/6$ the calculated value is $|\mathbf{g}\mathbf{b}| = 1/3$).

Stacking fault 5 in the top left corner in Figs. 2a–2e intersects the stacking fault in the $(1\bar{1}\bar{1})$ plane to form the sessile partial dislocation j with $\mathbf{b} = [010]/3$ bounded by the Shockley dislocation k with $\mathbf{b} = 1/6[112]$ on the other side.

In fact, the sessile partial dislocations with the Burgers vectors $\langle 110 \rangle/6$ and $\langle 100 \rangle/3$ are edge dislocations. As the core structure and the energy level of the dislocation in the forbidden band are determined mainly by the dislocation type (sessile or glide) and the orientation of the dislocation line with respect to its Burgers vector, it is possible to assume that unlike the glide dislocations (characterized by the wide range of orientations with respect to their Burgers vectors), sessile dislocations would have fixed levels in the forbidden band. However, neither the electrical nor the optical activity of Shockley and sessile partial dislocations in SiC have been discussed as yet.

CONCLUSIONS

It has been shown by TEM studies that silicon carbide films on Si(111) substrates contain stacking faults, partial glide dislocations limiting nonintersecting stacking faults, and sessile dislocations formed by intersections of stacking faults. It is also shown that stacking faults bounded by the Shockley partial dislocations have the widths ranging from ≈ 100 nm to ≈ 2 μm , which corresponds to the stacking-fault energies 0.1–2.0 mJ/m^2 . The sessile partial dislocations formed by intersecting stacking faults in different $\{111\}$ planes have the Burgers vectors $\langle 100 \rangle/3$ and $\langle 110 \rangle/6$ normal to the corresponding dislocation lines along $\langle 110 \rangle$ directions.

The procedure developed provides the determination of any possible Burgers vector of both Shockley and sessile partial dislocations formed by intersecting stacking faults in fcc crystals. This procedure can be especially useful in studying thin films usually containing dislocations with all possible Burgers vectors (contrary to dislocations induced by deformation of bulk materials, where only some preferable orientations of the Burgers vectors and dislocation lines can be obtained).

REFERENCES

1. H. Baumhauer, *Z. Kristallogr.* **50**, 33 (1912).
2. S. Limpijumngong and W. R. L. Lamprecht, *Phys. Rev. B* **57**, 12017 (1998).
3. A. Fissel, *J. Cryst. Growth* **212**, 438 (2000).
4. A. Fissel, B. Schroter, U. Kaiser, and W. Richter, *Appl. Phys. Lett.* **77**, 2418 (2000).
5. H. Siethoff and H. Alexander, *Phys. Status Solidi* **6**, 165 (1964).
6. A. V. Zaretskii, Yu. A. Ossipyan, I. I. Khodos, *et al.*, *Philos. Mag. A* **48**, 279 (1983).

7. K. Maeda, K. Suzuki, S. Fujita, *et al.*, *Philos. Mag. A* **57**, 573 (1988).
8. X. J. Ning and P. Pirouz, *J. Mater. Res.* **11**, 884 (1996).
9. M. H. Hong, A. V. Samant, V. Orlov, *et al.*, *Mater. Res. Soc. Symp. Proc.* **572** (1999).
10. M. H. Hong, A. V. Samant, and P. Pirouz, *Philos. Mag. A* **80**, 919 (2000).
11. S. Nakamura, *Group III Nitride Semiconductor Compounds* (Oxford Univ. Press, Oxford, 1998).
12. Yu. A. Ossipyan, V. T. Petrenko, A. V. Zaretskii, and R. Witworth, *Adv. Phys.* **35**, 115 (1986).
13. E. F. Schubert, L. D. Goepfert, and J. M. Redwing, *Appl. Phys. Lett.* **71**, 3224 (1997).
14. U. Kaiser, A. N. Gruzintsev, I. I. Khodos, and W. Richter, *Inorg. Mater.* **36**, 720 (2000).
15. P. B. Hirsch, A. Howie, R. B. Nicholson, D. W. Pashley, and M. J. Whelan, *Electron Microscopy of Thin Crystals* (Plenum, New York, 1965; Mir, Moscow, 1968).
16. D. J. H. Cockayne, *Z. Naturforsch. A* **27**, 452 (1972).
17. D. J. H. Cockayne, I. L. F. Ray, and M. J. Whelan, *Philos. Mag. A* **20**, 1265 (1969).

Translated by A. Zolot'ko

REAL STRUCTURE
OF CRYSTALS

Heterometry-Induced Defects and Stresses in Isomorphously Mixed Crystals of Varying Composition¹

M. A. Kuz'mina, S. V. Moshkin, and I. P. Shakhverdova

St. Petersburg State University, Universitetskaya nab. 7/9, St. Petersburg, 199164 Russia

Received May 17, 2000

Abstract—The comparative study of the distribution and density of dislocations and cracks in isomorphously mixed potassium–rubidium biphthalate crystals grown under the conditions of discrete and continuous changes of the solution composition with time. The method is developed for calculating the heterometry-induced internal stresses and the character of their variation in a crystal during its growth. It is established that formation of dislocations, cracks, and interzonal inclusions is associated with the effect of the heterometry-induced stresses, whereas the number of defects depends on the values of these stresses varying during crystal growth. © 2001 MAIK “Nauka/Interperiodica”.

INTRODUCTION

It is well known that nonuniform capture of isomorphous impurities by different parts of the crystal leads to incommensurability of the three-dimensional lattices of these parts (heterometry) and provides the formation and relaxation of internal stresses at defects [1–4]. Defect formation depends not only on the stress values but also on their signs and configurations [5]. We had the aim to reveal and study both similar and distinctive features of crystal defects at the discrete and the continuous variation of their composition on an example of isomorphously mixed potassium–rubidium biphthalate crystals.

Potassium–rubidium biphthalate crystals were grown from aqueous solutions by the method of temperature decrease in the dynamic mode [6, 7] under a constant relative supersaturation ($\Delta C/C_0 \approx 0.06$) with due regard for the dependence of the solubility on the temperature and the composition of the solution [6] and the variation of the crystal mass in time. The bizonal crystals with a discrete change in the compositions were obtained. They consisted of the internal zone (a plate with the (110) and (111) faces and the dimensions of $15 \times 20 \text{ mm}^2$ in the (010) plane and 2 mm in thickness cleaved along the cleavage plane) and the external zone (a 2–10 mm-thick layer extended or compressed in comparison with the internal zone). Since the change in the rubidium content gives rise to the changes the lattice parameters [6, 7], the heterometry-induced internal stresses arise at the zone boundaries [2]. We also grew the gradient crystals with continuously and monotonically varying composition along the growth direction on potassium biphthalate seeds [6].

Defects in the crystals grown were studied by the methods of optic microscopy, selective etching of cleavages along the (010) pinacoid, and X-ray diffraction [7]. Crystal plasticity was characterized by the dislocation density ρ (the number of pyramidal etching pits per unit area of the crystal cleavage along (010) with due regard for the angle formed by the (010) plane and the face under study). The brittleness was characterized by the cracking coefficient K (the total area of the surfaces of the crack mirrors located in the crystal volume studied to the value of this volume).

HETEROMETRY-INDUCED STRESSES

In growth of a bizonal crystal, the heterometry-induced stresses at the interzonal boundary vary due to the varying thicknesses of the internal and the grown zones. In a gradient crystal, they vary due to continuous variation of the composition along the growth direction. To calculate the values and the changes in these stresses, we used the model of an infinite plane crystal-line plate consisting of the internal and two symmetric external zones parallel the face studied. In the approximation of purely elastic deformations, we minimized the total stress energy in the plate, and determined the stresses σ_{ij} in the grown layer as functions of the growth time t . For a bizonal crystal, we have

$$\sigma_{ij}(t) = c_{ijkl}h(a_{kl}^{\text{in}} - a_{kl}^{\text{out}})/(tVa_{kl}^{\text{in}} + ha_{kl}^{\text{out}}),$$

where c_{ijkl} are the components of the tensor of elastic stiffness of the crystal, h is the thickness of the internal zone, V is the linear growth rate of the face, a_{kl}^{in} and a_{kl}^{out} are the projections of the k th unit-cell parameter onto the l th principal axis of the strain tensor of the face under consideration of the internal and external layers

¹ Additional materials can be obtained on the address <http://www.chat.ru/~moshkin/defect98.htm>.

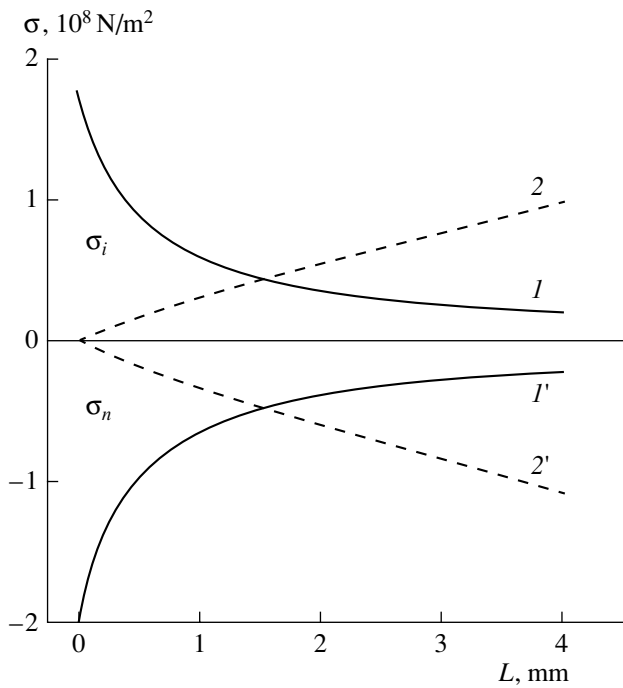


Fig. 1. Variations in the heterometry-induced stress intensities σ_i and the principal normal stress σ_n in the (010) growth sector calculated within the model of elastic stresses, at the growth front of the (1, 1') bizonal and (2, 2') gradient crystals at the maximum difference in the rubidium biphthalate concentrations (25 mol %) with an increase of the layer thickness along the direction L normal to the (010) plane.

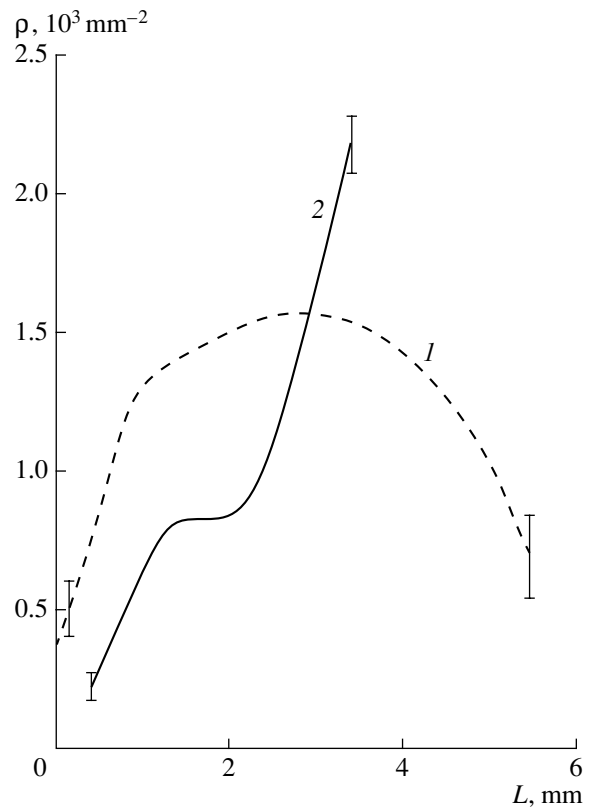


Fig. 2. The variation of the dislocation density ρ in the growth sector of the (010) pinacoid face along the growth direction L from the boundary with the seeding plate in the bizonal crystal (1) with the difference in the rubidium biphthalate concentrations for the zones equal to 2.5 mol %, and in a gradient crystal (2) with the maximum difference in the rubidium biphthalate concentration equal to 25 mol %.

in the unstressed state onto the principal axes of the strain tensor. For a gradient crystal and the linear variation of the composition in the growing layer in time, we have

$$\sigma_{ij}(t) = C_{ijkl} \left(\frac{k_{kl} a_{kl}^{in} (tV + h)}{a_{kl}^{in} V \ln((1 + k_{kl}t/a_{kl}^{in}) + k_{kl}h)} - (k_{kl}t - a_{kl}^{in}) \right) / (k_{kl}t + a_{kl}^{in}),$$

where $k_{kl} = fg_{kl}$, f is the coefficient of the linear temporal dependence of the rubidium biphthalate concentration in the crystal, g_{kl} is the coefficient of the linear dependence of the projection of the k th unit-cell parameter onto the l th principal axis of the strain tensor on the rubidium biphthalate concentration in the crystal. The expression for the stresses in the internal zone have a similar form. This model allows one to calculate the stress tensor in the plane parallel to the plane of zone intergrowth at an arbitrary point of the crystalline plate at any moment of crystal growth.

Figure 1 illustrates the calculation of the heterometry-induced stresses for a bizonal and gradient crystals in the above model. (The change of the maximum principal normal stress σ_n and the stress intensities σ_i determine the level of brittle and plastic deformation,

respectively [5]; we also took into account the experimental coefficients of rubidium distribution.) In the growth sectors of the prism (110) and bipyramid (111) faces the stresses change in the similar way. The calculation shows that, in a bizonal crystal, the stresses are the same in the whole volume of the growing zone and decrease during the growth process. In a gradient crystal, the stresses at the growth front increase in time, whereas in the bulk, their magnitude gradually decreases and, passing zero, change sign.

DISLOCATIONS, CRACKS, AND INCLUSIONS

Irrespective of the different zone compositions and the stress signs, the heterometry-induced dislocations in the bizonal and gradient crystals are concentrated in the external zones of the sectors of growing faces and are almost absent in the regions of edge growth. The analysis of the displacements of the vertices of the pyramidal etching pits in the (010) plane allowed us to evaluate the orientation of the dislocation lines in the growth sectors of various faces and to show

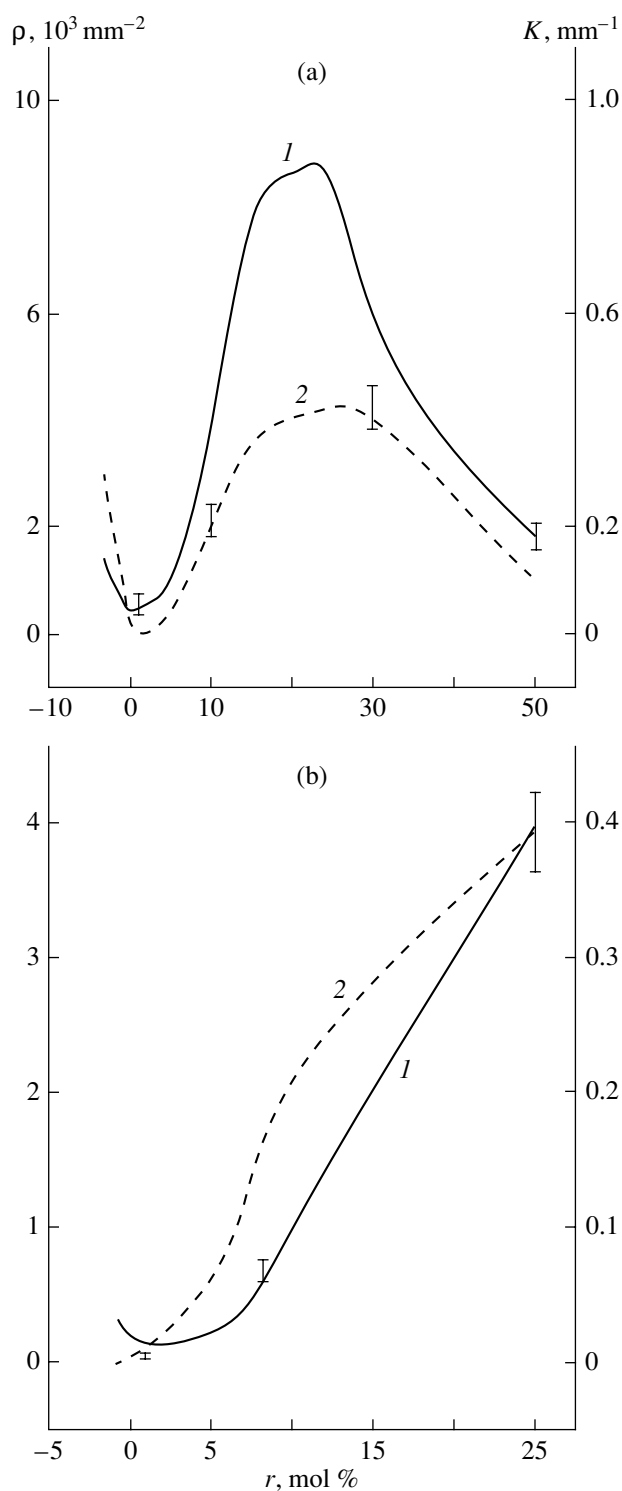


Fig. 3. Dislocation (1) densities ρ and (2) the cracking coefficient K in the growth sector of (010) pinacoid as functions of the differences in the rubidium biphthalate content in the zones (r , mol % rubidium biphthalate) of (a) bizonal crystals and the maximum difference in the rubidium impurity in the initial and final growth layers (r , mol % of rubidium biphthalate) (b) gradient potassium–rubidium biphthalate crystals.

that dislocations are practically normal to the growing faces. If the concentrations of the rubidium biphthalate impurity differ by more than 2.5 mol % in the {111} growth sectors of bizonal crystals, one observes the plane dislocation pileups oriented along the normal to the bipyramid edges.

In the crystals studied (Fig. 2), the dislocation density increases from the interzonal boundary; whereas in the bizonal crystals it passes through the maximum, and in the gradient crystals, it continuously increases toward the surface of the growing face. The maximum dislocation density in bizonal crystals is observed in the growth sectors {010} and {111}; its value increases with an increase of the difference in the impurity concentrations in the zones (Fig. 3a) and in the growth sectors of all the faces irrespectively of the sign of stresses. In gradient crystals, an increase of the composition gradient resulted in an increase of the number of arising dislocation (Fig. 3b). The different contents of rubidium impurity in the initial and final growth layer of the gradient crystals is proportional to the gradient of rubidium concentration in the growth sector {010} of these crystals, because the thicknesses of the layers grown along the [010] direction were practically the same (about 3 mm).

In bizonal and gradient crystals with the compressed external zone, the growth cracks are oriented along the (001) face (which corresponds to the secondary cleavage of the biphthalate crystal [8, 9]) and concentrated in the {010} growth sector. In some instances, the gradient crystal had the crack along the (010) plane in the vicinity of the seed (which is similar to the crack formation along the cleavage upon the removal of the uniaxial load along the [010] direction [8]), which seems to be caused by the sign reversal of the internal stresses during crystal growth. The cracks normal to the edges between these faces arise in the growth sectors {111} and {110}, with their nuclei being the planar dislocation pileups of the same orientation.

Under the extension or compression of the external zone of a bizonal crystals, the cracks along the (001) plane arise already if the concentrations of the rubidium biphthalate impurity differ by about 3 mol % (Fig. 3a), whereas in the gradient crystals, the crack formation under the compression starts at the difference in the rubidium biphthalate concentrations between the seeding plate and the growth front of 3.5–4.0 mol %, i.e., at considerable internal stresses (Fig. 3b). With an increase of the difference in concentrations of rubidium biphthalate between the zones and the compositional gradient, the total number of cracks in the growing zone increases (Fig. 3). Formation of macroscopic cracks in the compressed external zone of the crystals is decelerated because some microcracks merge into large cracks only at considerable stress reduction or at the change of their signs with an increase of the crystal thickness.

Planar liquid inclusions of non-diffusion nature [7] are formed in bizonal crystals at the zone boundaries in

the {010} growth sector if the difference between the rubidium biphthalate content exceeds 13 mol %; the number of inclusions increase with the difference in the zone compositions, whereas the size in the (010) plane decreases [7]. Formation of inclusions results in the reduction of the effective internal stresses at the interzone boundary. In gradient crystals, liquid inclusions arise with a decrease of the growth rates of the faces because of high stresses at the growth front at the final growth stages.

It was established that the number of defects (dislocations, cracks, interzonal inclusions) in the studied crystals increase with an increase of the difference in the concentrations in the zones in bizonal crystals and the composition gradient in gradient ones, which corresponds to an increase of the heterometry-induced internal stresses. The change in the number of defects during growth corresponds to the character of the changes in the heterometry-induced stresses calculated according to the model suggested above. The inverse dependence of the number of dislocations and cracks in bizonal crystals at considerable differences in the zone rubidium biphthalate concentrations is associated with a decrease of the effective internal stresses caused by interzonal inclusions.

ACKNOWLEDGMENTS

This study was supported by the Russian Foundation for Basic Research, project no. 97-05-64218.

The additional materials to the effect can be obtained at the address <http://www.chat.ru/-moshkin/defect98.htm>.

REFERENCES

1. I. I. Shafranovskii, *History of Crystallography in Russia* (Akad. Nauk SSSR, Moscow, 1962).
2. A. A. Shternberg, *Kristallografiya* **7** (1), 114 (1962) [*Sov. Phys. Crystallogr.* **7**, 92 (1962)].
3. Yu. O. Punin, in *Physics of Crystallization* (Tvers. Gos. Univ., Tver, 1992), p. 86.
4. Yu. O. Punin, in *Crystal Growth* (Nauka, Moscow, 1983), Vol. 14, p. 108.
5. M. A. Kuz'mina, Yu. O. Punin, S. V. Moshkin, and T. A. Karyakina, *Zap. Vseross. Mineral. O-va.* **126** (4), 31 (1997).
6. S. V. Moshkin, O. M. Boldyreva, T. I. Ivanova, *et al.*, *J. Cryst. Growth* **172**, 226 (1997).
7. M. A. Kuz'mina, S. V. Moshkin, O. M. Boldyreva, and I. P. Shakhverdova, in *Physics of Crystallization* (Tvers. Gos. Univ., Tver, 1994), p. 103.
8. V. R. Regel', V. I. Vladimirov, N. L. Sizova, *et al.*, *Kristallografiya* **34** (6), 1490 (1989) [*Sov. Phys. Crystallogr.* **34**, 892 (1989)].
9. V. R. Regel', N. L. Sizova, and T. N. Turskaya, *Kristallografiya* **41** (5), 918 (1996) [*Crystallogr. Rep.* **41**, 875 (1996)].

Translated by L. Man

PHYSICAL PROPERTIES
OF CRYSTALS

Resonance Excitation of Polaritons by Bulk Electromagnetic Waves in the Layered Systems with Anisotropic Substrates

A. N. Furs and L. M. Barkovsky

Faculty of Physics, Belarussian State University, Minsk, 220080 Belarus

e-mail: Barkovski@phys.bsu.unibel.by

Received October 5, 2000; in final form, June 20, 2001

Abstract—The possible resonance excitation of surface electromagnetic waves by the bulk waves at the interface between a positive transparent uniaxial crystal and an isotropic medium has been predicted. The existence of the surface waves is provided by anisotropy of one of the boundary media. The tensor relation between the vector amplitudes of an exciting bulk electromagnetic wave and the excited surface wave is established. The ratio of the moduli of the tangential components of these amplitudes is analyzed as a function of the angle of incidence and the polarization of the bulk wave. The numerical calculations are performed for the surface waves at the interface between paratellurite TeO_2 and a KRS-6 (TlBr 30%–TlCl 70%) crystal. © 2001 MAIK “Nauka/Interperiodica”.

INTRODUCTION

Recently, considerable attention has been focused on the theoretical and the experimental studies of surface polaritons in metals, semiconductors, and dielectrics [1–6]. Surface polaritons are the modes of an electromagnetic field with the amplitude exponentially decreasing with the distance from the interface. The simplest example of a system providing excitation of surface polaritons is the interface between isotropic media, with the positive permittivity of one medium and the negative permittivity of the other medium. No surface polaritons can propagate along the interface between isotropic media with the positive permittivities. Therefore, a medium with the negative permittivity is called a surface-active medium, while that with the positive permittivity, a surface-inactive medium [1]. Both natural and artificial media can be active—metals, plasma, and dielectrics in vicinity of the absorption lines. The important problem of the existence and excitation of the surface modes of an electromagnetic field at the interface between the optically anisotropic and the optically isotropic media is still insufficiently studied. It has been believed for quite a long time that one of the media should be surface-active; e.g., the permittivity tensor of an anisotropic medium should have negative principal values [1, 7]. Later [8, 9], it was shown that the surface activity is not the necessary condition for existence of surface electromagnetic wave. The boundary media can also be inactive; however, at least one medium should be anisotropic and the material parameters of the media should satisfy some additional requirements. The general conditions of the existence of surface electromagnetic waves at the interface between the isotropic medium and the anisotropic crystal of an arbitrary symmetry with the positively defined

permittivity tensor (that is, under the condition that the boundary media are inactive) were formulated in [10]. It was shown that surface modes in this system can arise only if the orientations of the planes of the crystal cut and the directions of the wave propagation relative to the symmetry elements belong to a certain bounded continuous set.

In our consideration, we used the general (coordinate free) operator–tensor approach to describe surface waves, the surface-impedance tensors, and the so-called integral formalism [11]. Although this formalism is equivalent to a more popular analysis with the invocation of partial inhomogeneous waves, its application seems to be more expedient because it allows one to derive consistently the dispersion equations for surface waves. The existence theorems based on the integral approach have been formulated earlier in the theory of surface acoustic wave (SAW) [12–15]. The existence of surface acoustic waves is directly related to the properties of exceptional (limiting) elastic waves in crystals [16, 17]. The formal similarity of the wave equations in optics and acoustics of anisotropic media facilitated the extension of a number of methods from the theory of surface acoustic waves to the description of the surface electromagnetic waves [10, 11].

The experimental studies of the surface polariton spectra are based on the use of Raman scattering, the optical, electron, etc., spectroscopies [1, 7], and also the well-known technique of the frustrated total internal reflection [18]. There are grounds to believe that the frustrated total internal reflection would also be efficient for excitation and observation of the surface electromagnetic waves at the interface between the surface-inactive media. Recently, the effect of resonance excitation of the surface acoustic waves has been predicted

in the “layer-on-substrate” systems [19, 20]. The general method of resonance excitation of acoustic and electromagnetic waves in such systems was described in [21]. In these publications, a large variety of wave fields in bicrystal systems was consistently described.

Below, we study possible resonance excitation of surface electromagnetic waves (the so-called D'yakonov waves [8]) at the interface between a surface-inactive uniaxial crystal and an isotropic layer. The excitation becomes possible because of the presence in the layer of inhomogeneous exponentially increasing waves which arose upon the total internal reflection of the incident bulk wave. The numerical calculations were made for a paratellurite (TeO_2) crystal coated with an isotropic KRS-6 (TlBr 30% – TlCl 70%) layer. The bulk wave propagates in an optically isotropic ZnSe crystal. The fundamental characteristic of the processes studied is the ratio of the moduli of the tangential components of the amplitudes of the excited surface wave and the exciting bulk wave. This ratio can attain a rather high value if the projections of the wave vectors of the incident and surface waves on the interface are close. The consideration is performed for monochromatic fields with the fixed frequency; all the relationships include the Fourier components of the permittivity tensors at this frequency. A more rigorous analysis requires the allowance for absorption in materials, which will be discussed in our following publications.

BASIC RELATIONSHIPS

Consider a layered nonmagnetic dielectric system (Fig. 1) consisting of an isotropic layer (II) of the thickness l with permittivity ϵ_f , a semi-infinite anisotropic substrate (III), which is a positive uniaxial crystal characterized by permittivity tensor ϵ , and an isotropic medium (I) with permittivity ϵ_c . Let the reference point be at the interface between the isotropic layer and the substrate and z be parallel to the unit vector \mathbf{q} of the interface normal. The substrate permittivity tensor ϵ and the inverse tensor ϵ^{-1} have the forms [22–24]:

$$\begin{aligned} \epsilon &= \epsilon_{\perp} + (\epsilon_{\parallel} - \epsilon_{\perp})\mathbf{c} \otimes \mathbf{c}, \quad \epsilon_{\parallel} > \epsilon_{\perp}, \\ \epsilon^{-1} &= a + (b - a)\mathbf{c} \otimes \mathbf{c}, \quad a = \frac{1}{\epsilon_{\perp}}, \quad b = \frac{1}{\epsilon_{\parallel}}, \end{aligned} \quad (1)$$

where \mathbf{c} is the unit vector directed along the optical axis, $\mathbf{c} \otimes \mathbf{c}$ is a dyad, $\epsilon_{\perp} = n_o^2$, and $\epsilon_{\parallel} = n_e^2$. Let the vector \mathbf{c} lie in the interface plane.

We are interested in possible excitation of surface electromagnetic wave at the II–III interface $z = 0$ by a bulk wave incident from the isotropic media I onto the isotropic layer. Let the angle of incidence be φ and the direction of the projection of the bulk-wave vector on the interface be specified by the unit vector \mathbf{b} forming an angle α with the vector \mathbf{c} ($\mathbf{c} = \mathbf{b}\cos\alpha - \mathbf{a}\sin\alpha$) (Fig. 1). At $l \rightarrow \infty$, the following conditions should be met to

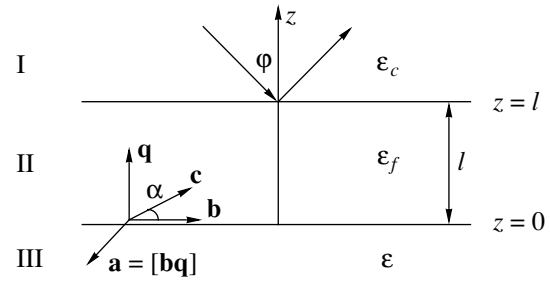


Fig. 1. Geometry of a layered dielectric system.

excite surface electromagnetic waves localized at the interface between the uniaxial crystal, III, and the isotropic layer, II,

$$\epsilon_{\perp} < \epsilon_f < \epsilon_{\parallel}, \quad \alpha_1 < \alpha < \alpha_2, \quad (2)$$

where the limiting angles α_1 and α_2 are specified by the formulas

$$\sin^2 \alpha_1 = \frac{\xi}{2} \{ 1 - \eta\xi + [(1 - \eta\xi)^2 + 4\eta]^2 \}^{1/2}, \quad (3)$$

$$\sin^2 \alpha_2 = \frac{(1 + \eta)^3 \xi}{(1 + \eta)^2 (1 + \eta\xi) - \eta^2 (1 - \xi)^2} \quad (4)$$

and $\eta = (\epsilon_{\parallel}/\epsilon_{\perp}) - 1$ and $\xi = (\epsilon_f - \epsilon_{\perp})/(\epsilon_{\parallel} - \epsilon_{\perp})$ [8]. We assume that in our case, the parameters ϵ_{\parallel} , ϵ_{\perp} , ϵ_f , and α are chosen in such a way that the conditions (2) are satisfied. In addition, let the following inequalities be fulfilled:

$$\epsilon_c > \epsilon_f, \quad \sin \varphi > \sqrt{\frac{\epsilon_f}{\epsilon_c}}. \quad (5)$$

Conditions (5) correspond to the total internal reflection of a bulk wave at the interface $z = l$; hence, inhomogeneous electromagnetic waves are excited in layer II.

In what follows, we use the notation $a_f = 1/\epsilon_f$ and $a_c = 1/\epsilon_c$ and introduce a dimensionless reduced wave frequency $\nu = \omega/(ck)$, where k is the projection of the incident wave vector onto the \mathbf{b} direction and c is the velocity of light in free space. The frequency ν is determined by the angle of incidence φ :

$$\nu = \sqrt{a_c} / \sin \varphi. \quad (6)$$

Let \mathbf{H}_{τ}^s be the tangential component (amplitude) of the magnetic field strength of the surface wave at the interface $z = 0$ and \mathbf{H}_{τ}^i and \mathbf{H}_{τ}^r be the tangential components of the magnetic field intensity of the incident and reflected waves at the interface $z = l$ which satisfy the equality $\mathbf{H}_{\tau}^s(z = l) = \mathbf{H}_{\tau}^i + \mathbf{H}_{\tau}^r$. The similar notation $[\mathbf{q}\mathcal{E}^s]$, $[\mathbf{q}\mathcal{E}^i]$, and $[\mathbf{q}\mathcal{E}^r]$, where $\mathcal{E} = \nu\mathbf{E}$, is also used for the amplitudes of the electric field intensity at the inter-

faces. The field amplitude \mathbf{H}_τ^s at the interface $z = 0$ between media II and III can be determined under the assumption that the amplitude \mathbf{H}_τ^i is set. When solving this problem, it is convenient to use the operator approach [25] without calculating the characteristics of the partial waves. The relation between tangential components of the fields at the interfaces $z = 0$ and $z = l$ is established by the characteristic layer matrix P (a spatial evolution operator or a propagator)

$$\begin{pmatrix} \mathbf{H}_\tau^i + \mathbf{H}_\tau^r \\ [\mathbf{q}\mathcal{E}^i] + [\mathbf{q}\mathcal{E}^r] \end{pmatrix} = P \begin{pmatrix} \mathbf{H}_\tau^s \\ [\mathbf{q}\mathcal{E}^s] \end{pmatrix} \quad (7)$$

with the block structure $P = \begin{pmatrix} P_{11} & P_{12} \\ P_{21} & P_{22} \end{pmatrix}$. The explicit

form of the operators P_{11} , P_{12} , P_{21} , and P_{22} will be given below. The surface impedance tensor of the wave γ is introduced as a ‘‘tensor coefficient of proportionality’’ between the tangential components of the electric and magnetic fields: $[\mathbf{q}\mathcal{E}] = \gamma\mathbf{H}_\tau$. Denote the surface-impedance tensors of the incident, reflected, and surface waves by γ_i , γ_r , and γ_s , respectively. Then Eq. (7) takes the form

$$\begin{pmatrix} I \\ \gamma_i \end{pmatrix} \mathbf{H}_\tau^i + \begin{pmatrix} I \\ \gamma_r \end{pmatrix} \mathbf{H}_\tau^r = P \begin{pmatrix} I \\ \gamma_s \end{pmatrix} \mathbf{H}_\tau^s, \quad (8)$$

where $I = -\mathbf{q}^\times \mathbf{q} = 1 - \mathbf{q} \otimes \mathbf{q} = \mathbf{b} \otimes \mathbf{b} + \mathbf{a} \otimes \mathbf{a}$ is the projection operator in the interface plane and \mathbf{q}^\times is the tensor dual to the vector \mathbf{q} [22, 23]. We can eliminate the field \mathbf{H}_τ^r from Eq. (8) by multiplying both sites of Eq. (8) on the left by the matrix $(\gamma_r - I)$,

$$2\gamma_r \mathbf{H}_\tau^i = (\gamma_r - I)P \begin{pmatrix} I \\ \gamma_s \end{pmatrix} \mathbf{H}_\tau^s,$$

where the relation between the surface impedances of the incident and reflected waves, $\gamma_i = -\gamma_r$, is taken into account. Then the relation between the \mathbf{H}_τ^i and \mathbf{H}_τ^s amplitudes is determined by the operator equation

$$\mathbf{H}_\tau^s = A\mathbf{H}_\tau^i, \quad (9)$$

where

$$\begin{aligned} A &= 2 \left[(\gamma_r - I)P \begin{pmatrix} I \\ \gamma_s \end{pmatrix} \right]^{-1} \gamma_r \\ &= 2(\gamma_r P_{11} - P_{21} + \gamma_r P_{12} \gamma_s - P_{11} \gamma_s)^{-1} \gamma_r, \end{aligned} \quad (10)$$

the superscript ‘‘minus’’ denotes an operation of pseudoinversion [25].

The surface impedance tensors of the incident and the reflected waves have the form [26]:

$$\gamma_r = -\gamma_i = v^2 \sqrt{\frac{a_c}{v^2 - a_c}} \mathbf{b} \otimes \mathbf{b} + \sqrt{a_c(v^2 - a_c)} \mathbf{a} \otimes \mathbf{a}. \quad (11)$$

The surface impedance tensor of the inhomogeneous surface electromagnetic wave in anisotropic substrate III can be calculated using the general formulas from [11], where Stroh–Barnett–Lothe formalism [12–14] for the surface acoustic waves is extended to the surface electromagnetic excitations. We have

$$\gamma_s = Q^-(-iI - S), \quad (12)$$

where the Q and the S tensors are given in the integral form

$$Q = -\frac{1}{\pi} \int_0^\pi (\mathbf{e}_2 \mathbf{e}_2)^- d\phi, \quad S = -\frac{1}{\pi} \int_0^\pi (\mathbf{e}_2 \mathbf{e}_2)^- (\mathbf{e}_2 \mathbf{e}_1) d\phi. \quad (13)$$

The integrands in Eq. (13) include the bilinear tensor forms of two vector arguments defined for two arbitrary vectors \mathbf{u} and \mathbf{v} as

$$\begin{aligned} (\mathbf{u}\mathbf{v}) &= -\frac{\mathbf{u}\mathcal{E}^{-1}\mathbf{v} \cdot \mathbf{a} \otimes \mathbf{a} + v^2 I \mathbf{u}^\times \mathcal{E}^{-1} \mathbf{v}^\times I}{\mathbf{a}\mathcal{E}^{-1}\mathbf{a} - v^2} \\ &\quad + v^2 \mathbf{b}\mathbf{u} \cdot \mathbf{b}\mathbf{v} I, \end{aligned} \quad (14)$$

where \mathbf{e}_1 and \mathbf{e}_2 are expressed in terms of the vectors \mathbf{b} and \mathbf{q}

$$\mathbf{e}_1 = \mathbf{b} \cos \phi + \mathbf{q} \sin \phi, \quad \mathbf{e}_2 = -\mathbf{b} \sin \phi + \mathbf{q} \cos \phi.$$

In Eq. (14), \mathcal{E}^{-1} is the tensor adjugate to the tensor \mathcal{E}^{-1} ($\mathcal{E}^{-1} \mathcal{E}^{-1} = \mathcal{E}^{-1} \mathcal{E}^{-1} = \det \mathcal{E}^{-1}$) [22, 23] and $\mathbf{b}\mathbf{u}$ and $\mathbf{b}\mathbf{v}$ are the scalar products of the vectors.

For a uniaxial crystal

$$\mathcal{E}^{-1} = ab - a(b - a)\mathbf{c} \otimes \mathbf{c}. \quad (15)$$

Substituting $\mathbf{u} = \mathbf{v} = \mathbf{e}_2$ into Eq. (14) and using Eqs. (1) and (15) we can determine, first, the tensor $(\mathbf{e}_2 \mathbf{e}_2)$ and then the pseudoinverse tensor $(\mathbf{e}_2 \mathbf{e}_2)^-$, specified by the equalities $(\mathbf{e}_2 \mathbf{e}_2)(\mathbf{e}_2 \mathbf{e}_2)^- = (\mathbf{e}_2 \mathbf{e}_2)^-(\mathbf{e}_2 \mathbf{e}_2) = I$. Upon simple but cumbersome transformations, we obtain

$$\begin{aligned} (\mathbf{e}_2 \mathbf{e}_2)^- &= [a \cos^2 \phi + (a - v^2) \sin^2 \phi]^{-1} \\ &\quad \times [b \cos^2 \phi + (d - v^2) \sin^2 \phi]^{-1} \\ &\quad \times \left\{ \frac{1}{v^2} [(d - v^2)(a - v^2) \sin^2 \phi \right. \\ &\quad \left. + (ab - v^2(a + b - d) \cos^2 \phi)] \mathbf{b} \otimes \mathbf{b} \right. \\ &\quad \left. + (b - a) \sin \alpha \cos \alpha \cos^2 \phi (\mathbf{b} \otimes \mathbf{a} + \mathbf{a} \otimes \mathbf{b}) \right. \end{aligned} \quad (16)$$

$$-\left[d \cos^2 \phi + (d - v^2) \sin^2 \phi \right] \mathbf{a} \otimes \mathbf{a} \Big\},$$

where $d = a \cos^2 \alpha + b \sin^2 \alpha$. In derivation of Eq. (16), we used the relations $\mathbf{e}_2^\times \mathbf{c} = [\mathbf{e}_2 \mathbf{c}]$ and $\mathbf{e}_2^\times \mathbf{e}_2^\times = \mathbf{e}_2 \otimes \mathbf{e}_2 - 1$. Integrating over ϕ with due regard for Eq. (13), we arrive at the tensor Q

$$\begin{aligned} Q &= \left[\sqrt{b(a - v^2)} + \sqrt{a(d - v^2)} \right]^{-1} \\ &\times \left\{ -\frac{1}{v^2} \left[\sqrt{(a - v^2)(d - v^2)} + \sqrt{ab} \right. \right. \\ &\quad \left. \left. - \frac{v^2(a + b - d)}{\sqrt{ab}} \right] \mathbf{b} \otimes \mathbf{b} \right. \\ &\quad \left. - \frac{1}{\sqrt{ab}} (b - a) \sin \alpha \cos \alpha (\mathbf{b} \otimes \mathbf{a} + \mathbf{a} \otimes \mathbf{b}) \right. \\ &\quad \left. + \left(\frac{d}{\sqrt{ab}} + \sqrt{\frac{d - v^2}{a - v^2}} \right) \mathbf{a} \otimes \mathbf{a} \right\}. \end{aligned} \quad (17)$$

It can be shown that the expressions for the tensor $(\mathbf{e}_2 \mathbf{e}_1)$ and, hence, also the tensor $(\mathbf{e}_2 \mathbf{e}_2)^\top (\mathbf{e}_2 \mathbf{e}_1)$ contain odd powers of $\cos \phi$ and $\sin \phi$. Therefore $S = 0$ and Eq. (12) acquires the form $\gamma_s = -iQ$. With Eq. (17) we obtain the expression for the surface impedance tensor

$$\begin{aligned} \gamma_s &= i \left[\sqrt{b(a - v^2)} + \sqrt{a(d - v^2)} \right]^{-1} \\ &\times \left\{ v^2 \left[d \sqrt{\frac{a - v^2}{d - v^2}} + \sqrt{ab} \right] \mathbf{b} \otimes \mathbf{b} \right. \\ &\quad \left. + v^2 (b - a) \sqrt{\frac{a - v^2}{d - v^2}} \sin \alpha \cos \alpha (\mathbf{b} \otimes \mathbf{a} + \mathbf{a} \otimes \mathbf{b}) \right. \\ &\quad \left. - \left[\sqrt{ab} (a - v^2) \right. \right. \\ &\quad \left. \left. + \sqrt{\frac{a - v^2}{d - v^2}} (ab - v^2(a + b - d)) \right] \mathbf{a} \otimes \mathbf{a} \right\}. \end{aligned} \quad (18)$$

The propagator P can be determined as the matrix exponent (exponential) $P = \exp(iklM)$, where the matrix M enters the system of differential equations

$$\frac{d}{dz} \begin{pmatrix} \mathbf{H}_\tau \\ [\mathbf{q} \mathcal{E}] \end{pmatrix} = ikM \begin{pmatrix} \mathbf{H}_\tau \\ [\mathbf{q} \mathcal{E}] \end{pmatrix},$$

which describes the propagation of inhomogeneous waves in an isotropic layer. The structure of propaga-

tor P is described by

$$\begin{aligned} P_{11} &= P_{22} = I \cosh \left(kl \sqrt{\frac{a_f - v^2}{a_f}} \right), \\ P_{12} &= i \sinh \left(kl \sqrt{\frac{a_f - v^2}{a_f}} \right) \\ &\times \left\{ -\frac{1}{v^2} \sqrt{\frac{a_f - v^2}{a_f}} \mathbf{b} \otimes \mathbf{b} + \frac{1}{\sqrt{a_f(a_f - v^2)}} \mathbf{a} \otimes \mathbf{a} \right\}, \quad (19) \\ P_{21} &= i \sinh \left(kl \sqrt{\frac{a_f - v^2}{a_f}} \right) \\ &\times \left\{ v^2 \sqrt{\frac{a_f}{a_f - v^2}} \mathbf{b} \otimes \mathbf{b} - \sqrt{a_f(a_f - v^2)} \mathbf{a} \otimes \mathbf{a} \right\}. \end{aligned}$$

Thus, the operator A in Eq. (9), which relates the tangential components of the magnetic fields of the incident and the excited surface waves, is determined by Eqs. (10), (11), (18), and (19). This operator can be regarded as a function of the frequency v (or the incidence angle ϕ) with v ranging from $v_{\min} = \sqrt{a_c}$ to $v_{\max} = \min\{\sqrt{d}, \sqrt{a_f}\}$. The lower limit of this range is set by Eq. (6). The upper limit corresponds to positive expressions under the root sign in Eqs. (18) and (19) (this signifies that the waves in layer II and substrate III are inhomogeneous). In the general case, A is a complex non-Hermitian operator. Here, we are primarily interested in the ratio of the moduli of the \mathbf{H}_τ^i and \mathbf{H}_τ^s field vectors $\rho = |\mathbf{H}_\tau^s|/|\mathbf{H}_\tau^i|$ (hereafter referred to as the coefficient of the surface-wave amplification with respect to the exciting bulk wave) (the phase relations between these vectors are of minor importance now). It is important that this coefficient at the fixed incidence angle ϕ is essentially dependent on the polarization of the incident wave and attains the maximum and the minimum values only at some (generally, elliptical) polarizations. The greatest possible value ρ_{\max} equals the norm of the operator A [27]. The latter can be determined from the formula

$$\rho_{\max} = \max\{\sqrt{\lambda_1}, \sqrt{\lambda_2}\}, \quad (20)$$

where λ_1 and λ_2 are the eigenvalues of the Hermitian operator $B = A^\dagger A$ and the cross indicates the Hermitian conjugation. The polarization of the incident wave which provides the maximum amplification is determined as the eigenvector of the operator B corresponding to the greatest eigenvalue. The second eigenvector, orthogonal to the first one, at the fixed ϕ , determines the minimum value of the amplification coefficient.

It should be emphasized that the coefficient ρ introduced above, characterizes the ratio of the moduli of the tangential field components and not of the complete vectors \mathbf{H}^s and \mathbf{H}^i , which can be determined from \mathbf{H}_t^s and \mathbf{H}_t^i with the use of the restoration matrices [25].

The reduced frequency $v = v_s$ of the surface wave in the system with one interface at $z = 0$ is the solution of the following dispersion equation [10]:

$$\det(\gamma_s - \gamma') = 0, \quad (21)$$

where the surface impedance tensor γ_s of the inhomogeneous wave in uniaxial crystal III is given by Eq. (18), whereas the surface impedance tensor of the wave in isotropic medium II is given by the formula

$$\gamma' = -iv^2 \sqrt{\frac{a_f}{a_f - v^2}} \mathbf{b} \otimes \mathbf{b} + i\sqrt{a_f(a_f - v^2)} \mathbf{a} \otimes \mathbf{a}. \quad (22)$$

Equation (21) can be reduced to the form

$$\frac{1}{\sqrt{b(a - v^2)} + \sqrt{a(d - v^2)}} \times \left\{ \left[d \sqrt{\frac{a - v^2}{d - v^2}} + \sqrt{ab} \right] \sqrt{a_f(a_f - v^2)} + \left[\sqrt{ab}(a - v^2) + \sqrt{\frac{a - v^2}{d - v^2}}(ab - v^2(a + b - d)) \right] \times \sqrt{\frac{a_f}{a_f - v^2}} \right\} + \sqrt{ab} \sqrt{\frac{a - v^2}{d - v^2}} + a_f = 0. \quad (23)$$

In the next section, we present the numerical data characterizing the maximum amplification coefficient ρ_{\max} depending on incidence angle φ .

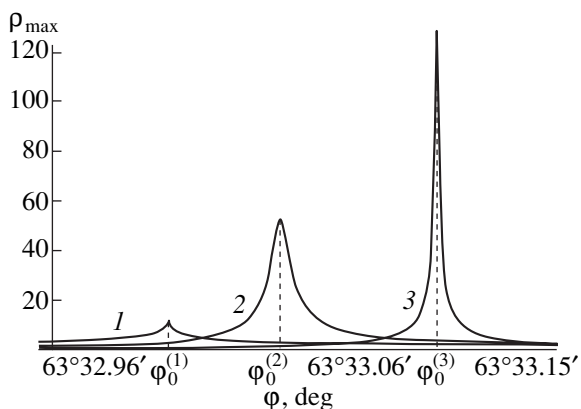


Fig. 2. Maximum amplification coefficient ρ_{\max} as a function of the incidence angle φ for different values of the parameter $\omega l/c$: (1) 25, (2) 40, and (3) 70.

RESULTS OF NUMERICAL CALCULATIONS FOR THE TeO_2 -KRS-6-ZnSe SYSTEM AND THEIR DISCUSSION

Consider the layered system (Fig. 1) consisting of the positive uniaxial paratellurite crystal TeO_2 (III) and the optically isotropic KRS-6 (II) and ZnSe (I) crystals. At the wavelength $\lambda = 0.589 \mu\text{m}$, the refractive indices of these crystals are $n_o = 2.2738$, $n_e = 2.4295$, $n_f = 2.3367$, and $n_c = 2.61$ [28], with the conditions $n_o < n_f < n_e$ and $n_c > n_f$ [see inequalities (2) and (5)] being satisfied. Although our consideration is limited to the analysis of only one system, it is obvious that the number of similar systems can be increased by using untraditional (composite, mesoscopic, etc. [29–31]) materials or the materials with tunable (modulated) parameters. Nevertheless, in all the materials, the refractive indices must obey the inequalities similar to those considered above.

Consider first the case of “free” surface waves in the system with one interface, so that TeO_2 and KRS-6 are the boundary media and the optical axis of the paratellurite crystal lying in the interface plane. We obtain the following inverse permittivities: $a = 0.19342$, $b = 0.16942$, and $a_f = 0.18314$. The range of the allowed angles α is determined by the limiting values $\alpha_1 = 40^\circ 44.5'$ and $\alpha_2 = 40^\circ 59.9'$ calculated using Eqs. (3) and (4). Assuming that $\alpha = 40^\circ 54'$ we obtain from the dispersion equation (23) the reduced frequency of the surface wave $v = v_s = 0.427929$.

Now, consider the surface waves at the interface between isotropic layer II and anisotropic substrate III (Fig. 1) which are excited by the bulk electromagnetic wave, with the angle α being the same. For isotropic medium I (ZnSe) $a_c = 0.14680$. For the reduced frequency v in the range from $v_{\min} = \sqrt{a_c} = 0.383142$ to $v_{\max} = \sqrt{d} = 0.427937$, we can perform the numerical calculations using Eqs. (10), (11), and (18)–(20) and determine the maximum amplification coefficient ρ_{\max} depending on the incidence angle φ at different values of the parameter $\omega l/c$ (Fig. 2). The curves obtained are of the resonance nature. The reduced frequencies $v_0^{(k)} = \sqrt{a_c} / \sin \varphi_0^{(k)}$ (k is the curve number) for the critical incidence angles $\varphi_0^{(k)}$ (at which the maximum amplification is attained) only slightly differ from the value v_s for the “free” surface wave calculated by Eq. (23). With an increase of the layer thickness l , the height of the resonance peak also increases, whereas its width decreases, and $v_0 \rightarrow v_s$. The resonance dependence $\rho_{\max}(\varphi)$ is seen already at $\omega l/c \approx 20$ (the layer thickness equals 3–4 wavelengths in vacuum). For $\omega l/c = 40$ (curve 2) and the incidence angle $\varphi_0^{(2)} = 63^\circ 33.04'$, the tangential component of the magnetic field \mathbf{H}_t^i of the exciting wave corresponding to the maximum amplification (52.80) is determined as the eigenvector of the operator $B = A^+A$ corresponding to

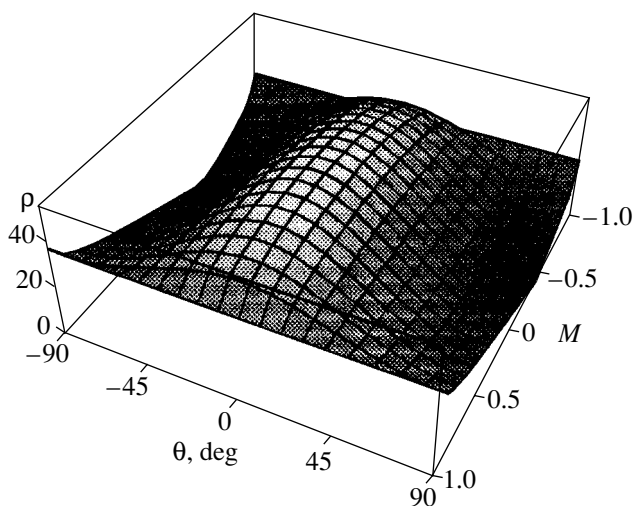


Fig. 3. Amplification coefficient ρ as a function of polarization of the incident wave at $\omega l/c = 40$.

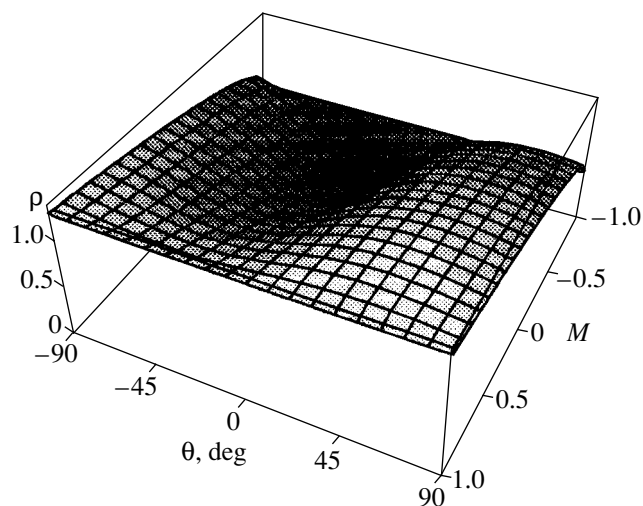


Fig. 4. Amplification coefficient ρ as a function of polarization of the incident wave at $\omega l/c = 2$.

the greatest eigenvalue and equals $0.99129\mathbf{b} + (0.00225 - 0.13167i)\mathbf{a}$. For an incident wave with the orthogonal polarization $\tilde{\mathbf{H}}_{\tau}^i = (-0.00225 - 0.13167i)\mathbf{b} + 0.99129\mathbf{a}$ ($\tilde{\mathbf{H}}_{\tau}^{i*} \mathbf{H}_{\tau}^i = 0$, the sign * denotes the complex conjugation), the coefficient ρ has the minimum value (0.00106). Changing continuously the polarization of the incident wave, it is possible to obtain (at $\varphi_0^{(2)} = 63^\circ 33.04'$) the intermediate values of the amplification coefficient ρ (from 0.00106 to 52.80). For every incidence angle, there exists the corresponding pair of mutually orthogonal polarizations for which the coefficient ρ takes the maximum and the minimum values and, thus, has the ranges of its variation. The upper limits of these ranges, ρ_{\max} , are shown in Fig. 2 as functions of the angle φ . The lower limits of these ranges were calculated to be monotonically dependent on φ .

The dependences of the coefficient ρ on the incident-wave polarization, characterized by the parameters M and θ are shown in Figs. 3 and 4 for the critical incidence angles $\varphi = \varphi_0$. The first parameter is determined as $M = \text{in}[\mathbf{H}^i \mathbf{H}^{i*}] / [|\mathbf{H}^i|^2]$, where \mathbf{H}^i is the complete vector of the magnetic-field intensity of the incident wave and $\mathbf{n} = (\mathbf{b} \sin \varphi_0 - \mathbf{q} \cos \varphi_0)$ is the wave normal. This parameter characterizes the ellipticity of the polarization (at $M = -1$ and $M = +1$, we have the left and right-hand circular polarizations and at $M = 0$, we have the linear polarization). The second parameter θ is the angle formed by the semimajor axis of the polarization ellipse and the plane of incidence. The resonance is observed for the waves with polarization close to the linear polarization in the incidence plane (Fig. 3). At small layer thicknesses, the asymmetry of the plot $\rho = \rho(M, \theta)$ with respect to the coordinate plane $M = 0$ and the plane $\theta = 0$ is revealed (Fig. 4). Thus, the amplification coefficients ρ are different at the right-and left-

hand circular wave polarizations. However, the different contributions of the polarizations are reversible. The change $\alpha \rightarrow -\alpha$ (the vector \mathbf{b} lies on the other side of the vector \mathbf{c} , Fig. 1), results in the mirror reflection of the surface $\rho = \rho(M, \theta)$ in the planes $M = 0$ and $\theta = 0$.

CONCLUSIONS

Thus, the method considered can be efficiently used to excite D'yakonov surface waves [8, 9], generated due to the difference in the symmetries of boundary isotropic and anisotropic media. The above consideration shows an important role of polarization for description of surface and bulk electromagnetic waves of various types. To determine the resonance incidence angles φ_0 for an isotropic layer whose thickness is equal to several wavelengths in a vacuum with sufficient accuracy, one can use dispersion equation (23) for the "free" surface modes in order to determine the reduced frequency v_s and then recalculate the incidence angles using Eq. (6). Figure 2 shows that the width of the resonance curves is small. However, it can be increased due to pronounced substrate anisotropy (which can also be ensured artificially).

The method of frustrated total internal reflection provides the record of the resonance excitation of the surface polaritons in the isotropic substrate from a decrease of the reflection coefficient of the wave incident at certain angles [1, 7]. Such a decrease of the reflection coefficient is caused by absorption of the energy of electromagnetic waves in the substrate (the substrate permittivity is a complex quantity and its real part is negative). In our case, the anisotropic substrate is nonabsorbing (the permittivities ϵ_{\parallel} and ϵ_{\perp} are positive). Therefore, the energies of the incident and the reflected waves are always balanced. Our calculations

show that the reflection operator R , relating the complete field vectors \mathbf{H}^i and \mathbf{H}^r (and not their tangential components!), is a unitary operator at any incidence angles. Therefore the intensities of the incident and the reflected waves, proportional to the squared moduli of the \mathbf{H}^i and \mathbf{H}^r vectors are equal.

Finally, we would like to indicate that if the resonance condition is fulfilled, the field distribution in the isotropic layer is determined mainly by two inhomogeneous partial waves with the amplitudes increasing exponentially with an approach to the interface $z = 0$ (that is, at $z \rightarrow +0$). Both these waves and partial waves in the anisotropic substrate on the other side of the interface satisfy the boundary conditions with insignificant corrections in such a way as if the other interface $z = l$ would not have existed at all. The same is true in the resonance excitation of the surface acoustic waves [19, 20].

REFERENCES

1. *Surface Polaritons: Electromagnetic Waves at Surfaces and Interfaces*, Ed. by V. M. Agranovich and D. L. Mills (North-Holland, Amsterdam, 1982; Nauka, Moscow, 1985).
2. M. M. Shabat, *Microwave Opt. Technol. Lett.* **16**, 122 (1997).
3. D. Mihalache, D. M. Baboiu, M. Cimmac, *et al.*, *Opt. Commun.* **108**, 239 (1994).
4. F. A. Burton and S. A. Cassidy, *J. Light-Wave Technol.* **LT8**, 1843 (1990).
5. Ze Cheng, *Phys. Rev. B* **51**, 10 017 (1995).
6. K. P. Lyshenyuk and F. N. Marchevskii, *Fiz. Tverd. Tela (St. Petersburg)* **37**, 217 (1995) [*Phys. Solid State* **37**, 116 (1995)].
7. V. M. Agranovich and V. L. Ginzburg, *Crystal Optics with Spatial Dispersion and Excitons* (Nauka, Moscow, 1979; Springer-Verlag, New York, 1984).
8. M. I. D'yakonov, *Zh. Éksp. Teor. Fiz.* **94** (4), 119 (1988) [*Sov. Phys. JETP* **67**, 714 (1988)].
9. N. S. Averkiev and M. I. D'yakonov, *Opt. Spektrosk.* **68** (5), 1118 (1990) [*Opt. Spectrosc.* **68**, 653 (1990)].
10. A. N. Furs and L. M. Barkovsky, *J. Opt. A* **1**, 109 (1999).
11. A. N. Furs and L. M. Barkovsky, *Microwave Opt. Technol. Lett.* **14**, 301 (1997).
12. A. N. Stroh, *J. Math. Phys.* **41**, 77 (1962).
13. D. M. Barnett and J. Lothe, *J. Phys. F* **4**, 671 (1974).
14. J. Lothe and D. M. Barnett, *J. Appl. Phys.* **47**, 428 (1976).
15. P. Chadwick and G. D. Smith, *Adv. Appl. Mech.* **17**, 303 (1977).
16. V. I. Alshits and J. Lothe, *Kristallografiya* **23**, 901 (1978) [*Sov. Phys. Crystallogr.* **23**, 509 (1978)].
17. V. I. Alshits, V. N. Lyubimov, N. F. Naumenko, *et al.*, *Kristallografiya* **30**, 213 (1985) [*Sov. Phys. Crystallogr.* **30**, 123 (1985)].
18. A. Otto, in *Optical Properties of Solids* (New Developments, Amsterdam, 1976), p. 677.
19. V. I. Alshits, A. S. Gorkunova, V. N. Lyubimov, *et al.*, *Kristallografiya* **44**, 639 (1999) [*Crystallogr. Rep.* **44**, 592 (1999)].
20. V. I. Alshits, A. S. Gorkunova, V. N. Lyubimov, *et al.*, *Kristallografiya* **44**, 858 (1999) [*Crystallogr. Rep.* **44**, 799 (1999)].
21. V. I. Alshits, A. S. Gorkunova, V. N. Lyubimov, *et al.*, in *Proceedings of the International Symposium "Trends in Continuum Physics," Trecop'98, Poznan, Poland, 1998* (World Scientific, Singapore, 1999), p. 28.
22. F. I. Fedorov, *Optics of Anisotropic Media* (Akad. Nauk BSSR, Minsk, 1958).
23. F. I. Fedorov, *Theory of Gyrotropy* (Nauka i Tekhnika, Minsk, 1976).
24. A. F. Konstantinova, B. N. Grechushnikov, B. V. Bokut', *et al.*, *Optical Properties of Crystals* (Nauka i Tekhnika, Minsk, 1995).
25. L. M. Barkovsky, G. N. Borzdov, and A. V. Lavrinenko, *J. Phys. A* **20**, 1095 (1987).
26. L. M. Barkovskii, G. N. Borzdov, and A. V. Lavrinenko, *Izv. Akad. Nauk BSSR, Ser. Fiz.-Mat. Nauk*, No. 2, 79 (1986).
27. R. A. Horn and C. R. Johnson, *Matrix Analysis* (Cambridge Univ. Press, Cambridge, 1985; Mir, Moscow, 1989).
28. A. A. Blistanov, V. S. Bondarenko, N. V. Perelomova, *et al.*, *Acoustical Crystals*, Ed. by M. P. Shaskol'skaya (Nauka, Moscow, 1982).
29. H. Gleiter, *Acta Mater.* **48** (1), 1 (2000).
30. J. P. Hirth, *Acta Mater.* **48** (1), 93 (2000).
31. N. Setter and R. Waser, *Acta Mater.* **48** (1), 151 (2000).

Translated by A. Zolot'ko

PHYSICAL PROPERTIES
OF CRYSTALS

Fracton Contribution to the Specific Heat
of the $\text{PbMg}_{1/3}\text{Nb}_{2/3}\text{O}_8$ Relaxor Ferroelectric
at Low Temperatures

S. N. Gvasaliya*, S. G. Lushnikov*, Y. Moriya**,
H. Kawaji**, and T. Atake**

* Ioffe Physical Technical Institute, Russian Academy of Sciences, St. Petersburg, 194021 Russia

** Tokyo Institute of Technology, 4259 Nagatsuta-cho, Midori-ku, Yokohama, 226-8503 Japan

Received December 27, 2000

Abstract—The specific heat of the $\text{PbMg}_{1/3}\text{Nb}_{2/3}\text{O}_8$ relaxor ferroelectric has been measured by the adiabatic calorimetry and the relaxation method in the temperature range 2–300 K. The low-temperature heat capacity data are compared with the experimental data on inelastic neutron scattering and discussed in the context of the present-day concepts. The analysis of various approaches to the description of the temperature dependence of the heat capacity showed that the experiment can be adequately described only within the framework of the fractal concept. The calculated value of the spectral dimension $\bar{d} = 1.6$ is consistent with the inelastic neutron-scattering data. © 2001 MAIK “Nauka/Interperiodica”.

INTRODUCTION

The perovskite-like relaxor ferroelectrics (or simply relaxors) described by the general formula $AB'_xB''_{1-x}O_3$ have long been studied [1]. Their wide practical applications and a number of unique physical properties has attracted the close attention of researchers. The relaxors differ from the classical ABO_3 perovskites by the presence of B' and B'' ions having different valences in the crystallographically equivalent positions of the B -sublattice. Disorder of the B -sublattice results in considerable change of the crystal-lattice dynamics [1]. Thus, the anomaly in the dielectric response in the vicinity of the ferroelectric phase transition is spread and its magnitude can attain giant values ($\epsilon \sim 10^5$), which fact allowed one to call the representatives of this family the compounds with giant electrostriction. Recent high-resolution electron microscopy studies revealed the presence of the nanoscale regions with the 1 : 1 order of the B' and B'' cations regardless of the stoichiometry [2, 3].

The $\text{PbMg}_{1/3}\text{Nb}_{2/3}\text{O}_8$ crystal (PMN) is the well-known model relaxor ferroelectric. The broad anomaly in the frequency-dependent dielectric response with the maximum near $T_C \sim 270$ K is not accompanied by any macroscopic changes in the structure. The structural phase transition is observed only in an electric field applied to the sample in the vicinity of 200 K [4]. In PMN, there is a regular set of ordered Mg and Nb clusters in the ratio 1 : 1 $\sim 2 \times 10^{-7}$ cm in diameter. The distance between the centers of the neighboring ordered clusters is 2.5×10^{-7} cm [2]. The topology of the nanocluster structure thus formed has not yet been studied,

but it certainly has an effect on the crystal lattice dynamics. It seems that the topology is responsible for the low-frequency excitations in the vibrational spectrum of PMN with the fracton spectral dimension determined from the generalized density of states in the course of experiments on inelastic neutron scattering [5, 6]. The small-angle scattering of the synchrotron radiation from PMN [7] indicate a possible formation of a self-similar structure of nanoclusters implemented in the form of fractals. Thus, it is reasonable to expect the presence in the PMN vibrational spectrum of the excitations characteristic of a fractal medium—fractons. It is highly probable that this role is played by a low-frequency mode with the frequency on the order of $\nu \sim 50 \text{ cm}^{-1}$ observed in the light scattering spectra [5]. Unfortunately, a more detailed analysis of the Raman scattering in PMN in terms of the spectral dimensions, corresponding to the fracton and Debye regimes, presents some difficulties. First, the existence of the selection rules for Raman scattering in crystalline solids limits the applicability of the fracton ideology developed for the analysis of the low-frequency light scattering spectra of noncrystalline condensed media. Second, the simulation of the inelastic light scattering for a number of classical fractal objects showed that the frequency dependence of the coupling coefficient of light and the atoms (or ions) in a condensed medium substantially modifies the frequency dependence of the scattered-light intensity [8]. To construct a model of the fractal PMN structure one has to investigate in detail its structure and vibrational spectrum. This stimulated the search for additional manifestations of the fracton dynamics in the vibrational PMN spectrum, which would have reflected the specific features of PMN orga-

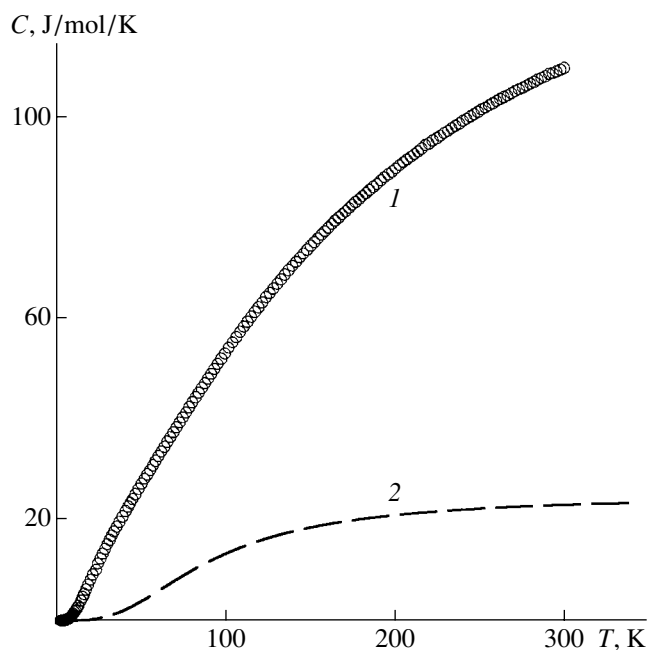


Fig. 1. The temperature dependence of the specific heat of the PMN relaxor ferroelectric in the temperature range 2–300 K: (1) experimental data and (2) contribution of the Debye heat capacity corresponding at $T_D = 376$ K [14].

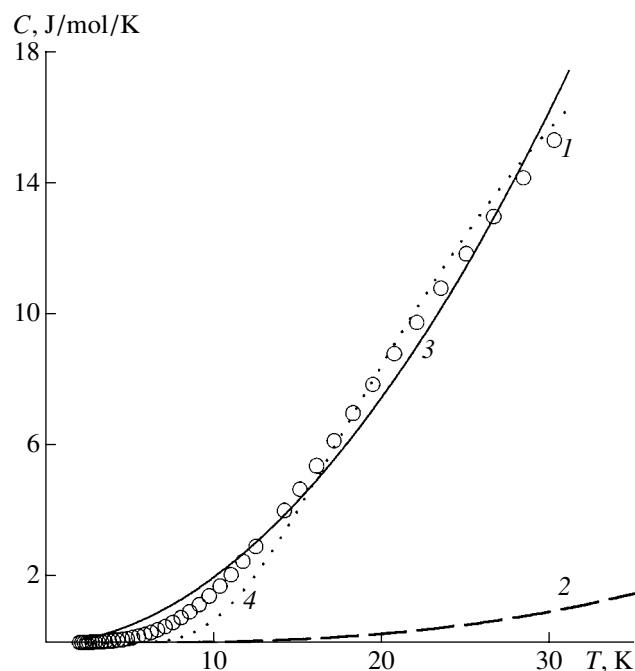


Fig. 2. Heat capacity of PMN in the low-temperature region: (1) experimental data, (2) the Debye contribution to heat capacity, (3) calculation according to the model of the two-level systems, and (4) calculation by the Einstein oscillator.

nization on the nanometer length scale. The analysis of the heat-capacity behavior at low temperatures offers a good opportunity for considering one of the stages of the above problem. The study of the temperature dependence of the heat capacity of PMN was reported in [9, 10]. However, only the differential heat capacity of PMN was measured in [9], while in [10] the measurements of heat capacity at low temperatures were made only at 7 K. Therefore, we decided to make precision measurements of the heat capacity of PMN.

EXPERIMENTAL

A PMN sample was synthesized by crystallization from melt [11]. The mixture of MgO (Rare Metallic Co., 99.9%) and Nb_2O_5 (Mitsui Mining & Smelting Co.) powders was placed into an agate mortar and heated for 24 h in a closed oven at the temperature of 1370 K. The product obtained, MgNb_2O_6 , was mixed with lead oxide, PbO (Rare Metallic Co., 99.99%), in the 1 : 7.5 weight ratio, and the mixture was placed into a platinum crucible. The crucible covered with a platinum foil was heated for 3 h in a vertical oven at 1510 K and then was slowly (for 200 h) cooled down to 1210 K and then, rapidly to room temperature. The mixture thus obtained was dissolved in hot nitric acid. The separated transparent PMN single crystals had a brown–yellow color and the maximum dimensions

$\sim 2 \times 2 \times 2$ mm³. The PMN structure was checked by the X-ray powder diffraction.

Precision measurements of the PMN specific heat in the range 13–300 K were performed with the aid of an adiabatic calorimeter [12, 13]. The temperature was measured by a 5187L (H. Tinsley & Co.) platinum resistance thermometer calibrated in the National Physics Laboratory (NPL) in the Great Britain with the use of the International Temperature Scale ITS-90. The accuracy of the specific-heat measurements was 0.1% at $T = 100$ K and was compared with the data obtained on the Standard Reference Material SRM720 (synthetic sapphire) from the National Institute of Standards and Technology (NIST, USA). The mass of the PMN crystal samples was 11.1106 g (0.034162 mol). The samples were placed into a calorimeter reservoir together with a small amount of helium whose pressure was 5 kPa at room temperature. The specific heat of the sample was determined as the difference between the total heat capacity of the calorimeter reservoir and the total heat capacity. At room temperature, the heat capacity of the sample was $\sim 20\%$ of that of the calorimeter reservoir. Neither supercooling, nor thermal relaxation were observed in the course of the measurements.

The specific heat in the range 2–50 K was measured by the relaxation method on a standard PPMS device (model 6000, Quantum Design Inc. as a basic unit). The relaxation measurements were performed on a PMN

single crystal [14.29 mg in weight (0.04394 mmol)]. The data obtained are in excellent agreement with the data obtained by adiabatic calorimetry.

RESULTS AND DISCUSSION

Figure 1 shows the temperature dependence of the specific heat C_p of PMN in the range 2–300 K. It is seen that, in the region of the diffuse phase transition ($\tilde{T}_C \sim 270$ K), this dependence has no anomalies. This fact and the absolute C_p values are consistent with the results reported in [10]. Consider C_p behavior in the low-temperature region ($T < 30$ K, Fig. 2) in more detail. In this region, one can readily separate the contributions additional to phonon ones to the crystal lattice dynamics.

According to the Debye theory, the low-temperature heat capacity of a crystal is determined by the acoustic phonons and can be described by the following equation:

$$C_D = 9R \left(\frac{T}{\theta_D} \right)^3 \int_0^{E_D/kT} \frac{e^x x^4}{(e^x - 1)^2} dx, \quad (1)$$

where $R = 8.314$ J/mol/K is the universal gas constant, θ_D is the Debye temperature, and $E_D = k\theta_D$ is the Debye energy. We used the Debye temperature $\theta_D = 376$ K obtained from the low-temperature acoustic measurements in [10, 14].

Figure 2 shows that the contribution of acoustic phonons (curve 2), which determines the Debye heat capacity, at $T < 12$ K is negligibly small and is about 5% of the experimentally observed heat capacity at $T \sim 30$ K. Therefore, the contribution of acoustic phonons cannot explain the experimental data obtained.

The excessive low-temperature heat capacity was observed, e.g., for canonic glasses, for which, similar to a number of other related disordered systems, the conventional method of description of the behavior of the low-temperature heat capacity is the formalism of two-level systems [15]. According to this formalism, one can expect a linear dependence of heat capacity, $C = C_D + AT$, at $T < 1.5$ K. We made an attempt to use this approach to take into account excessive heat capacity in PMN. However, our calculations (the least square procedure) showed that the formalism of the two-level systems is inapplicable in this case (Fig. 2, curve 3).

The low-temperature heat capacity, excessive with respect to the Debye contribution, can be explained by the presence of the low-lying optical mode in the elementary-excitation spectrum of the crystal. This approach can be fruitful for PMN if one takes into account the experimental data on inelastic neutron scattering [16]. The spectra of inelastic neutron scattering in PMN at $T = 650$ K were adequately described by the model of coupled “quasi-optical” mode and the trans-

verse acoustic phonon [16]. The frequency of the quasi-optical mode in the vicinity of the Brillouin-zone center was $\omega_0 = 2\pi\nu_0 = 0.287$ THz. Thus, it was expedient to describe excessive heat capacity in terms of the Einstein oscillator corresponding to this quasi-optical mode. In our calculations, we used the sum of the Debye contribution and the classical expression for the Einstein oscillator with the characteristic frequency $\omega_E = 2\pi\nu_E$; we obtained

$$C = 9R \left(\frac{T}{\theta_D} \right)^3 \int_0^{E_D/kT} \frac{e^x x^4}{(e^x - 1)^2} dx + 3R \left(\frac{\hbar\omega_E}{kT} \right)^2 \exp\left(\frac{\hbar\omega_E}{kT}\right) \left(\exp\left(\frac{\hbar\omega_E}{kT} - 1\right) \right)^{-2} \equiv C_D + C_E. \quad (2)$$

Figure 2 (curve 4) shows the results calculated with the use of Eq. (2) for $\nu_E = 1.6$ THz = 56 cm⁻¹. It is evident that the satisfactory agreement between the theory and the experiment can be attained only at $T > 15$ K. With lowering of the temperature, the calculated heat capacity decreases much faster than in the experiment. Thus, the introduction of the quasi-optical mode (Einstein oscillator) cannot explain the behavior of heat capacity in PMN at low temperatures. A similar approach was also used in [10], where the expression for C_E was corrected by an additional normalizing factor r , whose physical sense is unclear. Therefore, our data can hardly be compared with the data in [10].

Thus, the analysis of excessive low-temperature contribution to the heat capacity of PMN shows that its description requires the invocation of some other mechanisms. Taking into account the data on the density of the vibrational states $G(E)$ in PMN [5, 6], consider the contribution of fractons to the heat capacity in PMN at low temperatures.

Earlier, the fracton contribution to the low-temperature heat capacity of a number of compounds was considered in [16, 17] (see also references there). We discuss the fracton contribution to heat capacity of PMN in terms of the approach suggested in [16, 17] and modified for our goals. The expression for the heat capacity is obtained from the general relation

$$C_v = (\partial E / \partial T)_v = \frac{\partial}{\partial T} \left(\int d\omega G(\omega) n(\omega) \hbar\omega \right), \quad (3)$$

where $n(\omega)$ is the Bose–Einstein distribution function and $G(\omega)$ is the density of the vibrational states. Following [18], we assume that $G(\omega) \propto \omega^2$ at $\omega < \omega_{co}$ (the phonon mode with the spectral dimension d) and that $G(\omega) \propto \omega^{\tilde{d}-1}$ at $\omega_{co} < \omega < \omega_m$ (the fracton mode with the spectral dimension \tilde{d}). Under these assumptions,

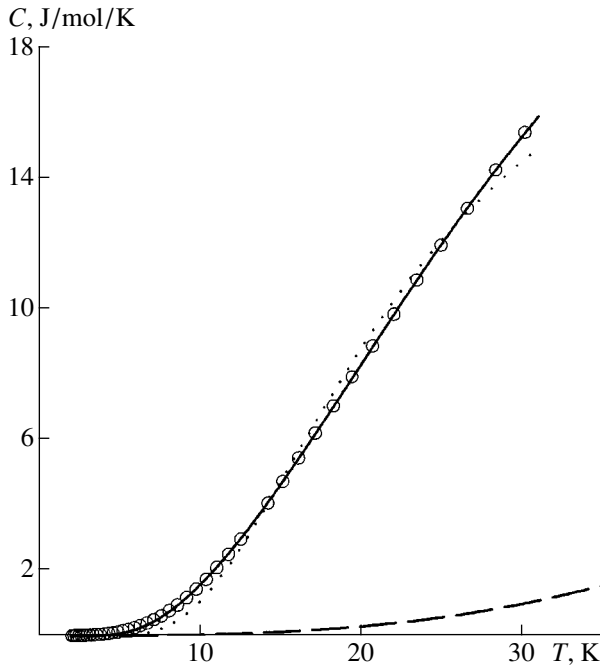


Fig. 3. Heat capacity of PMN in the low-temperature region: experimental data (circles), the Debye contribution to the heat capacity (dashed line), and the calculations by Eq. (4), variant *a* (solid line) and variant *b* (dotted line).

we have

$$C = 9R \left(\frac{T}{\theta_D} \right)^3 \int_0^{E_{co}/kT} \frac{e^x x^4}{(e^x - 1)^2} dx + AT^{\tilde{d}} \int_{E_{co}/kT}^{E_m/kT} \frac{e^x x^{\tilde{d}+1}}{(e^x - 1)^2} dx, \quad (4)$$

where $E_{co} = \hbar\omega_{co}$ is the energy of the crossover from the Debye to fracton regime, $E_m = \hbar\omega_m$ is the maximum energy at which the fracton regime is implemented (since the difference between C_v and C_p is negligibly small at all the temperatures considered here, hereafter the index is omitted).

The calculations by Eq. (3) should be performed with due analysis of the density-of-states function $G(E)$ in PMN [5, 6]. The spectral dimension $d = 2.8$ for the range 2–5 meV is quite consistent with the classical Debye regime, while the range 5–7 meV with the

dimension $\tilde{d} = 1.7$ corresponds to the fracton mode. Now, we have to consider the boundary between the phonon and the fracton modes and to establish whether it is diffused or clearly defined. This question is of primary importance for choosing the limits of integration in Eq. (4). At present, there is no universally accepted viewpoint on the type of the crossover from the phonon to fracton regime. This necessitated the use of two different procedures for calculating heat capacity, hereafter referred to as procedures (a) and (b). Procedure (a) involved fitting of the calculated heat capacity to the experimental data on the condition that all the parameters A , \tilde{d} , E_{co} , and E_m are free. In procedure (b), the parameter E_m is fixed whereas all the other three parameters are free. The E_m value is chosen upon the analysis of the vibrational-state density function [5, 6].

Figure 3 illustrates two fitting procedures based on Eq. (4). It is seen that the curves calculated in procedures (a) and (b) are very close to each other. Obviously, the calculations by Eq. (4) provide an adequate description of the experimental data in the whole temperature range analyzed. On the one hand, procedure (a) (Fig. 3, curve 3) shows better agreement with the experimental temperature dependence of the heat capacity. Here the parameters ($E_{co} = 2.9$ meV, $E_m = 13.3$ meV, and $\tilde{d} = 1.3$) differ from the corresponding values found from the data on inelastic neutron scattering [6] (the results of the calculation and the analysis of the data on inelastic neutron scattering are tabulated). On the other hand, the parameters obtained in procedure (b) are in good agreement with the data on inelastic neutron scattering (see table). The spectral dimension $\tilde{d} = 1.6$ calculated by the data on heat capacity practically coincides with the experimental data on inelastic neutron scattering. The experimental heat capacity exceeds by 5% the calculated one [by procedure (b)] in the vicinity of 30 K. This fact can be explained by the contribution of the low-frequency transverse optical phonon to the density of the states (and hence to the heat capacity). The consistent allowance for this contribution to the heat capacity is hardly possible because the low-frequency transverse optical phonon has rather strong dispersion in the Brillouin zone [19] and thus cannot be described by Einstein oscillator.

Thus, the approach taking into account the presence of fractons in the vibrational spectrum of PMN allows the description of the experimental data on heat capac-

The model parameters obtained by Eq. (4) and from the inelastic neutron-scattering data [6]

Calculation procedure	A	\tilde{d}	E_{co} , meV	E_m , meV	Standard deviation
<i>a</i>	0.060	1.3	2.9	13.3	0.001
<i>b</i>	0.062	1.6	5	7.2	0.13
Neutron-scattering data		1.7	5	7	

ity. The establishment of the type of the crossover requires some additional studies.

CONCLUSIONS

The analysis of the experimental temperature dependences of the specific heat of the PMN relaxor ferroelectric showed that its behavior in the range $2 < T < 30$ K cannot be attributed to phonon contribution. The use of the formalism of the two-level systems or the invocation of the quasioptical mode cannot explain the experimental data either. It is the fractal formalism that proved to be fruitful. An account for the fracton contribution provided the adequate description of the temperature dependence of the heat capacity at $T < 30$ K. The calculations performed yielded the spectral dimension $\tilde{d} = 1.6$ close to the value $\tilde{d} = 1.7$ determined from the data on inelastic neutron scattering.

ACKNOWLEDGMENTS

This study was supported by the Russian Foundation for Basic Research, project no. 99-02-18316. One of us, S.N.G., acknowledges the support of the International Soros Science Educational Program.

REFERENCES

1. G. A. Smolenskiĭ, V. A. Bokov, V. A. Isupov, N. N. Krainik, R. E. Pasynkov, A. I. Sokolov, and N. K. Yushin, *Physics of Ferroelectric Phenomena* (Nauka, Leningrad, 1985).
2. C. Boulesteix, F. Varnier, A. Llebariz, and E. Husson, *J. Solid State Chem.* **108**, 141 (1994).
3. P. Julin and A. Bursill, *Mod. Phys. Lett.* **7**, 609 (1993).
4. Z. G. Ye and H. Schmidt, *Ferroelectrics* **145**, 83 (1993).
5. S. G. Lushnikov, S. N. Gvasaliya, and I. G. Siny, *Physica B* (Amsterdam) **263–264**, 286 (1999).
6. S. N. Gvasaliya, S. G. Lushnikov, I. L. Sashin, and I. G. Siny, *Kristallografiya* **44**, 284 (1999) [*Crystallogr. Rep.* **44**, 250 (1999)].
7. S. D. Vakhrushev, A. A. Nabereznov, S. K. Sinha, *et al.*, *J. Phys. Chem. Solids* **57**, 1517 (1996).
8. V. Mazzacurati, M. Montagna, O. Pilla, *et al.*, *Phys. Rev. B* **45**, 2126 (1992).
9. A. Fouskova, V. Kohl, N. N. Krainik, and I. E. Mil'nikova, *Ferroelectrics* **34**, 119 (1981).
10. B. A. Strukov, E. L. Sorkin, V. M. Rizak, *et al.*, *Fiz. Tverd. Tela* (Leningrad) **31** (10), 121 (1989) [*Sov. Phys. Solid State* **31**, 1719 (1989)].
11. Z.-G. Ye and P. Tissto, *Mater. Res. Bull.* **25**, 739 (1990).
12. T. Atake, H. Kawaji, A. Hamano, and Y. Saito, *Rep. Res. Lab. Eng. Mater.*, Tokyo Inst. Technol. **15**, 13 (1990).
13. T. Tanaka, T. Atake, H. Nakayama, *et al.*, *J. Chem. Thermodyn.* **26**, 1231 (1994).
14. G. A. Smolenskiĭ, N. K. Yushin, S. I. Smirnov, and G. Gulyamov, *Fiz. Tverd. Tela* (Leningrad) **28**, 932 (1986) [*Sov. Phys. Solid State* **28**, 522 (1986)].
15. A. Heur, in *Tunneling Systems in Amorphous and Crystalline Solids*, Ed. by P. Esquinazi (Springer-Verlag, Berlin, 1998), p. 459.
16. A. A. Naverezhnov, S. B. Vakhurushev, B. Dorner, *et al.*, *Eur. Phys. J. B* **11**, 13 (1999).
17. S. Alexander, C. Laermans, R. Orbach, and H. M. Rosenberg, *Phys. Rev. B* **28**, 4615 (1983).
18. J. Kjems, in *Fractals and Disordered Systems*, Ed. by A. Bunde and S. Havlin (Springer-Verlag, Berlin, 1995), p. 303.
19. T. Nakayama, K. Y. Yakubo, and R. Orbach, *Rev. Mod. Phys.* **66**, 381 (1994).

Translated by A. Zolot'ko

Growth of Single Crystals of Monticellite CaMgSiO_4 : Cr from Melt by Floating Zone Technique and the Study of Their Composition

K. A. Soubbotin¹, E. V. Zharikov^{1,2}, L. D. Iskhakova³, and S. V. Lavrishchev¹

¹ *Laser Materials and Technology Research Center, Institute of General Physics, Russian Academy of Sciences, ul. Vavilova 38, Moscow, 117942 Russia*

e-mail: soubbot@lsk.gpi.ru

² *University of Chemical Technology, Miusskaya pl. 9, Moscow, 125190 Russia*

³ *Fiber Optics Research Center, Institute of General Physics, Russian Academy of Sciences, ul. Vavilova 38, Moscow, 117942 Russia*

Received September 25, 2000

Abstract—Crystallization of monticellite CaMgSiO_4 from melt by the floating-zone technique was studied at different compositions of feed rods. The compositions of rapidly cooled melts and different regions of grown crystals were investigated by the X-ray phase and microprobe analyses. The inclusions of secondary phases were identified. The range of most promising compositions of the charge for technology of growing large high-quality crystals is established. The mathematical model of the changes in the melt composition during monticellite crystallization is constructed. © 2001 MAIK “Nauka/Interperiodica”.

INTRODUCTION

Single crystals of complex oxides doped with Cr^{4+} ions are of great interest as activated media for 1.1–1.7- μm tunable solid-state lasers [1]. Presently, only two crystals—forsterite Mg_2SiO_4 and yttrium–aluminum garnet (YAG) $\text{Y}_3\text{Al}_5\text{O}_{12}$ —are used as hosts for Cr^{4+} ions. However, neither of these matrices is optimal for these ions, because, in both cases, the quantum yield of luminescence is very low. This is explained by undesirable nonradiative relaxation of the $^3\text{T}_2$ excited state of Cr^{4+} ions occurring in the above-mentioned crystals at room temperature and becoming very intense during heating of the activate medium of the laser. Therefore, serious efforts are made to search for new promising Cr^{4+} -doped crystals with improved spectroscopic characteristics.

One of these crystals is monticellite CaMgSiO_4 isostructural to forsterite [2, 3]. In this crystal, the luminescence lifetime of Cr^{4+} ions is 5.5 μs [2] and the quantum yield is about 30% [3] (for comparison, the analogous characteristics for YAG are 4 μs and 22%, respectively [4]). However, incongruent melting of monticellite [2, 5] complicates its growth and hinders its practical application.

For the first time, Cr^{4+} -doped monticellite single crystals were grown in 1997 [6]. We also managed to study those spectroscopic properties of these crystals, which could not be studied on powdered samples:

polarized absorption spectra, the refined luminescence spectrum, the kinetics of luminescence decay, etc. [7].

Nevertheless, the improvement of the growth technology of monticellite crystals appropriate for lasers is still an important problem. The solution of this problem calls for exhaustive investigation of crystallization in the ternary CaO – MgO – SiO_2 system, in particular, in the vicinity of the point corresponding to the stoichiometric monticellite composition ($\text{CaO} : \text{MgO} : \text{SiO}_2 \approx 1 : 1 : 1$), which would allow the determination of the optimum charge composition for growing high-quality monticellite crystals.

The phase ratios in this ternary system were examined in a number of studies [5, 8]. In particular, the phase diagram in Figs. 1 [5] and 2 demonstrates that the stoichiometric point of CaMgSiO_4 is located in the field of primary-crystallization of MgO , whereas the field of primary-crystallization of monticellite is somewhat shifted from this point toward SiO_2 .

At the same time, some important results in the studies cited above are inconsistent, in particular, the data on the behavior of the compound during melting are rather complicated and, as will be demonstrated below, strongly dependent even on small changes in the charge composition. There are almost no data on the behavior of the system during crystallization and subsequent cooling, with the only one exception—the data on mutual solid-phase solubility of monticellite and forsterite at different temperatures [5]. Moreover, the studies [5, 8] were performed for the equilibrium states, so

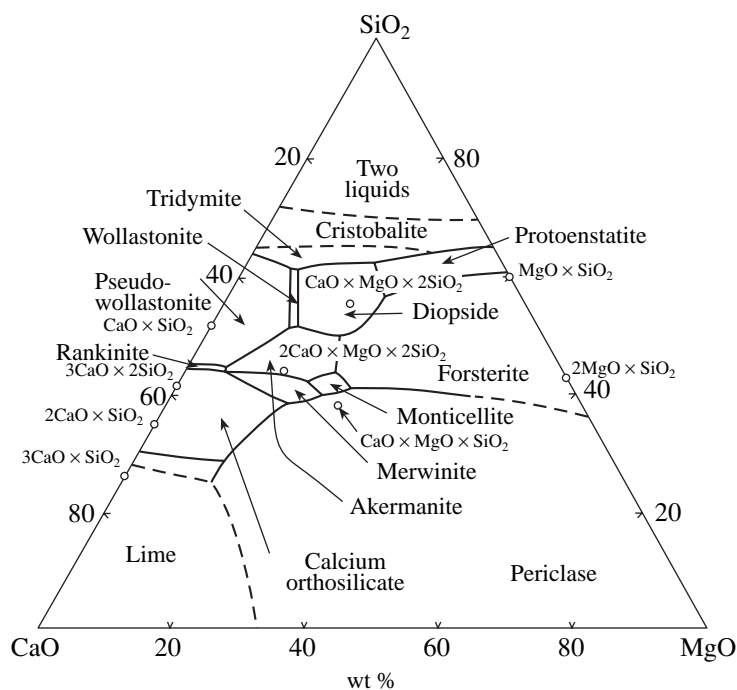


Fig. 1. Phase diagram of the ternary CaO–MgO–SiO₂ system [5].

that their results cannot be directly applied to the process of crystal growth. The presence of a Cr dopant in the charge can also introduce some changes.

The present study was aimed at investigation of the crystallization of chromium-doped monticellite and optimization of the composition of the initial charge for growth of CaMgSiO₄: Cr single crystals. For this purpose, we prepared a series of crystalline samples of different compositions and studied them by X-ray phase and microprobe analyses.

EXPERIMENTAL

The crystals were grown by the crucible-free vertical floating zone technique on an URN-3-ZP setup in air (the details of the crystal growth process were described elsewhere [9]). The floating zone melting technique was used by the following reasons:

(1) This method is rather “fast” and economic (10 g of the reagent is sufficient for preparing a feed rod for performing from two to three parallel growth experiments).

(2) In growth compounds melting incongruently, the melt composition is gradually changed, the floating zone melting technique allows one to follow the rate and the direction of these changes in the melt using its rapid cooling (several hundreds of degrees centigrade per second) with the subsequent determination of the composition by the microprobe analysis and the analysis of the mutual influence of the changes in the compo-

sitions of the melt and the growing crystal (in both of the major and the secondary phases).

The compositions of feed rods are shown in Fig. 2a. The experiments were performed within the concentration range determined in the preliminary study [6]. It should be noted that this range is partly outside the field of primary crystallization of monticellite determined in [5].

The initial reagents of high-purity grade were either dried at 120°C (calcium carbonate CaCO₃) or calcined at 600°C (MgO and SiO₂) to remove the moisture traces. Then they were weighted in the corresponding ratios, and upon the addition of Cr₂O₃ (0.2 wt %), were thoroughly mixed. The resulting mixture was pressed into rods sintered for 24 h at 1250°C to provide the necessary mechanical strength.

At the first stage of the study, forsterite single crystals of cut along the *c*-axis (the *Pnma* setting) were used as seeds; then we also used the seeds of monticellite crystals grown from the feed-rod composition (FRC 6) charge and having the same orientation. The rate of rod motion relative to the heating zone was 1.5 mm/h. The rotation rate was 30 rpm; we used counterrotation mode, which provided better stirring conditions in the melt zone.

X-ray powder diffraction analysis was made on conventional DRON-2 and DRON-4 diffractometers with the Ge internal standard.

Scanning electron microscopy and the microprobe analysis were performed on a Jeol JSM-480 setup. In the electron micrographs, the illumination of the region was proportional to the secondary electron-emission

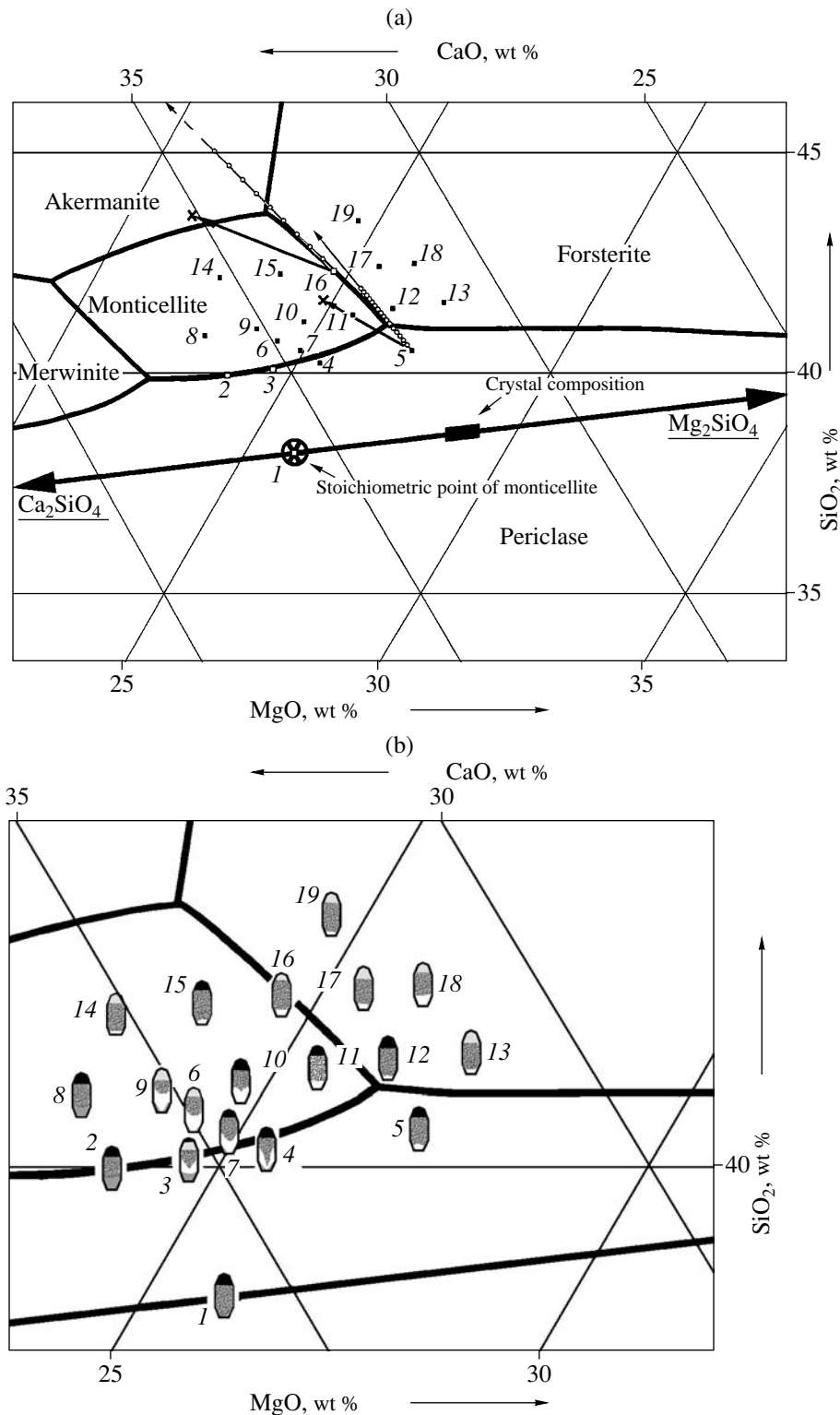


Fig. 2. Enlarged fragment of the phase diagram of the CaO–MgO–SiO₂ system showing the stoichiometric point and the field of primary crystallization of monticellite: (a) the compositions of the feed rods are shown by black squares with the sizes corresponding to the actual accuracy of weighting of the charge components; the actual directions of the changes in the melt composition during crystal growth are indicated by thick arrows (the melt compositions after growth completion determined by microprobe analysis are marked with crosses), the changes of the melt compositions calculated by Eq. (8) are indicated by thin arrows (the compositions obtained after each iteration are marked with circles); the thick line ended with two arrows represents the concentration line connecting Ca₂SiO₄ and Mg₂SiO₄; (b) the zone ratio in growing crystals as a function of the composition of the feed rod: □ is the transparent M zone; ◻ is the semitransparent greenish MP zone; ◼ is the defect MFA zone; ◽ is the transparent A zone; ◼ is the nontransparent polycrystalline tip.

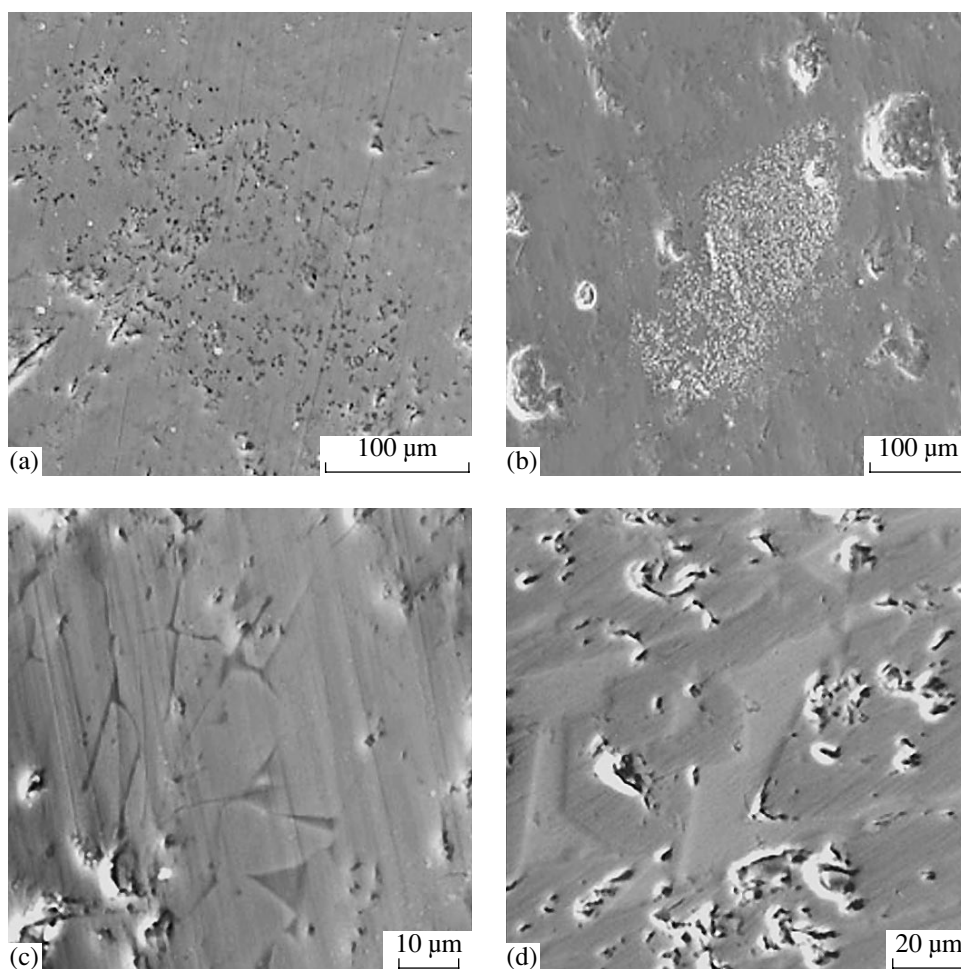


Fig. 3. Electron micrographs of the regions of quenched melts of various compositions: (a) FRC 12: MgO inclusions are seen as sets of dark spots; (b) FRC 11: inclusion of an agglomerate of small grains of the composition $\text{Ca}_{1.33}\text{Mg}_{0.67}\text{SiO}_4$ is seen as a set of light spots; (c) FRC 11: microinclusions of $\text{CaMgSi}_3\text{O}_8$ and $\text{CaMgSi}_2\text{O}_6$ appear as dark triangles and elongated rectangles, respectively; (d) FRC 15: inclusions of akermanite $\text{Ca}_2\text{MgSi}_2\text{O}_7$ are represented by irregularly shaped light regions; one can also see numerous cavities.

intensity from this region. Thus, inclusions of secondary phases as well as cracks, cavities, and other three-dimensional defects could be revealed as the regions having a contrast different from the contrast of the main phase.

RESULTS AND DISCUSSION

In the concentration range under investigation, the melts have a number of characteristic features sensitive even to small changes in the feeding-rod composition (FRC). In particular, melts of compositions closest to the stoichiometric point of monticellite (FRC 1–4, 6–8, and 10; Fig. 2a) are nontransparent at the first stages of crystal growth. They become transparent gradually within the time from 10 min to 2.5 h after the onset of the growth process. The melts of the feed-rods of other compositions are transparent in the whole growth process from the stage of feed-rod melting up to the rupture of the molten zone.

Moreover, at least two types of visible inclusions are observed at the initial stages of melting. The visual examination made during the melting process showed the first-type inclusions as light nontransparent regions up to 2 mm in length and up to 0.8 mm in thickness (against the rather dark background of the melt). The shape of these inclusions is very unstable, which indicates their suspension-like nature. This conclusion is confirmed by electron microscopy study of the rapidly cooled melt of FRC 12 (this transparent melt was chosen because of the absence of visible second-type inclusions). On the micrograph (Fig. 3a), the first-type inclusions are seen as small grains distributed in the main phase of the melt. According to the microprobe analysis data, the grain composition corresponds to MgO.

Inclusions of this type were observed in the transparent melts, FRC 5, 9, 12, and 13. Moreover, these inclusions are also unambiguously detected in nontransparent melts, FRC 6–8, which allows one to

assume their presence in all the other initially nontransparent melts (FRC 1–4 and 10; the visual observation of inclusions in these melts is rather difficult because of their nontransparency). This assumption seems to be logic if one takes into account that the above-mentioned compositions are rather close to the field of primary crystallization of MgO and the stoichiometric point of CaMgSiO_4 . At this point, MgO is the most high-melting phase of all the intermediate phases formed during melting [5, 8] and is dissolved only when all the secondary phases have already been dissolved. However, the conclusion that the MgO phase in the above-mentioned melts is formed during melting because of decomposition of other intermediate phases rather than is initially present in the feed rods seems to be premature and calls for additional study.

First-type inclusions disappear (are dissolved) within 2–3 min after the beginning of melting before seeding. This signifies that the MgO phase under the conditions used is not in equilibrium with the melt and that its formation during melting cannot be directly related to the characteristics of monticellite crystallization from melt.

Second-type inclusions are observed as small (up to 0.3 mm) stable particles, whose composition was determined by studying different regions of the metallographic section of the quenched transparent melt FRC 11 having no first-type inclusions. Several types of inclusions of secondary phases were detected. However, only relatively large agglomerates of small grains (Fig. 3b) of the composition $\text{Ca}_{1.33}\text{Mg}_{0.67}\text{SiO}_4$ were visible to the naked eye (this phase is also found in some crystals; see below).

Second-type inclusions are detected in some transparent (FRC 9 and 11) and initially nontransparent (FRC 3, 6, and 8) melts and also in melts with first-type inclusions. We cannot rule out the presence of these inclusions in any initially nontransparent melt.

Unlike first-type inclusions, the above particles can exist in the melts for rather long time after the onset of crystal growth (FRC 3, 6, and 8). These inclusions are also observed in these melts as they become transparent. These inclusions can also appear in the course of growth and can precipitate in the crystalline phase. Thus, this phase is in equilibrium with the melt and is dissolved only due to the corresponding change in the melt composition during crystal growth.

The melts are transparent from the beginning of growth and have no visually observable inclusions only the SiO_2 concentration considerably exceeds that in the FRC and the compositions far from both the stoichiometric point of CaMgSiO_4 and the primary-crystallization field of MgO, as is the case in FRC 14–19.

Microscopic inclusions were detected in both initially nontransparent and transparent melts. Presently, no clear and reproducible correlations between the type and the concentration of microscopic inclusions in melts and the degree of melt enrichment with a partic-

ular component or its distance from the field of primary crystallization of a given secondary phase have been found.

Among the microscopic inclusions found in the melts, we indicate the diopside inclusions, $\text{CaMgSi}_2\text{O}_6$, observed as elongated 1- μm -thick rectangles and triangular inclusions with the composition $\text{CaMgSi}_3\text{O}_8$ (Fig. 3c).

One more inclusion is imperfect akermanite, $\text{Ca}_2\text{MgSi}_2\text{O}_7$, in the elongated shape with a length of up to 100 μm (Fig. 3d). This inclusion is revealed in high concentrations in almost all rapidly cooled melts, including those, which were initially transparent.

Conceivably, the fact that the inclusions of such dimensions do not cause melt opalescence indicates that the akermanite inclusions were not present in the initial melts and were formed only during rapid cooling of the melt (similar to the crystalline phase of monticellite).

Crystals specially grown for studies were 10–15 mm in length and 6–7 mm in diameter. Small concentrations of Cr^{4+} ions provided the beautiful blue color of the grown crystals.

The crystals grown had a number of successive zones along the growth axis of the crystal, which have different shapes and compositions. The volume ratio of the zones depends on FRC and varies from the complete absence of a particular zone at the given FRC up to its predominance in the sample at the other FRC (Fig. 2b, table).

The zone M (monticellite) immediately following the seed is the zone of single-crystalline monticellite containing no inclusions of secondary phases (Fig. 4a). This zone is transparent, blue in color with noticeable pleochroism. The unit-cell parameters of monticellite calculated from the X-ray powder diffraction analysis data for this zone are $a = 10.987(3)$ Å, $b = 6.324(2)$ Å, $c = 4.816(1)$ Å, i.e., are somewhat less than the corresponding values determined previously for undoped monticellite [10]. The formulas determined from the microprobe analysis data are different for different regions of the samples and are varied from $\text{Ca}_{0.87}\text{Mg}_{1.13}\text{SiO}_4$ to $\text{Ca}_{0.92}\text{Mg}_{1.08}\text{SiO}_4$ (in Fig. 2a, this concentration region is seen as a black rectangle located on the Ca_2SiO_4 – Mg_2SiO_4 line). The limiting compositions go only slightly outside the concentration region of stability of monticellite determined earlier [11].

The M zone is not observed only in the crystals grown from FRC 2 and 8 (it seems that in these crystals, the M zone is “absorbed” by the well-developed MP zone; see below) and in the crystals grown from the stoichiometric charge (FRC 1). In all the crystals grown from the remaining FRC, the M zone manifests itself to a greater or a lesser extent (Fig. 2b, table). The charges used for FRC 6 and 9 are proved to have the compositions closest to the optimum composition. Crystals grown from these FRC are characterized by the largest

Characteristics of the crystals grown

FRC	Molar ratios of the components in FRC (CaO : MgO : SiO ₂)	Characterization of zones in samples			
		M (one-phase monticellite)	MP (monticellite + periclase + Ca _{1.33} Mg _{0.67} SiO ₄)	MFA (monticellite + forsterite + akermanite)	A (akermanite + impurities)
1	33.3 : 33.3 : 33.3	Absent	Absent	Single	Absent*
2	34 : 31 : 35	Absent	Up to 1/3 of the sample length	Up to 1/2 of the sample length	Absent
3	33 : 32 : 35	Up to 1/4 of the sample length	1–2 mm	Up to 1/2 of the sample length	Sometimes present
4	32 : 33 : 35	Up to 1/3 of the sample length	1–2 mm, at the periphery	Dominant	Absent
5	30 : 35 : 35	Insignificant	Absent	Dominant	Absent
6	32.7 : 31.7 : 35.7	Up to 1/2 of the sample length	Sometimes is observed at the periphery	Up to 1/2 of the sample length	Present
7	32.3 : 32.3 : 35.3	Up to 1/3 of the sample length	Sometimes is observed at the periphery	Dominant	Absent
8	34 : 30 : 36	Absent	2–3 mm	Up to 1/2 of the sample length	Absent
9	33 : 31 : 36	Up to 1/2 of the sample length	1–2 mm, at the periphery	Up to 1/2 of the sample length	Present
10	32 : 32 : 36	Up to 1/3 of the sample length	Absent	Dominant	Absent
11	31 : 33 : 36	1–2 mm	Absent	Dominant	Absent
12	30 : 34 : 36	Insignificant	Absent	Dominant	Absent
13	29 : 35 : 36	Insignificant	Absent	Dominant	Sometimes present
14	33 : 30 : 37	Insignificant	Absent	Dominant	Present
15	32 : 31 : 37	Insignificant	Absent	Dominant	Absent
16	31 : 32 : 37	1–2 mm	Absent	Dominant	Present
17	30 : 33 : 37	Insignificant	Absent	Dominant	Present
18	29 : 34 : 37	1–2 mm	Absent	Dominant	Present
19	30 : 32 : 38	Insignificant	Absent	Dominant	Present

* The word "absent" in the column "A zone" signifies that the tip of the sample is a nontransparent polycrystalline region.

volume fraction of the M zone and the highest optical quality. Therefore, this range of charge compositions is rather promising for the technology of growing large monticellite crystals by the Czochralski method.

The MP (monticellite + periclase) zone is observed in a number of crystals (Fig. 2b, table). The volume fraction of this zone has the tendency to increase with the approach of the FRC composition to the fields of primary crystallization of periclase, MgO and, especially, of merwinite Ca₃Mg(SiO₄)₂. Thus, the MP zone in the crystals grown from FRC 4, 6, 7, and 9 is observed only in the subsurface region of the crystals, thus "surrounding" the M zone, whereas the MP zone in crystals grown from FRC 3 extends over the whole cross section of the seeding region of the crystal and precedes the M zone. Finally, in the crystals grown from FRC 2 and 8, the MP zone is developed so well that it virtually completely "absorbs" the M zone.

Contrary to the M zone, the MP zone exhibits opalescence and has the greenish tint (in comparison with the other zones), which seems to be caused by the presence of two types of microscopic inclusions (see Fig. 4b). The darker phase is magnesium oxide (periclase). The lighter phase is characterized by an unknown set of X-ray diffraction reflections and has the molar composition CaO 44.7%, MgO 22.0%, and SiO₂ 33.3%. It can be assumed that this phase is a solid solution between monticellite and merwinite (for convenience, the formula of the latter phase can be written as Ca_{1.5}Mg_{0.5}SiO₄), although it was stated [5, 12] that no such solid-phase solubility can exist). It can also be assumed that it is a new compound described by the formula Ca_{1.33}Mg_{0.67}SiO₄ or Ca₄Mg₂Si₃O₁₂.

In ought to be remembered that both MgO and Ca_{1.33}Mg_{0.67}SiO₄ inclusions were also found in a number of melts (see above). This fact may indicate that

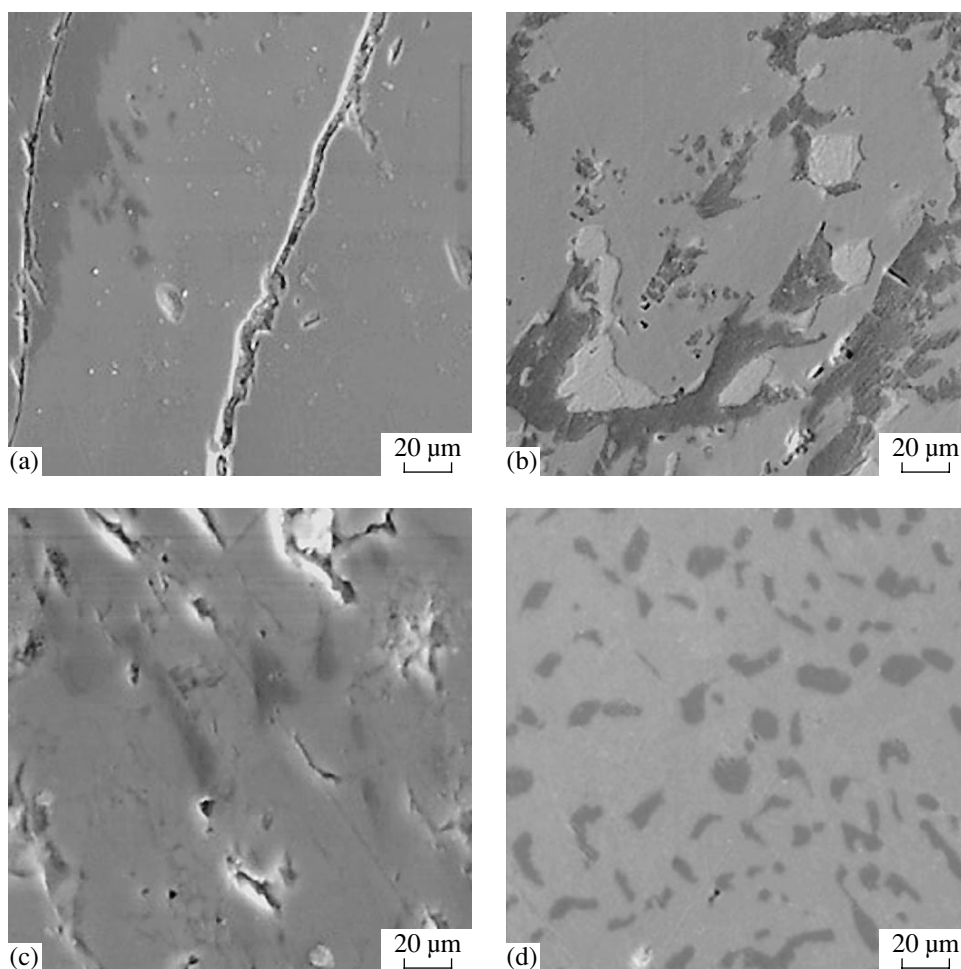


Fig. 4. Electron micrographs of the characteristic zones in the crystals: (a) M (the region of the forsterite seed is seen as a dark region on the left; cracks are seen as two narrow almost vertical bands); (b) MP (MgO appears in the form of dark regions; $\text{Ca}_{1.33}\text{Mg}_{0.67}\text{SiO}_4$ is seen as light regions against the gray background of the main CaMgSiO_4 phase); (c) MFA (inclusions of secondary phases are seen as dark regions; one can also see numerous cavities); (d) A (forsterite inclusions are seen as dark spots against the background of the main akermanite phase).

these impurities are caught by the crystal from melts; however, it seems that this mechanism is hardly probable, which is confirmed by the following. First, the MgO phase precipitates together with $\text{Ca}_{1.33}\text{Mg}_{0.67}\text{SiO}_4$ (Fig. 4b), whereas in melts, these phases are revealed separately. Second, in some melts (FRC 6 and 10), MgO inclusions are observed in melts, whereas the crystals have no MP zones containing these inclusions.

The MFA (monticellite + forsterite + akermanite) zone is formed either inside the M zone (from the center to the periphery as in FRC 3, 4, 7, and 10) or immediately follows it (in all the other cases). Like in two above-described zones, the main phase in this zone is monticellite. The MPA zone is nontransparent due to the presence of inclusions of secondary phases and the cracks caused by their presence (see Fig. 4c).

Considering the compositions of inclusions in the MFA zone, we can divide all the crystals into two groups. The first group consists of crystals grown from

FRC 5, 12, and 13 with MFA containing only small (up to 10 μm) forsterite inclusions. The second group includes all the remaining crystals with the MFA zone containing not only forsterite, but also inclusions of secondary phases and, first of all, akermanite.

The A zone (akermanite) is formed at the final stage of crystal growth with lowering of heating temperature, the corresponding decrease of the melt thickness, and the drastic increase of the actual velocity of the crystallization surface. This zone is often formed as a transparent single-crystalline region consisting of akermanite as the main phase and some inclusions at low concentrations (Fig. 4d). In some other cases, the crystal tip consists of polycrystalline substance containing several phases. We observed no obvious and reproducible correlation between FRC and the crystal tendency to form the transparent single-crystalline A zone (Fig. 2b, table), although SiO_2 -enriched FRC show certain tendency to form this zone.

To understand the reasons and the mechanisms of zone formation in crystals depending on FRC, we constructed a mathematical model the melt-composition variations during crystallization and compared the results for two characteristic FRC (5 and 16) obtained on the basis of this model with the melt compositions determined by X-ray microprobe analysis upon the completion of crystal growth.

MODEL OF CHANGES IN THE MELT COMPOSITION DURING CRYSTALLIZATION

As the first approximation, consider the cylindrical molten zone and assume that its length and diameter, the melt density, and the composition and diameter of a growing crystal remain constant throughout the growth process. Actually, the growth cones in the samples was feebly marked, and, as was mentioned above, the composition of the main crystal phase varied in an irregular manner within a very narrow range (Fig. 2a). Precipitation of secondary phases can be ignored. Then, dividing the growth process into small equal periods $\Delta\tau$, we can write the mass balance in the melt at each moment (the n th iteration) of the stationary growth mode in the form

$$\begin{aligned} m_n &= m_{n-1} + \Delta m_m - \Delta m_c \\ &= m_0 + n(\Delta m_m - \Delta m_c) \approx \text{const}, \end{aligned} \quad (1)$$

where m_0 is the initial weight of the melt; Δm_m is the weight of the portion of the feed rod melted for a period $\Delta\tau$ and Δm_c is the weight of the melt crystallized during the same period of time.

Apparently, $\Delta m_m = \Delta m_c$. Each of the above weights can be represented as follows:

$$\Delta m_m = \frac{\pi D_{fr}^2}{4} \Delta x_{fr} \rho_{fr}, \quad (2)$$

$$\Delta m_c = \frac{\pi D_c^2}{4} \Delta x_c \rho_c, \quad (3)$$

where D_{fr} and D_c are the diameters of the feed rod and the growing crystal, respectively, ρ_{fr} and ρ_c are the densities of the feed rod (with due regard for porosity) and the growing crystal, respectively, Δx_{fr} is the thickness of the feed-rod layer melted during time $\Delta\tau$, and Δx_c is the thickness of the layer crystallized during time $\Delta\tau$.

Since the upper and lower rods were shifted synchronously at all the stages of crystal growth except for the final stage, we can write the iteration step as $\Delta x_{fr} = \Delta x_c = \Delta x$.

Taking into account this fact, we obtain from Eqs. (2) and (3):

$$\frac{\pi D_{fr}^2}{4} \rho_{fr} = \frac{\pi D_c^2}{4} \rho_c = K, \quad (4)$$

where K is the constant introduced to simplify the further consideration.

The molar balance of the i th component of the melt (i is CaO, MgO, or SiO₂) at any moment in time can be written as follows:

$$\begin{aligned} v_n^i &= v_0^i + n(\Delta v_m^i - \Delta v_c^i) \\ &= \frac{m_0}{M_{fr}} c_{fr}^i + n \left(\frac{\Delta m_m}{M_{fr}} c_{fr}^i - \frac{\Delta m_c}{M_c} c_c^i \right), \end{aligned} \quad (5)$$

where v_n^i and v_0^i are the amounts of the i th component in the melt at the n th iteration step and in the initial melt, respectively, Δv_m^i and Δv_c^i are the molar "addition" of the i th component and its consumption, respectively, during the period $\Delta\tau$. The molar weights of the feed rod and the growing crystal, M_{fr} and M_c , respectively, should be distinguished because for monticellite, the charge composition differs from the composition of the growing crystal, although, as will be shown below, these weights are actually very close. Finally, c_{fr}^i and c_c^i are the mole fractions of the i th component in the feed rod and the growing crystal, respectively.

With due regard for Eqs. (2), (3), and (4), equation (5) can be rewritten in the simple linear form:

$$v_n^i = \frac{KL}{M_{fr}} c_{fr}^i + nK\Delta x \left(\frac{c_{fr}^i}{M_{fr}} - \frac{c_c^i}{M_c} \right) = K(A^i + B^i n), \quad (6)$$

where L is the length of the molten zone, and the expressions $(c_{fr}^i L / M_{fr})$ and $\Delta x (c_{fr}^i / M_{fr} - c_c^i / M_c)$ are denoted as A^i and B^i , respectively.

Then, the melt compositions during growth can approximately be evaluated as follows:

$$\begin{aligned} c_n^i &= \frac{v_n^i}{\sum_i v_n^i} = \frac{K(A^i + B^i n)}{K \left(\sum_i A^i + n \sum_i B^i \right)} \\ &= \frac{A^i + B^i n}{\frac{L}{M_{fr}} + n\Delta x \left(\frac{1}{M_{fr}} - \frac{1}{M_c} \right)}. \end{aligned} \quad (7)$$

In our case, the difference between M_{fr} and M_c is very small (for example, these values for FRC 9 are 157.4 and 155.7 g/mol, respectively). Consequently, the second term in the denominator of Eq. (7) is also very small in comparison with the first term and, thus, can be ignored. For the same reason, the term B^i in the numerator of this equation can be transformed by changing M_{fr} and M_c for the average value M_{av} without

an essential loss in the calculation accuracy. Then

$$c_n^i \equiv \frac{M_{fr}}{L} \left(\frac{Lc_{fr}^i}{M_{fr}} + \frac{n\Delta x}{M_{av}} (c_{fr}^i - c_c^i) \right) \quad (8)$$

$$\equiv c_{fr}^i + \frac{n\Delta x}{L} (c_{fr}^i - c_c^i).$$

Equation (8) demonstrates that the rate of the changes in the melt composition is inversely proportional to the molten-zone length. This conclusion seems to be promising for growth of single crystals of monticellite by the Czochralski method, in which the length of the molten zone can formally be considered as tending to infinity.

In the first approximation (without considering the influence of the precipitation of secondary phases), the melt composition changes linearly during growth under stationary conditions, i.e., the direction and rate of composition variation remain constant. The rate of the variation of the melt composition is proportional to the difference between the compositions of the feed rod and the growing crystal.

Figure 2a presents the results of the calculations for two characteristic compositions (FRC 5 and 16) with the use of Eq. (8) and the actual compositions of the melts quenched after the growth process.

In the case of FRC 5, the calculated and measured SiO₂ contents in the melt after growth completion are very close, and the substantial differences are observed only on the calcium–magnesium line. This difference between the measured and the calculated melt compositions is readily explained on the assumption that only forsterite precipitates in the growing crystal, which is confirmed by the microprobe analysis data for the MFA zone of this crystal.

The situation is quite different for FRC 16, where the actual concentrations of all three cations in the melt after growth completion considerably differ from the calculated values. These differences cannot be explained by forsterite-inclusion precipitation. At the same time, we also observed inclusions of akermanite in the MFA zones of these crystals (see above). Precipitation of these inclusions should lead to a lower rate of melt-composition variations in the direction toward the stoichiometric point of akermanite.

As can be seen from Fig. 2a, the step between the iteration points (indicated by empty circles) is substantially larger for FRC 16 than for FRC 5, although the same Δx (0.5 mm) was used in both cases. Equation (8) demonstrates that this is explained by different distances from FRC to the average composition of the main phase of the growing crystal.

Thus, a relatively low rate of the melt-composition variations for FRC 5, 12, and 13, there is not enough time for the composition to approach the crystallization field of akermanite. Apparently, this fact explains the

absence of akermanite inclusions in the corresponding samples.

According to Eq. (8), the compositions of the melts used for growth of crystals with the well-developed MP zone (FRC 2, 3, and 8) should approach rather rapidly the field of primary crystallization of merwinite. However, MgO and Ca_{1.33}Mg_{0.67}SiO₄ precipitates hinder this displacement and prevent the melt composition from “propagating” outside the field of primary crystallization of monticellite for quite a long period of time.

Thus, we have investigated crystallization of monticellite from melts of different non-stoichiometry, constructed the model to describe the change of the melt composition during crystallization, and found the optimum compositions for the initial charge.

ACKNOWLEDGMENTS

This study was supported by the Russian Foundation for Basic Research, project nos. 98-02-17340 and 99-02-18456.

REFERENCES

1. E. V. Zharikov and V. A. Smirnov, in *Wide-Gap Luminescent Materials: Theory and Applications* (Kluwer, Nowell, 1997), p. 13.
2. V. Petricevic, A. Seas, and R. R. Alfano, in *Technical Digest of Meeting “Advanced Solid State Lasers”* (Optical Society of America, New Orleans, 1993).
3. C. R. Pollock, D. B. Barber, J. L. Mass, and S. Markgraf, *IEEE J. Sel. Top. Quantum Electron.* **1** (1), 62 (1995).
4. S. Kück, K. Petermann, U. Pohlmann, *et al.*, *Phys. Rev. B* **51** (24), 17323 (1995).
5. R. W. Ricker and E. F. Osborn, *J. Am. Ceram. Soc.* **37** (3), 133 (1954).
6. K. A. Subbotin, S. V. Lavrishchev, V. A. Smirnov, and E. V. Zharikov, in *Proceedings of the II All-Russia Symposium “Processes of Heat and Mass Transfer, Growth of Crystals and Thin Films,” Obninsk, 1997*, p. 155.
7. K. A. Subbotin, E. V. Zharikov, V. A. Smirnov, and I. A. Shcherbakov, *Kratk. Soobshch. Fiz.*, Nos. 11–12, 16 (1997).
8. G. N. Rezen'kova, N. A. Sirazhiddinov, and N. Rakhmanbekov, *Izv. Akad. Nauk SSSR, Neorg. Mater.* **23** (4), 642 (1985).
9. K. A. Subbotin, E. V. Zharikov, V. A. Smirnov, and G. M. Kuz'micheva, in *Proceedings of the III International Conference “Crystals: Growth, Properties, Real Structure, Application,” Aleksandrov, 1997*, Vol. 1, p. 116.
10. H. Onken, *Tschemm's Mineral. Petrogr. Mitt.* **10**, 34 (1965).
11. G. M. Biggar and M. J. O'Hara, *J. Am. Ceram. Soc.* **52** (5), 249 (1969).
12. D. M. Roy, *Miner. Mag.* **31** (233), 187 (1956).

Translated by T. Safonova

CRYSTAL GROWTH

The Precrystallization State of Aqueous Salt Solutions

E. B. Treivus

*Institute of the Earth's Crust, St. Petersburg State University,
Universitetskaya nab. 7/9, St. Petersburg, 199164 Russia*

e-mail: treivus@cryst.geol.pu.ru

Received October 31, 2000; in final form, February 27, 2001

Abstract—The parameters characterizing the fluctuations in the concentration have been calculated for a great number of aqueous solutions of various salts both in the range of the cluster formation and in the critical range. The existence of an inflection point on the isotherms of concentration susceptibility preceding the transition of the solution to the supersaturated state has been established. It is found that (1) the inflection point indicates the complete hydration of the solution and the beginning of the active cluster formation in solution and (2) that, in fact, the cluster formation in the solution is a diffuse second-order phase transition. It is concluded that the clusters have the liquid-like structure and the diffuse boundaries. At a deviation of the solution concentration from its critical value, the critical index equals unity, in full accordance with the Landau theory of the mean field. © 2001 MAIK “Nauka/Interperiodica”.

INTRODUCTION

As far as we know, the concentration fluctuations in electrolytes in the range of their high concentrations in aqueous solutions have not been analyzed as yet. Below, we make an attempt to realize what this analysis can give for understanding the processes occurring in proximity to an equilibrium concentration in a solution at equilibrium and in the supersaturated state. These problems constantly attract the attention of all those engaged in crystal formation [1–3].

THEORETICAL EQUATIONS

According to [4], the averaged squared fluctuation in the concentration of a binary solution is described by equation:

$$\overline{\Delta c^2} = \frac{k_B T}{N \mu'_c}, \quad (1)$$

where k_B is the Boltzmann constant, T is the absolute temperature, N is the number of solvent molecules in that part of the solution volume for which this fluctuation is calculated (a closed system), μ'_c is the derivative of the chemical potential of the dissolved substance with respect to its concentration c under given pressure p and temperature T . The concentration c is written as the number n of particles of the dissolved substance per N molecules of the solvent [4]. In other words, this concentration is the ratio of the number of moles of the dissolved substance per mole of the solvent.

However, the above definition of the solution concentration is not used in practice, but one can readily pass to the equations alternative with respect to Eq. (1), in which the concentration is expressed either in molar

fractions x or in molality units m (the number of moles of the solute per kilogram of the solvent),

$$\overline{\Delta x^2} = \frac{k_B T x_w^2}{N \mu'_x}, \quad (2)$$

$$\overline{\Delta m^2} = \frac{k_B T}{\left(\frac{N}{55.1}\right) \mu'_m}. \quad (3)$$

Here, μ'_x is the derivative of the chemical potential of the dissolved substance with respect to x where x_w is the molar fraction of the solvent and μ'_m is the derivative of μ with respect to m .

Equations (1) and, hence, also equations (2) and (3) are valid for small fluctuations and the Gaussian law of their distribution [4]. It is expected that these conditions would be fulfilled in the range of diluted solutions. However, it is difficult to predict the limits of the concentrations for which these equations would yield the correct results. In the range of supersaturated solutions, and especially at concentrations close to critical, the equations yield, undoubtedly, wrong results. At high solution concentrations, one can consider the concentration susceptibility of the solution as a parameter that characterizes the fluctuation level in these media [5]. The relative concentration susceptibility is defined by any of the following two equations:

$$Y_x = \frac{k_B T}{\mu'_x}, \quad (4a)$$

$$Y_m = \frac{k_B T}{\mu'_m}. \quad (4b)$$

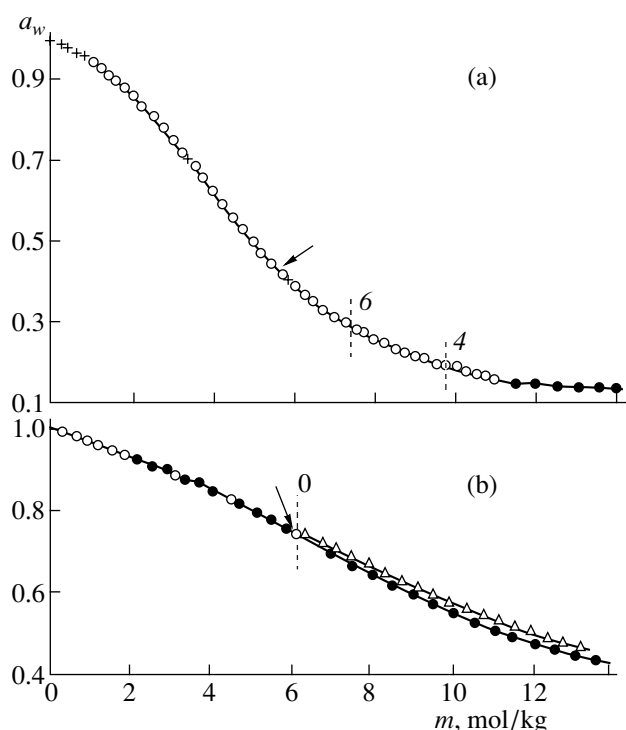


Fig. 1. Water activity for (a) CaCl_2 solutions according to data [6] (open circles), [7] (crosses), and [8] (filled circles) and (b) NaCl solutions according to data [7] (open circles), [8] (filled circles), and [9] (triangles) as a function of the solution content at 25°C . Vertical dashed segments denote either the boundary of under- or supersaturated media or a boundary between the regions of formation of crystal hydrates with different water concentration. Numbers at these segments indicate the number of water molecules in crystals. Arrows indicate the inflection points.

EXPERIMENTAL DATA AND THEIR PROCESSING

The Y and $\mu'/k_B T$ values were calculated from the data on water activity a_w in solutions. At present, the number of supersaturated aqueous solutions of the salts with the known a_w values amounts to 30 (practically, all the data obtained at 25°C). For many substances, the data were obtained up to extremely high supersaturations up to vitrification points. Thus, it is possible to reconstruct the general picture of the development of concentration fluctuations in aqueous solutions in the whole range of possible compositions.

The $\mu'_m/k_B T$ value is roughly calculated on the basis of the Gibbs–Duhem equation at constant p and T at the concentration expressed in the molality units as

$$\frac{\mu'_m}{k_B T} \cong -\frac{55.51 \Delta \mu_m}{k_B T \Delta m_1 m} = -\frac{55.51 \ln(a_{2w}/a_{1w})}{\Delta m_1 m}. \quad (5)$$

Here, a_{2w} and a_{1w} are water activities at the limits of the concentration interval $\Delta m = m_2 - m_1$. This interval was chosen in such a way that the variation in a_w within this

interval would not exceed 0.01 or 0.02. The calculated $\mu'_m/k_B T$ values should lie at the middle of the corresponding Δm interval. For the concentration expressed in molar fractions, we obtain

$$\frac{\mu'_x}{k_B T} \cong -\frac{x_w \ln(a_{2w}/a_{1w})}{x_1 \Delta x}. \quad (6)$$

The Y and $\mu'/k_B T$ curves for the solutions of all thirty substances studied have some common features. We discuss these characteristics for two salts.

CONCENTRATION SUSCEPTIBILITY OF SOLUTIONS

Consider aqueous solutions of CaCl_2 and NaCl . Their a_w values are given in Fig. 1. Note that the a_w data in [6, 7] were obtained by the isopiestic method and were, in fact, thoroughly smoothed results obtained in previous studies (the a_w value indicated in [6] was smoothed with due regard of the values determined in [6]). The a_w values in [8, 9] were determined by the method of levitated droplet, but the first method is more precise. The numerical a_w values are given in [6, 7], the coefficients of the sixth-order empirical polynomial with respect to m are indicated in [8]. A plot of the a_w values for the NaCl solutions is given in [9]. The computer processing of the latter yielded the equation

$$a_w = 0.957 + 0.00415m - 0.0105m^2 + 0.000855m^3 - 0.0000225m^4.$$

The range of the a_w values measured in CaCl_2 solutions in [7] was almost the same as in [6]. The a_w data for NaCl [7] range within the concentration of solution saturation. To simplify the consideration, these data are shown only partly in Fig. 1. At the same time, these data practically coincide with the data for CaCl_2 [6] and NaCl [8].

We should like to draw attention to the fact that both curves in Fig. 1 show inflection points (indicated by arrows).

The Y_m values calculated for the CaCl_2 solutions from data [7] (Fig. 2a) almost coincide with the analogous values calculated by data [6]. Therefore, Y_m determined from the a_w values [7] are shown only partly in Fig. 2a. The curve constructed by data [8] is less authentic in the given range of m values since it is constructed with the use of the a_w values measured by the less precise method. At the same time, it follows from Fig. 2a, the positions of both curves differ insignificantly. Large Y_m values for the CaCl_2 solutions calculated by the data from [8] are shown on the right side of Fig. 2a only partly. These values tend to infinity at finite m values in accordance with the concept of the susceptibility behavior in the critical region.

As is seen from Fig. 2b, the Y_m values calculated for the NaCl solutions [7, 8] are in a good agreement with each other. The Y_m curve constructed by data [9] is less reliable.

One can readily realize that if the solution concentration tends to zero, the variable Y should also tend to zero.

The Y_m curve has an inflection point above which the level of concentration fluctuations increases more rapidly (Fig. 2). As has already been mentioned, the inflection points on more reliable curves (see above) are indicated by arrows.

The inflection point is located in the range of undersaturated media, although for NaCl solutions, it corresponds to composition close to equilibrium. However, different values at the equilibrium solution concentration and at the solution concentration at the inflection point for all the substances whose Y_m curves are established rather reliably, (i.e., for most of the 30 systems considered) allows one to assume that for the NaCl solution these compositions are not identical. Some authors thoroughly studied the temperature dependences of some physical properties of aqueous solutions of salts such as viscosity, specific heat, electrical conductivity in the vicinity of the saturation state of these media. They pointed out that although the inflection points on these curves were close to the temperature point of the solution transition to the supersaturated state, nevertheless, these points never coincided.

The Y_x curves also had inflection points similar to those observed on the Y_m curves.

Now, consider the errors in the calculated Y_m parameter. First, consider as an example the most precise data. In [7], the values of water activity were tabulated at fixed intervals of water activity (0.01 or 0.02). As is well known, the water activity in salt solutions is determined by measuring the pressure of water steam above the solutions. This pressure is measured with an accuracy not less than 0.01 mm Hg. Since the pressure of pure water vapor at 25°C ranges within 23.75–23.76 mm Hg, the a_w value is precisely determined within four digits at $a_w > 0.42$ (i.e., unless the water vapor pressure would exceed 10 mm Hg) and within three digits in the range $0.42 > a_w > 0.042$, etc. The maximum experimental error should be equal to a half-unity of the latter significant digit of the a_w value. For example, for salts, this error is equal to 0.00005 in the vicinity of inflection points on the Y_m curves. It should be emphasized that this error is an error of individual a_w measurements. The error for smoothed a_w values [7] should be, at least, two times lower.

The concentrations values corresponding to the a_w values are indicated within an accuracy of ± 0.001 of the numerical value of m in [7]. Thus, the error in the determination of concentration can be taken to be equal to 0.0005 mol/kg of H₂O, whereas the m value in the region of the inflection range of the curves was about

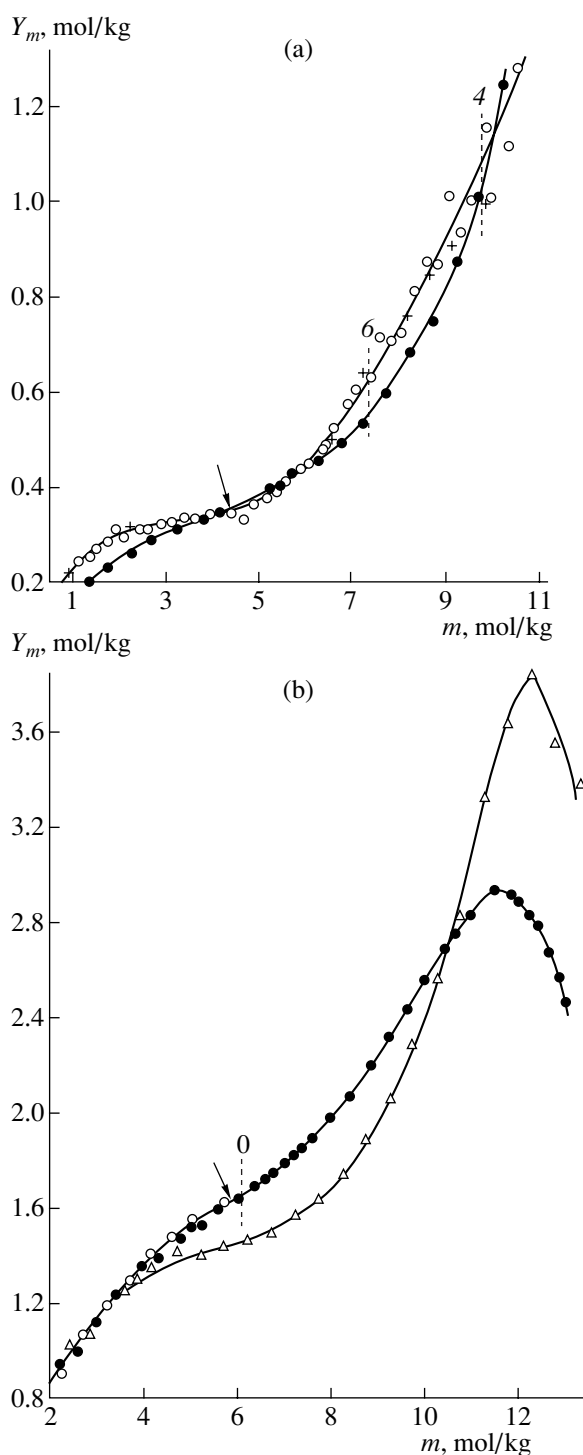


Fig. 2. Concentration susceptibility of aqueous solutions of (a) CaCl₂ according to data [6] (open circles), [7] (crosses), and [8] (filled circles) and (b) NaCl according to data [7] (open circles), [8] (filled circles), and [9] (triangles) as a function of salt concentration in the solution under atmospheric pressure at 25°C. For other notation see Fig. 1.

4.5 m for CaCl₂ solutions and about 6.0 m for NaCl solutions.

The theory of errors allows one to use the above errors in a_w and m variables to find only the maximum

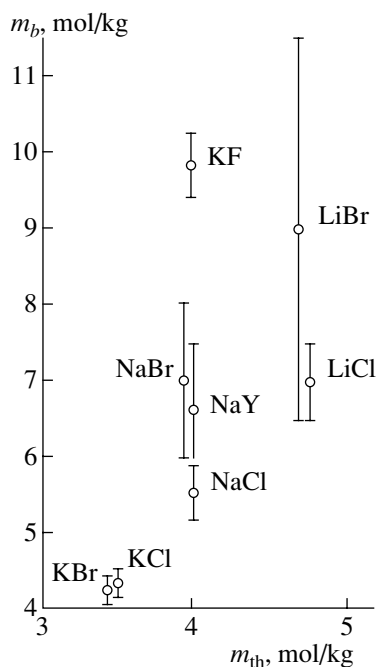


Fig. 3. Correlation between the solution concentration at the inflection point of the Y_m curve and the concentration at the threshold of complete hydration for aqueous solutions of a number of alkali metal halides [10].

possible error in the calculation of Y values. Our estimation shows for the solutions considered here that this error is about 30% of the Y_m value in the vicinity of the inflection point. This error relates to the ends of the error-distribution curve and, thus, is practically impossible and much greater than the root mean square error for Y , i.e., the error we are interested in and cannot estimate. However, each Y_m curve in Fig. 2 is characterized by a high point density and almost zero dispersion about these curves, at least, in the range of the inflection points. This fact allows one to state that the error corridor for the curves considered should be insignificant in this range. Note that it is this inflection point that we are interested in while considering the Y_m parameter.

We draw attention to a decrease of the fluctuation level in the range of the maximum supersaturations in the NaCl solutions (Fig. 2b). This phenomenon seems to be associated with a significant reduction in the particle mobility in solution (i.e., the trend to its “freezing”) at high supersaturations. Such features in the behavior of the Y parameter at high concentrations of supersaturated aqueous solutions are rather typical.

Now, we introduce a notion of the complete hydration threshold (th). This is such a solution concentration, m_{th} , at which all the water molecules are involved into the first hydration sphere of the ions of the dissolved substance [10]. It is clear that upon the transition through this threshold the level of concentration fluctuations should drastically increase, because of the lack of water molecules for hydration of electrolyte ions

outside this range. The stability of the solution to such fluctuations should essentially decrease. Thus, it is logical to consider the above inflection point on the susceptibility curve as a result of the complete salt hydration.

We determined solution concentrations m_b at the inflection points on the Y_m curves for the alkali metal halides with the known m_{th} values [10]. The m_b were calculated with due regard for tabulated a_w values [7]. The assumption that the m_b and m_{th} are parallel was confirmed (Fig. 3). The vertical bars at the points in Fig. 3 are the “ambiguity ranges” in the determination of m_b . At the left boundary of this interval (on the left of the m_b value), the Y_m curve should straighten, whereas on the right boundary, the Y_m parameter increases nonlinearly. The m_b value is defined as the m value in the middle of the ambiguity range. A considerable width of this interval for the LiBr solutions is explained by the fact that the Y_m curve within this interval is practically horizontal (the accuracy of the data does not allow one to determine the slope of the Y_m curve within this interval reliably).

At the same time, it is seen from Fig. 3 that the m_b values are always higher than the m_{th} values and that they differ by a factor of two for the substances with the maximum m_{th} values. The higher values of the former quantities can be explained by a number of reasons.

The solution composition at the complete hydration threshold was calculated in [10] under the condition that this threshold corresponds to the solution concentration at which each water molecule is located within the first hydration sphere either of a cation or of an anion. However, it should be taken into account that during further increase of the salt concentration in the solution, the solution concentration is changed in such a way that each water molecule is shared by the first hydration spheres of both ions. Possibly, this concentration (and not m_{th}) is responsible for dramatic increase of the solution concentration. Moreover, the calculations in [10] were performed under the assumption that the salts in solutions are completely dissociated. At the same time, it is well known, that even strong electrolytes do not dissociate completely. Therefore, the complete hydration should occur at higher solution concentration in comparison with the concentration indicated in [10]. Thus, the m_b concentration at the inflection point on the susceptibility curve, which indicates the beginning of an increase in solution unstability should always be higher than the m_{th} concentration according to [10]. Apparently, some other factors promote the difference between these values. Thus, the m_{th} values given in [10] should be considered only as approximate ones. It is clear why m_b has higher values for substances forming crystal hydrates (compare the positions of the points for KF and NaBr with the positions of the points for NaY and NaCl in Fig. 3), but it is unclear why the difference between m_b and m_{th} increases with an increase in m_{th} .

At present, the concepts of the cluster structure of highly concentrated solutions give rise to no doubt [1–3]. However, it remains unclear what concentrations provide the start of cluster formation in these solutions. It seems that the existence of the inflection point on the Y_m curves clarifies the situation. For example, the comparative study of the structure of the NiCl_2 aqueous solution [11] and some of its physical properties [12] led to the conclusion [12] that at the concentration of ~ 1.3 mol/kg of H_2O and at the temperature of 20°C , the structure of this solution is transformed into a cluster structure. The Y_m values for these solutions calculated on the basis of data [7] yield $m_b = 1.8$ mol/kg of H_2O (at 25°C). The difference between these two values can be attributed to the error in their determination. Note also that these numbers are not related to the NiCl_2 solubility (5.06 mol/kg H_2O at 25°C).

CONCENTRATION DERIVATIVE OF THE CHEMICAL POTENTIAL FOR THE DISSOLVED SUBSTANCE

The formation of the cluster structure in the solution was interpreted as a second-order phase transition [13]. Since the cluster rearrangement takes place within a certain concentration interval, it should be classified as a diffuse second-order phase transition [14]. The curves in Fig. 4 are typical of these transitions (see the inset in Fig. 4a). Note also that the curves in [14] were considered in application to the situation where the temperature was an argument. In our case, the argument is the solution concentration.

We should like to make some remarks about the reliability of the establishment of the $\mu'_m/k_B T$ lines. The most reliable curves are indicated by arrows (Fig. 4) and are characterized either by a small (as in the case of the Y_m parameter) or almost the zero scatter of the points. The different data also agree quite well. Thus, the error corridor for the curves considered on the scale of these plots should be insignificant. The zero error for two other curves is only an illusion caused by the fact that these curves were constructed with the use of the a_w polynomials. All the μ'_m/k_B lines are wavy, which is of interest for us.

The curve in Fig. 4a constructed by data [8] (filled circles) seems to be reliable at the right wing since it is consistent with the behavior of the chemical potential in the critical range of the solution.

The points corresponding to the inflection points of the Y_m in Fig. 2 constructed with the use of the a_w data are indicated by arrow 1 in Fig. 4. The points on the lines in Fig. 4 indicated by arrow 2 are the points where the tangents to these lines are parallel to the left-side tangents. The gap between the points indicated by arrows 1 and 2 is considered as a range where a diffuse second-order phase transition takes place. At the solution concentrations to the right of point 2, almost the

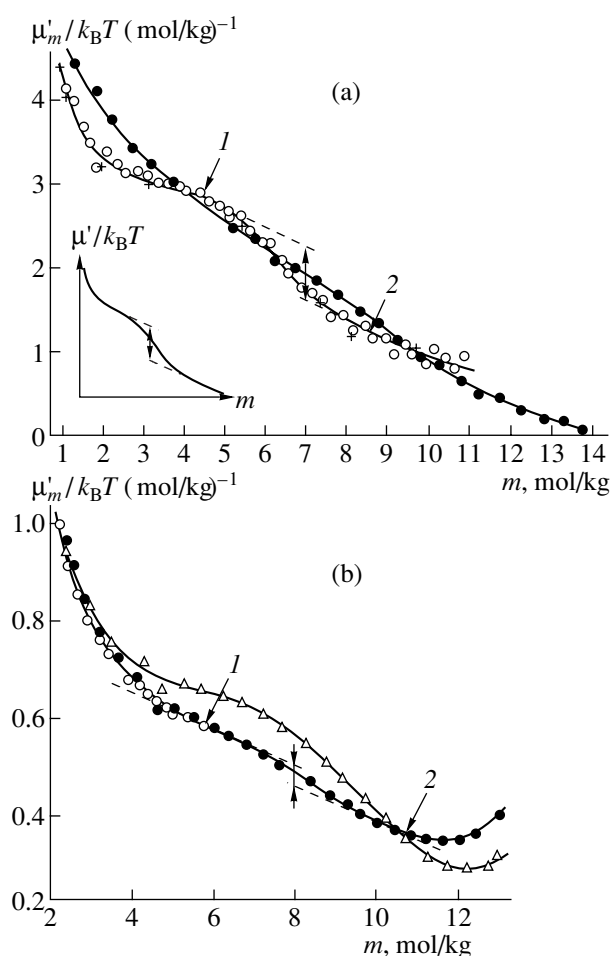


Fig. 4. Relative derivative of the chemical potential for (a) CaCl_2 according to data [6] (open circles), [7] (crosses), and [8] (filled circles) and for (b) NaCl according to data [7] (open circles), [8] (filled circles), and [9] (triangles) as a function of salt concentration in the solution. The inset in Fig. 4a shows schematically a diffuse second-order phase transition.

whole dissolved substance should be involved into cluster formation.

The points of both Y and the $\mu'_m/k_B T$ curves which correspond to equilibrium solution concentration show no anomalies or characteristic properties.

The length of the vertical segment between the tangents in Fig. 4 corresponds to a relative value of the phase effect, $\Delta(\mu'_m/k_B T)$, in the second-order phase transition.

There is no unique opinion about the cluster structure—it is still unknown whether the clusters have crystal structure or not. The low $\Delta(\mu'_m/k_B T)$ values (tenths and even hundredths of the energy of thermal motion of molecules (see table)) indicate their “liquidlike” character [13] and diffuse boundaries. A negative sign of this phase effect was predicted in [13].

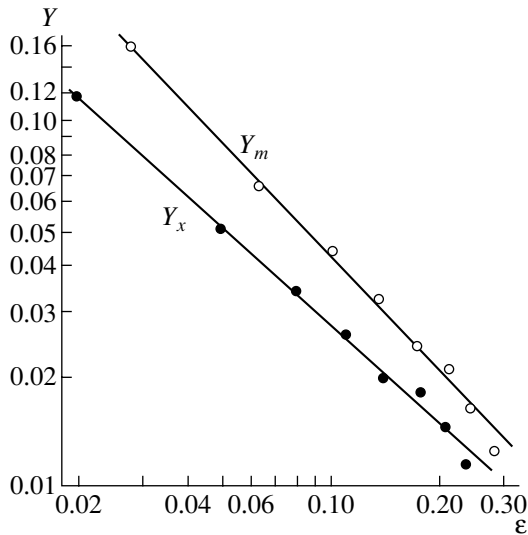


Fig. 5. Concentration susceptibility of CaCl_2 aqueous solutions as a function of the relative deviation of the solution concentration from its critical value at 25°C .

The equation which describes the temperature dependence of the thermodynamic potential in the range of the diffuse second-order phase transition is known [14]. By analogy, we can write this equation, we write

$$\mu'_m/k_B T = \mu'_b/k_B T + (L/k_B T)(m - m_b). \quad (7)$$

Here, $\mu'_b/k_B T$ is this function at $m = m_b$, i.e., at the initial point of the diffuse second-order phase transition (point *I* in Fig. 4), L is the inclusion function, whose approximate form can be written as [14]

$$\frac{L}{k_B T} = -\frac{1}{1 + \exp[\alpha/(m - m_b)]^\beta}, \quad (8)$$

where α and β are certain constants. Substituting Eq. (8) into Eq. (7) and performing necessary transformations, we obtain Eq. (7) in the form of a power function

$$y = \alpha z^\beta, \quad (9)$$

where

$$y = \ln \left[\frac{k_B T(m - m_b)}{\mu'_b - \mu'_m} - 1 \right], \quad z = m - m_b. \quad (10)$$

Parameters characterizing diffuse second-order phase transitions (cluster formation) in two aqueous solutions of salts

Substance	m_b^*	$\Delta(\mu'_m/k_B T)$	α	β
CaCl_2	4.3	-0.6	0.37	0.018
NaCl	5.9	-0.04	2.8	0

* Concentration m , mol/kg of H_2O .

Here, μ'_m is this variable at the solution concentration m .

Linearization of the dependence of y on z in double logarithmic coordinates allows the verification of Eq. (7) and determination of the α and β parameters. The curves between the arrows in Fig. 4 are constructed by Eqs. (7) and (8) with the use of the tabulated α and β values.

The curve $\mu'_m/k_B T$ for CaCl_2 solutions constructed by the data from [8] at the concentration approximately equal to 14 mol/kg of H_2O tends to zero (Fig. 4a). The solution whose composition coincides with the composition of CaCl_2 tetrahydrate has the concentration 13.88 mol/kg of H_2O . Thus, the critical concentration of the solution of a substance cannot exceed this value. The close values allow one to assume that, at least, in right-hand part of the plot, the results obtained in [8] are reliable and that the concentration equal to 13.9 mol/kg of H_2O should be considered as the critical concentration for the CaCl_2 solutions.

The experimental data obtained in the study of the critical phenomena are represented as the concentration susceptibility Y as a function of the relative temperature deviation from its critical value [5]. By analogy, we can write:

$$Y = k\varepsilon^\gamma, \quad (11)$$

where

$$\varepsilon = \frac{m_{\text{cr}} - m}{m_{\text{cr}}}$$

or

$$\varepsilon = \frac{x_{\text{cr}} - x}{x_{\text{cr}}},$$

where m_{cr} or x_{cr} is the critical concentration of the solution, γ is the critical index, and k is a constant.

The results shown in Fig. 2a are readily straightened in the coordinates of Eq. (11) on the double logarithmic scale (Fig. 5). In this case the index $\gamma = 1$. It is remarkable that this γ value is substantiated in the classical theory of critical phenomena for susceptibilities of different natures (magnetic susceptibility, isothermal compressibility) dependent on relative deviation of the temperature from its critical value [5, 15, 16]. Unfortunately, it is still unclear whether this γ value would be the same for other substances, since up to now the CaCl_2 solution is the only solution with the known critical concentration.

The formation of amorphized clusters preceding crystal nucleation in the solution indicates that nucleation is, at least, a two-barrier process in terms of the thermodynamic potential. The first barrier is relatively low, its overcoming is necessary for cluster formation; the second or the main barrier is relatively high and its

overcoming is necessary for transformation of the already formed cluster into a stable crystalline nucleus.

Thus, the data on the concentration fluctuations clarify the picture of transformations taking place in solutions with an increase of the concentration of the dissolved substance. These data also provide better understanding of the concepts of the complete hydration threshold, the process of cluster formation, phase transitions in solutions, etc.

ACKNOWLEDGMENTS

The author is grateful to I.A. Kasatkin for his help in computer-data processing. This study is supported by the Russian Foundation for Basic Research, project no. 00-05-65183.

REFERENCES

1. W. Polak and K. Sangwal, *J. Cryst. Growth* **152** (3), 182 (1995).
2. J. Nývlt, *Cryst. Res. Technol.* **31** (1), 1 (1996).
3. M. Bohenek, A. S. Myerson, and W. M. Sun, *J. Cryst. Growth* **179** (1), 213 (1997).
4. L. D. Landau and E. M. Lifshitz, *Course of Theoretical Physics*, Vol. 5: *Statistical Physics* (Nauka, Moscow, 1995; Pergamon, Oxford, 1980), Part 1.
5. M. A. Anisimov, *Critical Phenomena in Liquids and Liquid Crystals* (Nauka, Moscow, 1987).
6. J. A. Rard and S. L. Clegg, *J. Chem. Eng. Data* **42** (5), 819 (1997).
7. I. E. Voznesenskaya and G. I. Mikulin, in *Problems of Physical Chemistry of Electrolytic Solutions*, Ed. by G. I. Mikulin (Khimiya, Leningrad, 1968), p. 172.
8. M. D. Cohen, R. C. Flagan, and J. H. Seinfeld, *J. Phys. Chem.* **91** (17), 4563 (1987).
9. T. N. Tang, H. R. Munkelwitz, and N. Wang, *J. Colloid Interface Sci.* **114** (2), 409 (1986).
10. K. P. Mishchenko and G. M. Poltoratskiĭ, *Thermodynamics and Structure of Aqueous and Nonaqueous Electrolytic Solutions* (Khimiya, Leningrad, 1976).
11. M. P. Fontana, *Solid State Commun.* **18** (6), 765 (1976).
12. G. Maisaro, P. Migliardo, F. Wanderlingh, and M. P. Fontana, *J. Chem. Phys.* **68** (12), 5594 (1978).
13. Yu. O. Punin, in *Crystallography and Crystal Chemistry*, Ed. by V. A. Frank-Kamenetskiĭ (Leningr. Gos. Univ., Leningrad, 1973), Vol. 2, p. 138.
14. B. N. Rolov, *Diffuse Phase Transitions* (Zinatne, Riga, 1972).
15. Ya. O. Shablovskii, *Neorg. Mater.* **35** (3), 374 (1999).
16. I. I. Novikov, *Thermodynamics of Spinodals and Phase Transitions* (Nauka, Moscow, 2000).

Translated by T. Dmitrieva

Nature of Large-Scale Oscillations in Oxygen Concentration along the Growth Axis in Czochralski-Grown Silicon Crystals

V. V. Litvinov, A. N. Petukh, and Yu. M. Pokotilo

Belarussian State University, pr. Skoriny 4, Minsk, 220050 Belarus

e-mail: litvvv@phys.bsu.unibel.by

Received October 5, 1999; in final form, January 31, 2001

Abstract—Oxygen distribution in a Si crystal (100 mm in diameter) has been studied by the absorption method in the range of the absorption band of interstitial oxygen, $\lambda = 5.81 \mu\text{m}$. Large-scale fluctuations ($\sim 1 \text{ cm}$) of the oxygen concentration (N_0) along the growth axis were determined. Depending on the melt height, the regions of the chaotic and quasiperiodic changes were established, as well as the region of the constant N_0 value, and their relation to turbulent, quasiperiodic, and stationary modes of melt convection in crystallization. The values of the critical Rayleigh number for the melt transition from stationary to quasiperiodic (3×10^3) and from quasiperiodic to turbulent (1.7×10^4) convection modes are determined for growth of silicon crystals by the Czochralski method. The dominating modes of N_0 concentration oscillations at two incommensurable frequencies, $f_1 = 1.3 \times 10^{-3}$ and $f_2 = 6 \times 10^{-4}$ Hz, are assumed to be related to the oscillatory transfer of oxygen from the walls of the quartz crucible to the crystallization front and restructurization of the convective flow pattern of the melt in the course of crystal growth. © 2001 MAIK “Nauka/Interperiodica”.

It is well known [1, 2] that the nonstationary gravitational convection in growth of semiconductor single crystals is the main factor in the microinhomogeneous impurity distribution in the ingots grown. The convective heat and mass transfer in melt [3] results in the appearance of nonaxisymmetric thermal field and its perturbations. Therefore, the rotation of the crystal and the crucible in the nonaxisymmetric thermal field and the temperature oscillations at the crystallization front change the microscopic growth rate, and, as a consequence, give rise to fluctuations in the effective distribution coefficient of impurities in a growing crystal [1]. The impurity growth bands (strata) thus formed in the longitudinal and transverse directions of the ingot are characterized by the spatial period of the order of 100–300 μm depending on the growth conditions [4].

Recently, we revealed large-scale ($\sim 1 \text{ cm}$) N_0 oscillations along the growth axis of Czochralski grown Si crystals [5]. The correlation analysis showed that the dynamics of these oscillations in the course of ingot growth is of the determinate nature and cannot be caused by any random external factors [5]. The value of the correlation dimension [5] agree quite well with the analogous values for the turbulent mode of the nonstationary gravitational convection of melts [6].

The present study was aimed at the determination of the nature of large-scale N_0 oscillations along the growth axis of Si-crystals by analyzing the dynamics of Si incorporation into the crystals under the conditions of nonstationary melt convection.

The *p*-type Si crystals (100 mm in diameter) were grown from the charge (18–20 kg) in a crucible 330 mm in diameter in an industrial reactor without crucible rotation. The rotation rate of the ingot was 3–5 rpm; the pulling rate varied within 0.8–1.2 mm/min. The single crystals thus grown had no swirls, their resistivity ranged within 10–12 $\Omega \text{ cm}$, the dislocation density was less than 10 cm^{-2} . Oxygen concentration in Si ingots was determined by measuring the absorption coefficient with the aid of a spectrometer at $\lambda = 5.81 \mu\text{m}$. The method used for studying the longitudinal impurity distribution was considered elsewhere [7, 8]. The spatial resolution of the spectrometer (2–3 mm) was determined by the diameter of the light beam.

The coordinate oxygen profiles along the growth axis of the crystals were transformed into the temporal dependences with due regard for the pulling rate. The correlation analysis of the temporal changes in N_0 was made by the method suggested elsewhere [9] and considered for oxygen dynamics in silicon in [5]. The Fourier analysis of the temporal oscillations of N_0 with due regard for the macroscopic changes was made by the method suggested in [10].

The characteristic changes in N_0 with time for crystal growth and a decrease of the melt level h are shown in Fig. 1. The monotonic decrease of the average value of the oxygen concentration along the ingot (from its initial part to the ingot end) is a well known fact [1] and is explained by melt depletion of oxygen because of a decrease in the area of its contact with the crucible with a decrease in h . Another feature of the dependences

shown in Fig. 1 is the formation of three portions of the temporal oscillations of N_0 which are characterized by qualitatively different behavior with a decrease of the melt level. The random oscillations, $N_0(t)$, in region I become quasiperiodic in region II. Moreover, at low melt levels, N_0 can decrease in a jumpwise manner, and then, with further crystal growth, N_0 remains practically constant (region III).

The correlation analysis of region I yields the correlation dimensions 3.6, which corresponds to a surprising attractor in the phase space and is the mathematical image of the turbulent flow of a liquid [6]. The oscillation dynamics of N_0 in region II is characterized by a simple attractor of dimension 2, which corresponds to the quasiperiodic convection mode. The most pronounced N_0 pulsations in region III are uncorrelated and explained by the noise inherent in the setup used for measurements.

The Fourier-analysis of the $N_0(t)$ dependences in regions I and II are shown in Fig. 2. The frequency spectrum of region I (Fig. 2a) has weak spectral maxima against the background of the noise with broad bands characteristic of the random behavior of the system. The diffuse frequency components in region I are transformed into narrow spectral peaks at the incommensurate frequencies $f_1 = 1.6 \times 10^{-3}$ and $f_2 = 6 \times 10^{-4}$ Hz in region II (Fig. 2b). These modes can be attributed to the rotational strata, because their frequencies are much lower than the rotational frequencies of the ingot (8×10^{-2} Hz).

The analysis of the experimental data obtained shows three modes of gravitational convection of the melt in the process of silicon growth—turbulent in region I, nonstationary quasiperiodic in region II, and stationary in region III. The change in the convection mode occurs upon the attainment of the critical values of the Rayleigh number (Ra) determined by the formula

$$Ra = \frac{\alpha g h^4 \Delta T}{\nu \chi h},$$

where $g = 980 \text{ cm/s}^2$ is the free fall acceleration, $\alpha = 1.43 \times 10^{-4} \text{ K}^{-1}$, $\nu = 3 \times 10^{-3} \text{ cm}^2/\text{s}$, and $\chi = 0.125 \text{ cm}^2/\text{s}$ are the thermal expansion coefficients, kinematical viscosity, and heat conductivity of liquid Si, respectively [1].

The critical Rayleigh numbers (Ra_c) obtained are compared with the data [11–17] (Fig. 3) obtained for the melts of several semiconductors and mercury with due regard for the corresponding aspect ratios $\beta = D/h$, where D is the crucible diameter. All the experimental data are consistent with the data calculated theoretically in [18], where the dramatic increase in Ra at $\beta = (2-4)$ is explained by the effect of the side walls hindering convection.

With due regard for the above facts, one can conclude that the pulsation dynamics of N_0 observed during

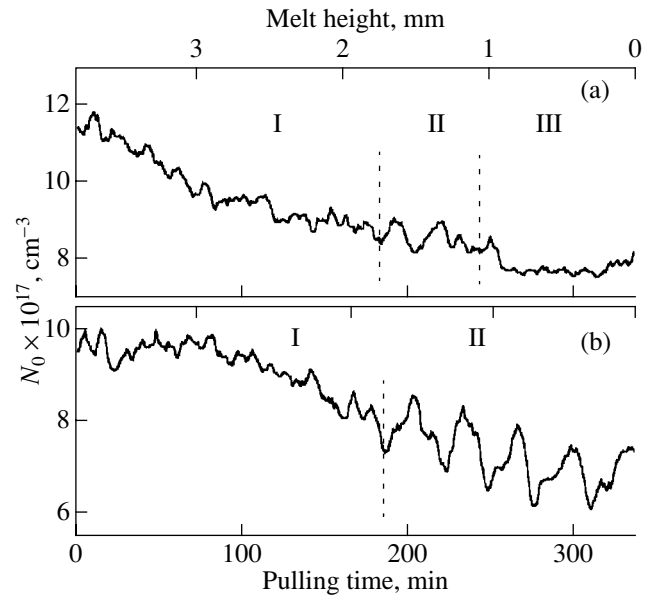


Fig. 1. (a, b) Oxygen concentration N_0 in two crystals as functions of the pulling time and the melt height in the course of crystallization. I, II, and III are the regions of the turbulent, quasiperiodic, and stationary modes of melt convection, respectively.

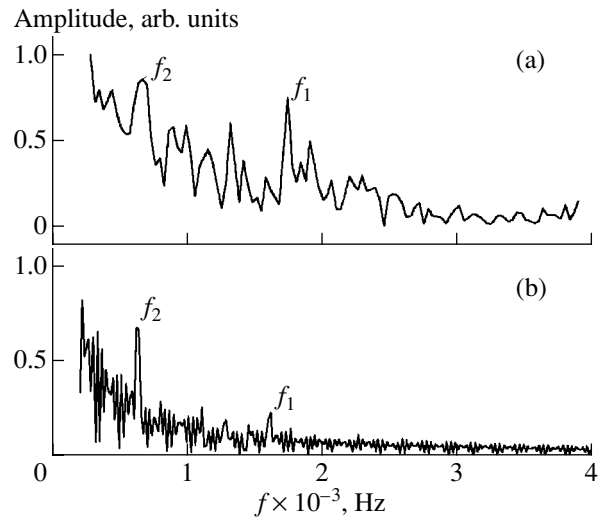


Fig. 2. The amplitude spectra of fast Fourier-transform of the temporal pulsations of oxygen concentration in regions (a) I and (b) II shown in Fig. 1.

growth of silicon single crystals reflects the characteristic behavior of liquids with low Prandtl numbers in the Rayleigh–Benard convection. It is well known [19] that the thermal gravitational convection is characterized by two time scales of the oscillator instability in diffusion of the pulse h^2/χ and the energy h^2/χ . Both scales are well seen in the measurements of temperature oscillations under the conditions of a convective

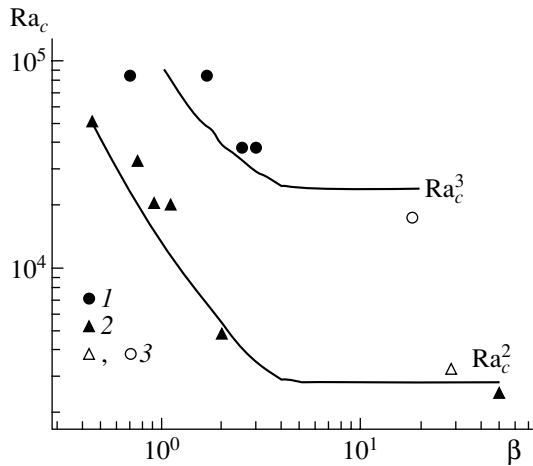


Fig. 3. Critical Rayleigh numbers (Ra_c) in the transition from stationary to quasiperiodic ($Ra_c^{(2)}$) and from quasiperiodic to turbulent ($Ra_c^{(3)}$) convection modes as functions of the aspect ratio $\beta = D/h$ for the melts of some semiconductors and mercury; 1 and 2 indicate the data obtained in [11–17], 3 indicates the data obtained in the present study.

flow of mercury [16, 17]. The frequency of the spatial fluctuations of oxygen in silicon observed earlier ($\sim 10^{-2}$ Hz) [4, 20, 21] also corresponds to the characteristic type of heat transfer, h^2/χ . Under our experimental conditions, the impurity bands on such a scale cannot be distinguished because of the insufficient spatial resolution of the spectrometer used. The frequencies obtained, $f_1 = 1.6 \times 10^{-3}$ and $f_2 = 6 \times 10^{-4}$ Hz, are close, by the order of magnitude, to the reciprocal diffusion time of the pulse $(h^2/\nu)^{-1} = 3 \times 10^{-3}$ Hz at $h = 1$ cm and the frequencies ($\sim 10^{-3}$ Hz) of the fluctuation modulations of the melt temperature under the conditions of nonstationary convection [21, 22]. We believe that the nonlinear convection of the pulse can lead to both oscillatory transfer of oxygen from the walls of the quartz crucible to the crystallization front and the low-frequency temperature oscillations of the melt because of, e.g., the changes in the convective structure of the oscillation pattern. It seems that both these factors determine the nature of the large-scale fluctuations of oxygen along the growth axis of silicon crystals.

REFERENCES

1. G. Müller, *Crystal Growth from the Melt* (Springer-Verlag, Berlin, 1988; Mir, Moscow, 1991).
2. M. G. Mil'vidskii, N. A. Verezub, A. V. Kartavykh, *et al.*, *Kristallografiya* **42** (5), 913 (1997) [*Crystallogr. Rep.* **42**, 843 (1997)].
3. N. V. Kurganetskiĭ, *Neorg. Mater.* **32** (3), 317 (1996).
4. A. M. Ėĭdenzon, N. I. Puzanov, and S. I. Kalyuzhnaya, *Kristallografiya* **35** (2), 433 (1990) [*Sov. Phys. Crystallogr.* **35**, 250 (1990)].
5. V. V. Litvinov, A. N. Petukh, Yu. M. Pokotilo, and V. I. Urenev, *Neorg. Mater.* **31** (2), 274 (1995).
6. A. Yu. Loskutov and A. S. Mikhaĭlov, *Introduction to Synergetics* (Nauka, Moscow, 1990).
7. V. V. Litvinov, Yu. M. Pokotilo, and V. I. Urenev, *Prib. Tekh. Ėksp.*, No. 4, 163 (1996).
8. V. V. Litvinov, A. N. Petukh, and Yu. M. Pokotilo, *Zh. Prikl. Spektrosk.* **64** (5), 655 (1997).
9. P. Grassberger and J. Procaccia, *Physica D* (Amsterdam) **9**, 3 (1983).
10. A. V. Kartavykh, Ė. S. Kopeliovich, M. G. Mil'vidskii, *et al.*, *Kristallografiya* **42** (4), 755 (1997) [*Crystallogr. Rep.* **42**, 694 (1997)].
11. M. Watanabe, M. Eguchi, and K. Kakimoto, *J. Cryst. Growth* **151**, 285 (1995).
12. M. Mohelcic, *J. Cryst. Growth* **97**, 42 (1989).
13. K. M. Kim, A. F. Witt, M. Lichtensteiger, and H. C. Gatos, *J. Electrochem. Soc.* **125** (3), 475 (1978).
14. G. Muller, C. Naumann, and W. Weber, *J. Cryst. Growth* **70**, 78 (1984).
15. K. J. Kolker, *J. Cryst. Growth* **50**, 852 (1980).
16. S. Fauve and A. Libchaber, in *Chaos and Order in Nature: Proceedings of the International Symposium on Synergetics, Schloss Elmau, Bavaria, 1981*, Ed. by H. Haken (Springer-Verlag, Berlin, 1981), pp. 25–35; *Synergetics* (Mir, Moscow, 1984), p. 234.
17. R. Krishnamurti, *J. Fluid Mech.* **60** (2), 285 (1973).
18. K. Stork and U. Muller, *J. Fluid Mech.* **71** (2), 231 (1975).
19. F. H. Busse, *J. Fluid Mech.* **52**, 97 (1972).
20. T. Kanda, K. Kusano, and H. Tomokage, *Jpn. J. Appl. Phys.* **35**, L1388 (1996).
21. K. Kakimoto, T. Shyo, and M. Eguchi, *J. Cryst. Growth* **151**, 187 (1995).
22. K. M. Kim, A. F. Witt, and H. C. Fatos, *J. Electrochem. Soc.* **119** (9), 1218 (1972).

Translated by L. Man

CRYSTALLOGRAPHIC
SOFTWARE

Structure Analysis by Reduced Data. II. Increase of Reproducibility of the Results of Diffraction Studies

A. P. Dudka and A. A. Loshmanov

*Shubnikov Institute of Crystallography, Russian Academy of Sciences,
Leninskii pr. 59, Moscow, 117333 Russia*

e-mail: dudka@rsa.crystal.msk.su

Received July 4, 2000

Abstract—The second part of the paper shows the advantages of the method of interexperimental minimization (IEM) over the conventional least squares (LS) method in the crystal-structure refinement. The new IEM method minimizes the norm of the differences between the data measured in independent experiments. The parameters of the structure model refined by the LS and the IEM methods are compared for four experimental data sets from an alexandrite crystal $\text{Al}_2\text{BeO}_4 : \text{Cr}^{3+}$. The model parameters calculated by the LS method from the initial experimental data sets showed insufficient reproducibility (the number of admissible values of the statistical-test criterion based on the normal-probability plot equals 5.6%). The use of the IEM algorithm increases the number of admissible values up to 38.9%. However, the use of fitting and statistical methods cannot provide a 100% reproducibility of all the model parameters automatically, which requires the reconstruction of the lost information on the characteristics of the experiment. © 2001 MAIK “Nauka/Interperiodica”.

INTRODUCTION

Independent experiments necessary for checking the reproducibility of the diffraction analysis of results can be performed in different ways. In the simplest case, one has to repeat the experiments on several specimens of the same material. The results obtained in such studies are analyzed, e.g., in [1–4].

The first project on the independent studies of two standard CaF_2 crystals was organized by the American Crystallographic Association in 1962, when these crystals were simultaneously studied in seven different laboratories. The results of this experiment were published in [5] and discussed in detail in [6–8]. Most of the measured experimental data sets turned out to be consistent within the accuracy of 5%. However, none of the authors claimed that the integrated intensities were measured with an accuracy higher than 2%. The discrepancies between the data measured in different experiments systematically depended on the scattering angle and structure-factor amplitudes, which, in turn, distorted the atomic-displacement and extinction parameters during the atomic-structure refinement.

In 1970, the results of a new large-scale international project on the study of organic crystals of D(+)-tartaric acid simultaneously in 16 laboratories (including three laboratories in the Soviet Union) were reported in [8–11]. The detailed analysis of the results of this international project revealed a number of problems. The main conclusion made from this project is as

follows. The reliability factors obtained in the LS refinement (1–2%) are considerably lower than the interexperimental differences (6–9%), because the calculated multiparametric structure factor “absorbs” all the systematic errors inherent in the experimental integrated intensities. As a consequence, the positional parameters, and especially the atomic-displacement parameters (ADPs), showed insufficient reproducibility.

The creation of the Cambridge Data Base of Structures [12] considerably increased the data available for studying the structural-data reproducibility. Thus, in 1986, the refined data were analyzed for 100 pairs of crystals [13]. In comparison with the results of the Project of 1970, the reproducibility of the positional parameters of nonhydrogen atoms considerably improved. However, not all the problems were completely solved. Thus, atomic-displacement parameters could not be compared because of their very low reproducibility. The standard deviations in the positional parameters of non-hydrogen atoms turned out to be underestimated, on the average, by a factor 1.4–1.45. Positive correlations were established between the errors in the positional parameters of atoms in similar chemical environment. The errors in the heavy-atom positions were determined less reliably than those in light-atom positions. The standard deviations in the unit cell parameters were also considerably underestimated (by a factor of five for the edges and 2.5, for the angles).

The project of the International Union of Crystallography [14] on the comparison of structural parameters and electron-density maps was performed on four X-ray and five neutron diffraction data sets [14]. The main conclusions made from this Project are as follows. The parameters of atomic coordinates are reproduced with a rather high accuracy; the coordinate parameters obtained from neutron-diffraction data are reproduced much better than those obtained from X-ray diffraction data. The atomic-displacement parameters have considerably different values. The deformation electron-density maps reproduce sufficiently well all the chemically important features of the crystal structures. To provide the solution of the problem, the Subcommittee on Statistical Descriptors of the International Union of Crystallography has formulated the requirements to the quality of structural investigations [15–17]. The progress achieved in the design of the equipment and the computational procedures allowed to outline the main directions of the development of precision structural studies in order to meet some of these requirements. The large number of publications to the effect showed that the measurement errors are distributed at random, in other words, revealed no considerable systematic errors.

The number of publications based on independent measurements of crystals (e.g., with the use of various types of radiation and some external factors) considerably increases. In this connection, we should like to mention here X-ray and neutron diffraction studies [18] and publications in which the experimental data are compared with the corresponding *ab initio* calculations.

Unfortunately, the problem of reproducibility of the numerical values of the refined parameters (the list of which has considerably increased for the recent 20 years) is still urgent. In some precision studies, the completely reproducible positional parameters and partly reproducible atomic-displacement parameters were obtained. It was indicated [19] that the most detailed and exhaustive analysis of the reproducibility of refined parameters for an atomic model can be performed with the use of the statistic test of the random character of parameter error distribution (the so-called *P*-test based on the analysis of the normal-probability plot [20–22]).

We came to the conclusion that even the best planned precision experiments performed on the most sophisticated modern instruments cannot provide the reproducibility of all the atomic-displacement parameters, which is associated with possible correlations between the parameters and, first of all, correlation of atomic displacements and the scale factor. Correlations between the parameters result in a considerable discrepancy between the calculated parameters and their reliable physical values and make them poorly reproducible.

In terms of mathematics, this fact is quite understandable, because the determination of the atomic-model parameters is an ill-posed problem—for nonlinear problems, the solution is neither stable nor unique [23]. Thus, using only the methods of local minimization (including LSM), one cannot solve this problem without the use of a number of good initial approximation [24]. In any case, the iteration process can stop at a certain point prior the attainment of the closest local (global) minimum by different reasons, including the effect of possible correlations between the model parameters. Thus, each new structural study yields, in fact, a new solution depending on the accuracy of the experimental data and the weighting scheme used.

The interexperimental minimization (IEM) minimizes the difference between the experimental data obtained in two experiments (the difference “experiment 1–experiment 2”) and, thus, makes these data more consistent. In the first part of this study [19], we demonstrated the improvement of the statistical criteria of data consistency using the intersecting data sets (the so-called cross-sets). It was also shown that the use of new more sophisticated methods considerably reduces the reliability factors in the LS structure refinement. This signifies that the algorithm of the interexperimental minimization allows one to pass from the neighborhood of the initial local minimum of the functional to the neighborhood of another deeper minimum.

Is this minimum is global and the same for all the refinement processes used in the repeated studies? Can this higher reproducibility of the experimental data automatically lead to better reproducibility of the atomic-model parameters refined and, if it can, then to what extent?

The answer to this question would have been obvious if the atomic-parameter values were not distorted by mutual correlations. Even if the experimental data sets coincide in the statistical sense, in the mathematical sense, they are different, and the interparam correlations would yield somewhat different results, whereas the refinement by each set of experimental data can stop prior to the attainment of the minimum [24]. Another aspect of the problem is associated with the fact that it is still unclear how thoroughly the experimental data should be collected and how thoroughly their primary treatment should be performed in order to exclude possible systematic errors and attain the necessary level of atomic-parameter reproducibility.

Below, we describe the further study of the structure of a lasing alexandrite ($\text{Al}_2\text{BeO}_4 : \text{Cr}^{3+}$) crystal with the use of four experimental data sets (1–4). The cross-sets are indicated by two figures, e.g., 12. The second-order cross-sets, i.e., the cross-sets obtained by averaging the data of the initial cross-sets, are written as hyphenated pairs of figures, e.g., 12–34. The focus is made on the mutual correspondence of the atomic parameters refined by different sets of experimental data.

CRITERIA OF THE QUALITY OF STRUCTURAL STUDIES

The main criteria for estimating the accuracy of the structural data are the R -factors obtained upon the structure-model refinement. The second group of the traditional criteria is comprised by the quantities that allow one to check the random character of the error distribution in the experimental data, S , and the appropriateness of the weighting scheme, χ^2 [16, 22].

The detailed information on the error distribution in the measured data and the mutual consistency of independent experimental data sets or the degree of the model-parameter reproducibility can be obtained from the normal-probability plot. The interpolation of the points lying on the straight line $y = Ax + B$ allows the introduction of the following criteria: the slope A , the intersection B , the degree of curve linearity (scatter of points) D , and some other criteria [25, 26].

The normal-probability plot is linear and has the unit slope and the zero intersection if the measured or calculated parameters have only random errors. The test requirements can be satisfied by two main methods—either by increasing the corresponding errors in the data (i.e., reducing the relative accuracy) or by decreasing the discrepancy between the similar quantities in different experiments. The visual linearity of the curves of all the tests indicates that the structure determination is correct. The invalidity of other criteria indicates certain shortcomings inherent in the model or the weighting scheme, which can be corrected in most instances. All the criteria associated with checking the statistical hypotheses are characterized by the predetermined ideal values $S = \chi^2 = A = 1$ and $B = D = 0$.

When testing the independent sets of experimental data, one has to calculate their relative scale factors (the so-called interfactors) K and K_w and the values of inter-experimental R_{12} and R_{w12} factors (the ideal values of the latter are unity and zero, respectively) [25, 26].

REPRODUCIBILITY OF THE ATOMIC-MODEL PARAMETERS

In the first part of this article ([19], Tables 2–4), we have proved that the relative accuracy of the results obtained by the IEM method is higher than that obtained by the LSM. However, the reliability of the obtained atomic parameters is more important. The problem whether the atomic models used in the structure analysis correspond to the physical reality or not are beyond the scope of this article. Nevertheless, we believe that, irrespectively of the model, its parameters should be reproduced in other independent studies of the same objects.

One of the constituent parts of the objective function in the interexperimental minimization is written as $\Phi \sim \Sigma(I_{1\text{obs}} - I_{2\text{obs}})^2$, where I_{obs} are the squared experimental structure factors. The refinement of the atomic model is

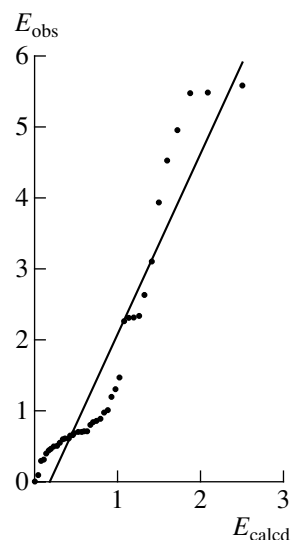


Fig. 1. Normal-probability plot and its linear interpolation for the model parameters obtained from experiments 2 and 4.

based on the assumption (although very probable but still to be confirmed) that a higher consistency of the experimental data sets, in turn, would improve the reproducibility of the structural results.

Consider, first, the refinement of the model parameters by the initial experimental data sets. Figure 1 shows the normal-probability plot for the atomic parameters obtained in the refinement of the structure model by experimental data sets 2 and 4 (the P -test). The slope A of the curve characterizes the agreement between the parameters of two models and the correctness of the calculation of the errors in the parameters refined in the LS procedure. The curve linearity (the average scatter in points D) and the closeness of the intersection point B to zero indicate the level of the systematic errors in the parameters. The root-mean square scatter in the parameter values $\langle(\Delta P/\sigma(P))^2\rangle^{1/2}$ has the same meaning as the slope A and is given here for easier comparison of the results with the results of the X-ray and neutron diffraction studies [18]. The maximum value of the normalized error $|\Delta P/\sigma(P)|_{\text{max}}$ is the most crucial parameter, whose ideal value, as far as we know, has not been attained as yet in any of the studies (for sampling of the given size, $|\Delta P/\sigma(P)|_{\text{max}} = 2.50$). The R -factor shows the level of the relative accuracy of the test; it is always possible to satisfy the test by increasing the error in parameter values and reducing the relative accuracy, in other words, the A and the R criteria are somewhat contradictory.

It is also necessary to check to what extent the refinement of the structure model by the cross-set would guarantee the determination of the atomic parameters with the numerical values that would be reproducible in the repeated studies better than with the use of the initial independent data sets.

Reproducibility of the model parameters of $\text{Al}_2\text{BeO}_4 : \text{Cr}^{3+}$ crystals

Data	A	B	$\langle(\Delta P/\sigma)^2\rangle^{1/2}$	$ \Delta P/\sigma _{\max}$	$\langle D \rangle$	R, %
12	1.81	-0.29	1.65	6.00	0.150	0.44
13	3.00	-0.28	2.81	6.30	0.078	0.30
14	2.95	-0.66	2.50	6.18	0.114	0.46
23	3.30	-0.57	2.89	8.47	0.064	0.34
24	2.55	-0.45	2.27	5.59	0.159	0.87
34	4.98	-0.78	4.45	9.73	0.115	0.73
12-13	2.28/2.64	-0.45/-0.23	1.96/2.49	6.12/6.37	0.067 /0.090	0.29/0.27
12-14	2.15/ 1.86	-0.46/-0.23	1.84/ 1.69	5.32/4.47	0.330/ 0.046	0.59/0.31
12-23	1.43 /2.50	-0.09 / -0.18	1.37 /2.38	3.31/5.65	0.046 / 0.065	0.17 /0.32
12-24	1.59 / 1.71	-0.33/ -0.06	1.36 / 1.68	3.60/ 1.68	0.108/ 0.053	0.41/0.31
12-34*	2.48/2.42	-0.30/-0.21	2.27/2.27	7.20/5.66	0.069 / 0.043	0.41/0.36
13-14	2.01/2.07	-0.27/ -0.06	1.83/2.14	4.20/4.72	0.076/ 0.047	0.36/0.34
13-23	1.09 / 1.29	-0.11/0.04	1.01 / 1.27	2.92/3.55	0.069 / 0.050	0.36/ 0.09
13-24*	2.89/3.58	-0.34/-0.57	2.65/3.18	6.45/9.47	0.079/0.073	0.22/ 0.15
13-34	1.04 / 1.11	-0.18 / -0.02	0.92/ 1.11	2.79/3.14	0.077/ 0.063	0.19 / 0.13
14-23*	2.15/2.44	-0.36/-0.40	1.91/2.16	5.59/5.49	0.131/0.087	0.70/0.32
14-24	2.03/2.79	-0.50/-0.70	1.77 /2.34	5.70/8.22	0.213/0.157	0.21/0.27
14-34	1.81 / 1.85	-0.02 / -0.14	1.82/ 1.75	3.71/4.03	0.074/ 0.036	0.30/0.39
23-24	2.35/3.07	-0.037/-0.34	2.09/2.76	5.03/6.83	0.088/0.095	0.55/ 0.11
23-34	1.37 / 1.21	-0.14 / -0.02	1.28 / 1.22	3.56/3.69	0.090/ 0.059	0.43/ 0.13
24-34	2.95/2.99	-0.44/-0.50	2.62/2.63	7.70/8.33	0.063 /0.077	0.29/ 0.17

Note: Asterisks indicate the independent cross-sets; bold figures indicate the admissible values of the criteria; the first six lines correspond to the initial data, the remaining lines correspond to the averaged sets and cross-sets.

The rigorous logical proof of better reproducibility of the results obtained by the IEM method can be obtained in the following way. If there are four independent data sets, one has to form the cross-sets and to calculate the P -test for the corresponding model parameters. Moreover, one has also to use not only the initial data sets, but the averaged data sets as well. If the test is successful, this signifies that the better criteria of the interexperimental fitting would guarantee a better reproducibility of the final results. Since this method is very labor-consuming, it is mainly of methodological value.

The results of the criterion test are indicated in table. Four independent data sets provide six variants of the interexperimental comparison. Six averaged (cross) sets allow the formation of 15 corresponding second-order sets for crossing or averaging sets (indicated after slash). Three second-order data sets (12-34, 13-24, and 14-23) are marked with an asterisk are absolutely independent. All the cross-sets were formed for three cycles with the same control keys in all the programs for all the experiments.

To facilitate the analysis of such a large volume of the information, the admissible values are indicated by bold figures. It is seen that the unsatisfactory reproduc-

ibility of the parameters obtained from the initial experimental data sets (two admissible values of total 36, i.e., 5.6% of all the data). The visual distortions of the P -test plots for other initial experimental data sets are similar to those shown in Fig. 1. The maximum curvature is possessed by the curve obtained for comparison of the models from experimental data sets 1 and 2, but, at the same time, the curve also has the best slope.

The worst characteristics were obtained for pair 34 which represents the experiments of the highest relative accuracy. Up to now, there have been no indications that these experimental data sets can include considerable systematic errors. However, it is well known that the experiments cannot be completely independent, because the data sets from specimen III were obtained on different diffractometers and, therefore, the application of the IEM method does not necessarily yield the maximum effect.

The unsatisfactory result of the test for the pair 34 is caused by the systematic overestimation of the atomic-displacements parameters in experiment 3, which, in turn, follows from the error in the selection of the scanning range cutting off the far peaks. Since the error due to profile termination having the shape close to Gaussian can be described by the exponential dependence, it

produces no effect on the R -factors of the refinement— $R/R_w = 1.040/1.003\%$ (Table 2 in [19]), but only distorts the values of the atomic-displacement parameters (ADPs). The discrepancies between these parameters and the results of experiments 3 and 4 are quite considerable, $R_{12} = 1.73\%$, but the curve curvature turned out to be insignificant; thus, the error can be identified with the drastically increased slope of the curve, $A = 4.98$.

A comparison of experiment 3 with other experiments is more satisfactory than the comparison of experiments 3 and 4 (the latter is the most precise of all the four experiments). The comparison of experiments 13 and 23 shows that, on the whole, the criteria take the same values as those obtained in comparison of the other experiments (12, 14, 24) (see table). Thus, we arrive at the second conclusion: only processing of the data of completely independent experiments can provide the compensation of the systematic errors in the measurements.

The consistent use of the averaged data sets and cross-sets increases the reproducibility of the results in comparison with the reproducibility of results obtained from the initial experimental data. We illustrate this conclusion by pairs of experiments 2 and 4 (Fig. 1), 34 and 12 (Fig. 2), and 13 and 24 (Fig. 3) for which the possible causes of plot distortions were considered above and in [19]. Cross-set 24 is based on the experimental data characterized by the systematic differences ([19], Fig. 1) giving rise to the systematic distortions of the parameters (Fig. 1). The cross-set 34 is characterized by the specific nature of systematic errors in the data and of the parameters (see above); the latter distort the corresponding curves of the plots to a lesser degree. The cross-set consists of the experimental data reproducible much better than the initial data ([19], Figs. 2 and 3). This results in the better reproducibility of the model parameters (Fig. 2, pair 34–12). For pair 24–13, the result is somewhat worse (Fig. 3), however, the plot characteristics in Fig. 1 are better.

The pronounced slope of the curve in Fig. 3 indicates the underestimated standard uncertainties of the atomic parameters, which, at the relative accuracy of 0.1–0.3%, can be explained by incorrect computational procedure in the program used. The degree of linearity of the curve constructed with the use of other cross-sets (with the only exception of pair 14–24) is even higher (table), with some of them being very close to ideal ones. To a certain degree, the latter fact can also be caused by their partial mutual dependence, and, therefore, these plots are not considered here.

The analysis of the criteria of the P -test for the parameters obtained from the averaged sets and the cross-set shows that, despite certain improvement, the complete reproducibility has not been attained. For the average sets, we obtained 23 admissible values from the total of 90 (i.e., 26.5%); for the cross-sets, 35 of the total of 90 (i.e., 38.9%). The calculation of the model parameters by the cross-sets improves the linearity cri-

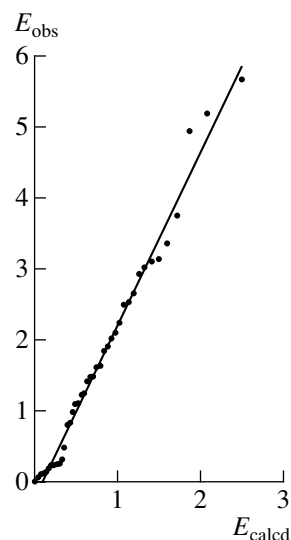


Fig. 2. Normal-probability plot and its linear interpolation for the model parameters obtained from independent cross-sets 34 and 12.

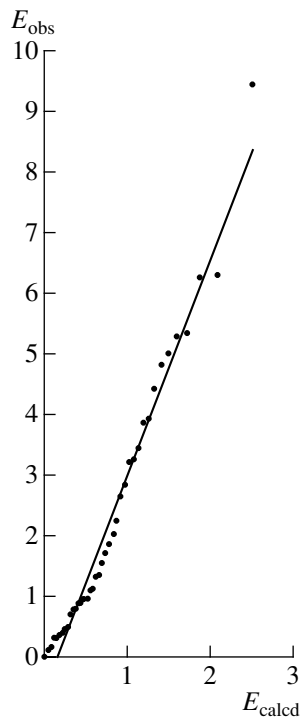


Fig. 3. Normal-probability plot and its linear interpolation for the model parameters obtained from independent cross-sets 13 and 24.

teria for the curves B and D , which indicates the absence of the systematic errors. We should like to emphasize once again the high relative accuracy of the parameter agreement—0.09–0.39% (usually, it cannot be better than 1%).

Nevertheless, the program is performed in the automatic mode and, without the allowance for impurity

(chromium) atoms in the crystals, it cannot completely compensate the model distortions caused by 90–95% correlations between the occupancies by the aluminum atoms and displacement parameter of these atoms and transform the plots of the *P*-test to its ideal form.

Moreover, some uncompensated distortions in the atomic parameters are due to the asymmetry in the electron-density distribution in crystals. The experimental data sets *a priori* include the errors caused by insufficiently correct allowance for absorption (experiment 1) and the error caused by peak cut-off (experiment 3).

The neglect of thermal diffuse scattering (TDS) also hinders the attainment of the ideal reproducibility of the results. Two independent experimental data sets can be characterized by the same uncompensated effect, which can lead to the same changes in the integrated intensities of the same reflections. However, this does not signify that the ADPs calculated from these data sets and the degree of the parameter reproducibility would also be the same (the effect of correlations).

Thus, insufficient reproducibility of the results can be caused by the loss of some information on various characteristics of the scattering process. Fitting and the statistic algorithms alone cannot compensate all the types of errors.

The correction for various types of systematic errors, which cannot be identified or compensated, should be interpreted as one of the variants of the normalization of the data to the absolute scale. If the experimental data sets are independent, then the concrete systematic errors would be inherent only in one of the experimental data sets and these errors can be compensated in the normalization block.

The allowance for the effect of impurity atoms suggests the separation of the structure model into the common and the individual parts and, in addition to the normalization to the scale factors and allowance for extinction, the data are also normalized with respect to the occupancy of atomic positions. Moreover, the approximate occupancies can be known either from growth or spectroscopic data, and therefore the problem can also be solved with the invocation of the information from the adjacent fields of physics.

CONCLUSIONS

The main goal of this study was to develop a number of methods for obtaining the sets of atomic-model parameters that can be reproduced with the use of another independently obtained experimental data for the given crystal. The interexperimental minimization (IEM) method allows one to obtain the normalized experimental data with high degree of reproducibility, which, in turn, increases the reproducibility of the final results—the atomic-model parameters.

We have compared the parameters of the models of the alexandrite structure $\text{Al}_2\text{BeO}_4 : \text{Cr}^{3+}$ refined over four experimental data sets. The use of the IEM proce-

dures in the automatic mode (three cycles) has shown the following.

The model parameters calculated by the initial experimental data are reproduced unsatisfactorily (Fig. 1, table).

The compensation of the systematic errors in the measured data is possible only if one uses the independent experimental data sets. The collection of experimental data with high relative precision from the same specimen cannot guarantee a higher reproducibility level, but provides an increase of the relative precision of the final results.

The use of the cross-sets increases the degree of reproducibility of the model parameters, but cannot provide the complete and statistically ideal reproducibility of the parameters automatically (even at the expense of the reduction of their relative precision).

The problem of reproducibility of results is caused by the loss of some information on scattering processes. The use of the mathematical algorithms alone cannot compensate all the types of such errors.

In the course of the experimental-data reduction to the absolute scale, one can use the theoretical premises for reconstruction of some of the lost information and compensation of the effect of some errors.

The alexandrite crystals studied contained small amount of chromium impurities, and the model refinement was characterized by 95%-correlations between the corresponding atomic parameters. The appropriate parameter refinement under these conditions will be discussed in the next part of this study.

ACKNOWLEDGMENTS

The authors are grateful to V.I. Simonov for his help in the conduction of experiments and to M.Kh. Rabadonov for the fruitful discussions and valuable remarks and V.N. Molchanov, I.A. Verin, and B.A. Maksimov for their help in measurements.

REFERENCES

1. S. C. Abrahams, *Acta Crystallogr.* **17**, 1190 (1964).
2. S. C. Abrahams and J. L. Bernstein, *Acta Crystallogr.* **18**, 926 (1965).
3. S. Miyake, *Acta Crystallogr., Sect. A: Cryst. Phys., Diff., Theor. Gen. Crystallogr.* **A25**, 257 (1969).
4. B. Dawson, *Acta Crystallogr., Sect. A: Cryst. Phys., Diff., Theor. Gen. Crystallogr.* **A25**, 12 (1969).
5. S. C. Abrahams, L. E. Alexander, T. C. Furnas, *et al.*, *Acta Crystallogr.* **A22**, 1 (1967).
6. J. K. Mackenzie and V. W. Maslen, *Acta Crystallogr., Sect. A: Cryst. Phys., Diff., Theor. Gen. Crystallogr.* **A24**, 628 (1968).
7. S. C. Abrahams, L. E. Alexander, T. C. Furnas, *et al.*, *Acta Crystallogr., Sect. A: Cryst. Phys., Diff., Theor. Gen. Crystallogr.* **A25**, 585 (1969).

8. A. M. Mathieson, *Acta Crystallogr., Sect. A: Cryst. Phys., Diffr., Theor. Gen. Crystallogr.* **A25**, 264 (1969).
9. S. C. Abrahams, W. C. Hamilton, and A. M. Mathieson, *Acta Crystallogr., Sect. A: Cryst. Phys., Diffr., Theor. Gen. Crystallogr.* **A26**, 1 (1970).
10. W. C. Hamilton and S. C. Abrahams, *Acta Crystallogr., Sect. A: Cryst. Phys., Diffr., Theor. Gen. Crystallogr.* **A26**, 18 (1970).
11. J. K. Mackenzie and V. W. Maslen, *Acta Crystallogr., Sect. A: Cryst. Phys., Diffr., Theor. Gen. Crystallogr.* **A24**, 607 (1974).
12. F. H. Allen, S. Bellard, M. D. Brice, *et al.*, *Acta Crystallogr., Sect. B: Struct. Crystallogr. Cryst. Chem.* **A35**, 2331 (1974).
13. K. Taylor and O. Kennard, *Acta Crystallogr., Sect. B: Struct. Commun.* **C42**, 112 (1986).
14. P. Coppens, J. Dam, S. Harkema, *et al.*, *Acta Crystallogr., Sect. A: Found. Crystallogr.* **40**, 184 (1984).
15. D. Schwarzenbach, S. C. Abrahams, H. D. Flack, *et al.*, *Acta Crystallogr., Sect. A: Found. Crystallogr.* **45**, 63 (1989).
16. *International Tables for Crystallography* (Kluwer, Dordrecht, 1992), Vol. C.
17. D. Schwarzenbach, S. C. Abrahams, H. D. Flack, *et al.*, *Acta Crystallogr., Sect. A: Fundam. Crystallogr.* **A51**, 565 (1995).
18. B. Iversen, F. K. Larsen, B. N. Figgs, *et al.*, *Acta Crystallogr., Sect. B: Struct. Sci.* **52**, 923 (1996).
19. A. P. Dudka and A. A. Loshmanov, *Kristallografiya* **46** (3), 565 (2001) [*Crystallogr. Rep.* **46**, 511 (2001)].
20. S. C. Abrahams and E. T. Keve, *Acta Crystallogr., Sect. A: Cryst. Phys., Diffr., Theor. Gen. Crystallogr.* **A27**, 157 (1971).
21. S. C. Abrahams, *Acta Crystallogr., Sect. A: Fundam. Crystallogr.* **A53**, 673 (1997).
22. *International Tables for X-ray Crystallography* (Kynoch Press, Birmingham, 1974), Vol. 4.
23. A. N. Tikhonov and V. Ya. Arsenin, *Solutions of Ill-Posed Problems* (Nauka, Moscow, 1979, 2nd ed.; Halsted Press, New York, 1977).
24. B. M. Shchedrin, I. N. Bezrukova, and E. M. Burova, in *Library of Programs for Studying Structures and Compositions of Materials by Diffraction Methods* (Mosk. Gos. Univ., Moscow, 1987), p. 3.
25. A. P. Dudka, A. A. Loshmanov, and B. P. Sobolev, *Kristallografiya* **43** (4), 605 (1998) [*Crystallogr. Rep.* **43**, 557 (1998)].
26. A. P. Dudka, A. A. Loshmanov, and B. A. Maksimov, *Kristallografiya* **43** (4), 613 (1998) [*Crystallogr. Rep.* **43**, 565 (1998)].

Translated by L. Man

JUBILEES

Marina Aleksandrovna Chernysheva (On the Occasion of Her 90th Birthday)



The dramatic events of the history of the 20th century—the history of science; the revolution in physics, which has changed our understanding of the physical picture of the world; the initial hostile attitude to new concepts and ideas on the structure of the macro- and microcosm and their final triumph—are all left behind. All the things and all the events go away—enormous and small; general and particular; Laue’s experiments, which proved the atomic structure of crystals; dramatic postwar discussions around new ideas and concepts, in particular, those of dislocations; the rise of the public interest in natural sciences in the middle of the century and its obvious decrease at the end of the century. And all these events have passed against the background of the large-scale social and historical changes.

Thus, it is remarkable to meet those people who witnessed all these events and participated in them and

the people whose memory stores the past, the lively feelings, and the memories of a witness. Their experience and understanding of the real values of the life can hardly be overestimated. Marina Aleksandrovna Chernysheva, the senior scientist of the Laboratory of Mechanical Properties of Crystals of the Shubnikov Institute of Crystallography of the Russian Academy of Sciences is one of such people.

Chernysheva was born on December 14, 1911 in St. Petersburg. Her father, Aleksandr Alekseevich Chernyshev, was one of the first graduates from the Polytechnic Institute, a future Academician, one of the organizers of Physicotechnical Institute, the founder and first director of the Leningrad Electrophysical Institute. He was an outstanding engineer and physicist of his time. Suffice it to say that among his inventions is the first high-voltage electrical transmission line, the first thermal cathode, the first electronic sweep in television. Her mother, Marina Gavrilovna had become a pediatric doctor “by promise.” She went into medicine after the death of her twelve-year-old son of typhus during the Civil War.

Chernysheva graduated from the faculty of radio physics of the Leningrad Polytechnic Institute in 1934 and became a post graduate student at the Institute of Civil Aviation. She had many dramatic turns in her life. One of them was her decision to leave post graduate studies in order to work at the *Svetlana* plant. Another turn took place when she left Leningrad for Moscow in 1939, where her father (then not a director any more but still an active scientist in Leningrad) as well as Nikolai Ivanovich Vavilov received a room in the Academic Hostel.

An announcement in a newspaper brought Chernysheva to the laboratory of electrical musical instruments at the Moscow Conservatory as a radio engineer and physicist. However, this new life was soon disrupted by the war. Laboratory was closed, and in the summer of 1942, Chernysheva, by an advice of her old acquaintance from her Leningrad days, Marina Viktorovna Klassen-Neklyudova, entered the Laboratory of Problems of Construction at the Geological Institute. Her first research was made in the field of strength of materials (then completely alien to her) and concerned the high-strength reinforced fiberglass- and binding resin-based materials with the hope to be able to use these materials later in the construction work in the peaceful future.

From the very moment of the organization of the Institute of Crystallography, Chernysheva started working at the Laboratory of Mechanical Properties. She studied twins in the Seignette salt. Upon the approval of Aleksei Vasil'evich Shubnikov, she successfully defended her dissertation on the phenomenon of twinning in a Seignette salt crystal. In this classical work, Chernysheva, for the first time, managed to study the real structure of the Seignette salt using polarized light and microfilming. She established that twinning components are the regions of spontaneous polarization or domains, that these domains are formed at inhomogeneities, and that it is these inhomogeneities in the real crystal structure that determine the distribution of domains in the Seignette salt. These results were recognized worldwide. Later Chernysheva together with Vladimir L'vovich Indenbom studied the individual characteristics of domains. Her experimental art was successfully complemented with the bright talent of her colleague—theoretician. The design and construction of a universal IPL-452 conoscope were highly evaluated and, in 1967, Chernysheva was awarded the Vavilov Prize. The boom triggered by studies of laser crystals in the 1960s and 1970s did not pass unnoticed for Chernysheva. She mastered the method of conoscopic flaw detection and performed the pioneering studies on stress relaxation in annealed corundum crystals.

The scientific work of Chernysheva is characterized by enthusiasm, devotedness, and temperament. Her experiments invite admiration with their thoroughness and results, with their adjustment and reliability. No matter what she is doing, she always does her best.

Being absolutely devoted to science, she has preserved all these qualities to this day. Working in cooperation with the Laboratory of Fluoride Materials of the Institute of Crystallography, Chernysheva initiated the conoscopic studies of defects in fluoride materials and the effect of growth conditions on their optical and mechanical properties. As a result, the optimum growth and cooling rates determined considerably improved the quality of these crystals.

Being a sound woman in her personal life, possessing fantastic accuracy in work, Chernysheva combines the realistic views with a certain inner carnival-like joy, festive mood, and romantic elation. She readily gets inspired and inspires others. She combines a researcher and an artist in one person. Her benevolence has become legendary and her obligatoriness has been widely recognized. She knows how to interact with people, to remove stress, and to create joyful and cheerful atmosphere around herself. Until today she has preserved brilliant memory. She is intelligent in a way that nobody can teach or learn. Her values are the main ones in life—work, friends, patriotism, and also something which pushes away the limits of the earthly life and reminds us about our spiritual duties.

All friends and colleagues cordially congratulate Marina Viktorovna Chernysheva with her 90th birthday and wish her good health and long years of creative work.

Translated by L. Man

MEMORIAL DATES

To the Memory of Valentin Yakovlevich Khaimov-Mal'kov (On the Occasion of His 75th Anniversary)



On June 6, 2001, friends and colleagues mark the 75th anniversary of a gifted scientist, a well-known expert in the field of crystallography, Valentin Yakovlevich Khaimov-Mal'kov.

Khaimov-Mal'kov lived a bright and full life. He was born on June 6, 1926 in Moscow in the family of old "bolsheviks." His life was far from being simple. Being a pupil of the tenth grade of the secondary school, he was drafted into the military service in the Soviet Army (1944) and participated in the Great Patriotic War of 1941–1945. In the period from 1947 to 1952 he studied at the Gorky State University. In 1952, Khaimov-Mal'kov started the post graduate study at the Institute of Crystallography of the USSR Academy of Sciences, and, after that, all his life was related to it.

Khaimov-Mal'kov's scientific life was very successful. His candidate dissertation was an important contribution to one of the most important fields of crystallography—crystallization pressure. This study was highly evaluated by Alexei Vasil'evich Shubnikov, who considerably influenced the whole scientific carrier of Khaimov-Mal'kov.

Twenty two years have passed since Khaimov-Mal'kov's death and, with each new year, it becomes

clearer how great his scientific erudition, how large the sphere of his scientific interests, how deeply his insight into new scientific problems were and how great an ability of prediction he possessed.

Crystallization pressure and the study of sectorial impurity distribution in single crystals grown from solution, optical inhomogeneity of lasing crystals, mechanical strength and its relation to the characteristics of laser radiation, new methods for synthesis of refractory single crystals, the distribution of volatile impurities during crystallization from melts, the effect of thermal treatment, the influence of irradiation and impurities on the radiation and optical processes in ruby and sapphire crystals, solid-phase chemical reactions in crystals during their growth and annealing in various media—this is only a short list of his interests and studies.

Khaimov-Mal'kov received pleasure from the creative process itself. He was very demanding in his work. He was always available too everybody who wanted to serve science. Crowds of people from various institutes of the whole country came to see him, and none left him in disappointment. Everybody received understanding, help, and support. Khaimov-Mal'kov helped many people to find their place in science, to prepare the materials for presentation or the defense of a dissertation, to interpret the new results, to correct the article, to prepare the program of further experiments or publications.

Khaimov-Mal'kov had published more than 85 articles. He was awarded the USSR State Prize for his studies on the synthesis of new crystalline materials.

Khaimov-Mal'kov was a patriot. He enjoyed the feeling of being useful and the satisfaction of the performed task, the sense of responsibility of a scientist to his country.

Khaimov-Mal'kov passed away on September 23, 1979.

All those who was happy to meet, work, and be friendly with this open, honest, upright, and wholesome man will always remember him. He has always been an example for all those who knew him.

E. Krivandina

Translated by L. Man

MEMORIAL DATES

To the Memory of Fedor Ivanovich Fedorov (On the Occasion of His 90th Anniversary)



On June 19, 2001, Fedor Ivanovich Fedorov, a scientist of the world level, a man of the encyclopedic knowledge, would have celebrated his 90th birthday. Fedorov successfully worked in various branches of physics. For more than 60 years of his scientific, scientific–organizational, and pedagogical activity, he made an enormous contribution to the development of physics and mathematics and teaching and preparation of scientific staff.

Fedorov was born on June 19, 1911 in the village of Turets in the Novgorod District (close to the city of Grodno) in a family of village teachers—Ivan Mikhailovich Fedorov (later a writer known under the pseudonym Yanka Mavr) and Varvara Fedorovna Adamovich. In 1931, he graduated from the physical–mathematical department of the pedagogical faculty of the Belorussian State University and started teaching physics and mathematics at the Pedagogical technical

school and a secondary school in city of Krichev in the Mogilev oblast.

However, the young teacher had a passion for science and, in a year, he entered the post-graduate course at the Physicotechnical Institute of the Belorussian Academy of Sciences. In a year, he was sent to the Leningrad University, where he became a post-graduate student of an outstanding physicist–theoretician Academician Vladimir Aleksandrovich Fock. His unique talent, ability to work, and purposefulness allowed Fedorov to learn the newest concept and methods of theoretical physics for a short period of three years and to solve a number of complicated problems in quantum electrodynamics. Fedorov’s style of research was characterized by the wish to solve general problems by using general approaches and also by the elegance of their mathematical description.

Upon the successful defense of the Candidate Dissertation, Fedorov went back to Minsk (1936). The first Candidate of Physics and Mathematics in Belorussia, he headed the Chair of Theoretical Physics at the Belorussian State University (1938–1962).

During the Great Patriotic War of 1941–1945, Fedorov taught physics and mathematics at the secondary school in a city of Kiselevsk of the Novosibirsk oblast, was a senior lecturer at the Chair of Physics of the Moscow Institute of Aviation Technology evacuated to Novosibirsk. In 1943, he became the Dean of the Physical–Mathematical Faculty of the Belorussian State University then located at the Skhodnya, Moscow Oblast. Upon his return to the destroyed Minsk, he devoted his life to restoration and organization of the normal activity of the faculty, whose dean he was until 1950.

In 1954, Fedorov successfully defended his Doctoral Dissertation dedicated to the invariant methods in optics of anisotropic media at the State Optical Institute in Leningrad and, thus, became the first Doctor in Physics and Mathematics in Belorussia.

Fedorov delivered lectures not only at the Belorussian State University; in 1958, he was invited to the Chair of Crystallography and Crystal Physics of the Physics Department of Moscow State University to deliver lectures on optics of anisotropic media. In 1962, he also delivered a course on the theory of elastic waves in crystals. His lectures always gathered large auditorium not only of students but also of experts in solid state physics and the scientists from the Institute of

Crystallography of the USSR Academy of Sciences. His lectures gained great popularity, the audience was under the influence of his rigorous logic, charisma, and the novelty of his scientific approaches. In 1958 he started cooperation with research scientists of various institutes of Moscow and Leningrad, and, first of all, with the researchers of the Institute of Crystallography.

Fedorov was closely related to the development of many fields of physics and mathematics in Belarus'. He actively participated in the organization of the Institute of Physics and Mathematics of the Belorussian Academy of Sciences, the first research institution of such a profile in Belorussia. Up to 1987, he headed the laboratory of theoretical physics. It is this institute that later provided the organization of almost all the Institutes of the Department of Physics, Mathematics, and Informatics of the National Academy of Sciences of Belarus'. Fedorov was one of the organizers of this Department (1963) and headed it up to 1987. He formulated and coordinated the research work in physics and mathematics. Today, the Department of Physics, Mathematics, and Informatics is one of the largest in the National Academy of Sciences of Belarus'—it consists of eight research institutes, which are among the leading organizations in many fields of physics and mathematics. His contribution to science and scientific organization have not passed unnoticed and, in 1956, he was elected a Corresponding Member, and, in 1966, a Full Member of the Academy of Science of the Belorussian SSR.

His many-sided scientific activity had always been characterized by generality of approaches and elegance of mathematical solutions. He developed the general covariant method based on the consistent use of invariance and covariance concepts in physics. The corresponding mathematical apparatus developed by Fedorov provided the formulation of the physical theory which allowed one to eliminate the use of particular coordinate systems.

Fedorov's was engaged into the development of four general fields of physics—crystal optics, crystal acoustics, theory of elementary particles, and the theory of relativity. He was also deeply interested in the methodology and history of physics and philosophy of natural science.

He was the first to construct the general theory of optical properties of all types of anisotropic media and the rigorous theory of crystal gyrotropy. In 1976, Fedorov was awarded the USSR State Prize for these works. In 1980, the phenomenon of the side deviation of a light beam under the conditions of total reflection was recognized to be a scientific discovery.

The first Fedorov's book entitled *Optics of Anisotropic Media* (1958) had become a guide book for several generations of researchers. This work is also well known abroad, although under another title. It was published by H.C. Chen under the title *Theory of Electromagnetic Waves. A Coordinate-Free Approach*. New York, McGraw-Hill, 1983. Its publication is an exam-

ple of an incredible plagiarism. In fact, the translation of a large part of Fedorov's *Optics of Anisotropic Media* and Chapter 4 of the *Theory of Gyrotropy* (1976) with the preservation of Fedorov's original notation was published by Chen in "his" book. At that time, it was impossible to prove Fedorov's authorship despite a number of publications to the effect in various Soviet and foreign sources. The second Fedorov's book written in co-authorship with V.V. Filippov entitled *Reflection and Refraction of Light by Transparent Crystals* was published in 1976.

In crystal acoustics, Fedorov created the general theory of elastic-wave propagation in media of an arbitrary symmetry. The results obtained made the basis of his monograph *Theory of Elastic Waves in Crystals* published in Moscow in 1965, then revised and published in New York in 1968. The Introduction to the American edition reads that the translation of the perfect treatise by Academician Fedorov into English is quite timely, that his consistent statement of all the aspects of this field of science is the most clear and directed straightforward to the goal. For his cycle of works on the theory of elastic waves, Fedorov was awarded the State Prize of the Belorussian SSR in 1972, the first prize in physics in Belorussia.

Within the general covariant approach developed by Fedorov, he created the unique mathematical basis for the description of all the types of elementary particles, their fundamental interactions, and the property of physical symmetry inherent in these particles. The main results obtained in this field are reflected in Fedorov's monograph *Lorentz Group* published in Moscow in 1979.

Fedorov published about 400 scientific works, including six large original monographs. His brilliant lectures delivered at the Faculty of Physics of the Belorussian State University up to the last days of his life always served an example and a standard of lecturer's skill. His scientific ideas, methods, and plans are being successfully developing by the scientific school of physicists created by him. He taught young scientists by personal example, his devotion to science, and his demands to himself and his work. More than 40 of his students became candidates and about 20, became doctors. Today, they themselves have students, Fedorov's scientific grandsons and great grandsons.

Fedorov always combined his scientific and research work with the dissemination of scientific knowledge. He was very active in the social sphere, was a member of the Directorship of the Soviet Peace Foundation, Member of the Soviet Commission on Gravitation, the editor-in-chief of the journal *Vestsi of the Belorussian Academy of Sciences*, member of the editorial boards of other scientific journals, the first President of the Belorussian Society of Physics, etc.

Despite his great activity in organization of science, Fedorov always remained an active researcher and a great theoretician who could not imagine a day without creative work. He continued working up to the last day of his life. He had the remarkable ability to work, enormous energy, and purposefulness. He died on October 13, 1994.

Fedorov achievements in science, scientific organization, pedagogical work, and social life were crowned by the award to him an honorary title of the Hero of Socialist Labor, Lenin Order (twice), Order of Red Banner of Labor, Order of Sign of Honor, etc. He was

also awarded the title of Honorary Scientist of the Belorussian SSR.

Fedorov was universally educated, he knew literature and art, wrote verses, played piano and chess, and loved sport.

Numerous colleagues and students will always remember Fedorov as a gifted scientist and an outstanding organizer of science, a benevolent man, and a wonderful teacher.

Translated by L. Man

INFORMATION

Thirteenth International Conference on Crystal Growth and Molecular Beam Epitaxy

Thirteenth International Conference on Crystal Growth and Molecular Beam Epitaxy

In the period from July 30 to August 4, 2001, the 13th International Conference on Crystal Growth and Molecular Beam Epitaxy was held in Kyoto, Japan. Altogether, about 1200 papers were presented to the Conference, i.e., by about 300 more than to the previous 12th Conference in 1998 in Jerusalem, Israel. The numbers of papers presented to the Conference by the participants from different countries are given in table.

All the communications were presented as posters. In addition, each participant was given 5 minutes for oral presentation. The Organizing Committee invited 100 official speakers, who were given a longer time for oral presentation.

Russia and the Ukraine were represented by large delegations (the second and the seventh largest delegations, respectively). Unfortunately, the quality of the papers presented by these countries can be only partly judged from the number of their invited speakers.

The representatives from China and India were extremely active. China is performing an active search for new materials, first of all, those for quantum electronics. Indian scientists presented mainly the studies on crystallization from solutions.

The Conference worked in twenty one sections. The greatest number of papers were dedicated to semiconductor crystals (250); growth of oxides and fluorides (180 papers). crystallization of films (about 190 papers), and the mechanism of growth and growth kinetics (about 100 papers). About 40 papers dealt with crystallization of proteins and colloidal particles, crystal growth under microgravity conditions, and new materials, of which two thirds were dedicated to nanostructures and organic semiconductors.

Almost all the theoretical papers considered particular problems in concrete substances. Great attention was given to the character of step motion on the surfaces which are in direct contact with the native vapors. Despite the widespread use of tunneling and atomic-

Number of papers presented to the 13th/12th conferences on crystal growth

Country	Number of papers*	Of them: invited papers**		
		Paper duration, min		
		40	30	15
Japan	569/90	2	35/8	12/38
Russia	138/159		0/1	1/22
USA	59/107	1	18/18	4/71
China	56/18			1/14
India	52/43			0/3
Germany	46/66	2	6/3	1/28
Ukraine	39/44			0/4
Korea	26/6			0/3
France	25/90		5/5	2/19
UK	20/30		2/5	0/12
Romania	18/18			0/2
Taiwan	16/7			0/4

Table (Contd.)

Country	Number of papers*	Of them: invited papers**		
		Paper duration, min		
		40	30	15
Netherlands	14/26		0/1	2/13
Israel	11/71		0/11	0/35
Hungary	11/11			1/4
Poland	11/13			0/2
Brazil	10/7			0/1
Spain	9/4		1/0	0/1
Singapore	9/4			2/0
Czech Republic	7/3			0/1
Australia	5/8			0/5
Armenia	4/5			0/2
Sweden	4/5			0/2
Switzerland	4/0	1/0	1/0	
Canada	3/4		1/0	0/2
Belarus, Belgium, Finland, Croatia, Yugoslavia: two papers from each country	10/34			
Austria, Argentina, Denmark, Bangladesh, Bulgaria, Italy, Tadzhikistan, Thailand, Turkey: one paper from each country	12/6			

* On average, each of the 100 participants presented 150 papers.

** At the 12th conference, each invited speaker was given 30 min. The duration of some of the oral presentations was 15 min.

force microscopy providing in some cases the visualization of elementary stages during crystal growth, no fundamentally new facts in the mechanisms of surface processes have been reported as yet.

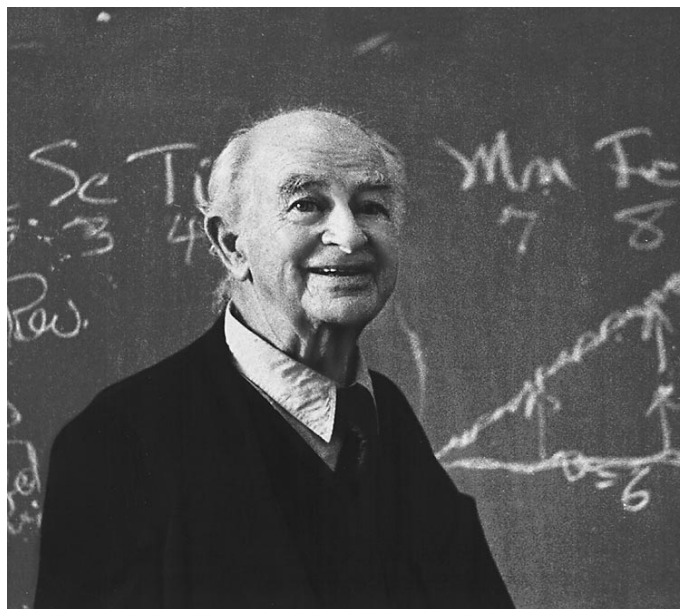
The Frank prize for the achievements in growth theory was awarded to D.T.J. Hurley (England) and S.R. Coriell (USA) for the quantitative description of the influence of convective flows and electric fields on crystal growth and morphological stability.

The Laudise prize was awarded to G. Mueller (Germany) for computer simulation of growth from melt and development of new growth technologies.

L. N. Rashkovich

Translated by L. Man

Linus Pauling, the Greatest Chemist of the 20th Century (On the Occasion of His 100th Anniversary)



This photograph was taken by L.A. Zasurskaya when L.C. Pauling visited the Chemistry Faculty of Moscow State University in 1983.

Linus Carl Pauling was born on February 28, 1901, at the very beginning of the 20th century, and died on August 19, 1994, when the main achievements of that last century were already outlined. Indeed, most of the important lines of the 20th century were intersected in the biography of this unique man.

Pauling was engaged in many different fields of science and was always at the forefront in solving the central problems, although he was not been right in every case. Sometimes, his enormous energy and temperament were somewhat excessive, but his participation in any discussion stimulated scientific progress—he knew how to make people think and work.

Pauling's major scientific achievement—his concept of a chemical bond—was developed in the late 1920s–early 1930s and was most completely stated in his famous book *The Nature of the Chemical Bond and the Structure of Molecules and Crystals*, first published in 1939. The second edition appeared in 1940 (additional copies of the second edition were also printed in 1942 and 1944). Since then, the book has repeatedly been printed and translated into dozens of languages. By the end of the 1940s, the book had received world recognition and for many years had served as the basis

of numerous courses of general, inorganic, and organic chemistry. It is hardly possible to find another book in the history of chemistry that had gained such popularity.

The first complete translation of the book into Russian was made by M.E. Dyatkina and was edited Ya.K. Syrkin under the title *The Nature of Chemical Bond* (Gostekhizdat, Moscow, 1947). The omission of part of the title (the words “and the Structure of Molecules and Crystals”) is unclear. The Pauling concept of chemical bond is still alive despite the fact that today it seems to be somewhat obsolete and even the expression “the nature of the chemical bond” is somewhat dubious, whereas *structural chemistry*, to which Pauling had made such a great contribution, is still being actively developed.

In 1954, the Nobel Committee awarded Pauling the prize in chemistry for “his research into the nature of the chemical bond and its application to the elucidation of the structure of complex substances.” In his Nobel lecture, Pauling said that future chemists would lean on new structural chemistry, including the exact geometrical relationships between atoms in molecules and the rigorous application of new structural principles and

that this methodology would ensure considerable new progress in the solution of biological and medical problems by chemical methods.

These words are remarkable for two reasons. In 1954, Pauling considered the widespread use in chemistry of rigorous quantitative structural data to be far-fetched.¹ Second, it is not the apparatus of quantum mechanics but the model structural representations that dominated in Pauling's vision of future chemistry.

Thus, in the late 1920s–early 1930s, the most important event in chemistry took place to a large extent due to Pauling insight and purposefulness.

Generally, it became clear why and how chemical bonds are formed. The basic studies in this field were performed by Heitler and London, who managed to interpret the formation of a hydrogen molecule, and by Born and Slater. Pauling extended these ideas to much more complicated systems and used them together with the concept of resonance as the basis of his theory.

Quantum chemistry (with its fantastic arsenal of new notions) came into being. Pauling's contribution to quantum chemistry was the development of the method of directed valence bonds, ideas of hybridization and overlap of atomic orbitals, and the concept of electronegativity of atoms and the partial ionic character of bonds. Simple and clear, many of these concepts are still successfully used (of course, with the stipulations of the existence of more rigorous, modern approaches). However, it should be taken into account that at almost the same time as Pauling's studies (or, probably, only slightly later), some other methods of quantum chemistry appeared, such as the method of molecular orbitals (developed by Lennard–Jones, Mulliken, and Hückel), which proved to be both more general and more accurate than the method of valence bonds.

Structural chemistry had come into being. It operated with model spatial concepts on the structure of atomic–molecular systems and differed from all the previous structural theories by the rigorous physical (or, more accurately, quantum-chemical) justification and the use of exact structural data obtained by the experimental physical methods. Being mainly a theoretician, Pauling constantly took part in the experimental studies as well; he started working in X-ray diffraction analyses at the dawn of his scientific career at the very beginning of the 1920s. Later, he also participated in electron diffraction experiments.

The first X-ray diffraction studies pioneered by W.H. Bragg and W.L. Bragg in 1913 and considerably developed in the 1920s were used as the basis for the development of crystal chemistry, which soon had become one of the best developed sections of structural chemistry and crystallography. W.L. Bragg (the son), Goldschmidt, and Pauling are justly recognized as the

founders of this science. Pauling created the system of crystallochemical radii (covalent, ionic, metal, and van der Waals), developed the principles for describing crystal structures in terms of the close packings of spheres or coordination polyhedra sharing the vertices, formulated the well-known electrostatic rule of valence for ionic crystals, and introduced the notion of a defect structure. All this material was complemented with new structural data and was stated in detail in the second edition of Pauling's book published in 1940 (translated into Russian in 1947).

The Second World War hindered the dissemination of Pauling's ideas but, nevertheless, by the middle of the century they had become widely known, although with a certain delay because, by this time, Pauling was deeply interested in other problems. He intuitively felt that the most essential achievements in chemistry of the 20th century would be associated with molecular biology and molecular medicine (the terms themselves appeared much later) and that it would be here that X-ray diffraction crystallography would find its most efficient application. Therefore, not losing his interest in quantum chemistry, whose development was under Pauling's guidance until the last days of his life, Pauling, with surprising courage and enthusiasm, started tackling biochemical problems.

From the mid-1930s up to 1951, the main objects of Pauling interest were proteins. In 1934, he made the first attempt (together with A.E. Mirsky) to draw some conclusions on protein structures based on the study of their biochemical functions. Later, he studied (together with C.D. Coryell) the effect of oxygenation on the magnetic properties of hemoglobin; in 1936, he started X-ray diffraction studies of amino acids and proteins at the California Institute of Technology. It was then that R.B. Corey *et al.* determined the crystal structures of some of the simplest amino acids. Yet, this was still far from the first structural determination of proteins.

The most successful research was made in immunology. In 1940, Pauling showed that antigens can perform the role of matrices providing for the folding of polypeptide chains, which resulted in the formation of specific antibodies instead of conventional globular proteins.² Thus, the instructive function of an antigen, which provides an infinite variety of antibodies synthesized by an organism, has been explained. The concept of mutual structural complementarity of an antigen and antibody was discussed in the article written by Pauling and Delbruck, an outstanding virologist and geneticist, who later was also awarded the Nobel prize.

In 1949, Pauling began to study sickle-cell anemia. The name of this hereditary and often lethal disease is explained by the fact that the erythrocytes of an infected person acquire a sicklelike shape and thus lose

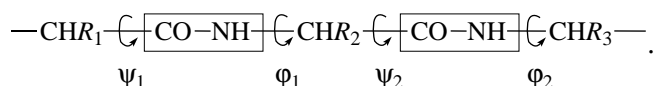
¹ It seems that even on the verge of the 21st century we still cannot say that structural concepts have finally taken their appropriate place in chemistry (P.M. Zorky, *Structural Chemistry at the Turn of the Century*, Russian Chemical Journal (in print)).

² It should be remembered that antigens are molecules and supramolecular formations, e.g., viruses, which are recognized by the organism as foreign and give rise to a certain immune response, in particular, the formation of antibodies.

the ability to transport oxygen. Pauling's incredible intuition led him to the assumption that the disease is carried in the break of the amino acid sequence in the polypeptide chain of hemoglobin, a protein providing oxygen transport in an organism. Three years later, Pauling, using electrophoresis, managed to single out normal and defect hemoglobins and proved that the structure of the defect hemoglobin has a "misprint": one of the aminoacid residues (that of the glutamine acid) is replaced by another (valine residue). Later, it was established that the molecule of human and higher animal hemoglobin consists of 574 amino acid residues in a rigorously defined sequence. As was revealed by Pauling, the replacement of only one of these residues results in an often mortal disease. Today, more than 50 varieties of anomalous hemoglobins giving rise to various pathological states have been discovered.

In 1951, an important event occurred—Pauling and Corey published their famous article on the structure of proteins, which summarized the experience gained over many years in this field. Using the X-ray diffraction data on various amino acids (the values of characteristic interatomic distances and valence angles and the values of van der Waals radii), Pauling and Corey performed the conformational analysis of the polypeptide chain, the basis of the structure of any protein molecule, and showed the following:

(1) The chain consists of relatively rigid plane CO-NH peptide units (formed due to coupling of amino acid residues) and linking CHR joints. The joining of two subsequent units can be characterized by the angles ψ and ϕ , which are the angles of rotation of the given chain link around the covalent C-C bond, and the angle ϕ of rotation of the subsequent C-N bond,



(2) It is sufficient to know the angles ψ and ϕ for each amino acid residue in order to describe the three-dimensional structure (conformation) of the main polypeptide chain.

(3) There are two advantageous methods for joining peptide units (with the characteristic values of angles ψ and ϕ); the periodic repetition of the first type of joining results in the formation of the α -helix, whereas the periodic repetition of the second type, to the extended β -structure in which the parallel β -strands are linked by hydrogen bonds into the β -sheet. The stabilization of the β -helix is also promoted by hydrogen bonds: the CO group of the n th amino acid residue is bound to the NH group of the $(n + 3)$ th residue.

At the same time, Pauling described four levels of structural description of the protein molecule: the *primary structure*, which describes the sequence of aminoacid residues; the *secondary structure*, which describes the presence and the ratio of the characteristic fragments such as the α -helix and the β -structure; the

tertiary structure, which reproduces the three-dimensional arrangement of atoms (or, at least, of aminoacid residues) given by their spatial coordinates; and the *quaternary structure*, which describes the presence of subunits (or subglobules forming the globulin molecules). These notions, which had been formulated prior to the first publication of the complete X-ray analysis of a protein, were soon confirmed by the structure determinations of hemoglobin made by Perutz and mioglobin made by Kendrew in 1960. Today, these notions form the basis for protein crystallography.

Not all the Pauling's scientific initiatives turned out to be successful. In the early 1950s, he tried to establish the general principle of the structure of a DNA molecule and published an article (1953) in which he mistakenly described it as a triple helix. However, Watson and Crick soon found the correct solution—the well-known double helix. They used to say that the fear of falling behind Pauling stimulated, to a large extent, their successful work.

In the late 1960s, Pauling became interested in the biological effect of vitamin C and soon began actively promoting this vitamin as a radical remedy against the common cold proceeding from his own and his wife's experience and even wrote the book entitled *Vitamin C, the Common Cold, and the Flu*. In the early 1970s, he formulated the concept of orthomolecular medicine, according to which vitamins and amino acids can create a specific optimal medium for the brain activity. These theories, once very popular, were not confirmed by subsequent studies and, to a large degree, were abandoned by experts in medicine and psychiatry. In 1979, Pauling published the book *Cancer and Vitamin C*, in which he stated that considerable doses of vitamin C would provide for a longer life and improve the condition of patients suffering from certain types of cancer. However, experts in cancer diseases have found his argument to be insufficiently grounded.

It seems that in this period, Pauling used insufficient facts and somewhat superficial concepts and recommendations, and it is a great pity that this resulted in the use of his name in commercial purposes and often in dubious and sometimes even unscrupulous propaganda of various drugs. However, one should not forget that the active life, enthusiasm, flame in the heart and eyes (see the photograph) still preserved to a rather old age by a man—who since the age of 38 suffered heavy chronic diseases—made one to believe that he really knew *How to Live Longer and Feel Better* (the title of Pauling's last book of 1986).

It is not accidental that we turn to Pauling's biography only at the end of this essay. The details of a scientist's life are too often considered at the very beginning of an article dedicated to his memory making one forget about the crux of the matter—the analysis of his scientific merits and his real scientific role. Still, it is impossible to pass over some unusual and, sometimes, even paradoxical facts of Pauling's life.

According to the questionnaire distributed to several hundred outstanding scientists of our time by the British *New Scientist*, Pauling is among the twenty greatest scientists of history along with Galileo, Newton, Darwin, and Einstein. At the same time, he is the only Nobel Prize winner who had not finished high school—he absolutely refused to attend the lectures on social disciplines, saying that all the necessary knowledge in this field he would be able to acquire by himself.

Another paradox is that Pauling, a great chemist-theoretician, whose level of knowledge in physics provided him the absolute trust of the most outstanding physicists of his time and who began his education at an agricultural college and graduated with a bachelor's degree in chemical technology. Later, at the age of 24, he graduated from the California Institute of Technology with a PhD in chemistry with distinction and a bachelor's degree in mathematical physics. The Guggenheim Fellowship allowed him to spend 1926–1927 in Europe, where he studied quantum mechanics under the guidance of Sommerfeld in Munich, Schrödinger in Zurich, Bohr in Copenhagen, and W.H. Bragg in London.

At the beginning of the Second World War, Pauling, called by his sense of duty, stopped his studies of proteins and started working for military purposes. He created several types of powerful explosives and rocket fuels, developed a special gauge for the oxygen content and an oxygen generator for submarines and aircraft (later, this apparatus was used to maintain the necessary oxygen content in capsules for prematurely born children and in surgical operations under anesthesia). Pauling's laboratory synthesized a substitute of the blood plasma for the emergency blood transfusion under field conditions. An outstanding contribution made by Pauling to the struggle against fascism had not passed unnoticed and in 1948, he was awarded the Presidential Medal for Merit.

In a time of peace, Pauling considered it his duty to struggle against the threat of a new war and the nuclear and radioactive threat to the environment; he waged this “war” with the energy and talent so characteristic of him.

Soon after the bombing of Hiroshima and Nagasaki, Pauling started a campaign against the use of this new type of weapon. Being a member of the National Security Council in 1945–1946, he delivered lectures against the danger of nuclear war. In 1946, he joined Einstein's Emergency Committee to inform the public about nuclear weapons. In 1957, he presented a petition to the UN with the requirement to ban nuclear tests, which was signed by more than 11 000 scientists from 49 countries, including more than two thousand Americans.

His active position as a peace maker often encountered various political obstacles, in particular, because of his allegedly pro-Soviet sympathies. In the early 1950s, he had to surmount considerable difficulties to

obtain a foreign passport. He obtained his passport without any limitations only upon being awarded the Nobel Prize.

In June 1961, Pauling and his wife Ava Helen Pauling convened a peace conference in Oslo, Norway, to prevent nuclear-weapons distribution. Soon afterwards, Pauling started the radiation survey, and in October 1962, he reported information that nuclear tests performed in 1961 alone doubled the level of radioactivity in the atmosphere in comparison with the preceding 16 years. He also wrote a draft on the agreement to ban such tests. In July 1963, the United States, Soviet Union, and Great Britain signed the agreement to ban of nuclear tests, which was based on the draft written by Pauling.

In 1962, Pauling was awarded the Nobel Peace Prize.

The merits of Linus Pauling are truly diverse and great, but the history of science will remember him first and foremost as the creator of quantum chemistry and, even more so, because he demonstrated his great wisdom and reserve during the celebration of his 90th birthday, when he exactly determined the place of quantum theory in modern chemical sciences.

“Chemistry has probably been fortunate in that a great amount of empirical knowledge about the properties of chemical substances had been obtained before the development of quantum mechanics. Chemists strove to understand these properties and, as a result, the classical structure theory of chemistry was developed. If the accumulation of large amounts of information about the properties of substances had not been gathered before quantum mechanics was formulated, it may well be that chemical structure theory would not have developed. In fact, at the present time, in 1991, little use is made by chemists of quantum mechanics except to the extent that the principles of chemical bond formation that were formulated on the basis of quantum mechanical principles are extensively used. Some use is made by chemists of accurate quantum mechanical treatments of molecular structure, but much more use is made of the chemical structure-theory model.”³

P.M. Zorky

*Head of Laboratory of Crystal Chemistry
of the Chemistry Faculty
of Moscow State University,
Doctor of Sciences (Chemistry), Professor*

Translated by L. Man

³ L. Pauling, *Foundations of Physics*, 1992, vol. 22, p. 829.

Dedicated to the 100th anniversary of Linus Pauling

Development of Pauling's Concepts of Geometric Characteristics of Atoms

S. S. Batsanov

Center of High Dynamic Pressures, Mendeleevo, Moscow oblast, 141570 Russia

e-mail: batsanov@gol.ru

Received June 25, 2001

Abstract—The evolution of the geometric characteristics introduced by Pauling and their dependence on the specific features of the structure and chemical bonds have been considered. The values of the covalent and van der Waals radii are given as well as their relationships and mutual transitions. © 2001 MAIK "Nauka/Interperiodica".

INTRODUCTION

The development of the methods of X-ray diffraction analysis gave rise to an increase of the radiation power, the reduction of exposures down to microseconds, the use of high and superlow temperatures, high and superhigh pressures, and the application of computers for collecting and processing experimental data and, as a result, to the revolutionary reduction of the total time necessary for complete structure determination.

At the first stage of the development of the X-ray diffraction analysis, it was difficult to collect experimental data, and the focus was made on the theoretical principles of the crystal structure formation and its dependence on the chemical composition of crystals and the thermodynamic conditions of crystal synthesis, which provided the optimization of the choice of the objects for studying and reduction of the bulk of calculations. This problem usually is solved by the most natural method of the structural chemistry—the representation of a molecule or a crystal as a system of interacting atoms. The main crystallochemical principles were formulated within the "atoms-in-molecules" method; even today, some of these principles have not lost their significance, although the progress achieved by quantum chemistry attributed new meaning to many classical concepts.

Linus Carl Pauling is one of the founders of structural chemistry. His hundredth anniversary is widely celebrated by scientists of many fields. Below, we consider the evolution of the notions and concepts first formulated by Pauling as well as the concrete values of some geometrical characteristics of atoms used to describe the structures of various substances and their chemical bonds.

Upon the establishment of the additive character of interatomic distances in crystals by W.G. Bragg, the next important step was made by Pauling, who considered the additive approach as a function of the type of the chemical bond. Thus all the atomic radii were divided into metal, covalent, ionic, and van der Waals radii. Below, we consider the covalent characteristics of atoms and their relation to other types of atomic radii.

Of course, today, some approaches used by Pauling look insufficiently justified theoretically; however, as he wrote in *The Nature of Chemical Bond and the Structure of Molecules and Crystals*, it is better to predict something with uncertainty than not to predict it at all. And indeed, even today, the synthesis of new substances and materials is developed based on the "atoms-in-molecules" approach, whose theoretical aspect was successfully developed by Bader [1].

Some structural correlations established by Pauling have not been interpreted until recently. In this respect, Pauling's scientific heritage should be studied further.

COVALENT RADII

Prior to consideration of the experimental material, we have to refine the terminology. A covalent radius is one-half of the bond length $A-A$. Since this value is essentially less than the peripheral (van der Waals) atomic dimension and since, for multiple bonds, the section of the σ -bond is less than the diameter of the π -cloud, a covalent radius is not a scalar but a vector. This should be remembered, e.g., when considering the dependence of the energy of carbon bonds on their length—with a decrease of the C–C bond length with the bond multiplicity, the bond strength (strength per bond) does not increase but decreases.

Half of the distances in diatomic molecules with a σ -bond (between atoms with the coordination number N_c equal to unity) are called the normal covalent radius r_1 ; half of the interatomic distance in the diamond structure is called a tetrahedral radius r_{tet} ; whereas half of the interatomic distance in the structures of the β -Sn type, an octahedral covalent radius r_{oc} . Since r_1 corresponds to a single bond, it is obvious that for the elements of group 4, $r_1 = r_{tet}$.

The systems of tetrahedral and octahedral radii were first calculated by Huggins [2] and Pauling [3]. The values of the tetrahedral radii of non-metal atoms were equal to or were even slightly less than the normal covalent radii, whereas those for metal atoms were larger than those. This difference in the dimensions of metal and non-metal atoms with an increase of the coordination number N_c becomes understandable if one takes into account that the bond length depends on the electron density. Thus, for typical metal atoms, the number of outer electrons ≤ 4 , for nonmetal atoms, ≥ 4 . The transition from $N_c = 1$ to 4 in the first case is accompanied by a decrease of the number of valence electrons per bond, whereas in the second case, the electron density of a bond remains unchanged.

At the beginning, the tetrahedral and the octahedral radii were used to consider different objects; r_{tet} was used for the compounds of the metals of the b subgroups (and Be) possessing tetrahedral structures, whereas r_{oc} , for the derivatives of the a elements (except of Be) which, under the normal thermodynamic conditions, form the structures with $N_c = 6$. However, in connection with the studies of polymorphous transformations at high pressures and temperatures and the studies of films grown on crystalline substrates having the structures different from those of the films, it became necessary to determine the r_{tet} radii for the elements of the a subgroup and the r_{oc} radii for the elements of the b subgroup. This was made by Van Vechten and Phillips [4] who calculated r_{tet} and r_{oc} for the same elements and established the equivalence of these radii in the $\text{Si} \rightarrow \text{Cl}$, $\text{Cu} \rightarrow \text{Br}$, and $\text{Ag} \rightarrow \text{I}$ series. They interpreted this equivalence by the compensation of a radius decrease by an increase of the effective charge of the nucleus, Z^* , because of the more pronounced mutual repulsion of electron pairs in the valence shell of an atom with an increase of the number of the group in the period.

The experimental studies of electron density for O–O [5] and the theoretical studies of electron density for (F–F) [6] bonds showed that the covalent F–F, O–O, and N–N bonds had no maximum on the line “connecting” the atoms, but, at the periphery, the electron density was excessive. This fact corresponds to the antibonding character of valence orbitals in an F_2 molecule, which provides a drastic increase of bond strength at positive ionization [7]. It was shown [8] that the allowance for this fact leads to the normal covalent radii

0.77 Å for F and O and 0.76 Å for N, which practically coincides with the carbon radius in diamond (in accordance with the conclusions made by Van Vechten and Phillips). At the same time, the Pauling and Phillips tetrahedral radii are different. Thus, for Cl, Br, and I they are 0.99 and 1.127, 1.11 and 1.225, 1.28 and 1.405 Å, respectively, whereas for Mg, Zn, and Cd, 1.40 and 1.301, 1.31 and 1.225, and 1.48 and 1.405 Å, respectively.

These discrepancies are explained by different goals of calculation of these radii. Initially, the systems of radii were calculated to “reproduce” the bond length by the additive methods. Later, the same radii were calculated for pure covalent compounds with the aim of their further use in the theoretical estimates. Often, the values obtained by both methods were either the same or very close. However, if the bonds in the compound used for additive calculations are not purely covalent, it is necessary to introduce the corresponding corrections. Schomaker and Stevenson [9] were the first to pay attention to this fact. They suggested to calculate the heteronuclear-bond length d_{AB} by the equation

$$d_{AB} = r_A + r_B - a\Delta\chi_{AB}, \quad (1)$$

where $a = 0.09$, r_A and r_B are covalent radii of the atoms A and B , and χ is electronegativity. A similar expression was also obtained in [10].

The above equation allows one to understand why the atomic radii calculated for elements forming the most polar bonds (F, O, and N) by additive methods are shorter than their covalent radii. For organogenic elements with $\chi = 2.5 \pm 0.5$, the “additive” and the experimental radii practically coincide, but in the transition to metals with low electronegativities which form polar bonds with these elements, the situation is considerably different. Therefore different systems of normal covalent atoms show a considerable scatter in the radii for the same elements [11–19] depending on the data used and the assumptions made in their calculations.

The whole experimental material was analyzed in [13, 17, 19], and the new values of covalent radii of the elements were determined directly from the interatomic distances in homonuclear molecules, simple bodies, and compounds containing the A_2 radicals; the additive method was applied only to the data on alkyl derivatives and metal hydrides, because only methyl (of all the monovalent ligands) and hydrogen possess the minimum electronegativity. Taking into account that the covalent radii of carbon (0.767 Å) and hydrogen (0.371 Å) are shorter than those for metals and that their compounds with C and H the latter have a negative charge (which compensates the decrease in their dimensions), the reduction of the polar bond length in comparison with the covalent bonds can be attributed to metals. Then, the covalent radii of metals should be equal to the difference in the bond lengths $d(M\text{--}CH_3)$ and $r(C)$ or $d(M\text{--}H)$ and $r(H)$ plus the Schomaker–Stevenson correction for bond polarity.

Table 1. Normal (upper rows) and crystal (lower rows) covalent radii of elements (in Å) (for hydrogen $r = 0.37$ and $r_{tet} = 0.42$ Å)

Li	Be	B	C	N	O	F			
1.34	0.98	0.85	0.77	0.73	0.73	0.71			
1.56	1.07	0.89	0.83	0.77	0.80	0.80			
Na	Mg	Al	Si	P	S	Cl			
1.65	1.42	1.29	1.18	1.11	1.03	0.99			
1.85	1.56	1.34	1.25	1.15	1.09	1.08			
K	Ca	Sc	Ti	V	Cr	Mn	Fe	Co	Ni
2.00	1.73	1.44	1.35	1.31	1.32	1.28	1.31	1.24	1.20
2.22	1.87	1.54	1.40	1.40	1.41	1.37	1.44	1.37	1.35
Cu	Zn	Ga	Ge	As	Se	Br			
1.12	1.23	1.25	1.22	1.23	1.19	1.14			
1.32	1.33	1.29	1.29	1.27	1.25	1.23			
Rb	Sr	Y	Zr	Nb	Mo	Tc	Ru	Rh	Pd
2.12	1.89	1.62	1.53	1.36	1.33	1.34	1.31	1.27	1.30
2.35	2.02	1.71	1.59	1.46	1.39	1.40	1.37	1.32	1.36
Ag	Cd	In	Sn	Sb	Te	I			
1.27	1.36	1.45	1.40	1.43	1.40	1.33			
1.46	1.46	1.49	1.46	1.46	1.46	1.42			
Cs	Ba	La	Hf	Ta	W	Re	Os	Ir	Pt
2.31	1.97	1.69	1.50	1.42	1.36	1.31	1.29	1.29	1.30
2.51	2.12	1.79	1.56	1.51	1.42	1.37	1.34	1.34	1.36
Au	Hg	Tl	Pb	Bi	Po	At			
1.24	1.33	1.48	1.47	1.50	1.43	1.43			
1.42	1.43	1.52	1.53	1.53	1.49	1.49			

The upper rows in Table 1 indicate the averaged (over the data for A_2 molecules and the $A-H$ and $A-CH_3$ bonds) values of the normal covalent radii of elements. It should be indicated that the additive radii of monovalent metals agree quite well with the experimental data determined from the bond lengths in A_2 (with the only exception being sodium), whose additive radius exceeds the experimental value by more than 0.1 Å, which can be explained by the participation of p -electrons in sodium bonding (the covalent radius of Na for p -electrons is by 0.25 Å larger than for the s -state [18]). The covalent radii were also determined with the use of the single radii by the Pauling method [20]. In the latter case, the tetrahedral and octahedral radii of metals were calculated from the normal covalent radii by introducing the correction for an increase in the coordination number according to the equation [21]

$$d = d_0 - A \log V, \quad (2)$$

where d_0 is the length of the bond with the unit valence (the σ -bond), A is the constant equal to 0.71 for covalent bonds, V is the ratio of the valence v to N_c or,

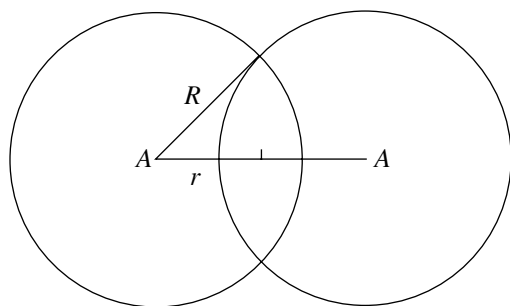
according to the equation [21]

$$d = d_0 - b \ln V, \quad (3)$$

where $b = 0.37$. The latter equation can be obtained from the Morse function, which describes the dependence of energy on the chemical bond length [23].

For the elements of 4b–7b subgroups, the tetrahedral radii are taken to be normal or are calculated by the additive method with the use of r_{tet} of metals. Taking into account that the Brown–Altermatt corrections [22] exceed the Pauling corrections [21] by a factor of 1.2 and that the Pauling and the Phillips radii differ by ~10%, it is clear that one has to develop an objective method for determining covalent radii for differently coordinated atoms.

An increase of an atomic covalent radius with the number of its ligands is provided by the constancy of the number of valence electrons given up by this atom for the formation of chemical bond. This requires the separation of atoms with an increase of their coordination number N_c , so that the total region of the overlap of electron clouds would not be changed. Proceeding from



Geometrical scheme of formation of an A_2 molecule. R is the van der Waals radius and r is the covalent radius (one-half of the bond length).

this principle, one can calculate the tetrahedral and the octahedral radii by the pure geometric method.

Let diatomic $A-A$ bond be formed as a result of the overlap of two isolated A atoms spaced by the distance equal to the sum of the covalent radii (figure). Denoting the radius of an isolated atom by R and the covalent radius by r , we arrive at the region of overlap of two atomic spheres equal to

$$\Delta V_1 = \frac{2}{3}\pi(R-r)^2(2R+r), \quad (4)$$

where subscript 1 indicates the number of bonds. If this number increases, whereas the number of valence electrons per atom remains unchanged, then, under the assumption of the constant electron density of the atom at the periphery, we arrive at the redistribution of the valence-electron cloud as a result of structural transformations in the form

$$\Delta V_1 = 2\Delta V_2 = 3\Delta V_3 \dots \quad (5)$$

The experimental data show that under such transformations, an elongation of the intramolecular bonds gives rise to a decrease of the dimension of the peripheral part of the atom [24, 25]. Thus, Eq. (5) can be rewritten as

$$(R_1 - r_1)^2(2R_1 + r_1) = n(R_n - r_n)^2(2R_n + r_n), \quad (6)$$

where the numerical subscripts indicate the changed values of the radii. The above expression is valid for monovalent atoms. For polyvalent atoms, instead of the number of bonds n , one has to take the ratio $N = n/v$. If the law of the R variation with the change in N is known, one can also determine r_n . In the first approximation, one can assume that R increases proportionally to an increase in r , i.e., that $R_N = \gamma R_1$, where $\gamma = r_N/(2r_N - r_1)$. Then the computational formula takes the form

$$(R_1 - r_1)^2(2R_1 + r_1) = N(\gamma R_1 - r_N)^2(2\gamma R_1 + r_N). \quad (7)$$

Thus, knowing r_1 and R_1 , one can calculate the r_N values for all the elements. The r_{tet} and r_{oc} values for the elements of the a -subgroups in the group valence calculated from the normal covalent radii r_1 are listed in

Table 1 and the radii of isolated atoms [26] are listed in the lower rows of the same table.

For crystal structures of the elements of the b -subgroups with $N_c = 4$ or 6, the chemical bonds are formed not only by valence electrons but also by lone pairs of electrons (the donor-acceptor interaction). To evaluate their contribution to the bond covalence, the following relationship was suggested [27]:

$$\Delta q = 1 - (IP - EA)/(IP + EA), \quad (8)$$

where IP and EA are the ionization potential and the affinity of an atom to electron. The value calculated by Eq. (8) should be added to the normal valence to yield the corresponding v_{cr} value for the crystal

$$v_{cr} = [v + \Delta q(N_c - v)]/v. \quad (9)$$

Since all the bonds in a regular tetrahedron or an octahedron are equal, the electron densities at the valence and the donor-acceptor interactions between the atoms are averaged, which is taken into account by dividing the total valence of an atom by v . Multiplying v_{cr} by the left-side part of Eq. (7), we obtain the change in the atomic radius with due regard for the participation not only of valence electrons but also of lone pairs of electrons. In a similar way, one can calculate a covalent radius of an atom in lower oxides, where the outer shell of an atom has electrons taking no part in bonding, e.g., for Fe^{II} , Sb^{III} , Pt^{IV} , etc. It is in this way that the tetrahedral and the octahedral covalent radii listed in Table 1 were calculated. All these values are intermediate between the values obtained by the Pauling and the Brown-Altmett methods for metals and by the Pauling and the Phillips method for non-metals.

The covalent radii of atoms in multiple bonds were determined from the lengths of π -bonds in homonuclear A_2 molecules or the analogous fragments in crystalline compounds [13, 17, 18, 26, 28, 29]; their averaged values are listed in Table 2 for the same valence states of atoms as in Table 1.

VAN DER WAALS RADII

An important geometric characteristic of an atom forming covalent bonds is its peripheral size along the direction of the chemical bond—the so-called intermolecular or van der Waals radius R . Although this notion was introduced by Magat [30] and Mack [31] only in 1932, the term itself and the first table of van der Waals radii were suggested by Pauling in his famous book [20]. The development of this concept is not considered here, and we send the reader to the review article to the effect [32]. Here, we only briefly characterize van der Waals radii and their relation to covalent radii of atoms.

First of all, it should be indicated that the system of van der Waals radii of organogenic atoms given by Pauling still in the first edition of *Nature of Chemical Bond and the Structure of Molecules and Crystals* (1939) has not lost its significance which is confirmed

by the following data:

	H	F	Cl	Br	I	O	S	N	C
Pauling (1939)	1.2	1.35	1.80	1.95	2.15	1.40	1.85	1.5	1.70 Å
Bondi (1964)	1.20	1.47	1.75	1.85	1.98	1.52	1.80	1.55	1.70 Å
Zefirov (1974)	1.16	1.40	1.90	1.97	2.14	1.29	1.84	1.50	1.71 Å
Gavezotti (1983–1999)	1.17	1.35	1.80	1.95	2.10	1.40	1.85	1.50	1.70 Å

Table 2. Covalent radii (in Å) of atoms with multiple bonds

A	r_{\equiv}	r_{\equiv}	A	r_{\equiv}	r_{\equiv}	A	r_{\equiv}	r_{\equiv}	A	r_{\equiv}
B	0.76	0.68	N	0.625	0.55	Cr	1.24	1.11	F	0.54
Al	1.28		P	1.00	0.93	Mo		1.13	Cl	0.89
C	0.67	0.60	As	1.11	1.05	W	1.255	1.15	Br	1.04
Si	1.07	1.00	Sb	1.31	1.17	O	0.605		I	1.23
Ge	1.13	1.06	Bi		1.33	S	0.94	0.87	Fe	1.17
Sn	1.32		V		1.19	Se	1.08		Co	1.16
Ti		0.97	Nb	1.36		Te	1.28		Ni	1.14
			Ta	1.37		Mn	1.22		Ru	1.17
						Tc	1.09		Os	1.08
						Re	1.19	1.13	Pt	1.17

However, until recently, the corresponding information for metals (for which molecular structures with a metal atom “open” for contacts are rather rare) has been insufficient and contradictory. Therefore the radii R for metals were estimated indirectly, in particular, using the Pauling formula [20]

$$R = r + 0.8 \text{ \AA}. \quad (10)$$

This equation and the invocation of crystallochemical and quantum mechanical considerations provided the calculation of van der Waals radii of all the elements of the Periodic System [13], although the substantiation of the Pauling equation (10) had been a problem for quite a long time.

It was shown [33] that the representation of diatomic $M-X$ bond as a superposition of two isolated (van der Waals) radii of the M and X atoms centered at the experimental interatomic distance d_{MX} yields the equation

$$R_M = (R_X^2 + d_{MX}^2 - 2d_{MX}r_X)^{1/2}. \quad (11)$$

In the first approximation, $d_{MX} = r_M + r_X$ and $r_M \approx r_X$, then, for a tetrahedral structure, we have

$$R = [d^2 + (0.8166d)^2 - 2dr]^{1/2} = 1.633r. \quad (12)$$

Since the average value of the covalent radii of the organogenic atoms is 1.2 Å, we obtain $R - r = 0.633 \times 1.2 = 0.76 \text{ \AA}$.

Equation (10) can also be derived in another way. Considering the transformation of a diatomic molecule

into the structure of monatomic metal (in terms of crystallography, an increase of the coordination number from 1 to 12), Batsanov [34] found that, according to Eqs. (2) and (3), the covalent radius should increase by 0.324 or 0.460 Å, respectively. Since the phase transformation results in the structure with equal interatomic distances, an increase of r in comparison with its value in a molecular structure should be accompanied by a decrease in R . Assuming that the scales of the changes of the covalent and the van der Waals radii are the same, we can conclude that the structural transformation of the *molecule-metal* type should result in the maximum changes in the atomic radii such that $R = r + 0.648/0.920$ or $R - r = 0.78 \pm 0.15 \text{ \AA}$.

CONCLUSION

The above systems of atomic radii were widely used to describe the structures of various molecules and crystals and also to characterize electronegativities of atoms. However, with the progress in the computational chemistry, some of Pauling's idea were considered to be somewhat obsolete, and many scientists came to the conclusion that the fixed values of covalent and van der Waals radii fail to characterize the real situation in principle, because it was proved experimentally that the transition from covalent to van der Waals distances for the same atoms in different structures was practically continuous [35–37]. To interpret this phenomenon, numerous new terms were used such as specific interactions [38], secondary bonds [39], new type of atomic

interactions that cannot be described within the classical theory of chemical bond [40], a new theory of strong interaction between atoms with closed electron shells [37], etc. However, there is no need for new terms and theories, because the experimentally observed changes in the distances are quite clear in terms of crystal chemistry and can be quantitatively described with the use of Eqs. (2) and (3).

When considering the whole spectrum of interatomic distances, one often ignores the fact that each shortened intermolecular distance always has the corresponding elongated intramolecular bond, whence follows the conclusion that when molecules are approaching, they can form ever stronger chemical bonds due to the change in the position of the electron cloud from the valence orbitals toward the intermolecular space [41]. Therefore, the lengths of shortened van der Waals contacts and elongated covalent bonds are mutually related. Zachariassen [42] was the first to pay attention to this fact, then his study was followed by the investigations performed by Bürgi [43, 36], Dubler and Linowski [44], and O'Keeffe and Brese [14, 15]. It was shown [45] that in the $I \cdots I \cdots I$ and $S \cdots S \cdots S$ systems, Eq. (3) and the known bond elongation can be used to obtain the values of shortened distances within the average errors of 0.03 and 0.02 Å, respectively.

It can readily be seen that the assumption about the transformation of a van der Waals bond into a covalent one because of the charge transfer is well justified. The change in the covalent bond in a I_2 molecule during the formation of the symmetric $I \cdots I \cdots I$ system is equivalent to that following from Eq. (3) if the coordination number of the central iodine atom increases from 1 to 2 ($V = 0.5$). The variation in the distances in $O-H \cdots O$ -type hydrogen bonds was considered in terms of Eq. (3) in [42, 14, 15]. The formation of the symmetric system of these and other types of hydrogen bonds corresponds to the change in the distances with an increase of the coordination number of hydrogen from 1 to 2. The variations in the long and short interatomic distances in the $Cl \cdots Sb-Cl$ system also result in the formation of symmetric 2.60 Å-long bonds, which corresponds to $V = 0.5$ [45].

Thus, the formation of a symmetric three-center system from the covalent and van der Waals bonds is analogous to the transformation of the end-bond into the bridge one in the process of molecule dimerization, $AX_n \longrightarrow A_2X_{2n}$, i.e., to an increase of the covalent bond length by ~ 0.13 Å and a decrease of the van der Waals bond length by ~ 0.67 Å (with due regard for the fact that $R - r = 0.80$ Å). All the variations in the interatomic distance recorded up to now occur within these intervals (doubled in the transition from a radius to the bond length).

Pauling not only established the relation between the covalent and van der Waals radii, but also showed that the normal covalent radii can be used to obtain metal radii by introducing the corrections for the coordination

and that the van der Waals radii are equivalent to the anionic ones. He derived the cationic radii from the experimental interatomic distances in crystals with the use of the values of the so-called effective charges of atomic nuclei. Thus, the whole set of geometric characteristics of atoms turned out to be mutually dependent and determined by the same characteristic—the electronic structure of an atom. Any application of these radii should take into account this fundamental fact.

Batsanov [45] showed that the crystallochemical approach can be used to evaluate the pressures under which molecular substances are compressed so that the covalent and van der Waals distances are leveled, i.e., the substance is transformed into the structure of a monatomic metal. In the cases, where such leveling results in elongation of a covalent bond beyond the existence range of bonds of the given type, the baric disproportioning of the substance takes place. For carbon-containing molecules having no bonds of multiplicity 0.5, the decomposition of the compressed substances under high pressures is accompanied by separation of carbon in the form of diamond. This transformation under high dynamic pressures occurring during detonation of explosives has already implemented on an industrial scale for aromatic and aliphatic hydrocarbons, nitrocompounds, and other organic substances. The thus produced material called “detonation diamond” can be considered as one of the practical application of Pauling's crystallochemical concepts.

Estimating Pauling's contribution to science, one can state that, in fact, he created the crystallochemical language. Bond polarity and multiplicity, hybridization, systematics of atomic radii, effective charges of atomic nuclei, optical and magnetic manifestations of chemical bonding, additivity of bond energy and deviation from it due to bond polarity, thermochemical electronegativity and the principle of electrical neutrality of atoms in stable molecules and crystals are widely used by chemists and crystallographers and are not only the means of describing various phenomena but also the means of their visualization. Thus, it is not surprising that Pauling is the most cited scientist in the world. The third edition of his main book *Nature of Chemical Bond and the Structure of Molecules and Crystals* is cited by more than 1000–1300 scientists each year, not mentioning the enormous number of references in numerous publications not referred to by the *Science Citation Index*.

His many-sided activities, outstanding achievements in various fields of the natural science, romanticism and humanism (he was awarded the Nobel Prize in Chemistry, the Nobel Peace Prize, and also the Lenin Peace Prize) brought him to forefront with the greatest representatives of the world culture. Although Pauling's activities belong to the entire world, including our country, we have to remember here that Pauling's theoretical concepts were severely criticized in our country

(the "struggle against the resonance theory"). Formally, the campaign was directed against the approximate character of the method of valence bonds and the concept of electronegativity. Suggesting nothing themselves, his critics considerably hindered the application and the development of these methods in our country. But as usual, time has brought everything into the proper place. Pauling's methods, including the concept of electronegativity, are now widely used in structural and physical chemistry, whereas the critics of these concepts are hardly remembered at all. They themselves try to forget and hide their useless attempts to cast a shadow on the ideas of a genius of the 20th century—Linus Carl Pauling.

REFERENCES

1. R. W. F. Bader, in *International Series of Monographs on Chemistry*, Vol. 22: *Atoms in Molecules: A Quantum Theory* (Clarendon, Oxford, 1994), p. 438.
2. M. L. Huggins, *Phys. Rev.* **28**, 1086 (1926).
3. L. Pauling and M. L. Huggins, *Z. Kristallogr.* **87**, 205 (1934).
4. J. A. van Vechten and J. C. Phillips, *Phys. Rev. B* **2** (6), 2160 (1970).
5. J.-M. Savariault and M. S. Lehman, *J. Am. Chem. Soc.* **102** (4), 1298 (1980).
6. K. L. Kunze and M. B. Hall, *J. Am. Chem. Soc.* **108** (17), 5122 (1986).
7. S. S. Batsanov, *Experimental Principles of Structural Chemistry* (Standarty, Moscow, 1986).
8. S. S. Batsanov, *Izv. Akad. Nauk SSSR, Ser. Khim.*, No. 5, 467 (1989).
9. V. Schomaker and D. P. Stevenson, *J. Am. Chem. Soc.* **63** (1), 37 (1941).
10. S. B. Zhang, M. L. Cohen, and J. C. Phillips, *Phys. Rev. B* **38** (17), 12085 (1988).
11. R. T. Sanderson, *J. Am. Chem. Soc.* **105** (8), 2259 (1983).
12. Y.-R. Luo and S. W. Benson, *J. Phys. Chem.* **93** (21), 7333 (1989).
13. S. S. Batsanov, *Zh. Neorg. Khim.* **36** (12), 3015 (1991).
14. M. O'Keeffe and N. E. Brese, *J. Am. Chem. Soc.* **113** (9), 3226 (1991).
15. M. O'Keeffe and N. E. Brese, *Acta Crystallogr., Sect. B: Struct. Sci.* **48** (2), 152 (1992).
16. R. J. Gillespie and I. Hargittai, *The VSEPR Model of Molecular Geometry* (Allyn and Bacon, Boston, 1990; Mir, Moscow, 1992).
17. S. S. Batsanov, *Izv. Akad. Nauk, Ser. Khim.*, No. 12, 2349 (1995).
18. D. Bergman and J. Hinze, *Angew. Chem. Int. Ed. Engl.* **35**, 150 (1996).
19. S. S. Batsanov, *Zh. Neorg. Khim.* **43** (3), 501 (1998).
20. L. Pauling, *The Nature of the Chemical Bond and the Structure of Molecules and Crystals* (Cornell Univ. Press, Ithaca, 1939, 1st ed.; 1960, 3rd ed.).
21. L. Pauling, *J. Am. Chem. Soc.* **69** (3), 542 (1947).
22. I. D. Brown and D. Altermatt, *Acta Crystallogr., Sect. B: Struct. Sci.* **41** (4), 244 (1985).
23. H.-B. Bürgi and J. D. Dunitz, *J. Am. Chem. Soc.* **109** (10), 2924 (1987).
24. S. S. Batsanov, *J. Phys. Chem. Solids* **53** (2), 319 (1992).
25. S. S. Batsanov, *J. Phys. Chem. Solids* **58** (3), 527 (1997).
26. N. L. Allinger, X. Zhou, and J. Bergsma, *J. Mol. Struct.: THEOCHEM* **312**, 69 (1994).
27. S. S. Batsanov, *Structural Refractometry* (Vysshaya Shkola, Moscow, 1976).
28. J. Paolini, *J. Comput. Chem.* **11** (10), 1160 (1990).
29. F. A. Cotton and R. A. Walton, *Multiple Bonds between Metal Atoms* (Clarendon, Oxford, 1993, 2nd ed.).
30. M. Magat, *Z. Phys. Chem. Abt. B* **16** (1), 1 (1932).
31. E. Mack, *J. Am. Chem. Soc.* **54** (8), 2141 (1932).
32. S. S. Batsanov, *Neorg. Mater.* **37** (9), 1031 (2001).
33. S. S. Batsanov, *J. Mol. Struct.: THEOCHEM* **468**, 151 (1999).
34. S. S. Batsanov, *Zh. Neorg. Khim.* **46** (9), 1519 (2001).
35. H. A. Bent, *Chem. Rev.* **68** (5), 587 (1968).
36. H.-B. Bürgi, *Angew. Chem.* **87** (13), 461 (1975).
37. P. Pyykkö, *Chem. Rev.* **97** (5), 597 (1997).
38. A. É. Masunov and P. M. Zorky, *Zh. Strukt. Khim.* **33** (3), 105 (1992).
39. M. A. Porai-Koshits, G. A. Kukina, Yu. N. Shevchenko, and V. S. Sergienko, *Koord. Khim.* **22** (2), 83 (1996).
40. L. G. Kuz'mina, *Koord. Khim.* **25** (9), 643 (1999).
41. K. Takemura, S. Minomura, O. Shimomura, *et al.*, *Phys. Rev. B* **26** (2), 998 (1982).
42. W. H. Zachariasen, *Acta Crystallogr.* **16** (5), 385 (1963).
43. H.-B. Bürgi, *Inorg. Chem.* **12** (10), 2321 (1973).
44. E. Dubler and L. Linowski, *Helv. Chim. Acta* **58** (8), 2064 (1975).
45. S. S. Batsanov, *Zh. Fiz. Khim.* **75** (4), 754 (2001).

Translated by L. Man

Dedicated to the 100th anniversary of Linus Pauling

A Comparative Analysis of Quantitative Ratios in Formulas of Chemical Compounds and Twins

N. L. Smirnova

Moscow State University, Vorob'evy gory, Moscow, 119899 Russia

e-mail: snl194@mail.ru

Received February 12, 2001

Abstract—A comparative analysis is performed for the distribution and the frequency of occurrence of the quantitative ratios between the chemical coefficients of binary chemical compounds, symbols of twinning faces, etc. Comparison is carried out using the modified Weiss–Goldschmidt prognostic ranked scheme. It is demonstrated that the Pauling parsimony law is combined with the Goldschmidt complication principle.
© 2001 MAIK “Nauka/Interperiodica”.

The composition of chemical compounds can be described qualitatively and quantitatively. In 1922, Aleksei Vasil'evich Shubnikov [1] first proposed a theoretical determination of the possible compositions of chemical compounds. He determined the compositions of binary chemical compounds from the ratios between the multiplicities of the space groups of symmetry. It was found that the number of variants for chemical compositions of binary compounds in which the *A* and *B* atoms each occupy only one position is equal to 13.

The purpose of the present work was to establish a correspondence between the compositions of binary chemical compounds, Shubnikov's compositions, symbols of twinning faces, etc.

For a binary compound A_mB_n , the ratio between the chemical coefficients $m : n$ can be represented in the condensed form as mn . The values of m and n can be obtained both from the chemical formulas and from the structural data. The compositions determined in these two ways do not necessarily coincide with each other, because the occupancy of atomic positions can be less than unity. In the present work, the formulas under consideration were derived only from the structural data. A total of 1054 structural types taken from [2] were analyzed and 1054 mn compositions were determined, of which only 137 compositions were different.

Analysis of these compositions was performed using a modified scheme based on the Weiss–Goldschmidt principle [3]. This scheme involves two initial simplest ratios, namely, $1 : 0$ and $0 : 1$. For brevity, these ratios are written as the simplified formulas 10 and 01, where 1 and 0 are the indices. A simple term-by-term summation of the formulas 10 and 01 gives the formula of a new step, viz., 11. The summation of the ratios 11 and 01 results in the formula 12 at the center of the

scheme (Fig. 1), the summation of 11 and 12 leads to the formula 23 at the left of the scheme, and the summation of 12 and 01 yields the formula 13 at the right of the scheme. By analogy, a term-by-term summation of the symbols gives a bar graph of all binary ratios (Fig. 1). In the bar graph, we present only the points corresponding to the ratios between the coefficients of the *A* and *B* atoms. The ratios encountered in ten and more structural types are shown by large open circles, the ratios attributed to three–nine structural types are depicted by medium open circles, and the ratios found in one or two structural types are represented by small open circles. Intermediate nonrealized ratios are designated by closed circles.

The formulas form arithmetic sequences which are characterized by the differences between the first terms. The longest sequence is represented by the following terms: 11, 12, ..., 1.48. This sequence can be written as 11(01), where the difference is equal to 01. In this sequence, the first terms 1–13 are realized (the fused part) and the next range of terms involves both realized and nonrealized formulas (the “beaded” part). The values of m and n are given only for certain ratios. The other ratios can be obtained from the first terms by consecutive addition of the differences when going along the sequence. For example, by adding 14 to the formula 15, we obtain 29, 3.13, 4.17, etc. This scheme involves all 13 Shubnikov's theoretical binary ratios: 11, 12, 13, 14, 16, 18, 1.12, 1.16, 1.24, 1.48, 23, 34, and 38. Virtually all these ratios are revealed in chemical compounds.

In addition to the ratios of the coefficients taken from [2], Fig. 1 shows the ratios of cation coefficients for 60 formulas of the minerals discovered recently [4]. For the cation coefficients, there are binary, ternary, and

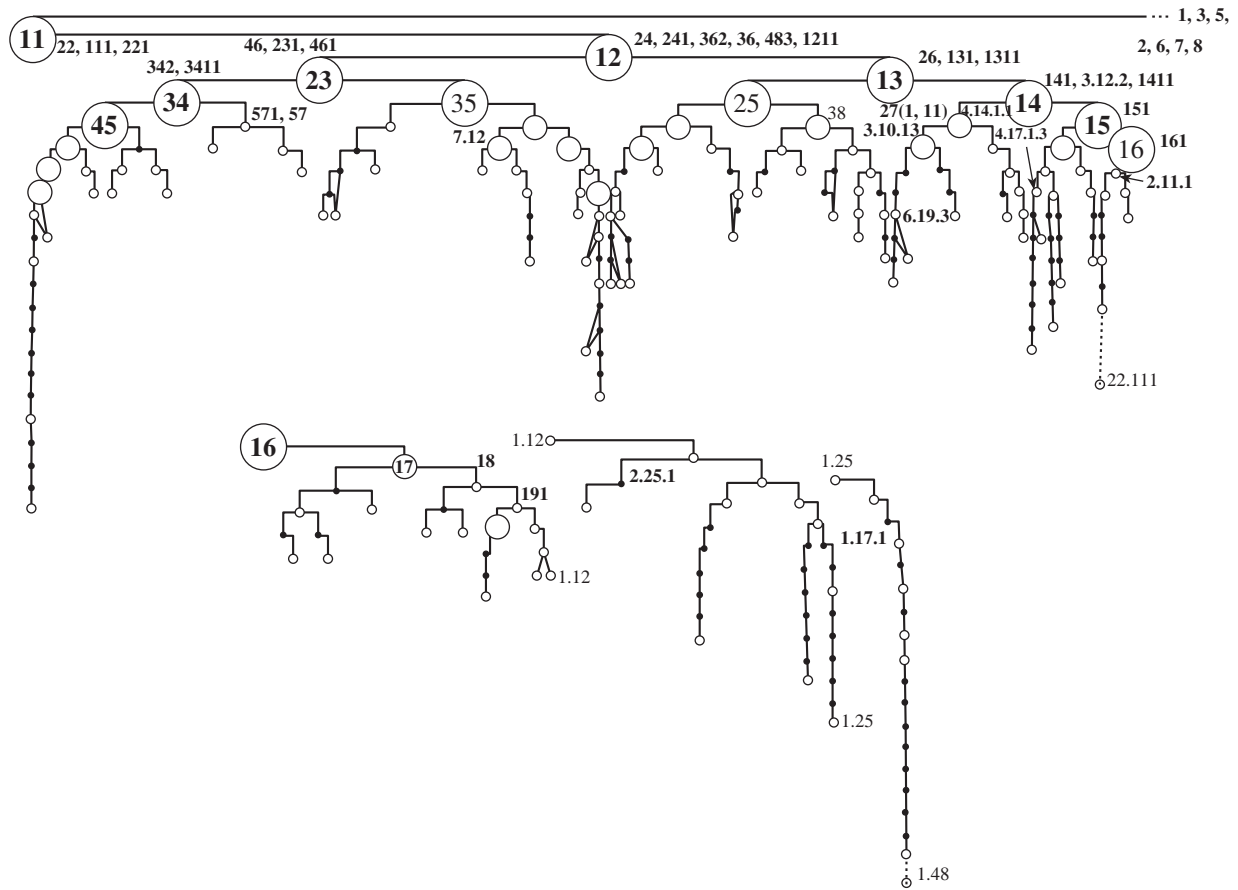


Fig. 1. Quantitative ratios of the coefficients in formulas of chemical compounds and cation parts of minerals.

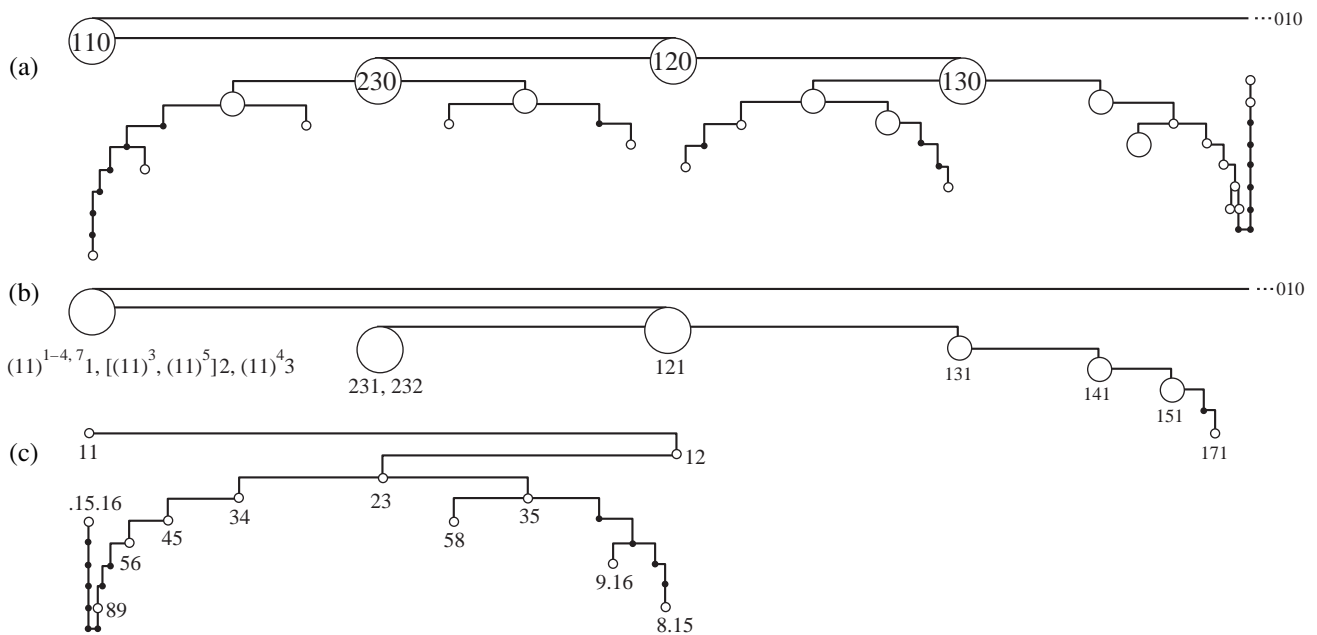


Fig. 2. (a, b) Symbols of the twinning faces and (c) intervals of a musical scale.

even quaternary ratios. The indices in these formulas are written in increasing order, and then the first (or first and second) indices are placed in the third (or third and fourth) positions. All the formulas derived for minerals are in boldface type. It follows from this scheme that the new ratios determined according to the data taken from [4] correspond, for the most part, to the ratios obtained earlier for compounds described in [2]. The first four series of the scheme (according to Goldschmidt, these series are referred to as the complication series) are completely filled, and the structural types with these coefficients are characterized by the highest frequency of occurrence, which is in excellent agreement with the Goldschmidt inference. However, unlike Goldschmidt's opinion, the fifth series is also filled; furthermore, there is a rather large number of other ratios in the subsequent series. It should be noted that the distribution of the quantitative ratios of chemical coefficients is not uniform, and they most frequently occur when going along arithmetic series. Therefore, the generalized law of small numbers (the Pauling parsimony law) is also confirmed by the example of the quantitative ratios of the coefficients for new chemical compounds, namely, minerals with a more complex composition.

Let us now consider the symbols of twin intergrowth faces. We can conveniently compare these symbols when they are also referred to as formulas. Figure 2 displays the scheme of ranking the formulas for twinning faces. As is clearly seen from Fig. 2, these formulas are described by a substantially simplified scheme, but the character of their distribution is similar to that observed for the ratios of chemical coefficients. The formulas with two nonzero indices and one zero indices are shown in Fig. 2a, and the formulas with nonzero indices are depicted in Fig. 2b. A number of ratios in Fig. 2b are represented in the condensed form. This makes it possible to put them in correspondence with the simpler formulas. For this purpose, a part of the formula is written in the form $(hk)^n$. For example, 111, 221, 331, 441, and 771 can be written as $(11)^11$, $(11)^21$, $(11)^31$, $(11)^41$,

$(11)^71$ or $(11)^{1-4,7}1$. As in the case of chemical compounds, ternary formulas are considerably simplified (i.e., contain a smaller number of numerals).

Moreover, the formulas of intervals (ratios between the frequencies of two tones) of a musical scale [5] are also depicted in the ranked scheme in the above manner. Among these formulas, we can distinguish a rather long Fibonacci sequence: 11, 12, 23, 35, and 58 (Fig. 2c). Unfortunately, our scheme leaves the reasons for the occurrence of just these intervals unclear. However, there is no doubt that in time the satisfactory explanation will be offered.

All the formulas in the above scheme can be the differentiation–integration points (in our case, these are the bifurcation points), even though this possibility is not necessarily realized.

In conclusion, it should be noted that the results obtained in this work combine two concepts, namely, the complication and furcation concepts. The law of small numbers, i.e., the parsimony law [6, 7], has been confirmed by new examples.

REFERENCES

1. A. V. Shubnikov, *Izv. Akad. Nauk SSSR*, 515 (1922).
2. P. Villars and L. D. Calvert, *Pearson's Handbook of Crystallographic Data for Intermetallic Phases* (American Society for Metals, Metals Park, 1985).
3. V. Goldschmidt, *Über Komplikation und Displikation* (Carl Winters Universität, Heidelberg, 1921; Geological Inst., Kola Research Center, Russ. Acad. Sci., Apatity, 1998).
4. A. P. Khomyakov, *Priroda*, No. 5, 62 (1996).
5. *System. Symmetry. Harmony*, Ed. by V. S. Tyukhtin and Yu. A. Urmantsev (Mysl', Moscow, 1988).
6. L. Pauling, *J. Am. Chem. Soc.* **51**, 1010 (1929).
7. N. L. Smirnova, *Kristallografiya* **46** (2), 276 (2001) [*Crystallogr. Rep.* **46**, 235 (2001)].

Translated by O. Borovik-Romanova

DIFFRACTION AND SCATTERING

Dedicated to the memory of Boris Konstantinovich Vainshtein (1921–1996)

The Development of Electron Crystallography*

A. L. Mackay¹

Dept. of Crystallography, Birkbeck College (University of London), Malet Street, London WC1E 7HX

e-mail: a.mackay@mail.cryst.bbk.ac.uk

Received June 4, 2001

Abstract—By the materials of the lecture delivered in the School on Electron Crystallography, Erice, Sicily, 1997 and published in Proceedings of NATO Advanced Study Institute on Electron Crystallography, Erice, Sicily, 1997, Series E, vol. 347, p. 1. © 2001 MAIK “Nauka/Interperiodica”.

Since we meet here in the ancient town of Eryx, full of the monuments of ancient and modern religions, we should remember that Archimedes lived in Sicily² and that his work combined science, mathematical theory, technology³ and computing.⁴ Traditional teaching in schools about the ancient Mediterranean classical traditions, dominated by myths and literature, has completely obscured the technological basis of that civilization,⁵ which, in fact, produced such devices as the *anti-Kythera mechanism*.⁶ This was an astronomical calculator, made in the first century BC, with some 30 gear wheels and of a complexity comparable to that of a modern mechanical clock. Probably Archimedes knew about the predecessors of such machines⁷ and he himself certainly used mechanical models and diagrams⁸

to discover mathematical results, which he later proved theoretically. He was killed during the Roman invasion of Syracuse while too absorbed with his thinking machine, his sand-table, the equivalent of the modern PC.

In ancient Sicily it was also known that the amber, imported from the Baltic, when rubbed with a cat skin, attracts small pieces of dry vegetable matter. The Greek word for amber is, of course, *electron*, but it is still not entirely clear how frictional electrification works, although this year is already the centenary of the characterization of the electron by J.J. Thompson. Using an instrument presaging the cathode ray oscillograph, Thompson measured electromotive force for the electron and regarded an electron as a particle. Later, the electron turned out to have wavelike properties too, and electrons have proved to be immensely useful in investigating matter. The experiment of producing a diffraction pattern by the interference of electrons passing through two parallel slits still furnishes one of the great paradoxes of physics showing that the world of quantum mechanics is not like our “common sense” everyday world. If the intensity of the beam of electrons is reduced, so that only one electron at a time goes through the system, a diffraction pattern is still obtained. Which slit does it go through?

The development of electron crystallography, and particularly the role of Boris Vainshtein in it, provides an interesting case history of the complex interactions of theory, experiment, and individual people in our century. All aspects of science are really linked together.

It is not necessary to go over the discovery in 1912 of the diffraction of X-rays by crystals and the subsequent development of crystal structure analysis.⁹ About 1912, Max von Laue, Arnold Sommerfeld (Ewald’s supervisor), and Paul Ewald had the idea at a café table in Munich. Friedrich and Knipping did the experiment,

* This article was submitted by the author in English.

¹ The author, while asserting his right to be recognized as the author of this article, renounces his copyright in it, so that the material is thus now in the public domain.

² (287–212 BC). An entertaining recreation of life in ancient Syracuse can be found in Mary Renault’s novel *The Mask of Apollo*.

³ The salt works at Trapani still pumps the brine with Archimedean triple helices.

⁴ Archytas (4 century BC), renowned for his mechanical devices, had also lived nearby. Archimedes was also in correspondence with Eratosthenes, Librarian of Alexandria, who had performed the supreme feat of the human intellect in measuring the radius of the Earth.

⁵ We suffer from the same problem today with “post-modernism” and the flight from objective reality.

⁶ This is the first of the erroneous *mind sets* with which this paper will be concerned. See: *Gears from the Greeks: The AntiKythera Mechanism—A Calendar Computer of 80 BC*, D.J. de S. Price (1975) and later papers.

⁷ Cicero (106–43 BC), Governor of Sicily in 75 BC, who rediscovered and restored the tomb of Archimedes (since again neglected and lost), may even have been seen the actual mechanism.

⁸ “certain things first became clear to me by a mechanical method, although they had to be demonstrated by geometry afterwards, because their investigation by the said method did not furnish an actual demonstration. But of course it is easier, when we have previously acquired, by the method, some knowledge of the questions, to supply the proof that it is to find it without any previous knowledge,” *The Method* (translated by T.L. Heath).

⁹ By far the best single textbook is that of W.L. Bragg, *The Crystal-line State* (1933) which, although now 64 years old, is absolutely essential reading.

and von Laue got the prize. Paul Ewald provided us with the geometrical tools of the reciprocal lattice and the Ewald sphere which are of the greatest use in visualizing what is happening.¹⁰ X-ray diffraction has been so successful, resulting in the knowledge of the structures of some 200000 materials, that it has induced a *mind set* preventing people from considering properly other techniques.¹¹ W.L. Bragg, the founder of X-ray crystal structure analysis, being involved in the discussions on the wave-particle duality of X-rays and electrons, was well aware of electron diffraction and devoted a chapter to this in his classic book. Following the theoretical predictions of Louis de Broglie made about 1923, it was expected that an electron with a velocity v and a mass m would have a wavelength $\lambda = h/(mv)$ associated with it.¹² In 1928 Davisson and Germer demonstrated the diffraction of 65 to 600 eV from the surface of crystal of nickel and, at much the same time, G.P. Thompson (the son of J.J. Thompson) showed the photographically recorded diffraction patterns produced by the passage of 60 kV electrons through thin films of gold. The techniques of electron diffraction were then rapidly assimilated to those of X-ray diffraction, and electron crystallography had begun.

When a new technique appears, the usual first strategy is to rush round and look at everything at hand.¹³ This happened with electron diffraction, and the characteristics of the technique rapidly appeared together with information about various substances examined with it. In the second stage, the new technique is seen in the light of the existing techniques and theories. In particular, since waves are now found to be associated

with particles, older techniques using one kind of waves can be transferred to newer techniques with (usually) shorter wavelengths. We see two clear periods in electron crystallography—the first concerned with electron diffraction and the second with electron microscopy. These are perhaps now followed by a much more general approach to radiation and structure and the combination of methods.

ELECTRON DIFFRACTION

The attractive properties of electron diffraction were at once apparent. To summarize:

(1) The wavelength to be expected for an electron beam is extremely short, less than a tenth of the diameter of an atom, and thus there were possibilities of great resolving power.

(2) Electrons are very strongly scattered by matter, perhaps 100 000 times as much as X-rays, so that “a minute speck of crystal is sufficient to give diffraction effects” (Bragg). The scattering is so strong that, even for a very thin specimen, electrons are scattered more than once. It is, in fact, much better here to consider electrons as waves and to picture the wave field in the crystal. For X-ray diffraction it is usually assumed that multiple diffraction (Renninger effect) does not take place. If it does, then a smaller crystal is used and the difficulty is avoided, but just those observations which contain information about the phases are neglected.

With multiple scattering (or standing wave fields), very complex diffraction patterns are produced. This was quickly found by S. Kikuchi (1928), whose name thus became attached to a particular class of diffraction patterns.

Electrons are scattered by atoms and molecules in the gaseous state and this technique has developed steadily from that day to this¹⁴ with increasing refinements, most noticeably by the combination of other techniques like mass spectroscopy.

(3) J.J. Thompson had shown that a beam of electrons could be deflected by electrical and magnetic fields.

This meant that,

(a) in contrast to X-rays, a beam of electrons could readily be focussed and thus possibilities for making electron-optical instruments, particularly a microscope, could be envisaged.

(b) For atoms, electrons are scattered by the electric potential, whereas X-rays are scattered by the electron density.¹⁵ The inner potential of a crystal is equivalent to a refractive index. If the X-ray scattering factor for an atom is f then the electron scattering factor

¹⁰ Everyone concerned to know “wie es eigentlich gewesen ist” should read Ewald’s collection: *Fifty Years of X-ray Diffraction*, International Union of Crystallography, 1962. As W.L. Bragg himself said, “you cannot realize how difficult the structure of pyrite was to solve” (having non-intersecting three-fold axes).

¹¹ The same mind set was also evident in 1984 in the resistance to the discovery of quasicrystals. The paradigm of “crystal structure analysis by X-ray diffraction” has now been varied in all three terms: *crystal structure*, *X-rays*, and *diffraction*. As we will see later, there were also other mind sets relating to the state of science in the USSR, which were not disrupted until the shock of the Sputnik satellite in 1957.

¹² It is convenient to remember, without confusing them, two similar formulae: (1) The wavelength in Angstroms associated with an electron accelerated by a potential of V volts is given (approximately) by $\lambda = 12.3/\sqrt{V}$. (2) The wavelength in Angstroms of the X-rays with an energy of V kilovolts is (approximately) $\lambda = 12.3/V$. Thus, 100-kV-electrons have a wavelength of about 0.04 Å; 1.5-Å electrons correspond to 70 V. The characteristic X-rays from a copper anode have a wavelength of 1.54 Å and correspond to a voltage of 8 kV. Although a 100-kV-electron may be stopped by a micron thickness of metal, the most penetrating X-rays which may be associated with these 100-kV-electrons have a wavelength of 0.12 Å and will require several millimeters of lead for protection. Relativity must be taken into account for more exact calculations of wavelength. Electrons in an electron microscope travel at an appreciable fraction of the speed of light.

¹³ *Micrographia* by Robert Hooke (London, 1665) is a classic account of all the discoveries made by one of the first to use the optical microscope.

¹⁴ I. Hargittai and M. Hargittai, *Stereochemical Applications of Gas-Phase Electron Diffraction*, VCH, Weinheim (1988).

¹⁵ Electron density is not the same as charge density. It means the density of electrons whose charge is neutralized locally by the corresponding positive nuclear charge. The concept of charge density is fraught with difficulties.

is proportional to $(Z-f)$, where Z is the atomic number (the number of electrons in the atom). The scattering curves for X-rays and electrons thus go differently. For electrons, light atoms scatter more compared with heavier atoms than for X-rays and, in particular, hydrogen atoms have substantial scattering power.

(c) It followed also that electrons could be selected for their energies (and thus wavelengths) by a combination of electrical and magnetic fields.

(4) The notation and concepts developed for X-ray diffraction could be immediately transferred. An electron beam of 100 kV energy corresponds to a wavelength of about 0.04 Å. Bragg's law of diffraction $\lambda = 2d\sin\theta$ could be directly applied and indicated that the diffraction angles corresponding to those used for X-ray diffraction were in the range of one degree, where $\sin\theta$ is close to θ itself. This meant that, when the Ewald sphere representation of the geometry of diffraction was used, the pattern could be seen to be an almost undistorted section through the reciprocal lattice.

We may follow briefly the various schools which developed electron diffraction from 1928.

CRYSTAL STRUCTURE ANALYSIS BY ELECTRON DIFFRACTION

The equipment required for electron diffraction was not complicated, and many people began experiments. At Imperial College in London, G.I. Finch, continuing from G.P. Thompson, used reflection diffraction to characterize surfaces such as the oxide layer on steel piston rings. His apparatus was made locally and required a wine bottle (with the bottom cut off) to use as the main insulator and gun housing. Finch used to explain what a lot of research was necessary to find just the right kind of bottle.

In Japan, S. Kikuchi started a tradition of electron optics which became very important, especially much later when people came back from the Navy after 1945 and founded the Japan Electron Optics Company.

In Russia, where there was a very strong mineralogical and crystallographic tradition, the structure of

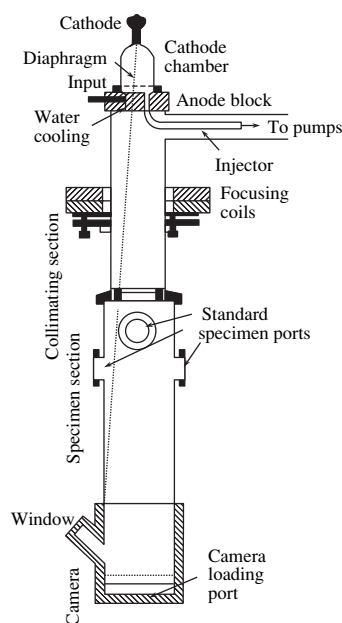


Fig. 1. The electron diffraction camera used by G.I. Finch at Imperial College, London.

ammonium chloride was determined using electron diffraction in 1933 by Lashkarev and Usyskin who found the positions of the hydrogen atoms.

Z.G. Pinsker, the head of the electron diffraction laboratory at the Institute of Crystallography in Moscow, said that he had made some significant discoveries,¹⁶ but that his most important discovery was that of Boris Vainshtein who joined Pinsker's group after the war and quickly developed his own research style. The Russian laboratory built several electron diffraction cameras (Fig. 2) and began to apply them to crystal structure analysis, building on the prewar work.

¹⁶ Z.G. Pinsker's book *Electron Diffraction* (USSR Acad. Sci., Moscow, 1949) appeared in English translation in 1953. B.K. Vainshtein's book, *Structure Analysis by Electron Diffraction* appeared in Russian in 1965 and in English in 1964. B.B. Zvyagin's book, *Electron Diffraction Analysis of Clay Mineral Structures*, appeared in English in 1967 (Plenum).

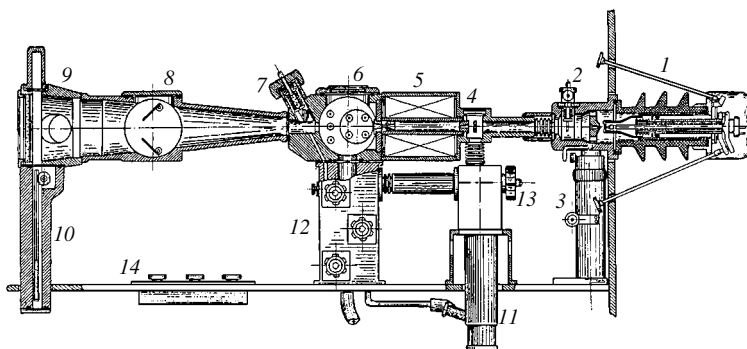


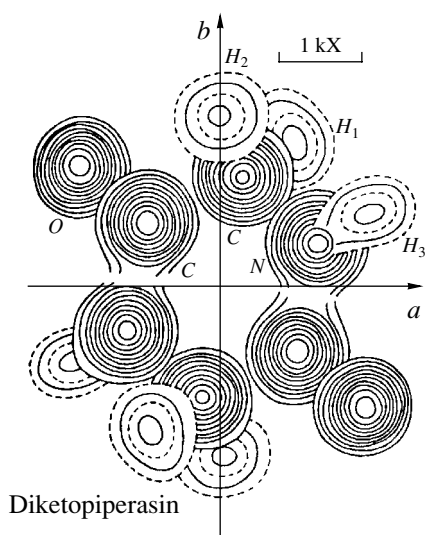
Fig. 2. The early electron diffraction camera used at the Institute of Crystallography in Moscow.

They determined a number of crystal structures more or less following the procedures for X-ray work. Their techniques had a number of features favoring success in this:

(a) they used very small crystals ordered into textures, that is crystals with strong preferred orientation. Considerable trial and error effort was put into obtaining suitable textures where the crystallites were sufficiently small and well-aligned. The specimen carried could be tilted (to at least 60°) to expose textures where flakes lay parallel to the substrate. The technique was very suitable for clay minerals, where appreciable single crystals did not exist, and Boris Zvyagin developed this topic with great success solving structures which were then impossible by X-ray methods;

(b) the electron beam had a diameter of about 1 mm where it struck the specimen (which was usually supported on a collodion film). Thus, many crystallites of various sizes contributed to the diffraction pattern and, with variations in orientation, the intensities of individual crystallites added (rather than the amplitudes). All these factors contributed to the minimization of the effects of multiple scattering (dynamic scattering). For dynamic scattering, the first approximation is that the intensities are proportional to F (the structure factor) rather than to F^2 squared. Usually the exponent of F was refined for the best fit;

(c) at first, at least, the number of parameters to be refined was small compared with the number of reflections available and crystal-chemical considerations reduced the number of possible structures.



It happens that I first intellectually encountered Boris Vainshtein in translating his early paper *The Application of Harmonic Analysis in Electron Diffraction* which appeared in the reports of the Soviet Academy of Sciences in 1949¹⁷ in which the determination of the structure of barium chloride monohydrate by

¹⁷ B.K. Vainshtein and Z.G. Pinsker, Dokl. Akad. Nauk SSSR, 64 (1), 49–52 (1949).

electron diffraction was reported. The paper mentioned that hydrogen atoms could be detected and pointed to the difference between the scattering curves of the same atom for electrons and for X-rays. On the basis of the hint that the use of electrons and X-rays for the same material was equivalent to the method of isomorphous replacement,¹⁸ I applied for a research studentship at Imperial College. I did not get it, and my colleagues, to whom I circulated the translation, took no notice. In 1956, I met Boris Vainshtein at a crystallographic meeting in Madrid and, later, at the Institute of Crystallography where Bernal was giving lectures. In 1962, I joined Pinsker's group at the Institute of Crystallography, not very successfully, for a few months. I was at least able to get to know everyone, learn what was going on and see how the equipment worked. The cold war was then in the temporary stage of a modest "thaw." In fact Boris Vainshtein was then, having become Director of the Institute in 1962, moving onto the structure analysis of proteins, which he did also with great success against very considerable odds. To get out a front-line scientific paper in the Soviet Union required several times the effort needed in America. In the period from 1945 to 1960, many structures were determined. These included: $\text{NiCl}_2 \times \text{H}_2\text{O}$ and related compounds; *diketopiperazine* (see figure above); Cu/Mn and Cu/Mg alloys; $\text{CuCl}_2 \times 3\text{Cu}(\text{OH})_2$; poly- γ -methyl-L-glutamate; PbBi_4Te_7 ; thio-urea and urea; they were notable for showing the possibilities of electron diffraction, particularly as regards finding the positions of H atoms and showing other light atoms in the presence of heavy ones. From 1962, Boris had to do the strategic scientific planning for all sections of a very large institute (reaching about 1000 people, half in the workshop growing crystals and producing instruments for sale, these included large single crystal sapphire windows for the US space program) and he contributed important papers on almost all aspects of crystallography. The workshop was necessary because it was easier to have them grind up a lens in order than to get it from an outside source. It also earned foreign exchange, some of which could be used for really essential imports. Life was always rather difficult. Nevertheless, Boris continued to supervise work in electron diffraction and in 1993 produced, with Vera Klechkovskaya, a study¹⁹ of Langmuir–Blodgett films (using an electron microscope) for which the technique is well suited.

ELECTRON MICROSCOPY

The electron microscope was developed from the cathode ray oscillograph with gradual improvements.

¹⁸ A.L. Mackay, Suppl. al Nuovo Cimento, 10, 387–414 (1953), p. 395. For some years I abstracted the whole of *Kristallografiya* and other Russian journals.

¹⁹ B.K. Vainshtein and V.V. Klechkovskaya, *Electron Diffraction by Langmuir–Blodgett Films*, Proc. R. Soc. Lond. A 442, 73–84 (1993).

Since the resolving power of a microscope is roughly $\lambda/2$ and 100-kV-electrons have a wavelength of 0.04 Å, the resolving power of the electron microscope is potentially very great but it was (and is) limited by the nature of the magnetic and electric lenses. The spherical aberration of magnetic lenses is always positive and can be minimized but cannot be cancelled out by lenses of negative spherical aberration as is done in the optical case. Useful magnification began to appear about 1939 and immediately after war, the crystallographer R.W.G. Wyckoff was appointed Science Attaché at the American Embassy in London. Since he had just shown the arrangement of protein virus particles in a crystal, he would only take the job if he could bring his electron microscope to the Embassy with him and continue research work. This was really the first direct pictorial demonstration of how identical particles stack up to make a crystal. We will not follow these developments but jump to the date of 1956 when it was realized that the resolving power of the microscope had reached about 10 Å²⁰ and that this was comparable with the spacings of the Bragg planes in crystals. The dramatic step was accomplished by Jim Menter with a Siemens electron microscope at Tube Investments near Cambridge, and he showed the pictures of the lattice of platinum phthalocyanine (11 Å lattice planes). This was also very important because the pictures also showed the presence of dislocations in the lattice thus confirming what had hitherto been theoretical speculations. The main textbook of the sixties written by Hirsch *et al.* [2] was much more concerned with the development of dislocation studies and the complexity of the interaction of electrons with crystals, and the structure analysis was hardly mentioned.

With this lattice imaging, microscopists slowly began to realize that in the formation of an electron microscope image the relative phases of the beams making up the image are not lost, although they may be distorted, and that microscopy presents possibilities for solving the phase problem, which then appeared as the dominating difficulty of X-ray crystal structure analysis.

GENERALIZED MICROSCOPY

At this stage, we should look back to the work of Ernst Abbe in Jena who established the wave theory for the resolving power of the optical microscope (1882). He showed that in order to resolve the lines in a diffraction grating the microscope objective must accept, besides the central beam, at least, the first-order diffracted beam, so that the image is produced as a result of the superposition of these two beams. The equation $d = \lambda/(2n \sin \alpha)$ ²¹ is engraved on his memorial in Jena.

²⁰ Angstrom unit is 10^{-8} cm. Since atoms have radii of 1 to 2 Å, crystallographers prefer to continue with this term rather than to use nanometers (1 nm = 10 Å) as international obligations require.

²¹ With the refractive index n and $n \sin \theta$ is the numerical aperture.

It was known²² that tilting the illumination so that the direct beam and one first-order diffracted beam pass symmetrically through the system (thus suffering the same aberrations) effectively doubles the resolving power of the microscope. Understanding of this took some time to reach electron microscopists. It was the beginning of the appreciation of the contrast transfer function and the recognition that, in the electron microscope, the phases of scattered waves are not lost. The contrast transfer function was developed by H.H. Hopkins about 1957 for the design of lenses for television cameras with about 600 lines, where the requirements, aperture rather than resolution, differ from those of, e.g., high-resolution surveying cameras. When you buy a high-fi audio amplifier, what you pay for is the frequency response curve. All frequencies should be amplified to the same extent. The same applies to buying an electron microscope but the curve of how phases are changed on transmission through the system is necessary as well as the amplitude response. The ear is rather insensitive to the relative phases of the various waves which add to make up what we hear,²³ whereas the eye is very sensitive to phases. The simple symmetrical diagram deriving from Abbe (Fig. 3) is fundamental for understanding optical and electron microscopy and the applications of image processing.

A small point source of monochromatic radiation is defined by an aperture; waves spread from the source and are focussed by a lens onto the plane D of the diffraction pattern. If an object, a diffraction grating, is placed at the first lens, it diffracts the incident beam into a series of spectra and these beams also are focussed in the plane D . If we put screen or film at D the diffraction pattern would be recorded as an intensity distribution. The relative phases of the various beams making the pattern would be lost. However, there is no screen to stop them, the beams continue diverging from each other until they meet the second lens which converges them so that they overlap and interfere to give the image in the plane S' . If a screen is placed in the diffraction plane, we can control which orders of diffraction go to make up the final image. In particular, a double periodic object gives a series of point spectra (the reciprocal lattice), whereas nonperiodic noise gives diffracted intensity distributed over the spectrum, so that the points of the reciprocal lattice can be selected and the noise can

²² For example the *Encyclopaedia Britannica* article *Microscope*, vol. 18, p. 398 (9th edn., 1910).

²³ That is, a single ear is rather insensitive to the relative phases of the sine waves of different frequencies which are conceived as adding linearly to give a single tone, although it may register such phase differences as difference in "attack." However, the ear is nonlinear and produces harmonics and sum and difference tones. The hearing system is, of course, very sensitive to phase differences due to different path lengths of the same pulse as perceived by the two ears together, which provides directionality. There is much new information as to how the aural system works and, in particular, there is evidence of a local oscillator which may supply a reference phase (like a superheterodyne receiver on the brink of oscillation).

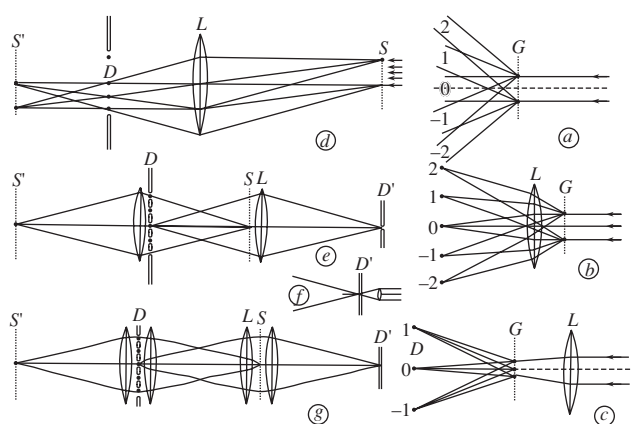


Fig. 3. The optical diffractometer.

be reduced. As demonstrated by M.J. Buerger, the relative phases of the diffracted beams can also be altered. Thus, image processing can begin. This was developed first by this optical analogy and later by computer. Thus, a two-stage optical diffractometer was developed by Klug and de Rosier.²⁴ The laser appeared at much the same time and greatly facilitated the instrumentation.

(a) Diffraction of a parallel monochromatic beam by a grating of period a . Diffracted beams appear at deviations θ given by $\lambda = na\sin\theta$.

If the grating G has a sinusoidal distribution of scattering power, only the first order appears.

(b) The parallel diffracted beams can be focussed with a lens L to produce points in the diffraction plane.

(c) The lens may be either side of the grating.

(d) If the diffracted beams continue beyond the diffraction plane, they superimpose in the image plane to give an image S' of the grating S .

(e) Monochromatic light from a pinhole D' is focussed in the diffraction plane D , where each diffracted beam gives an image of the pinhole. Note the symmetry of the system where S' is also the image of S .

(f) A broad parallel beam from a laser may be focussed onto the pinhole to give an intense monochromatic source.

(g) With a screen in the plane of the diffraction pattern D , selected parts of the diffraction pattern can be allowed to proceed through holes in the screen to combine to give a filtered image of S at S' .

We may note, in yet another example of the mind set phenomenon, that Fritz Zernicke (1888–1966) had great difficulty in finding acceptance of his invention of the phase contrast microscope in 1938. Zeiss (Jena) resisted it for a decade, it being believed that Abbe had said the last word on the subject. Further, only recently, Carl Zeiss (Oberkochen) found that their key develop-

ment of energy filtering of the electron microscope image was very slow to be appreciated. This permits selection, on the basis of their characteristic losses, of what atoms are to contribute to the picture.

In 1948, Denis Gabor published his key paper *A New Microscopic Principle*²⁵ which described the principles of holography. At much the same time both W.L. Bragg²⁶ and Martin Buerger Massachusetts Institute of Technology (MIT) were coming rather close to the same discovery. Buerger invented the precession camera (for X-ray diffraction) so that he could produce an undistorted picture of a section of the reciprocal lattice on a crystal. This film reversed, black spots becoming white holes, was then to become the source of diffracted light rays in "the two-wavelength microscope." The idea was to perform the first step, diffraction, with X-rays and the second stage, superposition of the diffracted beams, with monochromatic light. A magnification factor of the ratio of the wavelengths would result. Buerger managed to reconstruct an image of iron sulfide, but only by inserting the *known* phases of each beam with a rather cumbersome optical phase shifting device. Bragg pointed out that the principle of holography was already in use in that the phases of X-ray beams diffracted by a central heavy atom as Pt in platinum phthalocyanine (J.M. Robertson) or iodine in cholesteryl iodide (C.H. Carlisle and D. Crowfoot) effectively determined the phases by swamping the contributions of the other atoms. As in everything he touched, W.L. Bragg cut straight through to a simple pictorial understanding of the physical principles involved.

The first image processing to give an actual picture of a crystal structure was done in 1929 by W.H. Bragg for diopside,²⁷ who had pointed out the extremely important physical principle that a grating with a sinusoidal distribution of scattering power gives only the first order of reflection (all higher orders are zero) and correspondingly, in a diffraction pattern, each reflection can be attributed to a sinusoidal density wave of appropriate amplitude spatial frequency. Thus, a *picture* of diopside was produced by the *linear superposition* of sine waves on a photographic plate. It is, of course, necessary that these waves should also be combined in the correct phase. Later (around 1955), it was realized that about 80% of the "information" in a crystal structure resided in the phases and only about 20%, in the amplitudes of the reflections. Thus, exact measurement of the amplitudes is not critical²⁸ but preservation of the

²⁵ Nature, 161, 777–778 (May 15, 1948) and Proc. Roy. Soc., A 197, 454 (1950).

²⁶ *Microscopy by Reconstructed Wave-Fronts*, Nature, 166, 399–400 (September 2, 1950).

²⁷ Zeit. f. Krist., 70, 488 (1929).

²⁸ A.D. Booth proposed to determine the structures of centro-symmetric crystals from the accidentally absent (or very weak) reflections on the grounds that, for these, the scattering by all the atoms together cancels out and that this is thus very sensitive to their exact positioning (personal communication about 1950 when he was at Birkbeck College).

²⁴ A. Klug and D.J. de Rosier, Nature, 217, 130 (1966) and A. Klug, *Chemica Scripta*, 14, 245–256 (1978–79); Nobel Symposium *Direct Imaging of Atoms in Crystals and Molecules*, August 6–10, 1979.

phase relationships of the scattered beams, even in a distorted form, is vital. In an *actual* crystal, the sinusoidal electron density waves are not independent of each other and add *nonlinearly*. The Karle–Hauptman determinant, which is the basis of the direct methods of determining phases,²⁹ derives directly as an expression of this nonlinearity.

IMAGE PROCESSING

Ideas of image processing developed slowly, step by step, using the concept of the optical diffractometer with diffraction, filtering, and, then, reconstruction. It began with the utilization of *a priori* knowledge of symmetry to get better information about a single repeated element. Thus, Roy Markham, dealing with an object with sixfold rotational symmetry, printed the plate six times to superpose the symmetrically related units. This was essentially what Francis Galton³⁰ had done to produce a face of an average criminal, the average tubercular face, and even the face of Alexander the Great (by superposing the images of a dozen coins). It is important to realize that you get nothing for nothing, but that any foreknowledge can be used to limit the remaining uncertainties. Galton assumed in advance that the average portrait would have two eyes in a particular orientation, and he lined up his individual pictures correspondingly without subjective guesswork. F.P. Ottensmeyer, seeking to avoid getting protein molecules, lined up in parallel in a crystal according to the very exact requirements of nature, tried the same method of superimposing many electron-microscope images of molecules of a particular protein lying in random orientations. He was cruelly slaughtered by J. Dubochet³¹ at the Nobel Symposium of 1979, who showed images exactly like those of protein molecules produced by Ottensmeyer but where there had been no protein specimen whatever. The recognition of molecules and still less identification of their orientations had been a subjective delusion. Aaron Klug's discussion of this was less cruel and more analytic but equally devastating. Nevertheless the method begins to work when the number of details to be recognized in the object is large [compared with the 5 parameters (position in the direction of the beam is not needed) necessary for specifying the orientation and position]. This is to be seen in the remarkable work on the core protein of

the hepatitis B virus very recently published by two groups, where resolutions of 7.4 Å and 9.0 Å were reached from 6400 and 600 particles, respectively.³² Identity of the particles used is based on prior physico-chemical methods of selection and represents hard-won information.

Thus, direct methods of X-ray crystal structure analysis depend on the *a priori* knowledge that the crystal is composed of atoms and that the electron density is nowhere negative. Similarly to the Rayleigh criterion for resolving two point objects, the first diffraction peak of one should lie on the first diffraction minimum of the other, corresponding to a resolution of 0.5λ , could be greatly improved on, if we knew exactly the expected diffraction from each object. This applies, of course, also to radar, and permits the distinction between one big airplane and two smaller ones if we know the characteristic scattering from each type.

CRYSTALS

It is a test for purity that a material crystallizes and it is the definition of a crystal that it is composed entirely of identical units identically situated. This assumption is the price paid for X-ray crystal structure analysis. However, not all crystals answer to this description and they are then characterized as poorly crystallized, disordered, flaky, etc. in disparagement. However, real matter knows other modes of ordering and does not always correspond to the preconceptions of the crystallographers. Quasicrystals were just one of many surprises, and there must be many others to come.

Thus, this workshop is devoted to the art of obtaining by electron microscopy three-dimensional images of various objects, about which we have certain other information. We may know (or believe, perhaps, erroneously) something about their constitution and about their symmetry and this *a priori* information may be used to separate out from the incoming images what we wish to know from what we already know. We will realize here that seeing is not a simple passive act but that, as in many other fields of life, what we see in a situation depends on the cultural preconceptions which we bring with us.

Eighty years ago, W.H. Bragg and W.L. Bragg had the superb vision that the atomic world, miraculously foreseen by Democritus and Lucretius, was just like the real world, only smaller.³³ With quantum mechanics our preconceptions have changed as the wave/particle

²⁹ Jerome and Isabella Karle and Herbert Hauptman, encountering still another *mind set*, this time among crystallographers, had some difficulty in getting their methods accepted, but now these are universally applied for the solution of small and medium crystal structures. Crystals with very large molecules (now up to MW 700 000) rely on the heavy atom method which resembles holography.

³⁰ Francis Galton; *The Life and Work of a Victorian Genius*, D.W. Forrest, London (1974). *Composite Portraiture*, Appendix (pp. 221–241) to *Inquiries into Human Faculty* (1883) Everyman edn., Dent, London (1907).

³¹ J. Dubochet, *Chemica Scripta*, 14, 293 (1978–1979).

³² S. Böttcher, S.A. Wynne, and R.A. Crowther, *Determination of the Fold of the Core Protein of Hepatitis B Virus by Electron Cryomicroscopy*, *Nature*, 386, 88–91 (March 6, 1997) and J.F. Conway, N. Cheng, A. Zlotnick, P.T. Wingfield, S.J. Stahl, and A.C. Steven, *Visualization of a 4-Helix Bundle in the Hepatitis B Virus Capsid by Cryoelectron Microscopy*, *Nature*, 386, 91–94 (March 6, 1997).

³³ W.H. Bragg used Lucretius' title, *On the Nature of Things* for his own series of lectures at the Royal Institution.

duality has turned out to be much more complex and counter-intuitive than W.H. Bragg's explanation that physicists use the wave theory on Mondays, Wednesdays and Fridays and the particle theory on Tuesdays, Thursdays and Saturdays. The electron microscope now serves as a kind of matching transformer which connects directly our every-day human senses with the world of atoms, just as Galileo's telescope connected him to the cosmos, revealing phenomena, like the moons of Jupiter, which were counter-intuitive to the prevailing world view of that time and place.³⁴

REFERENCES

1. W. L. Bragg, *The Crystalline State* (Bell, London, 1933; ONTI, Moscow, 1938), Vol. 1.
2. P. B. Hirsch, A. Howie, R. B. Nicholson, *et al.*, *Electron Microscopy of Thin Crystals* (Butterworths, London, 1965; Mir, Moscow, 1968).
3. Z. G. Pinsker, *Electron Diffraction* (Akad. Nauk SSSR, Moscow, 1949; Butterworths, London, 1952).
4. E. Ruska, *The Early Development of Electron Lenses and Electron Microscopy* (Hirzel, Stuttgart, 1980).
5. B. K. Vainshtein, *Structure Analysis by Electron Diffraction* (Akad. Nauk SSSR, Moscow, 1956; Pergamon, Oxford, 1964).
6. B. K. Vainshtein, *Modern Crystallography*, Vol. 1: *Fundamentals of Crystals, Symmetry of Crystals, Methods of Structural Crystallography*, Ed. by B. K. Vainshtein, A. A. Chernov, and L. A. Shuvalov (Nauka, Moscow, 1979; Springer-Verlag, Berlin, 1994, 2nd ed.).
7. B. K. Vainshtein, V. M. Fridkin, and V. L. Indenbom, *Modern Crystallography*, Vol. 2: *Structure of Crystals*, Ed. by B. K. Vainshtein, A. A. Chernov, and L. A. Shuvalov (Nauka, Moscow, 1979; Springer-Verlag, Berlin, 1995, 2nd ed.).
8. B. B. Zvyagin, *Electron Diffraction Analysis of Clay Mineral Structures* (Nauka, Moscow, 1964; Plenum, New York, 1967).

³⁴ For Galileo's connection with atomism and trans-substantiation see P. Redondi, *Galileo—Heretic*.

Specular Reflection of X-rays under the Conditions of Grazing Diffraction in a Crystal with an Amorphous Surface Layer

V. A. Bushuev*, R. M. Imamov**, É. Kh. Mukhamedzhanov**, and A. P. Oreshko**

* Moscow State University, Vorob'evy gory, Moscow, 119899 Russia

** Shubnikov Institute of Crystallography, Russian Academy of Sciences,
Leninskij pr. 59, Moscow, 117333 Russia

Received November 9, 2000

Abstract—Specific features of the anomalous angular dependence of the specular-reflection intensity under the condition of noncoplanar grazing X-ray diffraction in a crystal coated with an amorphous surface film were revealed and studied experimentally. The phenomenon was analyzed theoretically and its high sensitivity to the presence and the thickness of a several-nanometer-thick amorphous film was shown. The experimental data were used to determine the thickness and the density of a native oxide layer formed on the surface of a silicon single crystal. © 2001 MAIK "Nauka/Interperiodica".

INTRODUCTION

X-ray reflection from perfect single crystals under the conditions of strongly asymmetric diffraction is widely used for collimation and monochromatization of the X-ray radiation [1]. In the limiting case, where reflecting atomic planes and the crystal surface form the angle close to the Bragg angle, the incident or the diffracted beam propagates at a small grazing angle to the crystal surface, which is comparable to the critical angle of the total external reflection. In this connection, an important role in the formation of diffraction reflection is played by specular reflection of X-rays. The dynamical theory of strongly asymmetric coplanar diffraction in which the incident, diffracted, and specularly reflected waves propagate in the same plane was developed in [2–6].

X-ray diffraction and the phenomenon of total external reflection are efficiently used for studying the structure of thin subsurface layers in single crystals and crystals coated with an amorphous or a crystalline film [7] (see also the review papers [6, 8, 9]). Under the conditions of strongly asymmetric Bragg diffraction, the extinction length decreases, which provides the study of thin surface layers and films whose thickness is of the order of 100 nm.

The next important step in the study of superthin (of the order of several nanometers) crystalline layers and even individual monolayers was made in [10], where a new scheme for diffraction experiment was suggested. This scheme allowed the study of X-ray diffraction from atomic planes normal to the crystal surface (at the inclination angle $\psi = 0$ as in the conventional Laue case). However, an incident X-ray beam forms a rather small grazing angle φ_0 with the crystal surface and is

specularly reflected from it. The diffracted wave in the crystal also propagates at a small angle to the surface, and, therefore, the so-called specularly reflected diffracted wave is formed in vacuum above the crystal. This wave leaves the crystal at an exit angle φ_h and provides the information on the structure of the subsurface layer. Since the incident specularly reflected and diffracted waves propagating in vacuum lie in different planes, this diffraction scheme in the grazing geometry is noncoplanar.

The rigorous dynamical theory of noncoplanar diffraction from an ideal crystal and a crystal coated with an amorphous film was considered elsewhere [11, 12]. In particular, a practically important equation $\varphi_h^2 = \varphi_0^2 + \alpha$ relating the exit angle of the specularly diffracted wave, φ_h , and the parameter $\alpha = 2\Delta\vartheta \sin 2\vartheta_B$ of the angular deviation $\Delta\vartheta = \vartheta - \vartheta_B$ from the Bragg angle ϑ_B in the diffraction plane was derived, from which it follows that the change in the diffraction angle ϑ by fractions of an angular second should result in the change of the exit angle φ_h of several minutes, $\delta\varphi_h = (\sin 2\vartheta_B / \varphi_h) \delta\vartheta \sim (10^2 - 10^3) \delta\vartheta$. Unlike [10], the latter fact allows one to avoid the beam collimation with respect to the diffraction angle and, instead of measuring the intensities $I_h(\Delta\vartheta)$ of the diffraction reflection (rocking) curves, one can study the differential intensities as a function of the exit angle $I_h(\varphi_h)$ at a constant grazing angle φ_0 . The necessary beam collimation with respect to angles φ_0 and φ_h at a level of 1–3 angular minutes can readily be attained with the aid of several slits. The refusal from double collimation allows a considerable increase of the recorded signal intensity and simplification of the experiment. Moreover, for a fur-

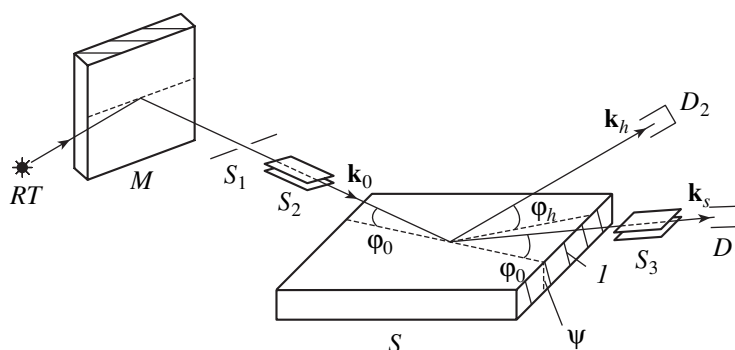


Fig. 1. Experimental scheme for recording specular reflection under the conditions of grazing Bragg diffraction. *RT* is an X-ray tube, *M* is a monochromator, *S* is the specimen, \mathbf{k}_0 , \mathbf{k}_s , and \mathbf{k}_h are the wave vectors of the incident, specularly reflected, and diffracted waves, respectively; *D*₁ and *D*₂ are the detectors recording specularly reflected and diffracted X-rays, *S*₁–*S*₃ are the collimating slits, *l* are the reflection planes with the inclination angle ψ .

ther increase of the intensity without loss in information power, there is no need to collimate the beam with respect to the exit angle φ_h . Thus, it becomes possible to measure the integrated intensity $I_h(\varphi_0)$. These concepts have successfully been implemented in [13, 14] for designing a specular X-ray diffractometer with a specimen located in the vertical plane. The conclusions about high sensitivity of the integrated curves $I_h(\varphi_0)$ to the presence of amorphous films and their thicknesses (of several nanometers and thicker) made in [12] were experimentally confirmed in [15].

The theory of grazing diffraction from an ideal crystal whose reflecting planes form a small angle $\psi \neq 0$ with the surface normal was constructed in [16–18]. The necessity of such an analysis was dictated by the practice of cutting and subsequent treatment of crystals whose surface should be rigorously parallel to the atomic planes, because even small inclination angles (of the order of $\psi \sim 0.5'–3'$) would result in considerable changes in diffraction intensities [16–18]. The crystals with an inclination angle of $\psi \sim 3^\circ–4^\circ$ are also used in a number of semiconductor technologies. The measurements made in the integral [18] and differential [18, 19] modes showed the high sensitivity of the intensity and the shape of the rocking curves to the inclination angles $\psi \geq 1'$ and the thicknesses of the amorphous and boundary layers with $d \geq 1$ nm.

The results obtained in [10, 11] have triggered a large number of studies aimed at the further development of the kinematical approximation of diffraction under the conditions of total external reflection [20–23], the modified dynamical theory [19, 24], which provides the analytical solution of the diffraction problem in the whole angular range φ_0 , φ_h except for a narrow interval in the vicinity of the critical angle of the total external reflection, and the matrix method to describe the grazing diffraction from multilayer structures with the smooth variation in deformation and the amorphization degree over the crystal depth [25, 26].

We should like to emphasize that all these theoretical and experimental studies considered the behavior of the rocking curves, but totally ignored the angular dependence of the specular-reflection intensity. At the same time, it was indicated in [9] that the presence of an amorphous film on the crystal surface can noticeably change the angular behavior of the specular-reflection intensity depending on the deviation $\Delta\vartheta$ from the Bragg condition at the fixed grazing angle.

Below we describe the first experimental study of specular reflection of X-rays from a silicon single crystal with a surface amorphous oxide layer under the conditions of grazing diffraction. Then results obtained are compared with the conclusions drawn from the theory developed in [27].

THEORY OF THE PHENOMENON

Consider an ideal single crystal whose reflecting atomic planes form an angle ψ with the surface normal (Fig. 1). Let a plane monochromatic wave $\mathbf{E}_0 \exp(i\mathbf{k}_0 \mathbf{r})$ with the wave vector $k_0 = 2\pi/\lambda$, be incident onto the crystal surface at a grazing angle φ_0 , where λ is the wavelength of the X-ray radiation. Now, determine the amplitudes of the specularly reflected, E_s , and the diffracted, E_h , waves at $z < 0$ above the crystal surface (the *z*-axis is directed into the crystal bulk along the surface normal \mathbf{n}).

The rigorous equations which describe these waves at arbitrary grazing angles φ_0 are rather cumbersome [16, 27] since one has to solve the dispersion equation of degree four

$$(\varepsilon^2 + 2\gamma_0\varepsilon - \chi_0)(\varepsilon^2 + 2\gamma_h\varepsilon - \chi_0 - \alpha) - C^2\chi_h\chi_{\bar{h}} = 0, \quad (1)$$

where $\gamma_0 = \sin\varphi_0$, $\gamma_h = \gamma_0 - 2\sin\psi \sin\vartheta_B$, χ_g are the Fourier components of crystal polarizability ($g = 0, h, \bar{h}$), and $C = 1$ or $C = \cos 2\vartheta_B$ for the σ - or π -polarized radiation, respectively, and $\alpha = 2\Delta\vartheta \sin 2\vartheta_B$ characterizes the angular deviation $\Delta\vartheta$ of the incident radiation from

the Bragg angle in the diffraction plane. The quantity ε to be determined describes the change in the wave vector of the wave \mathbf{q}_0 refracted in the crystal in comparison with the wave vector \mathbf{k}_0 in vacuum,

$$\mathbf{q}_0 = \mathbf{k}_0 + k_0 \varepsilon \mathbf{n}, \quad (2)$$

which follows from the continuity condition for the tangential components \mathbf{k}_0 and \mathbf{q}_0 . Since the X-ray polarizability is $|\chi_g| \sim 10^{-5}$, we have $\varepsilon \ll 1$. If the angles φ_0 and ψ obey the inequalities $\varphi_0, \psi \ll 1$, then $\gamma_0 \approx \varphi_0$ and $\sin \psi \approx \psi$ (in practice, these conditions are satisfied within an accuracy not less than one percent at angles less than 15°).

In the general case of the inclination angle $\psi \neq 0$, dispersion equation (1) can be solved only numerically. In the reflection from a thick crystal in the Bragg geometry ($\gamma_h < 0$) one has to select only two roots of four ε_j ones, such that their imaginary parts would obey the inequality $\text{Im}(\varepsilon_j) > 0$ [16].

The detailed analysis at arbitrary angles φ_0 and φ_h was made elsewhere [27]. In this section, for the sake of simplicity we limit the consideration to the case, where the grazing angles φ_0 and φ_h for the incident and the diffracted waves exceed critical angle of the total external reflection $\varphi_c = (\text{Re}|\gamma_0|)^{1/2}$ by a factor of 1.5–2.0. Then, according to [16], the exit angle is

$$\varphi_h = [(\varphi_0 - 2\psi \sin \vartheta_B)^2 + \alpha]^{1/2}.$$

Formally, this results in the fact that the terms ε^2 in (1) can be ignored. As a result, equation (1) reduces to the quadratic equation whose solution has the form [1, 7]

$$\varepsilon = (1/4\gamma_0)[\alpha b + \chi_0(1 + b) \pm \{[\alpha b - \chi_0(1 - b)]^2 + 4bC^2\chi_h\chi_{\bar{h}}\}^{1/2}], \quad (3)$$

where $b = \gamma_0/\gamma_h$ is the coefficient of reflection asymmetry ($b < 0$), whereas the sign before the square root is determined by the conditions $\text{Im}(\varepsilon) > 0$. If the angular deviation $\Delta\vartheta$ considerably exceeds the half-width of the rocking curve, i.e., $\Delta\vartheta_B = C|\chi_h|/|b|^{1/2}\sin 2\vartheta_B$ (in this case, there are no strong diffraction reflection), then $\varepsilon \approx \chi_0/2\varphi_0$.

The amplitude coefficient of the diffraction reflection $R_h = E_h/E_0$ is determined by the equation well-known in the two-beam dynamical theory

$$R_h = (2\varphi_0\varepsilon - \chi_0)/C\chi_{\bar{h}}. \quad (4)$$

At the maximum, the rocking curve from an ideal crystal, $P_{h0} = (\varphi_h/\varphi_0)|R_h|^2$, and the incident radiation penetrates the crystal for an extinction length

$$L_{\text{ex}} = 1/(k_0 \text{Im}(\varepsilon)) = \lambda(\varphi_0\varphi_h)^{1/2}/\pi C|\chi_h|. \quad (5)$$

On the other hand, in terms of physics, the neglect of the terms ε^2 in (1) signifies that in the angular range

$\varphi_0, \varphi_h \geq (1.5-2)\varphi_c$, the effect of specular reflection on the diffraction reflection can be ignored (the reverse statement is not true). Indeed, far from the diffraction range, the dependence of the fields of the incident, specularly reflected, and refracted radiation on the coordinate z takes the form $E_0(z) = E_0 \exp(ik_0\varphi_0 z)$, $E_s(z) = E_s \exp(-ik_0\varphi_0 z)$, and $D_0(z) = D_0 \exp(ik_0\Phi_0 z)$, respectively, where $\Phi_0 = (\varphi_0^2 + \chi_0)^{1/2}$. From the continuity condition at the crystal surface $z = 0$ for the fields and their first derivatives with respect to z it follows that the amplitude coefficient of the specular reflection, $R_s = E_s/E_0$, is determined by the Eq. $R_s = R_F$, where

$$R_F = (\varphi_0 - \Phi_0)/(\varphi_0 + \Phi_0). \quad (6)$$

If the grazing angle $\varphi_0 \geq 1.5\varphi_c$, then $\Phi_0 \approx \varphi_0 + \chi_0/2\varphi_0$. Thus, it follows from Eq. (6) that $R_F \approx -\chi_0/4\varphi_0^2$, i.e., $|R_F| \approx 0.25(\varphi_c/\varphi_0)^2 \ll 1$ and the depth of the field penetration $L_s = 1/(k_0 \text{Im}(\Phi_0))$ is determined mainly by photoabsorption

$$L_s \approx \lambda\varphi_0/\pi \text{Im}(\chi_0). \quad (7)$$

Since $\text{Im}(\chi_0) \ll |\chi_h|$, it follows from (5) and (7) that $L_{\text{ex}} \ll L_s$. At grazing angles exceeding the critical angle of the total external reflection by a factor 1.5–2.0, the amplitude of the specular reflection is negligibly small in comparison with the amplitudes E_0 and E_h , whereas the depth of the field penetration is determined mainly by the diffraction reflection. According to Eq. (2), the refracted wave has the form $D_0(z) = D_0 \exp[ik_0(\varphi_0 + \varepsilon)z]$. Then the continuity condition for the fields and their derivatives yields

$$\begin{aligned} E_0 + E_s &= D_0, \\ \varphi_0(E_0 - E_s) &= (\varphi_0 + \varepsilon)D_0. \end{aligned} \quad (8)$$

With due regard for Eq. (8), the amplitude coefficient of specular reflection under the conditions of the Bragg diffraction from an ideal crystal can be described by the simple equation

$$R_s = -\varepsilon/(2\varphi_0 + \varepsilon), \quad (9)$$

where the quantity $\varepsilon(\Delta\vartheta)$ is set by Eq. (3). Since $\varepsilon \ll 2\varphi_0$, the angular dependence of specular reflection is determined mainly by the behavior of the function $\varepsilon(\Delta\vartheta)$. In other words, diffraction produces a noticeable effect on the specular reflection and, therefore, the anomalous angular behavior of specular reflection described by Eq. (9) is determined by the anomalous behavior of the effective refractive index of the crystal in the diffraction range $n(\Delta\vartheta) = 1 + \varepsilon\varphi_0$. One can readily see that at $\Delta\vartheta \gg \Delta\vartheta_B$, Equation (9) is reduced to the well-known Fresnel formula (6).

The characteristic feature of specular reflection under the diffraction conditions is the pronounced anomaly in the angular dependence of the intensity $P_s(\Delta\vartheta) = |R_s|^2$. It has the form of the dispersion-type

curve with the minimum and the maximum in the vicinity of the diffraction angles $\Delta\vartheta_{1,2} = \Delta\vartheta_0 \mp \Delta\vartheta_B$ corresponding to the range of total diffraction reflection, where $\Delta\vartheta_0 = \text{Re}(\chi_0)(1-b)/2b\sin 2\vartheta_B$ (solid curves 1 in Figs. 2 and 3). For the first time, the anomalous behavior of the specular reflection was considered in [9]. It should be indicated that the curves describing the secondary-radiation yield $I_{sp} \approx 1 + |R_h|^2 + 2v_i \text{Re}(R_h)$ with the exit depth small in comparison with the extinction length L_{ex} , where $v_i = C|\text{Im}(\chi_h)|/\text{Im}(\chi_0)$ also have similar shapes [7]. The analogy becomes obvious upon representing the function $\varepsilon(\Delta\vartheta)$ in (9) in terms of the amplitude coefficient of diffraction reflection (4):

$$R_s \approx -(\chi_0/4\varphi_0^2)(1 + vR_h), \quad (10)$$

where $v = C\chi_h/\chi_0$. Similar to the methods of X-ray standing waves (XRSW) [7, 9], the second multiplier in Eq. (10) characterizes the wave-field amplitude at the crystal surface. However, unlike the quantity v_i in the equations for secondary-radiation intensities, the quantity v for specular reflection in Eq. (10) is determined by the ratio of the complete complex polarizabilities χ_h and χ_0 , and not only of their imaginary parts.

The existence of the minimum and the maximum of the rocking curves $P_s(\Delta\vartheta)$ is caused by the fact that $|R_h|^2 \approx |b|$ in the whole range of strong diffraction reflection, whereas the phase of the amplitude reflection coefficient R_h in Eq. (10) varies almost linearly from π at $\Delta\vartheta = \Delta\vartheta_1$ to zero at $\Delta\vartheta = \Delta\vartheta_2$. In this case, $R_h(\Delta\vartheta_{1,2}) = \mp |b|^{1/2}$, i.e., $|b|$ can have different signs, which results in the formation of the minimum and the maximum of the angular dependence of the specular-reflection intensity. At small grazing angles ($\varphi_0 \ll 2\psi\sin\vartheta_B$), the asymmetric reflection coefficient is $|b| \ll 1$, which results in a rather small difference in the intensities $P_s^{\max} - P_s^{\min}$. With an increase of the grazing angle φ_0 , the quantity $|b|$ increases, and therefore the contrast of the specular reflection curves also increases (curves 1 in Figs. 3a and 3b). Simultaneously, the rocking-curve width and the angular range of the anomaly on the curve of specular reflection also decrease.

Now consider the specular and diffraction reflection from a crystal whose surface is coated with a plane-parallel homogeneous amorphous film of an arbitrary thickness d and polarizability χ_1 . The field in the film is due to the superposition of two eigenwaves, $E_l(z) = A_0 \exp(ik_0\Phi_1 z) + A_s \exp(-ik_0\Phi_1 z)$, where $\Phi_1 = (\varphi_0^2 + \chi_1)^{1/2}$. Using the continuity conditions for the fields and their derivatives at the vacuum–film and film–substrate

interfaces, we arrive at the system of four equations

$$\begin{aligned} E_0 + E_s &= A_0 + A_s, \\ \Phi_0(E_0 - E_s) &= \Phi_1(A_0 - A_s), \\ A_0 F + A_s F^{-1} &= D_0 f, \\ \Phi_1(A_0 F - A_s F^{-1}) &= (\varphi_0 + \varepsilon)D_0 f, \end{aligned} \quad (11)$$

where

$$F = \exp(ik_0\Phi_1 d), \quad f = \exp[ik_0(\varphi_0 + \varepsilon)d].$$

The solution of system (11) yields the following equation for the amplitude coefficients of reflection from the crystal coated with an amorphous film under the conditions of grazing Bragg diffraction:

$$R_s = (\varphi_0 - \Phi_1 S)/(\varphi_0 + \Phi_1 S), \quad (12)$$

where

$$\begin{aligned} S &= (1 - rF^2)/(1 + rF^2), \\ r &= (\Phi_1 - \varphi_0 - \varepsilon)/(\Phi_1 + \varphi_0 + \varepsilon). \end{aligned}$$

One can readily see that at $d=0$ (no film) equation (12) reduces to Eq. (9) for an ideal single crystal, because, in this case, $E = 1$ and $S = (\varphi_0 + \varepsilon)/\Phi_1$. In the case of a rather thick absorptive film, the phase factor tends to zero, $F \rightarrow 0$, and the reflection coefficient (12) reduces to the Fresnel equation $r_1 = (\varphi_0 - \Phi_1)/(\varphi_0 + \Phi_1)$, which describes reflection from the medium–film interface with the film polarizability χ_1 . As was to be expected, in this case, diffraction produces no effect on specular reflection.

Far from the diffraction range, the amplitude coefficient of specular reflection for a film of an arbitrary thickness, $R_{s0} = R_s(|\Delta\vartheta| \gg \Delta\vartheta_B)$, is also determined by Eq. (12) in which r should be substituted by $r_0 = (\Phi_1 - \Phi_0)/(\Phi_1 + \Phi_0)$. Thus, we obtain

$$R_{s0} = (r_1 + r_0 F^2)/(1 + r_0 r_1 F^2). \quad (13)$$

If a film is amorphous for X-rays and has the polarizability $\chi_1 = \chi_0$ coinciding with the substrate polarizability, the coefficient of reflection from the film–substrate interface in (13) is $r_0 = 0$, and, therefore, $R_{s0} = R_F$ [see Eq. (6)], which does not allow one to make any conclusion either about presence of an amorphous film or about its thickness based on the intensity data for specular reflection $P_{s0} = |R_{s0}|^2$. At the same time, under the diffraction conditions, the function $R_s(\Delta\vartheta)$ (12) remains sensitive to the film thickness even in the latter case. This is explained by the nonzero value of the coefficient r of X-ray reflection from the film–substrate interface because of different refractive indices of the substrate, $1 + \varphi_0\varepsilon(\Delta\vartheta)$, and the film, $1 + \chi_1/2$.

Under the conditions $\varphi_{0h} \gg \varphi_c$, the rocking-curve intensity from a crystal coated with a film only slightly decreases in comparison with the rocking-curve intensity

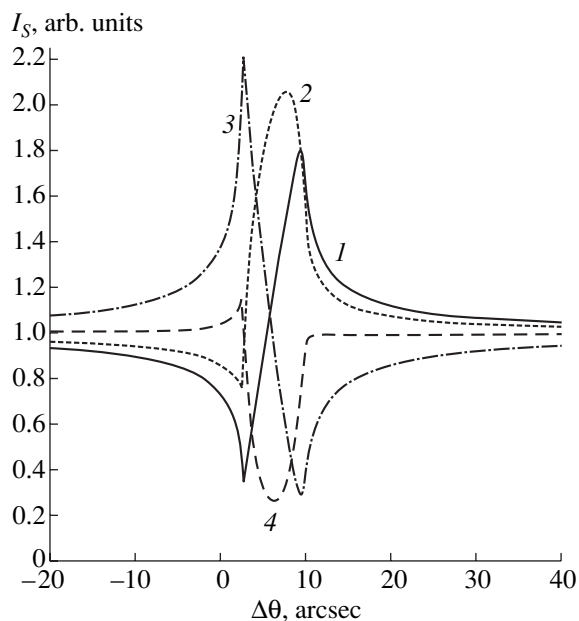


Fig. 2. Effect of the amorphous-film thickness on the angular dependence of the specular-reflection intensity at the fixed grazing angle. The thickness d of an oxide film on the silicon surface equals (1) 0 (an ideal single crystal), (2) 1, (3) 3, and (4) 4 nm; $\text{CuK}\alpha$ radiation, $\varphi_0 = 50'$, $\psi = 3^\circ$, $\text{Si}(2\bar{2}0)$ reflection.

for an ideal crystal because of absorption in the film: $P_h = P_{h0} \exp[-(\varphi_0^{-1} + \varphi_h^{-1})\mu_1 d]$, where $\mu_1 = k_0 \text{Im}(\chi_1)$.

Figure 2 shows the specular-reflection curves $I_s(\Delta\vartheta) = P_s/P_{s0}$ normalized to the specular-reflection intensity far from the diffraction range. The calculations were based on the rigorous theory [27] for various thicknesses of the amorphous film and the fixed value of the grazing angle φ_0 . It is seen that the change in the film thickness for fractions of a nanometer results in a considerable change in the angular behavior of the specular-reflection curves. It should also be indicated that in the angular range $\varphi_{0h} \geq 1.5\varphi_c$, the calculations by approximate Eqs. (9) and (12) almost coincide with the exact calculations (curves 2 and 3 in Fig. 3). The discrepancy observed in the range of smaller grazing angles is explained by an increased effect of specular reflection on the wave-field structure in the film and in the substrate [27].

Figure 3 illustrates the effect of the grazing angle φ_0 on the specular-reflection curves from an ideal crystal and a crystal coated with an amorphous film. It is seen that with an increase of the grazing angle, the sensitivity of the specular reflection to the presence of the amorphous film and its thickness d increases. This is explained by an increase in the exponent $k_0\Phi_1 d$ of the phase-sensitive coefficient F in Eq. (12) with an

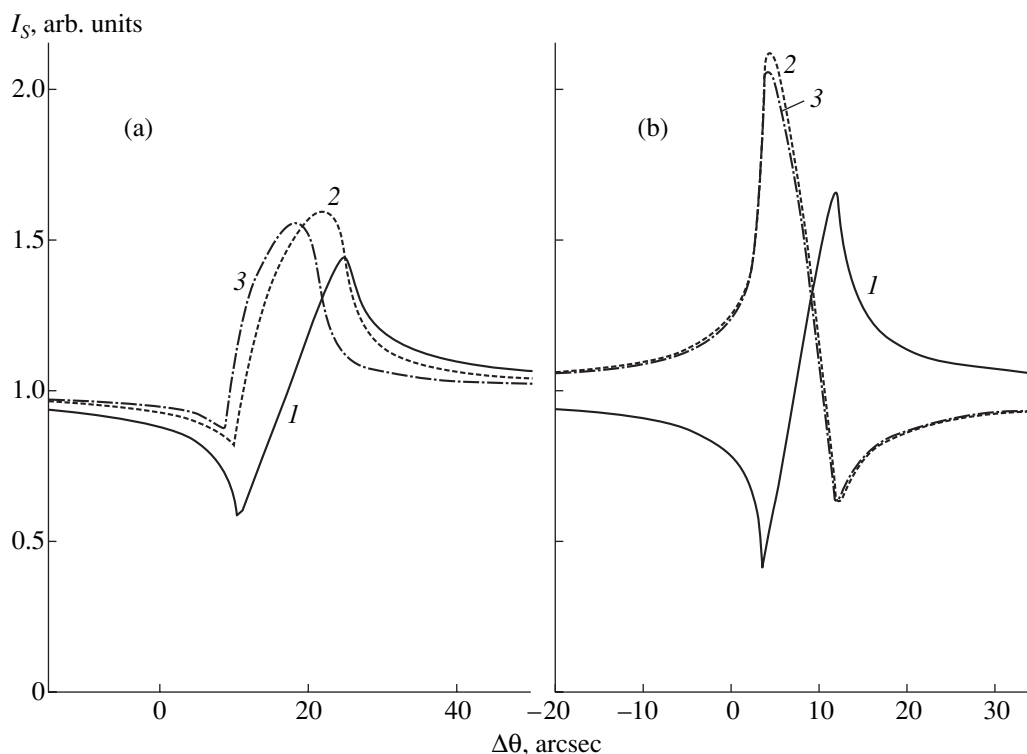


Fig. 3. Specular-reflection curves at grazing angles (a) $\varphi_0 = 20'$ and (b) $\varphi_0 = 40'$. (1) An ideal crystal, (2) a crystal with an amorphous SiO_2 film of thickness $d = 3$ nm, and (3) the curve calculated by the approximate Eq. (12); $\text{CuK}\alpha$ radiation, $\psi = 3^\circ$, $\text{Si}(2\bar{2}0)$ reflection.

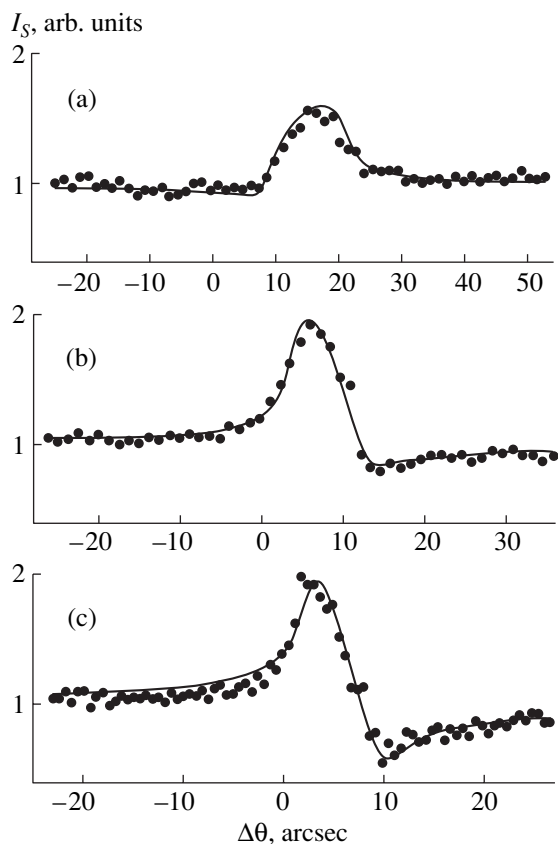


Fig. 4. Angular dependences of the specular-reflection intensities of CuK_{α} radiation from a silicon single crystal coated with an amorphous oxide film under the conditions of grazing Bragg diffraction at the grazing angles φ_0 (a) 23° , (b) 39° , and (c) 49° . Dots indicate the experimental data, solid lines indicate the theoretical calculation.

increase of the angle φ_0 . However, the absolute specular-reflection intensity drastically decreases (by the law $1/\varphi_0^4$).

EXPERIMENTAL

All the measurements were made in the double-crystal scheme and the parallel dispersion-free (n , $-n$) geometry of the crystal arrangement. The schematic of the experiment is shown in Fig. 1. The specimen was a silicon wafer 40 mm in diameter and 350 μm in thickness treated in polishing etchants. The wafer surface formed an angle $\psi = 3^\circ$ with the (111) crystallographic planes along the $[1\bar{1}0]$ direction. The high quality of the treated crystal was proved by the preliminary studies performed by the method of high-resolution triple-crystal X-ray diffractometry which revealed no residual damaged crystalline layer on the specimen surface. Thus, we assumed that the specimen surface was coated only with a very thin (2–4 nm) layer of the native oxide [7–9].

The source of $\text{CuK}_{\alpha 1}$ radiation was a standard 0.8 kW fine-focus X-ray tube. The radiation was horizontally collimated with the use of the strongly asymmetric (220) reflection from a perfect silicon crystal. The asymmetry factor of the crystal-monochromator was equal to $b_m = 0.03$, which corresponded to the horizontal divergence of the reflected X-ray beam of $0.9''$. The slit S_1 was used to separate the $K_{\alpha 1}$ line from the general X-ray spectrum. The vertical beam divergence determined by the dimensions of the focus and the slit S_2 at the collimator exit was equal to 2.3 arcmin. The angular intensity distribution of the incident beam in the vertical plane was preliminarily measured by scanning with the use of a narrow slit S_3 located before the detector D_1 prior to the location of the specimen.

The noncoplanar grazing diffraction was obtained from the (220) planes forming an angle of 87° with the specimen surface. Scanning in the vicinity of the Bragg angle was made at three fixed grazing angles of the X-ray beam: $\varphi_0 = 23, 39,$ and 49 arcmin. In this case, the detectors D_1 and D_2 recorded the intensities of the specularly reflected and diffracted waves, respectively. The specular-reflection curves were measured at large deviations $\Delta\vartheta = \pm 150''$ from the Bragg angle. The time of the intensity accumulation at each point was selected in a way to provide the statistical accuracy not worse than three-five percent.

RESULTS AND DISCUSSION

The experimental results are shown by dots in Fig. 4. With an increase of the grazing angle, the asymmetry of the experimental specular-reflection curves changes, and their amplitude increases. On the whole, this agrees with the behavior of curves in Fig. 3. It should also be indicated that the corresponding rocking (diffraction-reflection) curves (not shown in Fig. 4) are practically equivalent to the rocking curves calculated for an ideal crystal. The results of processing of the experimental specular-reflection data under the conditions of grazing noncoplanar diffraction are shown by solid lines in Fig. 4. The theoretical calculations were performed on the basis of the rigorous equations for the specular-reflection intensities [27] with due regard for the convolution with the reflection curve of the asymmetric crystal-monochromator and the convolution with the function of the angular distribution of the incident-beam intensity in the vertical plane. The experimental curves were processed using the minimization of the functional $Q(d, \chi_1) = N^{-1} \sum_i |I_{s,i}^{\text{exp}} - I_{s,i}^{\text{theor}}| / I_{s,i}^{\text{exp}}$ characterizing the average relative discrepancy between the theoretical and experimental values, where N is the number of points on the experimental curves and i is the number of points corresponding to the diffraction angles $\Delta\vartheta_i$. The minimization reduced to the variation of the film thickness d and film polarizability χ_1 .

The analysis of all the data on the minimization of three specular-reflection curves obtained from one specimen at three different grazing angles provided the determination of the average thickness of the oxide film and the film polarizability with a rather high accuracy— $d = 2.8 \pm 0.05$ nm and $\chi_1 = (-13.59 + i0.18) \times 10^{-6}$, respectively. At the obtained χ_1 -value, the density of the amorphous film is $\rho = 2.1 \pm 0.06$ g/cm³. The value of ρ was calculated with allowance for the dispersion corrections Δf_j to the amplitude of atomic scattering (in the forward direction) [28] and the mass attenuation coefficients τ_j [29] calculated by the general equations for the real and imaginary parts of polarizability in the multi-component medium:

$$\chi_{0r} = -(\rho N_A r_0 \lambda^2 / \pi B) \sum_j c_j (Z_j + \Delta f_j),$$

$$\chi_{0i} = (\rho \lambda / 2\pi B) \sum_j c_j A_j \tau_j,$$

where ρ is the material density, $r_0 = e^2/mc^2$ is the classical electron radius, N_A is the Avogadro number, Z_j is the charge of the nucleus of the j th kind (in our case, silicon and oxygen), $B = \sum_j c_j A_j$, A_j are the atomic numbers, and c_j is the number of the j th kind atoms per formula unit ($c_j = 1$ and 2 for silicon and oxygen in SiO₂, respectively). For comparison, the densities of the hexagonal modification of crystalline quartz, the cubic and the tetragonal cristobalite phases, and fused quartz are 2.65, 2.32, and 2.07–2.21 g/cm³, respectively.

It should be remembered that the specular reflection curves under the conditions of grazing diffraction are much more sensitive to small film thicknesses than the curves obtained by the conventional total external reflection method [7, 8], in which the existence of the film on the crystal surface is established by measuring the specular reflection curves as functions of the grazing angle φ_0 during $\vartheta/2\vartheta$ scanning and the subsequent analysis of the thickness oscillations with the period $\Delta\varphi_0 \approx \lambda/2d$ at angles $\varphi_0 > \varphi_c$. Indeed, because of a rapid decrease of the intensities of the specular reflection curves (from five to six orders of magnitude at $\varphi_0 \leq 10\varphi_c$), this traditional method is efficient only for rather thick ($d \geq \lambda/4\varphi_c \sim 10$ nm) films (the critical angles of total external reflection for silicon single crystals with oxide films are 13.4' and 12.7', respectively). Figure 5 shows the calculated specular-reflection curves from the film–substrate system. It is seen that for thin films, the specular-reflection curves only slightly differ from the corresponding curves for the substrates. The curve has almost no oscillations (especially at $d \leq 5$ nm) and the film manifests itself only in a certain change of the specular-reflection intensity in comparison with the reflection from an ideal surface, so that the labor-consuming measurements of the absolute intensity are required. The comparison of the curves in Figs. 2 and 3 with those in Fig. 5 clearly demonstrates the advantages of the specular-reflection method under the conditions

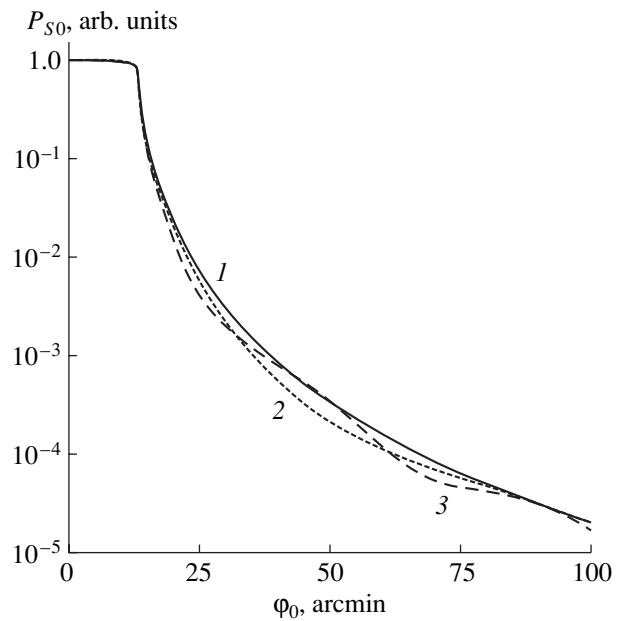


Fig. 5. Dependence of the specular-reflection intensity of CuK α radiation on the grazing angle φ_0 far from the diffraction range. The thickness d of the SiO₂ film is (1) 0 (an ideal silicon single crystal), (2) 3, and (3) 6 nm.

of grazing diffraction in comparison with the traditional method.

For real objects, the traditional total external reflection method is also encounters difficulties because the specular-reflection intensity decreases with an increase of the grazing angle somewhat faster owing to the inevitable presence of small-scale surface roughness. This is quite understandable because that the Fresnel reflection coefficients $r_{0,1}$ in Eq. (13) are multiplied by the Debye–Waller factor $f_{0,1} = \exp[-2k_0^2\varphi_0^2\sigma_{0,1}^2]$, where σ_0 and σ_1 are the root-mean-square heights of the relief at the film–substrate interface and on the film surface, respectively. Under the conditions of grazing diffraction, one has to analyze also the angular behavior of the normalized $I_s(\Delta\vartheta)$ curves for which the division of the intensity P_s by specular-reflection intensity P_{S0} far from the diffraction range weakens the effect of the roughness height on the function I_s . Indeed, since in the angular range $\varphi_0 \geq 1.5\varphi_c$, the reflection coefficients $r, r_{1,2} \ll 1$, it follows from Eqs. (12) and (13) that the ratio R_s/R_{s0} is

$$\frac{R_s}{R_{s0}} \approx [\chi_1 - (\chi_1 - 2\varphi_0\varepsilon)f_{0,1}F^2] / [\chi_1 - (\chi_1 - \chi_0)f_{0,1}F^2],$$

where $f_{0,1} = \exp[-2k_0^2\varphi_0^2(\sigma_0^2 - \sigma_1^2)]$, whence it follows that, if, e.g., $\sigma_0 = \sigma_1$, the curve $I_s(\Delta\vartheta)$ becomes independent of the roughness height.

As has already been indicated, the specular-reflection curves under the conditions of X-ray grazing diffraction are similar to the photoelectron- and fluores-

cence-yield curves for thin layers in the method of X-ray standing waves, but the mechanisms of their formations are quite different. Indeed, the anomalies in the curves of the secondary-radiation-yield are provided by the coherent shift of the film atoms with respect to the nodes and antinodes of an X-ray standing wave formed due to diffraction reflection from the substrate. In our case, the angular dependence of the specular-reflection curves is caused by the anomalous behavior of the refractive index of the substrate in the range of diffraction reflection and the interference of the waves specularly reflected from the film surface and the film-substrate interface.

Despite the fact that at angles $\varphi_0 > 1.5\varphi_c$, the specular-reflection coefficient is very low, the intensity of the specularly reflected wave can be rather high and can exceed by several orders of magnitude the intensity of the photoelectron or fluorescence yields in the method of X-ray standing waves. Indeed, the estimation of the fluorescence-radiation intensity P_F from the film showed [27] that at the angles $\varphi_0 \sim (2-4)\varphi_c$, it is described by the relationship

$$P_F/P_S \approx 8c\beta^{-1}(d/\lambda)(\varphi_0^3\chi_{1i}/\chi_1^2)\Delta\Omega,$$

where c is the relative concentration of the fluorescing atoms, β is the coefficient of electron conversion, and $\Delta\Omega$ is the solid angle of recording. For example, if $d \approx 1$ nm, $\lambda \approx 0.1$ nm, $\beta \sim 10-50$, $c \approx 0.5$, $\Delta\Omega \approx 2\pi$, and $\varphi_0 \approx 2\varphi_c$, then at the characteristic polarizabilities $|\chi_{1i}| \approx 10^{-5}$ and $\chi_{1i} \approx 0.02|\chi_{1i}|$, we have that the P_F/P_S ratio is $\sim 3 \times (10^{-3}-10^{-2})$, i.e., the intensity of the specularly reflected wave exceeds the intensity of the fluorescence yield by one to two orders of magnitude. It should also be indicated that recording of the soft fluorescence radiation from oxygen atoms is possible only in a vacuum and is associated with considerable technical difficulties. The perspectives of the application of specular reflection under the noncoplanar grazing diffraction conditions to solution of practical problems are also associated with these problems.

CONCLUSIONS

Thus, we reported here the first experimental detection and the study of the anomalous angular behavior of specular reflection of X-rays under the conditions of noncoplanar X-ray diffraction in a crystal coated with an amorphous film. The phenomenon is interpreted theoretically. The developed theory satisfactorily agrees with the experiment. It is shown that the specular-reflection curves are highly sensitive to the thickness of an amorphous layer several nanometers thick and even thicker. The optimum grazing angles are determined to range from 1.5 to 3-4 critical angles of total external reflection. The specular-reflection intensity in this angular range is by one to two orders of magnitude higher than the intensity of the secondary processes in the method of X-ray standing waves which allows us to

state that at smaller grazing angles, the specular-reflection intensity should increase, whereas the method sensitivity to the film thickness should considerably decrease. Using the method of mathematical simulation of the specular-reflection curves, we determined both the thickness and the density of the native SiO₂ oxide film coating the surface of the silicon single crystal studied.

ACKNOWLEDGMENTS

This work was supported by the Russian Foundation for Basic Research, project no. 00-02-17716, and the Ministry of Industry, Science, and Technologies of the Russian Federation, subprogram *Physics of Solid-State Nanostructures*, project no. 98-3009.

REFERENCES

1. Z. G. Pinsker, *X-ray Crystal Optics* (Nauka, Moscow, 1982).
2. P. Farwig and H. W. Schurmann, *Z. Phys.* **204** (2), 489 (1967).
3. S. Kishino and K. Kohra, *Jpn. J. Appl. Phys.* **10** (5), 551 (1971).
4. T. Bedynska, *Phys. Status Solidi A* **19** (1), 365 (1973).
5. J. Hartwig, *Phys. Status Solidi A* **37** (2), 417 (1976).
6. A. M. Afanas'ev, R. M. Imamov, and E. Kh. Mukhamedzhanov, *Crystallogr. Rev.* **3** (2), 157 (1992).
7. A. M. Afanas'ev, P. A. Aleksandrov, and R. M. Imamov, *X-ray Diffraction Diagnostics of Submicron Layers* (Nauka, Moscow, 1989).
8. M. A. Andreeva, S. F. Borisova, and S. A. Stepanov, *Poverkhnost*, No. 4, 5 (1985).
9. A. M. Afanas'ev and R. M. Imamov, *Kristallografiya* **40** (3), 446 (1995) [*Crystallogr. Rep.* **40**, 406 (1995)].
10. W. C. Marra, P. Eisenberger, and A. Y. Cho, *J. Appl. Phys.* **50** (11), 6927 (1979).
11. A. M. Afanas'ev and M. K. Melkonyan, *Acta Crystallogr., Sect. A: Found. Crystallogr.* **39** (2), 207 (1983).
12. P. A. Aleksandrov, A. M. Afanas'ev, M. K. Melkonyan, and S. A. Stepanov, *Phys. Status Solidi A* **81** (1), 47 (1984).
13. A. L. Golovin and R. M. Imamov, *Phys. Status Solidi A* **77** (1), K91 (1983).
14. A. L. Golovin, R. M. Imamov, and S. A. Stepanov, *Acta Crystallogr., Sect. A: Found. Crystallogr.* **40** (3), 225 (1984).
15. A. L. Golovin and R. M. Imamov, *Phys. Status Solidi A* **80** (1), K63 (1983).
16. P. A. Aleksandrov, A. M. Afanas'ev, and S. A. Stepanov, *Kristallografiya* **29** (2), 197 (1984) [*Sov. Phys. Crystallogr.* **29**, 119 (1984)].
17. P. A. Aleksandrov, A. M. Afanas'ev, and S. A. Stepanov, *Phys. Status Solidi A* **86** (1), 143 (1984).
18. P. A. Aleksandrov, A. M. Afanas'ev, A. L. Golovin, *et al.*, *J. Appl. Crystallogr.* **18** (1), 27 (1985).
19. A. M. Afanas'ev, S. M. Afanas'ev, A. V. Esayan, and F. R. Khashimov, *Poverkhnost*, No. 12, 35 (1988).

20. G. H. Vineyard, *Phys. Rev. B* **26** (8), 4146 (1982).
21. S. Dietrich and H. Wagner, *Phys. Rev. Lett.* **51** (16), 1469 (1983).
22. H. Dosch, B. W. Batterman, and D. C. Wack, *Phys. Rev. Lett.* **56** (11), 1144 (1986).
23. O. G. Melikyan, *Kristallografiya* **36** (3), 549 (1991) [*Sov. Phys. Crystallogr.* **36**, 300 (1991)].
24. A. M. Afanas'ev and O. G. Melikyan, *Phys. Status Solidi A* **122** (2), 459 (1990).
25. M. A. Andreeva, K. Rocete, and Yu. P. Khapachev, *Phys. Status Solidi A* **88** (2), 455 (1985).
26. S. Stepanov and R. Kohler, *J. Phys. D* **27** (7), 1922 (1994).
27. V. A. Bushuev and A. P. Oreshko, *Fiz. Tverd. Tela (St. Petersburg)* **43** (5), 906 (2001) [*Phys. Solid State* **43**, 941 (2001)].
28. T. Cromer and D. Liberman, *J. Chem. Phys.* **53** (5), 1891 (1970).
29. M. A. Blokhin and I. G. Shveitser, *X-ray Spectrum Handbook* (Nauka, Moscow, 1982).

Translated by L. Man

Calculation of Radial Distribution Function from Incomplete Experimental Diffraction Data

E. A. Soldatov and A. I. Mashin

Nizhni Novgorod State University, Nizhni Novgorod, 603600 Russia

e-mail: root@sold.sci-nnov.ru

Received January 25, 1999; in final form, June 1, 2000

Abstract—A method for calculating atomic radial distribution functions for amorphous materials has been suggested. The method is based on the principle of the maximum informational entropy. Under the condition of a limited amount of the experimental diffraction data, the method allows one to obtain the unique solution and considerably reduces the errors caused by series termination, which are inherent in traditional computational methods based on the Fourier transform. A criterion of using the method of optimum information is formulated, and the reliability of the data obtained are quantitatively estimated. The advantages of the method are demonstrated on the computation of the short-range order in hydrogenated amorphous silicon. © 2001 MAIK “Nauka/Interperiodica”.

The calculation of the radial distribution function (RDF) $\rho(r)$ related to experimentally measured intensities $I(s)$ of diffracted rays by the well-known relationship [1]

$$I(s) \sim \int_0^{\infty} \rho(r) \sin(sr)/(sr) dr \quad (1)$$

is a practically important problem often encountered in diffraction studies of materials.

The traditional method of determination of $\rho(r)$ is based on the use of the Fourier transform of expression (1) with an infinite upper integration limit. In practice, the intensity curve $I(s)$ is determined within a finite (and not infinite from 0 to ∞) interval of s values. In transmission diffraction experiments, the rays scattered at small angles overlap with the primary beam, whereas, in the reflection geometry, they overlap with the specimen edges, which hinders the determination of the intensity in the range of s -values from zero up to a certain s_1 value. On the side of large s values, this limit is associated with the apparatus function and, in the best case, with the maximum possible scattering angle. In practice, its value is still lower. As a result, we arrive at numerous solutions for $\rho(r)$, which make the above relationship an identity. Thus, the main problem in the analysis of the intensity curve is the estimation, reduction, or complete elimination of the effect of the experimental intensities termination from the side of large s values. In comparison with the termination at low s values, the influence of this effect on the position and the shape of the maxima and the area under these maxima is prevailing [2]. In the computations with the use of the Fourier transform, the termination on the side of large s -values gives rise to numerous auxiliary maxima. The

negative effects caused by insufficient number of the experimental data can be reduced by various methods of which the most widespread are the regularization methods and the representation of the functions sought in the form of some analytical expressions [3, 4].

At present, one often processes the experimental data by various modifications of the maximum-entropy method providing the mathematical formalization of the principle of information optimum. This approach was formulated by Janes as the formal method for substantiation of statistical mechanics [4, 5] and is widely used in processing of experimental data [6]. Recently, we have seen ever increasing use of the maximum-entropy method in crystallography [7–9]. According to the principle of information optimum, the most appropriate model of all the models of physical systems that are equally consistent with the initial experimental data is the model containing the minimum amount of information or having the maximum information entropy. If the system can be described by the probability distribution, this principle reduces to the requirement of the maximization of the information-entropy of the distribution and is called the principle of the maximum information entropy. The general consideration shows that the models of various physical systems constructed on the basis of this principle and the conclusions made on their basis are the most reliable ones in terms of information. However, the objective criteria providing the quantitative estimates of the reliability of the data obtained by the methods of optimum information have not been obtained as yet.

The present study was aimed at the study of the applicability of the principle of the maximum information entropy for the reconstruction of the RDF and for-

mulation of a criterion for estimating the reliability of the results obtained.

The radial distribution function providing the optimum information was constructed by optimizing the Shannon information functional [10] in the form

$$H(\rho) = -\int \rho(r) \log \rho(r) dr \rightarrow \max. \quad (2)$$

Following [1], we considered the RDF $\rho(r)$ related to the intensity of the scattered radiation $I(s)$ by the following formulas:

$$i(s) = \int \rho(r) \frac{\sin(sr)}{sr} dr, \quad (3)$$

$$\rho(r) = \frac{2}{\pi} \int i(s) sr \sin(sr) ds, \quad (4)$$

where

$$i(s) = \frac{I(s)}{nf^2} - 1,$$

n is the number of scattering atoms, and f is the atomic scattering factor for the given radiation.

The discrete variant of the above equations is

$$i_k = \sum_{k=1}^M \rho_k \frac{\sin(s_k r_k)}{s_k r_k}, \quad (5)$$

$$\rho_k = \frac{2}{\pi} \sum_{k=1}^N i_k s_k r_k \sin(s_k r_k), \quad (6)$$

where N determines the number of the intensities used for the reconstruction and M is the number of the RDF values.

The analytical solution of the variational problem of optimizing the information functional is now reduced to the solution of the system of nonlinear equations of the type

$$\rho(r) = \exp \left[\sum_{n=m}^M \lambda_n \sin(s_n r) \right]^2. \quad (7)$$

The number of the Lagrange factors λ_n equals the number of the intensity values I_n used in the RDF reconstruction and amounts up to several hundred values.

The sought for a physically sound solution requires the use of the following condition:

$$\rho(r) \geq 0. \quad (8)$$

Figures 1 and 2 present the angular dependence of the intensities of electron scattering and the model radial distribution functions calculated by the traditional method and the method based on the approach described above. It is seen from Fig. 2 that the data calculated by the traditional method deviate from the initial model much more pronouncedly than the curve obtained by optimizing the information functional (2).

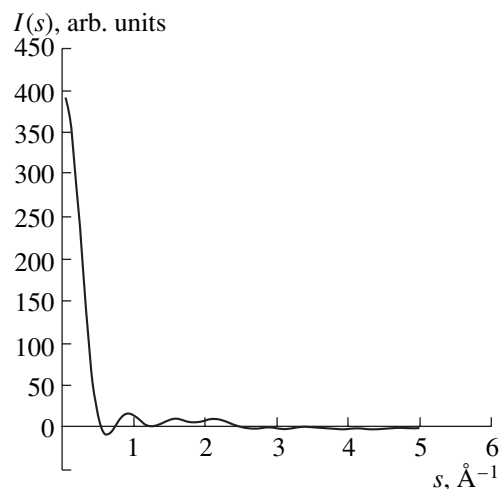


Fig. 1. Model of the angular dependence of electron scattering intensities.

The criterion of the reliability of the results obtained by the traditional methods of processing the experimental data is the accuracy with which the object was restored. In many instances, such estimates are based on the linear theory of errors, which allows one to relate the accuracy of the experimental data determination to the accuracy of the object restoration. Moreover, it also takes into account the “experimental” data that should have been present but, in fact, were absent because of the real experimental conditions or because some parameters of the physical systems cannot be measured in principle. These approaches are rather well developed and widely used [2]. The formulation of the problem in the methods of optimum information used in processing of experimental data is quite different. It is impossible to estimate *a priori* the influence of the lacking data, because, in the course of data processing, the experimental data should be used in the “theoretical construction.” Thus, the reliability of the approaches based on optimum-information principle in comparison with the reliability of the traditional methods is determined by the degree of reliability with which these methods “reproduce” the lacking experimental data. Therefore we suggest here the following approach for determining the degree of reliability of the results obtained. The problem is solved by using not the whole set of the experimental data but only a part of it. At the first stage of the study, the data, which, in accordance with the experimental conditions, are close to experimentally unattainable ones (i.e., the intensities at the smallest and the largest diffraction angles) are ignored. Upon the creation of the model of the physical system based on these reduced or imperfect experimental data, one has to calculate the set of the experimental data that were ignored at the first stage on the basis of the model obtained. Only then, the calculated and the measured but earlier ignored data, are compared. The degree of the

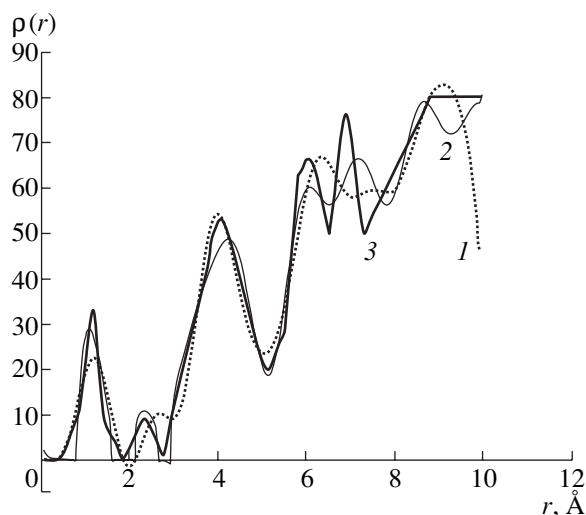


Fig. 2. RDF curves calculated by the (1) traditional method and (2) the method of optimizing the information functional and (3) the model curve.

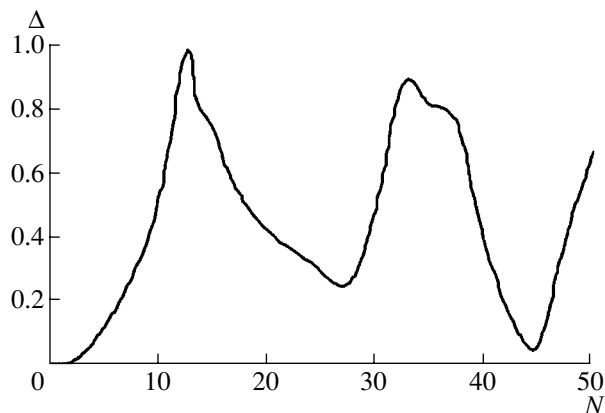


Fig. 3. Dependence of the relative discrepancy between the initial intensity data and the predicted curve as a function of the number of the ignored data.

reliability of the theoretical–informational approach is evaluated from the agreement of these two data sets.

Figure 3 shows the discrepancy between the initial and the predicted data sets obtained from the experimental diffraction intensities as a function of the number of ignored (not considered) data. The total volume of the experimental data in this case is $N = 50$. The discrepancy equal to unity signifies the complete (100%) disagreement of these data. In this case, the method suggested above gives no advantages over the traditional Fourier method. It is seen from Fig. 3 that the discrepancy is a nonmonotonic function and that the reconstruction is rather successful (in the sense of the criterion formulated above) even if a small number of the intensity values were used. The maximum discrepancy arises each time when we ignore (do not consider)

a set of the data located between two minima on the intensity curve.

Figure 4 exemplifies the use of the new method of calculating the atomic RDF based on the experimental scattering curves obtained in the electron diffraction experiments on thin films of α -Si : H synthesized by decomposition of silane in the high-frequency glow-discharge plasma at the substrate temperature 250°C. The transition from the scattered intensities to the RDF was made by both traditional method [1] (curve 1) and optimization of the information functional (curve 2). Curve 1 is characteristic for the RDF of amorphous silicon films [12]—the first and the second maxima are considerably blurred; in the range of small r , the RDF shows negative values having no physical sense. Using the method described in [1], we established that the average radius of the first coordination sphere equals $r_1 = 2.34 \pm 0.04$ Å, the first coordination number equals $n_1 = 3.8 \pm 0.2$, the second coordination number equals $n_2 = 15$, and the valence angle equals $\varphi = 119^\circ$. Thus, the parameters of the first coordination sphere are close to those of the crystalline material and are admissible for amorphous films, whereas the parameters of the second coordination sphere are quite dubious. Slightly lower (in comparison with the data for the crystalline material) first coordination number can be explained by a lower (by about 10–12%) density of the amorphous film. However the second coordination number considerably exceeds the value of 12 characteristic of crystalline silicon and is inconsistent with the reduced density of the amorphous material.

The calculation of the short-range order parameters by the methods suggested in [12] slightly improves the situation, especially for the second and the following spheres. In this case, the second maximum on the RDF curve can be interpreted as the result of the pronounced overlap of the second and the following coordination spheres. Assuming that the atomic distribution in each coordination sphere obeys the normal distribution law and using the mathematical methods of optimization, one can obtain a more detailed information about each of these spheres. The reliability of the results obtained is determined by the number of unknown parameters. Using the method suggested in [12], we obtained $n_2 = 11.3 \pm 0.9$ and $\varphi = 112^\circ \pm 6^\circ$. These values for the second coordination sphere are quite consistent with the modern ideas on the structure of amorphous silicon films. However, the accuracy of these data is rather low, because the pronounced overlap of the coordination spheres forced us to vary all the parameters of the normal distribution law in the process of mathematical optimization. Curve 2 in Figure 4 is calculated by our method. As was indicated above, it corresponds much better to the true distribution of atoms in the amorphous material. It is seen from Fig. 4 that the RDF has narrower maxima and no negative values. The parameters of the first coordination sphere (except for the curve width) coincide with those calculated by the traditional

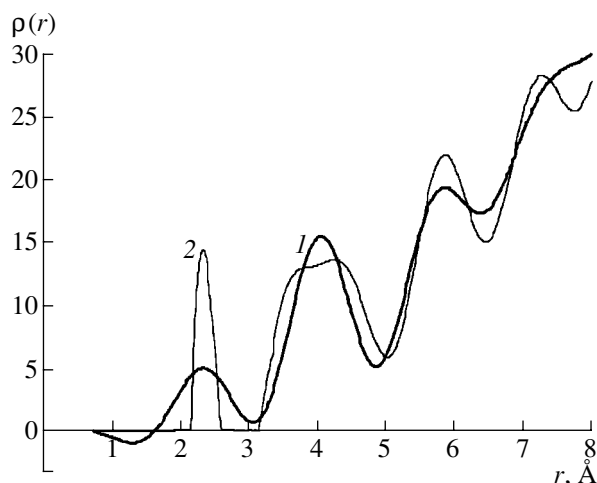


Fig. 4. RDF for hydrogenated amorphous silicon calculated from the experimental electron-scattering intensities by (1) the traditional method and (2) the method of optimizing the information functional by Eq. (2).

method. A decrease in the width of the first maximum allows us to eliminate the interatomic distances having no physical sense, which are always present in the RDF calculated by the conventional method from diffraction data. Because the maxima are narrower, the shape of the second RDF maximum allows one to measure the radii of the second and one of the third coordination spheres directly and then to estimate the dihedral angle. Thus, the number of fitting parameters and the ranges of their variation for curve 2 in the method [12] can be reduced, which increases the accuracy of their determination. Upon the corresponding calculations, we obtained $n_2 = 10.1 \pm 0.5$ and $\varphi = 109^\circ \pm 4^\circ$. In this case, the errors are determined by the accuracy of the apparatus used in the experiment.

Thus, the use of the method suggested in this study for calculating RDF, which is based on the optimization

of the information functional, provides a considerable increase of the reliability of the data on the short-range order structure of an amorphous material under the conditions of reduced volume of the experimental diffraction data.

REFERENCES

1. L. I. Tatarinova, *Electron Diffraction Analysis of Amorphous Substances* (Nauka, Moscow, 1972).
2. F. A. Brusentsev, *Mathematical Methods for Solving Some Problems of Solid State Physics and Structural Chemistry on Computers* (Naukova Dumka, Kiev, 1973).
3. A. S. Krylov and B. M. Shchedrin, *Kristallografiya* **34**, 1088 (1989) [*Sov. Phys. Crystallogr.* **34**, 657 (1989)].
4. E. T. Jaynes, *Phys. Rev.* **106**, 620 (1957).
5. E. T. Jaynes, *Proc. IEEE* **70**, 939 (1982).
6. C. J. Gilmore, *Acta Crystallogr., Sect. A: Fundam. Crystallogr.* **52**, 561 (1996).
7. E. A. Soldatov, É. A. Kuz'min, V. V. Ilyukhin, *et al.*, *Dokl. Akad. Nauk SSSR* **255**, 862 (1980) [*Sov. Phys. Dokl.* **25**, 953 (1980)].
8. É. A. Kuz'min, E. A. Soldatov, and V. V. Ilyukhin, *Kristallografiya* **26**, 1048 (1981) [*Sov. Phys. Crystallogr.* **26**, 665 (1981)].
9. E. A. Soldatov and S. I. Ovsetsin, *Information-Theoretical Methods in Structural Analysis of Crystals* (Nizhne-Novg. Gos. Univ., Nizhni Novgorod, 1997).
10. C. Shannon, *Works on Information and Cybernetics Theory: Collection of Articles* (Inostrannaya Literatura, Moscow, 1963).
11. O. N. Kassandrova and V. V. Lebedev, *Analysis of the Results of Observations* (Mir, Moscow, 1979).
12. V. N. Gordeev, A. I. Popov, and V. I. Filikov, *Izv. Akad. Nauk SSSR, Neorg. Mater.* **16**, 1733 (1980).

Translated by L. Man

THEORY OF CRYSTAL STRUCTURES

Fractal Images of Quasicrystals as an Example of Penrose Lattice

V. V. Yudin and Yu. A. Karygina

Far East State University, Vladivostok, Russia

e-mail: july@ift.phys.dvgu.ru

Received June 6, 2000

Abstract—The Penrose lattice, an example of quasicrystals, is considered as a fractal set. The generation of these sets in the graph tree form is considered. The problem of percolation of informodynamic characteristics and fractal dimensions defined in terms of the information entropy is solved for the constructed graphs. © 2001 MAIK “Nauka/Interperiodica”.

In 1984, the group headed by Shechtman obtained the metal alloy of the composition $\text{Al}_{86}\text{Mn}_{14}$ [1] later called a quasicrystal. Since then, the interest in these unique objects has not diminished. On the one hand, quasicrystals are characterized by the presence of the symmetry axis forbidden in the classical crystallography. On the other hand, they possess a long-range order, which is confirmed by their diffraction patterns. The geometric image that can possess such characteristics is a fractal. In other words, one can assume that all the quasicrystals would essentially be fractal objects. The planar model of a quasicrystal is a Penrose lattice. It seems to be logic to generate such a tiling by invoking the methods of the fractal geometry. First, consider a Penrose lattice as a linguistic structure, construct an alphabet, and formulate some grammatical rules. The alphabet corresponding to a Penrose lattice is dual three-level one. The first (letter) level is formed by two gold or *g*-triangles (Fig. 1a). The icosceless triangles with the unit lateral sides are called gold triangles, since the values of their bases $\alpha_1 \approx 1.618$ and $\alpha_2 \approx 0.618$ are obtained from the golden section equation, $\alpha^2 - \alpha - 1 = 0$. The second (syllable) level of the alphabet is a pair of *g*-rhombuses (“obtuse” and “acute” ones) obtained by join of two *g*-triangles along a particular side (Fig. 1b). The third (sentence) level consists of two ten-vertex polygons (Fig. 1c) of which the starlike (or simply star) one has the point of “pentasymmetry” and the dorsal one possesses the dorsal symmetry and the point of “pentacoordination.” Both ten-vertex polygons are built by five obtuse and five acute rhombuses. Now, formulate the corresponding rules—the exclusion rules for certain combination at the highest level of the alphabet. They read as follows:

—a star ten-vertex polygon can form a join only with the intersection in the form of an acute rhombus and only with the dorsal ten-vertex polygons;

—dorsal ten-vertex polygons can form (a) a join with the intersection along the arrow head (a shadowed

element in Fig. 1) and (b) a join without intersection, which is formed by a pair of thick rhombuses such that the axes of ten-vertex polygons should form angles of 36° , 72° , and 144° .

Now proceed to the construction of a tiling using the methods of the fractal geometry. Consider the generation of a Penrose lattice in the direction of “deflation.” Any element allowed by a Penrose lattice can serve as a global center of a fractal figure. Then rhombuses are divided as is shown in Fig. 2. As a result, we arrive at a

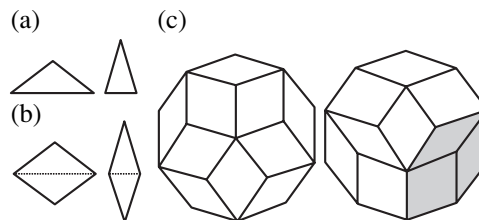


Fig. 1. Alphabet for Penrose lattices: (a) the first, (b) the second, and (c) the third levels.

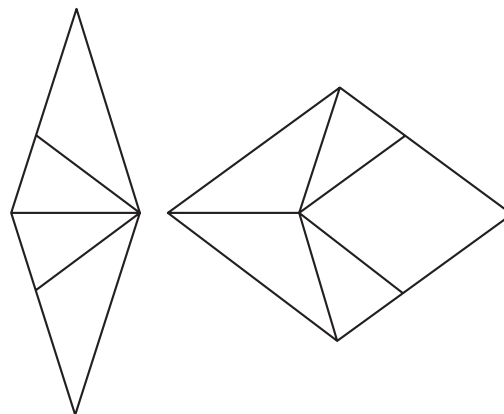


Fig. 2. Tiling with *g*-rhombuses.

tiling pattern with second-generation rhombuses. To construct the rhombuses of the following generations, the iteration procedure is used. The coefficient of the deflation scale has the form

$$K^n = (\alpha_2 + 1)^n = \alpha_1^n = F_n \alpha_1 + F_{n-1}, \quad (1)$$

where n is the iteration order and $F_n = F_{n-1} + F_{n-2}$ are the numbers of the Fibonacci sequence. The coefficient given by (1) is an irrational number and, therefore, the generated tiling should have “sources” and “sinks” [2]. Below we present a Penrose lattice generated by the elements of our alphabet, i.e., rhombuses and ten-vertex polygons. Lattices growing from g -rhombuses are shown in Fig. 3. One can readily see that the grammatical rules formulated earlier at the level of ten-vertex polygons are also valid here. The strict similarity of the tilings considered is revealed at the m th step of the iteration process, $m = (6n + 1)$, which means that an exact copy of the polygon diminished by a factor of K^m can be found exactly in the rhombus center. One can interpret this tiling in another way. Because of the internal symmetry (rhombuses of the next generations), one can attribute a “spin” to a rhombus position in the plane and single out a point of “pentacoordination” (the so-called barycenter) lying on the g diagonal of the initial rhombus (for lattice growing from an acute rhombus, this point arises beginning with the level $n = 3$). Then the spin flip occurs at each iteration step, whereas the barycenter oscillates about the g -diagonal by the law $\sum_{n=0}^{\infty} (-1/K)^n$ and, at $n \rightarrow \infty$, it converges to the sink point, which divides the g -diagonal of the initial rhombus into segments whose ratio obey the golden proportion.

Figure 4a shows the atomic model of the structure of the quasicrystal alloy [3]. Comparing this structure with the fractal frameworks in Fig. 4b, one can draw a conclusion that the Penrose lattice is the projection of the quasicrystal model possessing the fivefold symmetry axis.

Now, we represent this scenario of tiling in the tree form (Figs. 5a and 5b) and consider the trees obtained with the tree constructed for a Fibonacci sequence. All the trees in Fig. 5 are nonperiodic but show a certain rigorous alternation of the points with different degree of branching. We use the enumerating polynomials as the graph characteristics in the form

$$T(\xi) = \sum_{q=1}^{\infty} T_q \xi^q, \quad (2)$$

where T_q us the number of the root trees with branching q .

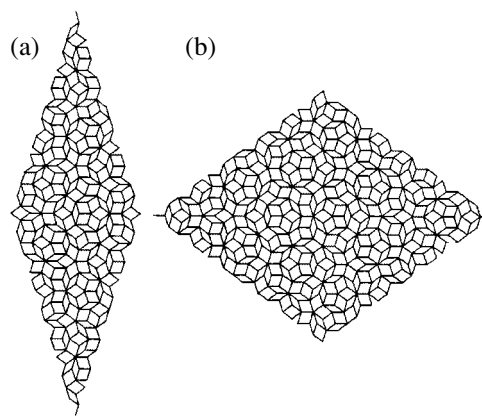


Fig. 3. Penrose lattices growing from (a) an acute and (b) an obtuse g -rhombuses.

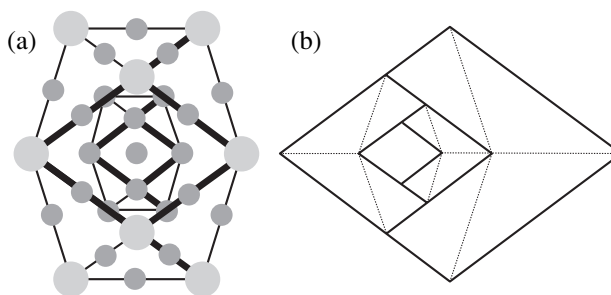


Fig. 4. (a) Guyot–Audier atomic model of the (Al,Si)–Mn structure. Large spheres depict Mn, small ones, Al and (b) fractal frameworks for four generations of a Penrose lattice growing from an obtuse rhombus.

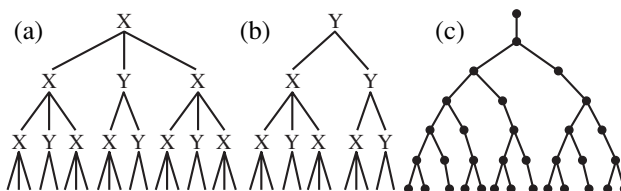


Fig. 5. Cayley's trees (a) for the scenario of constructing the Penrose lattices from an obtuse, (b) an acute g -rhombuses, and (c) the Fibonacci sequence.

Now, introduce the n -flow such that

$$\begin{aligned} T_n^{(x)}(\xi) &= F_{2n} \xi^3 + F_{2n-1} \xi^2, \\ T_n^{(y)}(\xi) &= F_{2n-1} \xi^3 + F_{2n-2} \xi^2, \\ T_n^{(F)}(\xi) &= F_n \xi^2 + F_{n-1} \xi^1, \end{aligned} \quad (3)$$

where $T_n^{(x)}(\xi)$, $T_n^{(y)}(\xi)$, and $T_n^{(F)}(\xi)$ are the Cayley's enumerating polynomials in Figs. 5a, 5b, and 5c, respectively, ξ^q is the q -tuple branching point, and n is the hierarchy number. One can see that the even levels of

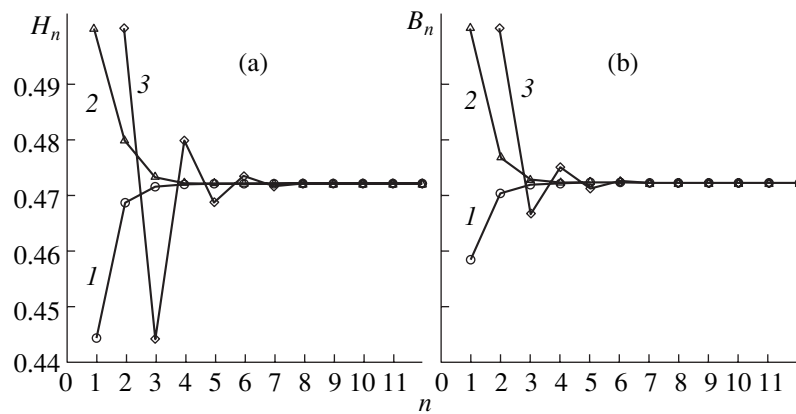


Fig. 6. Hierarchic percolation of (a) entropy and (b) divergence on trees: (1) for the scenario of Penrose lattice construction from the obtuse and (2) acute g -rhombuses, and (3) for the Fibonacci sequence.

the Fibonacci tree ($T_n^{(x)} \sim T_{2n}^{(F)}$) correspond to the tree in Fig. 5a, whereas the odd levels of the Fibonacci trees, to the tree in Fig. 5b. One can readily see from Figs. 5a and 5b that obtuse rhombuses form only a triple branching point ($x \sim \xi^3$), whereas acute ones, a double branching point ($y \sim \xi^2$). The total number of the points at the n th level is

$$T_n^{(x)} = F_{2n+1}, \quad T_n^{(y)} = F_{2n}, \quad T_n^{(F)} = F_{n+1}. \quad (4)$$

The probability of formation of q -tuple branching bushes at the n th iteration step is

$$p_n(\xi^q) = T_n(\xi^q)/T_n \quad (5)$$

at

$$n \rightarrow \infty \quad p_n^{(x)}(\xi^3) = p_n^{(y)}(\xi^3) = p_n^{(F)}(\xi^2) \rightarrow \alpha_2,$$

$$p_n^{(x)}(\xi^2) = p_n^{(y)}(\xi^2) = p_n^{(F)}(\xi) \rightarrow \alpha_2^2.$$

Now, consider the probabilistic enumerating poly-

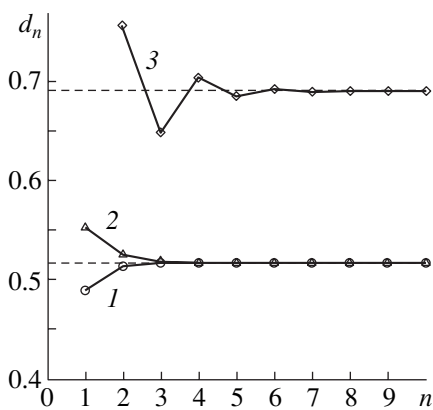


Fig. 7. Hierarchic percolation of the fractal dimension on trees (1) for the scenario of the Penrose lattices growing from an obtuse and (2) from an acute g -rhombuses and (3) for the Fibonacci sequence.

nomials:

$$P_n(\xi) = \sum_q p_n(\xi^q) \xi^q. \quad (6)$$

At large n , the probabilistic enumerating polynomials of the trees have the form

$$P_{n \rightarrow \infty} = \alpha_2 \xi^{i+1} + \alpha_2^2 \xi^i, \quad (7)$$

where i is the minimum tree branching.

Now follow the flow of the informodynamic characteristics along the tree hierarchy. The intrinsic entropy of the levels is

$$H_n = \sum_q H_n^V(\xi^q), \quad (8)$$

where $H_n^V(\xi^q) = (p_n(\xi^q))^\alpha (\tilde{p}_n(\xi^q))^\beta$ is the entropy functional in the Vaida form. In our case, the superscripts $\alpha = \beta = 1$; $\tilde{p}_n(\xi^q)$ is the complement of the probability $p_n(\xi^q)$. Dynamics of the entropy flow over hierarchies is shown in Fig. 6a. All the entropies rapidly converge to $2\alpha_2^3 \approx 0.472$ which, coincides with the entropy values for g -triangles.

Now calculate the symmetrized Bongardt divergence in the Vaida form, which characterizes the distance between two distributions (in our case between two levels)

$$B_n = \frac{1}{2} \sum_q [p_n(\xi^q) \tilde{p}_{n+1}(\xi^q) + p_{n+1}(\xi^i) \tilde{p}_n(\xi^q)]. \quad (9)$$

This dependence is shown in Fig. 6b. At higher hierarchies of the divergence and higher-level entropy, this dependence converges to $2\alpha_2^3$. Representing the entropy and the divergence in the vector form [4] and using the corresponding definitions, we obtain $H_n + B_n = H_{n+1}$. At high-level hierarchies, the triangle constructed on these vectors is a three-point simplex. Tak-

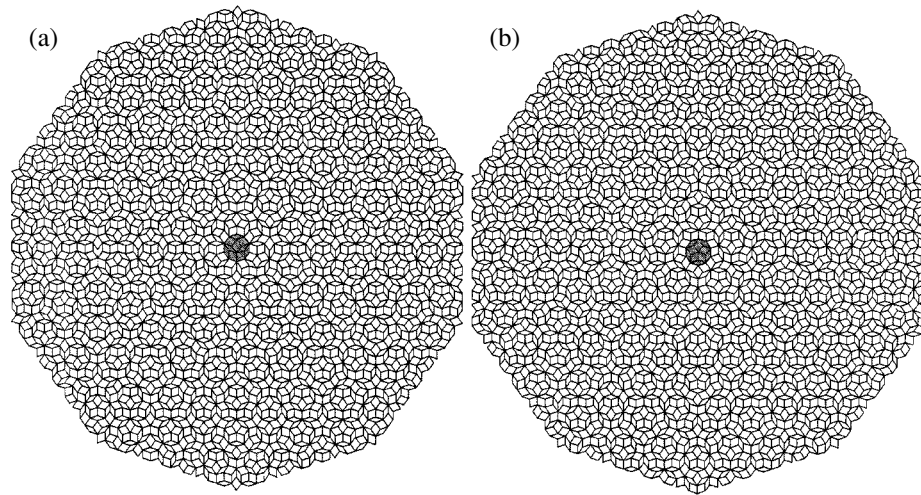


Fig. 8. Penrose lattices growing from (a) a dorsal and (b) a star ten-vertex polygon.

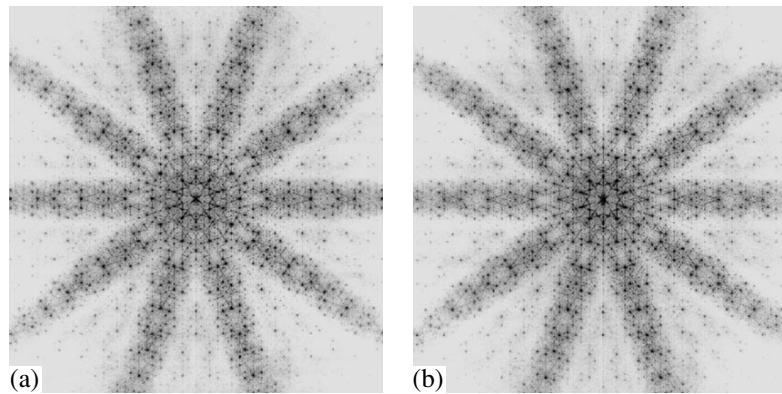


Fig. 9. Diffraction patterns for the Penrose lattices growing from (a) a dorsal and (b) a star ten-vertex polygon.

ing into account the strict correspondence between the degree of tree branching and the type of the rhombus formed on the lattice, one can state not only that the construction procedure is regular and correct in terms of entropy, but also that the lattice itself is regular at the level of g rhombuses.

Now, introduce the fractal dimension of a tree via the informodynamic characteristics

$$d_n = \frac{H_n^{Sh}(p_n)}{\sup H_n^{Sh}(\bar{p}_n)}, \quad (10)$$

where $H_n^{Sh}(p_n) = -\sum_q p_n(\xi^q) \ln p_n(\xi^q)$ is the entropy in the Shannon form on the probabilistic enumerating polynomials of Cayley's trees (the sentence entropy composed of the symbols ξ^q), $\sup H_n^{Sh}(\bar{p}_n) = \ln(1 + \sum_q q p_n(\xi^q)) = \ln(1 + \bar{\xi})$ is the upper estimate of the Shannon entropy for moderate branching $\bar{\xi}$ (the

entropy of the symbol $\bar{\xi}$). In terms of linguistics, the fractal dimension (10) is the ratio of the "capacities" of a sentence and a letter. Dependence (10) is shown in Fig. 7. The value of fractal dimension for the Fibonacci tree calculated by this method coincides with the fractal dimension obtained earlier in [5].

Now consider a lattice in which the generating elements are ten-vertex polygons (Fig. 8). The diffraction patterns of these lattice (Fig. 9) are characterized by the fivefold rotational symmetry. Similar to Penrose lattice growing from rhombuses, one observes spin flip at the level of the fractal framework, but in the case of a lattice growing from the star ten-vertex polygon, the situation is much more complicated (Fig. 10). The barycenter of the Penrose lattice (the sink point), which started from the star ten-vertex polygon, remains static at all the iterations and coincides with the geometric center of tiling. The point of pentacoordination of the fractal framework of a dorsal ten-vertex polygon oscillates along the dorsal axis according to the law $(-1/K)^n$ and converges to the geometric center of the lattice which remains

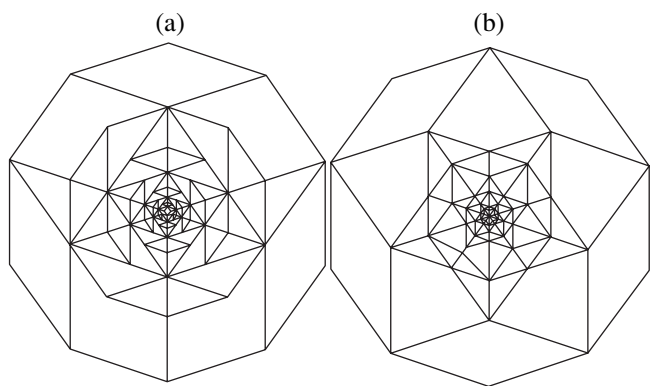


Fig. 10. Fractal frameworks of seven generations of quasicrystal structures growing from (a) dorsal and (b) star ten-vertex polygons.

static. The probabilistic enumerating polynomials of the construction of tilings from ten-vertex polygons and rhombuses coincide. Thus, the corresponding entropies, Bognardt divergences, and fractal dimensions should also coincide.

The examples considered here show that fractals can be successfully used to describe quasicrystal structures and allow us to draw the conclusion about the “gold” equivalence of the fractal objects with the fivefold axes in terms of entropy.

REFERENCES

1. D. Shechtman, I. Blech, D. Gratias, and J. W. Cahn, *Phys. Rev. Lett.* **53**, 1951 (1984).
2. G. A. Domrachev and A. I. Lazarev, *Fiz. Tverd. Tela (St. Petersburg)* **41**, 799 (1999) [*Phys. Solid State* **41**, 720 (1999)].
3. D. Gratias, *Recherche* **178**, 788 (1986).
4. E. A. Lyubchenko, Candidate's Dissertation in Physics and Mathematics (Dal'nevost. Gos. Univ., Vladivostok, 1998).
5. A. I. Olemskoï and A. Ya. Flat, *Usp. Fiz. Nauk* **163** (12), 1 (1993) [*Phys. Usp.* **36**, 1087 (1993)].

Translated by L. Man

STRUCTURE OF INORGANIC COMPOUNDS

Crystal Structure of Calcioburbankite and the Characteristic Features of the Burbankite Structure Type

Yu. V. Belovitskaya*, I. V. Pekov*, E. R. Gobechiya*,
Yu. K. Kabalov*, and V. V. Subbotin**

* Faculty of Geology, Moscow State University, Vorob'evy gory, Moscow, 119899 Russia
e-mail: mineral@geol.msu.ru

** Institute of Geology, Kol'skiĭ Research Center, Russian Academy of Sciences,
ul. Fersmana 14, Apatity, Murmansk oblast, 184200 Russia

Received July 6, 2000

Abstract—The crystal structure of calcioburbankite $(\text{Na,Ca})_3(\text{Ca,RE,Sr,Ba})_3(\text{CO}_3)_5$ found in carbonatites from Vuoriyarvi (North Kareliya) was solved by the Rietveld method. The experimental data were collected on an ADP-2 diffractometer ($\lambda\text{CuK}\alpha$ radiation; Ni filter; $16.00^\circ < 2\theta < 130.00^\circ$; the number of $(\alpha_1 + \alpha_2)$ reflections was 455). All the calculations were performed within the sp. gr. $P6_3mc$; $a = 10.4974(1) \text{ \AA}$, $c = 6.4309(1) \text{ \AA}$, $V = 613.72(1) \text{ \AA}^3$; $R_{wp} = 2.49\%$. The structure was refined with the use of the anisotropic thermal parameters for the (Na,Ca) and (Sr,Ba,Ce) cations. The comparison of the crystal structures of all of the known hexagonal representatives of the burbankite family demonstrates that the burbankite structure type (sp. gr. $P6_3mc$) is stable, irrespectively of the occupancy of the ten-vertex polyhedra predominantly with Ca, Sr, or Ba cations and the occupancies of the positions in the eight-vertex polyhedra. © 2001 MAIK "Nauka/Interperiodica".

INTRODUCTION

Calcioburbankite $(\text{Na,Ca})_3(\text{Ca,RE,Sr,Ba})_3(\text{CO}_3)_5$ belongs to the burbankite family comprising hexagonal and pseudo-hexagonal monoclinic carbonates described by the general formula $A_{3-4}B_{2-3}(\text{CO}_3)_5$, where $A = \text{Na}$, Ca , or \square and $B = \text{Sr}$, Ba , RE , or Ca (or, sometimes, Na). In calcioburbankite, the position B is predominantly occupied by calcium. This mineral was discovered in 1995 in alkaline hydrothermolites from Saint-Élier (Quebec, Canada) [1]. The structure of the mineral has not been studied as yet.

Calcioburbankite found in carbonatites from the Vuoriyarvi alkaline ultrabasic massif (North Kareliya) was characterized mineralogically in 1999 [2]. In this study, we determined the crystal structure of the mineral by the Rietveld method.

EXPERIMENTAL

The mineral under study originates from calcite carbonatites and occurs in associations with dolomite, phlogopite, apatite, sulfides, and some other minerals. Calcioburbankite exists in the form of massive granular greenish-yellow aggregates. Under hydrothermal conditions, calcioburbankite is unstable and is readily replaced by calcite, ancylite-(Ce), barite, strontianite, and other mineral aggregates.

The cationic composition of calcioburbankite (Table 1) was studied by X-ray spectral analysis by the analyst Ya.A. Pakhomovskii on a Cameca MS 46

instrument at the Institute of Geology of the Kol'skiĭ Research Center of the Russian Academy of Sciences, Apatity.

The X-ray spectrum of a powdered sample was obtained on an ADP-2 diffractometer ($\lambda\text{CuK}\alpha$ radiation; Ni filter; $16.00^\circ < 2\theta < 130.00^\circ$; 2θ scanning technique; 0.02° per scan step; the exposure time 15–20 s; the number of $(\alpha_1 + \alpha_2)$ reflections 455). All the computations were performed by the WYRIET program (version 3.3) [3] within the sp. gr. $P6_3mc$. We used as the starting model the crystal structure of burbankite found in hydrothermolites from the Kukisvumchorr mountain (the Khibiny massif, the Kola Peninsula) [4]. The ionic scattering curves were used. The peak profiles were approximated by the Pearson VII function with 6FWHM. The asymmetry was refined for $2\theta < 40^\circ$. The refinement was carried out by adding gradually the parameters to be refined with the continuous automatic modeling of the background until the moment when the R factors attained the constant values. The isotropic refinement converged to the R_{wp} factor = 2.56%.

Some characteristics of the data collection and the results of the calcioburbankite structure refinement with the anisotropic (the A and B cations) and isotropic (the oxygen and carbon atoms) thermal parameters are listed in Table 2. The experimental (solid line) and calculated (dots) X-ray spectra of the mineral are shown in the figure. The atomic coordinates, the isotropic ther-

Table 1. Unit-cell parameters and the cationic compositions of structurally studied minerals of the burbankite family

Characteristic	Calcioburbankite	Burbankite (low-rare-earth)	Burbankite	Burbankite	Burbankite	Khanneshite	Remondite-(Ce)	Petersenite-(Ce)
Sp. gr.	$P6_3mc$	$P6_3mc$	$P6_3mc$	$P6_3mc$	$P6_3mc$	$P6_3mc$	$P2_1$	$P2_1$
a_0 , Å	10.4974(1)	10.5263(1)	10.5313(1)	10.52(4)	10.512(2)	10.5790(1)	10.412(4)	20.872(4)
b_0 , Å	10.4974(1)	10.5263(1)	10.5313(1)	10.52(4)	10.512(2)	10.5790(1)	10.414(4)	10.601(2)
c_0 , Å	6.4309(1)	6.5392(1)	6.4829(1)	6.51(2)	6.492(2)	6.5446(1)	6.291(3)	6.367(1)
β , deg	120	120	120	120	120	120	119.80(5)	120.50(1)*
V_0 , Å ³	613.72(1)	627.49(1)	622.68(1)	–	621.3	634.31(1)	591.9	1213.9(4)
Z	2	2	2	2	2	2	2	4
Cationic composition, wt %								
Na ₂ O	13.27	8.51	10.61	11.44	8.34	11.86	17.16	17.38
CaO	10.80	10.04	6.96	10.86	11.47	5.37	10.54	1.32
SrO	8.44	36.28	33.73	12.86	25.08	9.04	3.98	1.70
BaO	11.36	9.91	7.92	11.62	11.47	22.99	–	0.32
Y ₂ O ₃	–	0.48	0.57	–	<0.03	–	0.24	–
La ₂ O ₃	6.17	1.32	2.94	–	3.37	4.07	11.60	14.49
Ce ₂ O ₃	10.86	0.44	5.74	–	5.39	10.46	14.99	23.66
Pr ₂ O ₃	0.58	–	0.45	–	0.46	1.01	1.49	2.00
Nd ₂ O ₃	2.56	–	1.36	–	1.26	3.60	3.34	5.82
Sm ₂ O ₃	–	–	–	–	0.14	–	0.50	0.60
$\Sigma(RE_2O_3)$	(20.17)	(1.76)	(10.49)	15.12	(11.08)	(19.14)	(32.394)	(46.57)
Total	64.04	66.98	70.28	64.96**	67.47***	68.40	64.314****	67.29
References	Present study	Belovitskaya <i>et al.</i> , 2000 [4]	Belovitskaya <i>et al.</i> , 2000 [4]	Voronkov and Shumyatskaya, 1968 [6, 10]	Effenberger <i>et al.</i> , 1985 [5]	Belovitskaya <i>et al.</i> (in press)	Ginderow, 1989 [7, 10]	Grice <i>et al.</i> , 1994 [8]

Note: * In the original study, b_0 and c_0 are interchanged. The analysis showed additionally (wt %): ** K₂O, 0.99; MgO, 0.35; Al₂O₃, 1.05; Fe₂O₃, 0.48; SiO₂, 0.19; *** Gd₂O₃, 0.41; Tb₂O₃, 0.05; **** Eu₂O₃, 0.09; Gd₂O₃, 0.24; Dy₂O₃, 0.07; Ho₂O₃, 0.01; Er₂O₃, 0.03; Yb₂O₃, 0.03; Lu₂O₃, 0.004.

Table 2. Characteristics of the refinement of the crystal structure of calcioburbankite by the Rietveld method

Characteristic	Value	Characteristic	Value
Sp. gr.	$P6_3mc$	R_{exp}	6.92
2θ scanning range, deg	16.00–130.00	R_B	3.35
Number of reflections	455	R_F	2.98
Number of parameters in the refinement	54	s^*	0.36
R_p	1.88	DWD**	1.33
R_{wp}	2.49	σ_x^{***}	1.384

* $s = R_{wp}/R_{exp}$, where R_{exp} is the expected value of R_{wp} .

** The Durbin–Watson statistics [11].

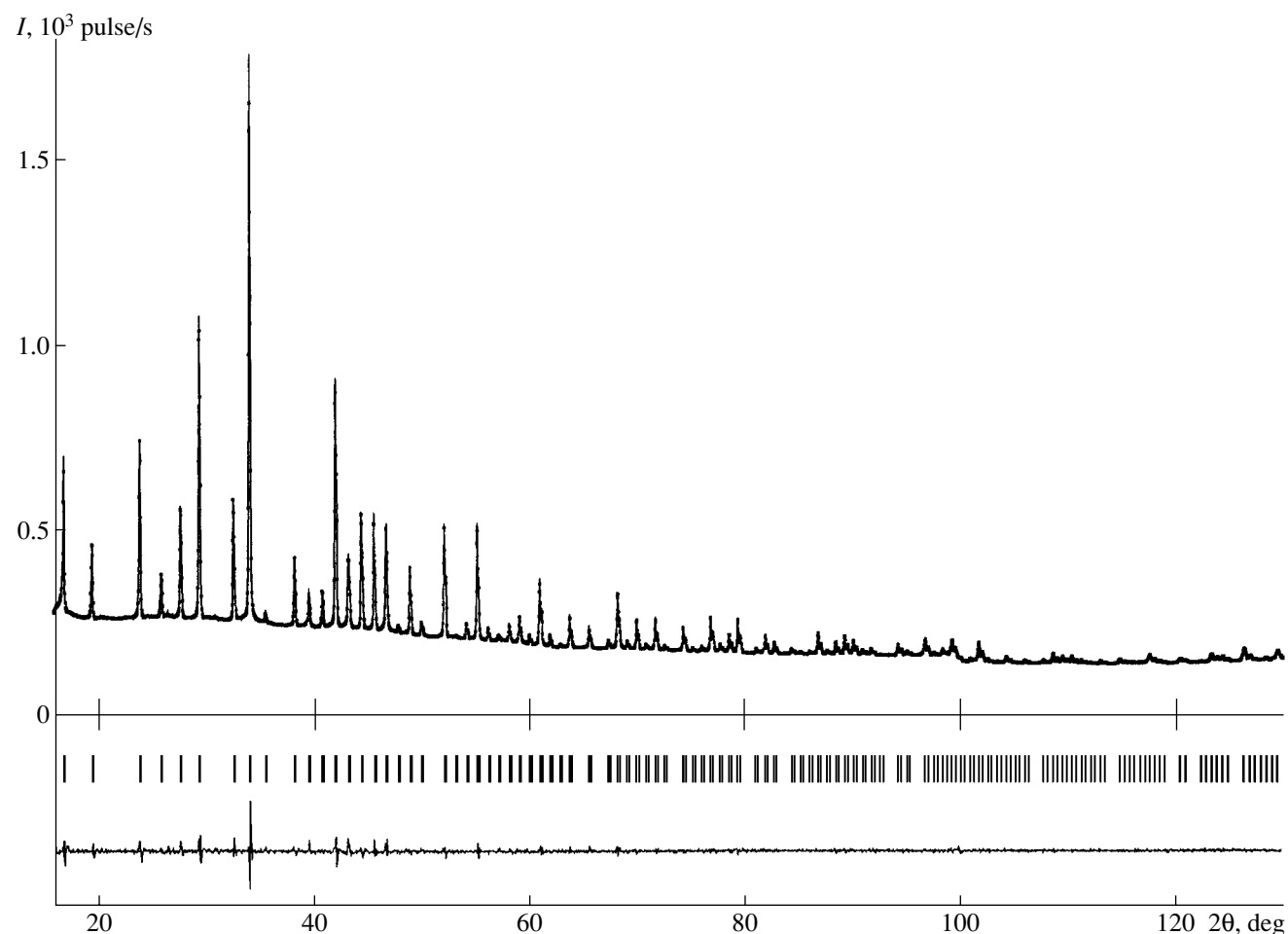
*** The multiplier for calculations of standard deviations [12].

mal parameters, and the occupancies of the positions in the calcioburbankite structure are listed in Table 3.

RESULTS AND DISCUSSION

Similar to the burbankite structure [5, 6], the crystal structure of calcioburbankite contains two independent

cationic positions in the centers of eight- and ten-vertex polyhedra (A and B , respectively) formed by oxygen atoms and three types of triangular carbonate groups denoted as $C(1)$, $C(2)$, and $C(3)$ having different orientations. The average distances in the polyhedra are as follows: $A-O$ is 2.51 Å; $B-O$ is 2.67 Å; and $C(1)-O$, $C(2)-O$, and $C(3)-O$ are 1.23, 1.36, and 1.28 Å, respec-



Experimental (solid line) and calculated (dots) X-ray spectra of calcioburbankite.

Table 3. Structural and thermal parameters (\AA^2) and occupancies of positions in the structure of calcioburbankite

Atom	Characteristic	Value	Atom	Characteristic	Value	
A	<i>x</i>	0.5241(6)	C(2)	<i>z</i>	0.88(1)	
	<i>y</i>	0.4759(6)		<i>B_j</i>	1(1)	
	<i>z</i>	0.317(2)	C(3)	<i>x</i>	0.3333	
	<i>B_j</i>	1.4(2)		<i>y</i>	0.6667	
	<i>q</i> (Na)	2.22(2)		<i>z</i>	0.49(2)	
	<i>q</i> (Ca)	0.48(1)	O(1)	<i>B_j</i>	2(1)	
	<i>q</i> (RE)*	0.09(1)		<i>x</i>	0.376(1)	
B	<i>x</i>	0.8406(1)		<i>y</i>	0.088(2)	
	<i>y</i>	0.1594(1)		<i>z</i>	0.633(2)	
	<i>z</i>	0		<i>B_j</i>	1.1(4)	
	<i>B_j</i>	1.01(9)		O(2)	<i>x</i>	0.926(1)
	<i>q</i> (RE + Ba)*	1.17(1)			<i>y</i>	0.074(1)
	<i>q</i> (Ca)	0.94(1)	<i>z</i>		0.344(4)	
	<i>q</i> (Sr)	0.54(1)	O(3)	<i>B_j</i>	1.8(6)	
<i>q</i> (Na)	0.43(1)	<i>x</i>		0.4037(8)		
C(1)	<i>x</i>	0.797(2)		<i>y</i>	0.5963(8)	
	<i>y</i>	0.203(2)	<i>z</i>	0.476(7)		
	<i>z</i>	0.55(1)	O(4)	<i>B_j</i>	0.5(4)	
	<i>B_j</i>	5(2)		<i>x</i>	0.776(1)	
C(2)	<i>x</i>	0	<i>y</i>	0.224(1)		
	<i>y</i>	0	<i>z</i>	0.359(5)		
			<i>B_j</i>	1.8(6)		

* All RE were refined with the use of the *f* curve of cerium.

tively. In calcioburbankite, the ten-vertex polyhedra are occupied predominantly by Ca. This is reflected in both unit-cell parameters of calcioburbankite (whose values are lower than those of burbankite). The *B* position is occupied by Ca, Sr, RE, and Ba and a small amount of Na. The incorporation of Na atoms into the ten-vertex polyhedra is typical of remondite, which is a monoclinic representative of the burbankite family [7]. However, unlike the positions in burbankite and khanneshite, the *A* position in the calcioburbankite structure, is occupied not only by Na and Ca, but also by a small amount of RE (Table 3). The presence of lanthanides in the *A* position in the minerals of this structure type is observed for the first time. The refinement of the structure based on the standard model containing only Na and Ca atoms in the eight-vertex polyhedra resulted in the unreasonable thermal parameters for these cations. The calcioburbankite formula established by the X-ray diffraction analysis is $(\text{Na}_{2.23}\text{Ca}_{0.49}\text{RE}_{0.09})_{2.81}(\text{Ca}_{0.95}\text{RE}_{0.69}\text{Sr}_{0.55}\text{Ba}_{0.50}\text{Na}_{0.44})_{3.13}(\text{CO}_3)_5$ and somewhat differs from the formula $(\text{Na}_{2.87}\text{Ca}_{0.16})_{3.03}(\text{Ca}_{1.14}\text{Sr}_{0.55}\text{Ba}_{0.50}\text{Ce}_{0.44}\text{La}_{0.25}\text{Nd}_{0.10} \times \text{Pr}_{0.02})_{3.00}(\text{CO}_3)_5$ determined by the electron probe analysis. Most likely, this difference can be attributed to the

variations in the composition of the specimen under study. Our and other well-known results demonstrate that the intraphase inhomogeneity is typical of the minerals of the burbankite group.

Minerals of the burbankite family crystallize in three structure types—burbankite (sp. gr. $P6_3mc$), remondite (sp. gr. $P2_1$; the unit cell is close to that of burbankite but with the angle γ being slightly different from 120°), and petersenite (sp. gr. $P2_1$ with the unit-cell parameter a_0 twice exceeding that of remondite) (Table 1). The crystal chemistry of the monoclinic representatives of this family has well been studied [7, 8], whereas the structures of the hexagonal representatives has been considered only in two articles [5, 6] devoted to burbankite with the *B* position occupied simultaneously by RE, Ca, and Sr. We noticed that the powder X-ray diffraction patterns of burbankites of various compositions essentially differ from one another [4], which gives the impetus to their systematic study. We compared burbankite with the typical composition with low-rare-earth burbankite [4], khanneshite (a barium analog of burbankite), and calcioburbankite. All these minerals appear to be isostructural and differ only in the nature of the divalent cations (Sr, Ba, or Ca) occupying

mainly the *B* position. Therefore, the burbankite structure type is very stable and is retained as long as the *B* position is occupied mainly by divalent cations of different sizes. This structure type persists over a wide range of the RE^{3+}/M^{2+} ratios from the terminal member $(Na_2,Ca)(Sr,Ca,Ba)_3(CO_3)_5$ [4], which is virtually free of rare-earth elements, to, at least, calcioburbankite of the composition $(Na_{2.2}Ca_{0.5}RE_{0.1})_{2.8}(Ca_{1.0}RE_{0.7}Sr_{0.6}Ba_{0.5}Na_{0.4})_{3.2}(CO_3)_{5.1}$ with the highest content of rare-earth elements in all the structurally studied hexagonal representatives of this family. Only the presence of *RE* (in a type-forming amount) and, correspondingly, filling of the position *A* only with Na lowers the symmetry down to monoclinic because of the deviation of the angle γ from 120° [7]. The fact that the *A* position in the eight-vertex polyhedron is partial vacant (which was found by Effenberger *et al.* [5]), which was confirmed in our study [4], cannot prevent the formation of the burbankite structure type either.

Thus, the crystal structures of all the known hexagonal representatives of the burbankite family have been studied. These minerals form a continuous isomorphous series. In this respect, the burbankite structure type can be considered as unique, because all the Ca-, Sr-, and Ba-dominant phases are not only isostructural (the examples of this isostructurality are well known, (aragonite–strontianite–witherite), but also exhibit the complete isomorphous miscibility. Even in minerals, whose structures contain large cavities (zeolites and pyrochlores) and where divalent cations are present in type-forming amounts, no ratio of the type $Ca : Sr : Ba \approx 1 : 1 : 1$ was ever observed. Analysis of the known data demonstrates that the minerals containing simultaneously considerable amounts of Ba and Ca are characterized by their ordered distribution over different structural positions (double Ba,Ca-carbonates, wenkite, etc.). A substantial accumulation of Sr in calcium minerals or of Ba in strontium minerals often leads to the change of the structure type (the apatite group and olgite). The only exception is made by the hexagonal members of the burbankite family.

ACKNOWLEDGMENTS

This study was supported by the Russian Foundation for Basic Research and by the National Science Foundation of China (NSFC), joint project no. 99-05-39019.

REFERENCES

1. J. van Velthuizen, R. A. Gault, and J. D. Grice, *Can. Mineral.* **33**, 1231 (1995).
2. V. V. Subbotin, A. V. Voloshin, Ya. A. Pakhomovskii, and A. Yu. Bakhchisaraitsev, *Zap. Vseross. Mineral. O–va*, No. 1, 78 (1999).
3. J. Schneider, in *Profile Refinement on IBM-PC: Proceedings of the International Workshop on the Rietveld Method, of the International Union on Crystallography, Petten, 1989*, p. 71.
4. Yu. V. Belovitskaya, I. V. Pekov, and Yu. K. Kabalov, *Kristallografiya* **45** (1), 32 (2000) [*Crystallogr. Rep.* **45**, 26 (2000)].
5. H. Effenberger, F. Kluger, H. Paulus, and E. R. Wolfel, *Neues Jahrb. Mineral., Monatsh.* **4**, 161 (1985).
6. A. A. Voronkov and N. G. Shumyatskaya, *Kristallografiya* **13** (2), 246 (1968) [*Sov. Phys. Crystallogr.* **13**, 192 (1968)].
7. P. D. Ginderow, *Acta Crystallogr., Sect. C: Cryst. Struct. Commun.* **45**, 187 (1989).
8. J. D. Grice, J. van Velthuizen, and R. A. Gault, *Can. Mineral.* **32**, 405 (1994).
9. L. S. Borodin and Yu. L. Kapustin, *Dokl. Akad. Nauk SSSR* **147** (2), 462 (1962).
10. F. Cesbron, C. Gilles, P. Pelisson, and J.-C. Saugues, *C. R. Acad. Sci., Ser. II: Mec., Phys., Chim., Sci., Terre Univers.* **307**, 915 (1988).
11. R. Hill and H. Flack, *J. Appl. Crystallogr.* **20**, 356 (1987).
12. J.-F. Berar and P. Lelann, *J. Appl. Crystallogr.* **24**, 1 (1991).

Translated by T. Safonova

STRUCTURE
OF INORGANIC COMPOUNDS

Three-Layer Monoclinic $3M_2$ Polytype of Muscovite Revealed from Oblique-Texture Electron Diffraction Patterns

A. P. Zhukhlistov*, B. B. Zvyagin*, and T. I. Getmanskaya**

* Institute of Geology of Ore Deposits, Petrography, Mineralogy, and Geochemistry, Russian Academy of Sciences, Staromonetnyĭ per. 35, Moscow, 109017 Russia

e-mail: zvyagin@genome.eimb.relarn.ru

** All-Russia Institute of Mineral Research, Staromonetnyĭ per. 31, Moscow, 109017 Russia

Received July 17, 2000

Abstract—The inhomogeneous (complex) polytype $3M_2$ of finely dispersed muscovite with the structure formed by layers with different parity of azimuthal orientations (561) or relative rotations [112] was identified for the first time using the oblique-texture electron diffraction patterns. The specimen had no rigorous order in layer alternation, which is reflected in the distortion of the reflection positions and intensities. It is shown that the most probable defects reduce to the replacement of the layer orientations characteristic of the $3M_2$ polytype by layer orientation characteristic of the $2M_2$ polytype. This fact indicates that, under certain conditions, the prismatic coordination of interlayer cations in micas is preferable. © 2001 MAIK “Nauka/Interperiodica”.

INTRODUCTION

Micas are a classical example of polytypism in crystal structures. The three-story tetrahedron–octahedron–tetrahedron (TOT) layers consisting of two tetrahedral (T) and one octahedral (O) sheets are bound by interlayer cations and, because of the hexagonal geometry of their lattice, can have six different azimuthal orientations related by rotations by angles multiple of 60° . These orientations are determined by the layer axis a_i ($i = 1, 2, \dots, 6$) parallel to the common a -axis of the structure [1, 2]. Depending on the octahedron occupancies, one can distinguish tri- and dioctahedral TOT layers. The former TOT layers are always centrosymmetric (CS), whereas the latter ones can also be only axially symmetric (AS) and their tetrahedral sheets are related not by the center of inversion in the vacant octahedron of the octahedral sheet, but only by the twofold axis of the sheet [3]. Dioctahedral CS and AS layers (often denoted as *trans*- and *cis*-vacant layers) form the independent sets of polytypes. Below, only the set of mica polytypes formed by CS layers is considered.

In addition to simple polytypes satisfying the homogeneity condition, there also exist complex (inhomogeneous) polytypes, which, being periodic, still are characterized by nonequivalent positions for each layer among all the other layers and nonequivalent transitions between the neighboring layers. The polytypes of various micas are described by short symbols indicating the alternation period and the symmetry ($1M$, $3T$, $6H$, etc.) and the detailed symbols expressed in terms of the absolute layer orientations (1, 2, 3, ..., 6) [1] or rel-

ative rotations of adjacent layers (0, ± 1 , ± 2 , 3) corresponding to the angles 0° , $\pm 60^\circ$, $\pm 120^\circ$, and 180° [2].

Micas consisting of CS layers can give only six simple polytypes, namely, $1M$ (33... or [0]); $2M_1$ (24... or $[2\bar{2}]$); $3T$ (351... or $[2]_3$); $2M_2$ (45... or $[1\bar{1}]$); $2O$ (36... or $[33]$); and $6H$ (321654... or $[1]_6$) [4], of which only the polytype $6H$ has not been found as yet. The number of possible complex polytypes rapidly increases with an increase of the number of layers per repetition period and equals 5, 26, 83, and 401 at the periods equal to 3, 4, 5, and 6 layers [2]. However, in fact, only 22 inhomogeneous polytypes of micas with the periods of 3, 4, 5, 6, 8, 9, 10, 11, 14, and 23 layers have been found. Of them, 19 polytypes were first identified by X-ray diffraction methods and three, by oblique-texture electron diffraction patterns [5–10]. These polytypes are related mainly to trioctahedral and lithium-containing micas such as biotites, siderophyllites, zinnwaldites, and lepidolites. The layer orientations of most inhomogeneous micas are associated with rotations multiple of 120° , which preserves the octahedral coordination of interlayer cations; the layers have the same parity of azimuthal orientations. If the orientations of the adjacent layers have different parity (rotations multiple of 60°), these cations have the prismatic coordination [11]. Inhomogeneous micas with only odd relative rotations of the adjacent layers (regularly alternating different parities of azimuthal orientations) have not been encountered as yet. The mixed (irregularly alternating) parities of these orientations turned out to be inherent only in three micas, whereas the polytype 3341 ([0132], $4TC_3$) was formed in the synthetic lithium-containing

fluorphlogopite [2], whereas the closely associating and structurally related 561 and 565161 polytypes ($[11\bar{2}]$ and $[1\bar{1}2\bar{1}\bar{1}2]$, $3M_2$ and $6M_1$) were found only in the natural lepidolites in Norway [9, 10]. Therefore the surprising fact—the existence of a complex polytype $3M_2$ with the mixed parity of the azimuthal layer orientations identified from the oblique-texture electron diffraction patterns for dioctahedral mica of the muscovite composition—seems to be very important.

GENERAL INFORMATION ON THE SPECIMEN STUDIED

Finely dispersed muscovite (sericite) $3M_2$ is found in the ore of the Akchatau (Central Kazakhstan) molybdenum–tungsten deposit relating to greizen middle-depth formations. Muscovite $3M_2$ is a product of post-tectonic mineralization from low-concentrated aqueous carbonic acid solutions in the process of pseudomorphous metasomatism at temperatures 220–60°C, which indicates the favorable conditions for the development of closed “forced equilibrium” microsystems [12]. This mica is represented by yellowish grey and apple-green dense finely dispersed aggregates; in association with dickite, gearksutite, and pyrite, this mica occupies the spaces between the tungstanite, topaz, and fluorite nests partly replacing and corroding topaz and fluorite. Sometimes it also occurs in the form of fiberlike veinlets of muscovite forming a fine network inside dickite aggregates. The size of muscovite aggregates ranges within 0.1–1.0 cm.

ELECTRON DIFFRACTION STUDIES

Oblique-texture electron diffraction patterns from polycrystalline specimen tilted to the primary electron beam showed a number of hk ellipses characteristic of layer silicates with the hkl reflections. Reflections with both h and k indices multiple of three ($06l$, $33l$ on ellipse V) indicated the 10-Å-interlayer distance characteristic of micas. The chemical analysis indicated that this mica can be described by the crystallochemical formula typical of muscovite $(K_{0.91}Na_{0.01}Ca_{0.01}) \cdot (Al_{1.91}Fe_{0.05}^{3+}Mg_{0.02}Mn_{0.01}) \cdot (Si_{3.12}Al_{0.88})O_{10}(OH)_2$. The positions of the $0kl$ and hhl reflections on ellipses I, III, and V indicated the monoclinic unit cell with three-layer repetition period and normal projection of the c -axis onto the ab plane, $-\mathbf{c}_n = [-0.2, 0]$. Using the conventional electron diffraction formulas for oblique-texture patterns, we determined the unit cell parameters as $a = 5.20$ Å, $b = 9.00$ Å, $c = 30.06$ Å, $\beta = 91.95^\circ$.

The value $-\cos\beta/a = 0.200$ shows the deviation of the monoclinicity angle from its ideal value $\beta_{id} = 93.4^\circ$ for which $-\cos\beta/a = 1/3$. Such deviations are usually caused by the decrease of the ideal value $\mathbf{s}_3 = [-1/3, 0]$ of the displacement vector of the successive T, O sheets inside the TOT layers caused, in turn, by ditrigonal

rotation of the bases of octahedra in the dioctahedral micas and the related rotations of the vectors \mathbf{s}_i ($i = 1, 2, \dots, 6$) through the angles multiple of 60° [13]. The sequence of CS TOT layers with the azimuthal orientations i, j, \dots is described in terms of the displacement symbols as $0s_i s_j 0s_i s_j 0 \dots$, or, in a shorter form, as $0ii0jj0 \dots$ for a repetition period $c_n = 2\sum s_i$. Taking this into account, one can determine the three-layer polytype that can have such a value of the angle β . Assuming that $\mathbf{s}_3 = [0.3, 0]$, we obtain the value $\mathbf{c}_n = [-0.4, 0]$ for the polytype $1M$ (0330...), which, in fact, was established for the muscovite $1M$ [12]. Using the same \mathbf{s}_3 value for six three-layer mica polytypes, namely, for $3T$ (0330550110... or [222]), $3M_1$ (0330330660... or [033]), $3M_2$ (0550660110... or $[11\bar{2}]$), $3TC_1$ (0440440660... or $[02\bar{2}]$), $3TC_2$ (0110110220... or $[01\bar{1}]$), and $3TC_3$ (0220330550... or [123]), one can calculate \mathbf{c}_n within the translation of the base-centered lattice of the layer silicates. These are $[0, 0]$, $[-0.4, 0]$, $[-0.2, 0]$, $[0, -0.4]$, $[-0.3, 0.1]$, and $[-0.4, 0]$.

The geometry of the $20l$ and $13l$ reflections on ellipse II, their number, and intensities allowed us to exclude from consideration the polytypes $3T$ and $3TC_1$ because the equal parities of layer orientations make them similar to the simple polytype $1M$. The positions of these reflections also excluded the polytype $3TC_2$ with a triclinic unit cell. Two \mathbf{c}_n values, $[-0.2, 0]$ and $[-0.4, 0]$, yield the same positions for these reflections but their indices hk on ellipse II are different, so that the internal and external reflections of the quartets should have the inverse intensity ratios. Only the polytype $3M_2$ is consistent with the intensities of reflections on ellipse II and, which is especially important, with the positions and intensities of the $02l$ and $11l$ reflections on ellipse I.

VIOLATION OF RIGOROUS ORDER OF LAYER ALTERNATION IN THE STRUCTURE OF MUSCOVITE $3M_2$

The detailed analysis of the geometry and intensities of reflections on oblique-texture electron diffraction pattern from muscovite $3M_2$ showed some deviation from the expected features. These deviations depend on reflection indices and cannot match one unit cell and one order of layer alternation.

It turned out that the values of $-\cos\beta/a$ calculated from reflections lying on ellipses I, II, III, and V slightly differ and are equal to 0.225, 0.224, 0.207, and 0.182, respectively, at one projection of the c -axis onto the layer normal being the same, $c\sin\beta$. At $-\cos\beta/a \approx 0.200$, the $\bar{2}0l$ and $\bar{1}3l$ reflections located on ellipse II should form quartets with the equally spaced external $13l$ and $\bar{1}.3.l + 1$ and internal $20l$, $\bar{2}.0.l + 1$ reflections (Fig. 1). However, in the actual fact, instead of quartets, we observed only pairs of reflections (Fig. 1c) also

characteristic of the ideal case $-\cos\beta/a = 1/3$ (Fig. 1a), we observed only pairs of reflections (Fig. 1c), which seem to be formed by merge of neighboring reflections $13l$, $20l$, $\bar{2}.0.l + 1$ and $\bar{1}.3.l + 1$, m displaced from their ideal positions. The displacements are also observed for some rather strong $\bar{1}3l$ reflections, whereas the neighboring $\bar{2}0l$ reflections are very weak. In this case, the intensities of reflections on ellipse II are well consistent with the calculated reflections. For reflections $02l$ and $11l$ on ellipse I, the intensities of the $02l$ reflections are somewhat weakened in comparison with the calculated ones and are considerably diffuse. For $04l$ and $\bar{2}2l$ reflections on ellipse III, the discrepancy between the experimentally observed and calculated intensities becomes more pronounced. In fact, only the $22l$ and $\bar{2}2l$ reflections with $l = 3n$ are present, whereas the $04l$ reflections are considerably weakened. The $06l$ and $\bar{3}3l$ reflections of ellipse V are represented by triplets of uniformly distributed $3.3l - 1$, $06l$, and $\bar{3}.3.l + 1$ reflections; the internal reflections are much weaker than the external ones.

To reveal the real structural characteristics of muscovite $3M_2$ responsible for the observed distortion of the diffraction patterns, we calculated the theoretical intensities for a finite sequence of 24 layers of $3M_2$ with various defects in layer alternation for the $1M$, $2M_1$, $3T$, and $2M_2$ types. In the models considered here, the strict sequence of the $3M_2$ layers was interrupted by the links of various lengths of the $1M$, $2M_1$, $2M_2$, and $3T$ sequences, so that the $3M_2$ zones turned out to be in different azimuthal orientations. The diffraction characteristics were calculated by the program in which the

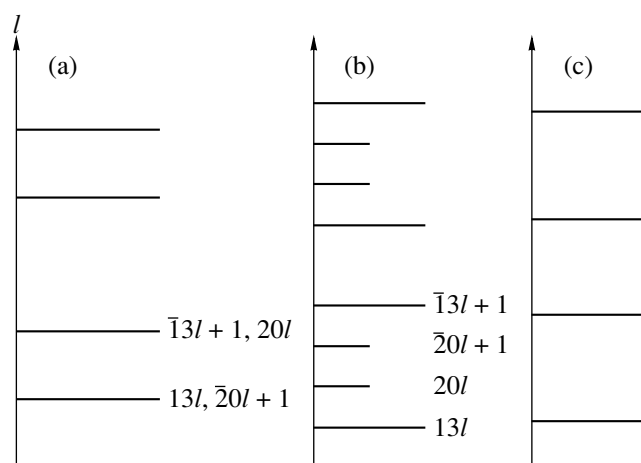


Fig. 1. Scheme of reflection arrangement on ellipse II of the oblique-texture electron diffraction pattern from muscovite $3M_2$ calculated at two $-\cos\beta/a$ values (a) $1/3$, (b) 0.200 , and (c) observed on real oblique-texture electron diffraction pattern.

structure factors of arbitrary sequence of arbitrary numbers of mica layers were expressed in terms of the scattering amplitudes of individual layers and the phase factors in the orthogonal coordinate system with due regard for the real distortions of the layers and their relative positions.

We considered the following possible stacking faults in the sequence of the layers in the $3M_2$ structure. For the $1M$ -type stacking faults: $2\bar{1}\bar{1}(0)_n, \dots, \bar{1}\bar{2}\bar{1}(0)_n, \dots$. For the $2M_1$ -type stacking faults: $2\bar{1}\bar{1}(\bar{2}\bar{2})_n, \dots, 2\bar{1}\bar{1}\bar{2}(\bar{2}\bar{2})_n, \dots, 2\bar{1}\bar{1}\bar{2}(\bar{2}\bar{2})_n, \dots, 11\bar{2}\bar{2}(\bar{2}\bar{2})_n, \dots, 11\bar{2}(\bar{2}\bar{2})_n, \dots, \bar{1}\bar{2}\bar{1}(\bar{2}\bar{2})_n, \dots$. For the $3T$ -type stacking faults: $\bar{1}\bar{1}\bar{2}(222)_n, \dots, \bar{2}11(222)_n, \dots, \text{and } \bar{1}\bar{2}\bar{1}(222)_n, \dots$. For the $2M_2$ -type stacking faults: $2\bar{1}\bar{1}\bar{1}(\bar{1}\bar{1})_n, \dots, 2\bar{1}\bar{1}(\bar{1}\bar{1})_n, \dots, \bar{2}\bar{1}\bar{1}\bar{1}(\bar{1}\bar{1})_n, \dots, \bar{2}11(\bar{1}\bar{1})_n, \dots, 11\bar{2}(\bar{1}\bar{1})_n, \dots, \bar{1}\bar{2}\bar{1}(\bar{1}\bar{1})_n, \dots, 1\bar{2}\bar{1}\bar{1}(\bar{1}\bar{1})_n, \dots$. In all the cases, the symbol \dots indicates one of the six possible variants of the continuation of the layer sequence inherent in the $3M_2$ structure: $\bar{2}\bar{1}\bar{1}$, $11\bar{2}$, $\bar{1}\bar{2}\bar{1}$, $2\bar{1}\bar{1}$, $\bar{1}\bar{1}\bar{2}$, and $\bar{1}\bar{2}\bar{1}$.

The above characteristics of electron diffraction patterns are best explained by the presence of the type- $2M_2$ “defects” in muscovite $3M_2$. The stacking faults in the layer sequence manifests themselves most clearly in the merge and displacement of the maxima on the diffraction profiles calculated for the $20l$ and $13l$ reflections of ellipse II (Fig. 2). The presence of the type- $2M_2$ defects results in the formation of pairs instead of quartets of reflections characteristic of the defect-free $3M_2$ structure; the calculated profiles have pairs of reflections on ellipse II in the positions corresponding to positions of reflections observed on the electron diffraction patterns. For the defects of the types $1M$, $2M_1$, and $3T$, one should observe either pairs of reflections displaced in the opposite directions in comparison with the reflections really observed on electron diffraction patterns, or the triplets of reflections with the middle reflection absent on diffraction patterns. The type- $2M_2$ defects agree much better with the diffraction characteristics observed on ellipses III and V on the diffraction patterns. Reflections on ellipse I are inappropriate for estimating the effect produced by defects of various types.

EXPERIMENTAL RESULTS AND DISCUSSION

Oblique texture electron diffraction patterns, the most efficient experimental material for the polytype analysis in finely disperse layer silicates, allowed us to reveal and uniquely identify, for the first time, the inhomogeneous muscovite polytype $3M_2$ in which the alternating layers are characterized by the mixed parity of azimuthal orientations. This mica has pairs of adjacent layers rotated by angles 120° and 60° with respect to

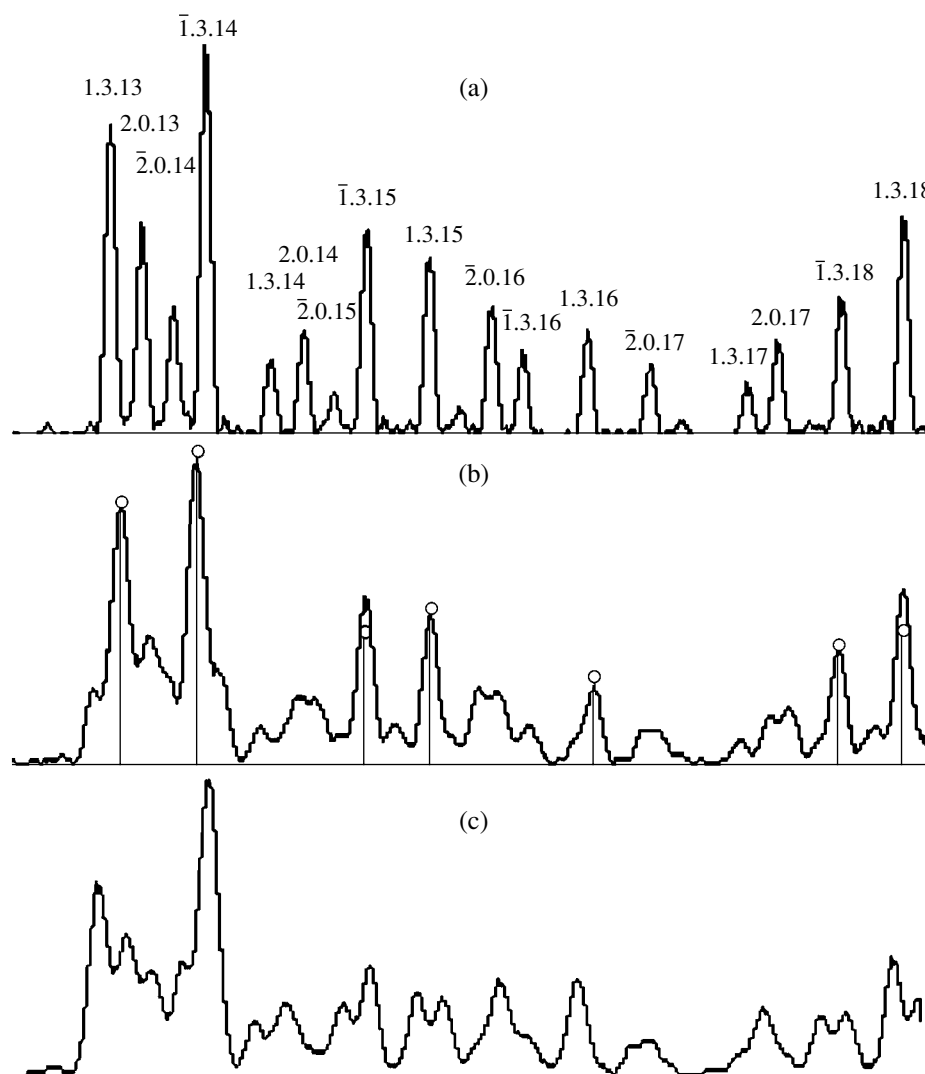


Fig. 2. Intensity profiles of $20l$ and $13l$ reflections on ellipse II of the oblique-texture electron diffraction pattern calculated for the sequence of 24 layers of muscovite $3M_2$ (a) without defects in the layer sequence at $-c \cos \beta / a = 0.200$ and (b, c) with defects in the layer sequence of types (b) $2M_2$ and (c) $1M$, $2M_1$, and $2T$. The vertical segments ended with circles on the profile in Fig. 2b indicate the positions and the intensities of reflections observed on electron diffraction patterns.

one another, which is characteristic of micas with the same and alternating parities of the azimuthal orientations of the successive layers. The interlayer cations are either in the octahedral or the trigonal-prismatic coordination. In the polytype $3M_2$, both these interlayer spacings coexist and alternate in the proportion 1 : 2. In the real muscovite $3M_2$, this order is also interrupted by the defects in layer alternation according to the law of $2M_2$. As a result, the inhomogeneity in this mica has a triple meaning indicating (i) nonequivalence of the relative orientations of the adjacent layers for different pairs, (ii) different parity of these orientations resulting in the formation of nonequivalent interlayers, and (iii) the interruption of the rigorous periodicity by the incorporation of the $2M_2$ -type defects.

The occurrence in nature not only of lepidolite but also muscovite $3M_2$ is consistent with the remarkable fact that the homogeneous polytype $2M_2$ is also known only for lepidolite and muscovite. Obviously, under the specific conditions of crystallization of these micas, the prismatic coordination of interlayer cations is more advantageous than octahedral, and, therefore, the corresponding defects break the rigorous periodicity of the muscovite $3M_2$ structure. It should be indicated that the high-resolution electron microscopy study of the lepidolite $3M_2$ [10] and selected-area electron diffraction study revealed the complex polytype $6M_1$ (615651 or $[1\bar{2}1\bar{1}2\bar{1}]$), which can be considered as a result of the periodic inversion of the constituent fragments of the $3M_2$ structure by the elements of the $2M_2$ structure.

ACKNOWLEDGMENTS

This study was supported by the Russian Foundation for Basic Research, project nos. 96-05-64983, 99-05-65430, and 00-05-64614.

REFERENCES

1. B. B. Zvyagin, *Electron Diffraction Analysis of Clay Mineral Structures* (Nauka, Moscow, 1964; Plenum, New York, 1967).
2. M. Ross, H. Takeda, and D. R. Wones, *Science* **31**, 191 (1966).
3. A. P. Zhukhlistov and B. B. Zvyagin, in *Proceeding of the 7th EUROCLAY Conference, Dresden, 1991*, p. 1211.
4. J. V. Smith and H. S. Yoder, *Miner. Mag.* **31**, 209 (1956).
5. A. Baronnet, *Phase Transit.* **16/17**, 477 (1989).
6. A. P. Zhukhlistov, B. B. Zvyagin, and V. I. Pavlishin, *Z. Kristallogr. B* **185**, 624 (1988).
7. A. P. Zhukhlistov, M. A. Litsarev, and V. I. Fin'ko, *Dokl. Akad. Nauk* **329**, 500 (1993).
8. A. P. Zhukhlistov, M. A. Litsarev, and V. I. Fin'ko, *Dokl. Akad. Nauk* **342**, 504 (1995).
9. S. W. Bailey and O. H. J. Christie, *Am. Mineral.* **63**, 203 (1978).
10. A. S. Rule, S. W. Bailey, K. J. T. Livi, and D. R. Veblen, *Am. Mineral.* **72**, 1163 (1987).
11. A. P. Zhukhlistov, B. B. Zvyagin, S. V. Soboleva, and A. F. Fedotov, *Clays Clay Miner.* **21**, 465 (1973).
12. V. S. Urusov, V. R. Tauson, and V. V. Akilov, *Geochemistry of Solids* (GEOS, Moscow, 1997).
13. B. B. Zvyagin, Z. V. Vrublevskaya, A. P. Zhukhlistov, *et al.*, *High-Voltage Electron Diffraction Analysis in Studies of Layer Silicates* (Nauka, Moscow, 1979).

Translated by L. Man

STRUCTURE
OF INORGANIC COMPOUNDS

Refined Crystal Structure of Lovozerite
 $\text{Na}_2\text{CaZr}[\text{Si}_6\text{O}_{12}(\text{OH},\text{O})_6] \cdot \text{H}_2\text{O}$

N. A. Yamnova, Yu. K. Egorov-Tismenko, and I. V. Pekov

Faculty of Geology, Moscow State University, Vorob'evy gory, Moscow, 119899 Russia

e-mail: natalia_yamnova@mail.ru

Received December 29, 2000

Abstract—The structure of Na,Ca,Zr-silicate lovozerite, $\text{Na}_2\text{CaZr}[\text{Si}_6\text{O}_{12}(\text{OH},\text{O})_6] \cdot \text{H}_2\text{O}$, from the Khibiny alkaline massif (the Kola Peninsula) was refined by single-crystal X-ray diffraction analysis (Syntex P1 diffractometer, $\lambda\text{MoK}\alpha$ radiation, $2\theta/\theta$ scanning technique). The refinement ($R_{hkl} = 0.077$, 1531 independent reflections; anisotropic thermal parameters) confirmed the trigonal system proposed for the mineral earlier (sp. gr. $R\bar{3}$; $a = 10.18(1) \text{ \AA}$, $c = 13.13(2) \text{ \AA}$, $Z = 3$) and revealed the presence of two additional positions (C and B) statistically occupied by Ca and Na atoms (and partly by Mn) and H_2O molecules, respectively. © 2001 MAIK “Nauka/Interperiodica”.

The crystal structure of the alkali zirconium silicate lovozerite was first solved in 1960 within the monoclinic space group $C2$ ($a = 10.48 \text{ \AA}$, $b = 10.20 \text{ \AA}$, $c = 7.33 \text{ \AA}$, $\beta = 92^\circ 30'$) [1]. Lovozerite can be considered as a parent mineral for a large group of natural and synthetic compounds, whose structures are based on a framework of six-membered silicon–oxygen (lovozerite-type) rings linked through isolated M -octahedra. The cavities of the framework are occupied by Na atoms and H_2O molecules. Later [2], lovozerite of composition $(\text{Na}_{2.5}\text{Ca}_{0.5}\text{Mg}_{0.2})_{3.2}(\text{Zr}_{0.7}\text{Fe}_{0.2}^{3+}\text{Ti}_{0.1})_{1.0}(\text{Si}_{5.8}\text{Al}_{0.2})_{6.0}\text{O}_{13.0}((\text{OH})_{5.2}\text{Cl}_{0.2})_{5.4}$ found in pegmatites from the Khibiny massif (the Kola Peninsula) was studied by the X-ray diffraction method. It was shown that the mineral belongs to the trigonal system ($a = 10.18 \text{ \AA}$, $c = 13.01 \text{ \AA}$) with the possible space groups $R\bar{3}2$, $R\bar{3}m$, and $R\bar{3}m$. The matrix of the transformation of the trigonal unit cell into the monoclinic one has also been reported: $(-1/3 \ -2/3 \ -2/3; 1 \ 0 \ 0; -1/3 \ -2/3 \ 1/3)$. The parameters of the monoclinic unit cell thus obtained ($a = 10.53 \text{ \AA}$, $b = 10.18 \text{ \AA}$, $c = 7.32 \text{ \AA}$, $\beta = 92^\circ 40'$) were virtually equal to those determined previously [1]. It should be noted that the lovozerite formula $\text{Na}_2\text{ZrSi}_6\text{O}_{15} \cdot 3\text{H}_2\text{O} \cdot 0.5\text{NaOH}$ proposed as the most probable in [1] is incorrect, because it takes no account of the presence of divalent cations, which, according to the data of chemical analysis, should be present in this mineral. This incorrectness is also evidenced by the results of all the more recent studies, which revealed that divalent cations occupy the position C in the lovozerite structural type. The crystallochemical analysis of lovozerite-like compounds [3, 4] demonstrated that their structures consist of identical pseudocubical ($a = 7.5 \text{ \AA}$) block units of the general formula $A_3B_3C_2M[\text{Si}_6\text{O}_{18}]$ (Fig. 1). The vertices of the blocks

are occupied by M cations ($M = \text{Zr}, \text{Ti}, \text{Mn}, \text{Fe}, \text{Ca}, \text{Sn}, \text{Cd}, \text{etc.}$) octahedrally coordinated by oxygen ions. The Si cations are located in the centers of six octants of each block. The centers of the remaining two octants (along one of the threefold axes of the prototype cell) are also occupied by octahedrally coordinated C cations ($C = \text{Ca}, \text{Mn}, \text{Na}, \text{etc.}$). The positions at the midpoints of the edges (A) and in the centers of the faces (B) of the above-mentioned blocks are filled predominantly with Na cations (more rarely, with Fe, Ti, Mn, Ca, Cd, or H). The diversity of the structures of the minerals of the lovozerite group is associated with the variations in the mode of filling of the above positions in the block and in the mode of junction of the adjacent blocks.

The ambiguity of the results of lovozerite investigation [1, 2] as well as the lack of the structural data for the trigonal modification of the mineral described in [2] gave impetus to the refinement of its crystal structure.

The lovozerite specimen was selected from a small veined rischorrite pegmatite stripped by the Apatitovyĭ Tsirk quarry at the Rasvumchorr mountain in the south of the Khibiny alkaline massif (the Kola Peninsula). The pegmatite is composed of potash feldspar, nepheline, black prismatic aegirine-diopside, green fibrous aegirine, alkaline amphibole, eudialyte, lamprophyllite, and lovozerite as the main minerals. Lomonsovite, magnesiumastrophyllite, pectolite, calborsite, rasvumite, hisingerite, etc. are present in minor amounts. Lovozerite replaces eudialyte crystals and is developed as a rim and, sometimes, as massive grained complete pseudomorphs up to 3–4 cm in diameter (isometric grains of sizes up to 1–1.5 mm) and has the sandy-yellow or the creamy color. Relics of the primary ultra-agpaitic paragenesis indicate that these pseudomorphs after eudialyte were originally composed of

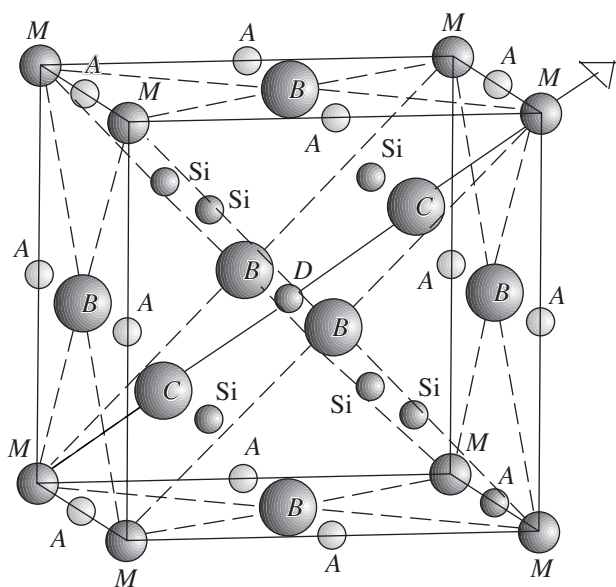


Fig. 1. Schematic arrangement of the atomic positions in the cubic "prototype unit cell" of the lovozerite structural type [4].

zirsinalite $\text{Na}_6\text{CaZrSi}_6\text{O}_{18}$. As the alkalinity of the medium decreased, this mineral lost some sodium, which was accompanied by hydration, and transformed into lovozerite stable under these conditions. The chemical composition of the lovozerite was studied by the electron probe analysis. Quantitatively, sodium and water contents were determined by the wet method. The average composition (wt %) is as follows: Na_2O , 7.7; K_2O , 0.6; CaO , 4.6; MgO , 0.1; MnO , 1.4; Fe_2O_3 , 2.0; SiO_2 , 58.7; TiO_2 , 0.5; ZrO_2 , 15.4; HfO_2 , 0.3; Nb_2O_5 , 0.1; H_2O^+ , 10.3; the sum is 101.7. The empirical formula (with respect to $\text{Si}_6(\text{O}, \text{OH})_{18}$): $(\text{Na}_{1.52}\text{K}_{0.08})_{\Sigma 1.60} \cdot (\text{Ca}_{0.50}\text{Mn}_{0.12}\text{Mg}_{0.02})_{\Sigma 0.64} (\text{Zr}_{0.77}\text{Fe}_{0.15}\text{Ti}_{0.04}\text{Hf}_{0.01})_{\Sigma 0.97} \cdot [\text{Si}_6\text{O}_{12.61}(\text{OH})_{5.39}]_{\Sigma 18} 0.82\text{H}_2\text{O}$.

EXPERIMENTAL

X-ray diffraction data were collected from a single crystal of dimensions $0.15 \times 0.15 \times 0.25$ mm. The parameters and the symmetry of the trigonal unit cell ($a = 10.18$ Å, $c = 13.13$ Å) were refined on an automated single-crystal Syntex $P\bar{1}$ diffractometer. The X-ray data were collected on the same diffractometer. The details of the X-ray diffraction study are given in Table 1. The systematic absences of the hkl reflections not satisfying the condition $-h + k + l = 3n$, and the non-equivalence of the pairs of the hkl and khk reflections indicate the rhombohedral Bravais lattice and two possible space groups— $R3$ and $R\bar{3}$. All the subsequent calculations were carried out with the use of the AREN program package [5]. At the first stage, the monoclinic system proposed in [1] was tested by refining the lovo-

zerite structure in the monoclinic C -centered unit cell with the parameters $a = 10.54$ Å, $b = 10.18$ Å, $c = 7.33$ Å, $\beta = 92^\circ 79'$. The matrix of the transformation from the R - to the C -centered cell was as follows: $-1/3 \ -2/3 \ -2/3; 1 \ 0 \ 0; -1/3 \ -2/3 \ 1/3$. The atomic coordinates reported in [1] were used as the starting model. The refinement of the model by the least-squares method within the possible space groups $C2/m$, $C2$, and Cm gave inadequate results due to the considerable scatter in the interatomic distances in the Si-tetrahedra and the high reliability factors (0.17, 0.15, and 0.12, respectively). Hence, the subsequent calculations were carried out within the acentric space group $R3$. The starting model was refined isotropically by the least-squares method to $R_{hkl} = 0.12$. The difference electron density synthesis revealed two additional maxima with the coordinates $x_1 \approx 0.25$, $y_1 \approx 0$, $z_1 \approx 0.75$ and $x_2 \approx 0.01$, $y_2 \approx 0.5$, $z_2 \approx 0.1$ (coincided with the C and B positions, respectively) of the pseudocubic block typical of the lovozerite structural type (Fig. 1). It was assumed that the C position is occupied by Ca, Na, and Mn cations, whereas the B position is occupied by H_2O molecules. The distribution of the cations over all independent crystallographic positions was determined by refining the occupancies and then the atomic scattering curves were chosen with due regard for the data of chemical analysis, the determination of the effective ionic radii of the cations, the thermal parameters of the atoms, and the average cation–oxygen distances. The refinement of the model by the least-squares method with allowance for mixed filling of some cationic positions gave the minimum final reliability factors $R_{hkl} = 0.104$ and 0.077 in the isotropic and anisotropic approximations, respectively. The distribution of the cations is indicated in Table 2.

The detailed crystallochemical formula of lovozerite is $(\text{Na}_{2.2}\text{K}_{0.1})(\text{Ca}_{0.4}\text{Na}_{0.2}\text{Mn}_{0.1})(\text{Zr}_{0.8}\text{Fe}_{0.1}\text{Ti}_{0.03}\text{Hf}_{0.03}) \cdot [\text{Si}_6\text{O}_{12}(\text{OH})_3(\text{OH}_{0.6}\text{O}_{0.4})_3] \cdot 0.9\text{H}_2\text{O}$. The idealized formula is $(\text{Na}, \square)_3(\text{Ca}, \text{Na}, \square)\text{Zr}[\text{Si}_6\text{O}_{12}(\text{OH})_3(\text{OH}, \text{O})_3] \cdot \text{H}_2\text{O}$. The anionic portion of the structure was separated into the O^{2-} ions and $(\text{OH})^-$ groups based on the results of calculations of the local valence balance according to Pyatenko [6]. The high values of the atomic thermal parameters and a rather high R_{aniso} factor (0.077) are explained by an insufficiently high quality of the single crystal used and, consequently, insufficiently high quality of the experimental data and the presence of vacancies. The final coordinates of the basis atoms and the equivalent thermal parameters are given in Table 2.

RESULTS AND DISCUSSION

On the whole, the refinement of the lovozerite structure confirmed the initial model [1], based on the framework of six-membered rings of the $[\text{Si}_6\text{O}_{12}(\text{OH})_3(\text{OH}, \text{O})_3]$ tetrahedra (the average Si–O distances in the Si(1)- and Si(2)-tetrahedra are 1.55 and 1.60 Å, respectively) sharing the oxygen vertices with isolated M -octahedra (the M –O distances vary from 2.0

Table 1. Principal details of X-ray diffraction study of lovozerite

Characteristic	Value
Crystal dimensions, mm	0.15 × 0.15 × 0.20
Automated single-crystal diffractometer	Syntex $P\bar{1}$
Radiation	Mo K_{α}
Monochromator	Graphite
Sp. gr.	$R3$
Unit-cell parameters	$a = 10.18(1) \text{ \AA}$ $c = 13.13(2) \text{ \AA}$ $V = 1180(3) \text{ \AA}^3$
Number of formula units, Z	3
Scanning technique	$2\theta/\theta$
Maximum $\sin\theta/\lambda$	1.064
Scan rate	4–24 deg/min
Number of measured reflections with $I > 1.96 \delta(I)$ within the reciprocal-space hemisphere	1531
Number of independent reflections	753
Program package	AREN
Reliability factors R_{hkl} :	
isotropic refinement	0.104
anisotropic refinement	0.077
Weighting scheme used in the least-squares procedure	$w = 1/(A + F + BF^2)$ $A = 2F_{\min}$ $B = 2/F_{\max}$

Table 2. Coordinates of the basis atoms and individual thermal parameters in the lovozerite structure

Atom (position)	Position multiplicity	Position occupancy	x/a	y/b	z/c	$B_{\text{eq}}, \text{ \AA}^2$
(A)	9	0.73Na + 0.03K	0.341(3)	0.172(2)	0.166(2)	4.3(3)
(B)	9	0.3H ₂ O	0.002(8)	0.462(6)	0.006(4)	4.4(3)
(C)	3	0.35Ca + 0.20Na + 0.08Mn	0	0	0.742	6.2(2)
(M)	3	0.80Zr + 0.14Fe + 0.03Ti + 0.03Hf	0	0	0	2.9(2)
Si(1)	9	Si	0.4829(8)	0.5172(8)	0.2208(6)	3.3(2)
Si(2)	9	Si	0.1835(5)	0.3696(6)	0.0952(5)	2.2(1)
O(1)	9	O	0.447(3)	0.224(3)	−0.003(2)	7.3(6)
O(2)	9	(OH, O)	0.555(3)	0.424(3)	0.248(2)	6.5(5)
O(3)	9	(OH)	0.208(2)	0.104(2)	0.325(1)	3.1(3)
O(4)	9	O	0.336(3)	0.433(4)	0.159(2)	8.8(9)
O(5)	9	O	0.101(2)	0.184(2)	0.091(1)	3.1(3)
O(6)	9	O	0.601(2)	0.667(2)	0.161(1)	4.9(4)

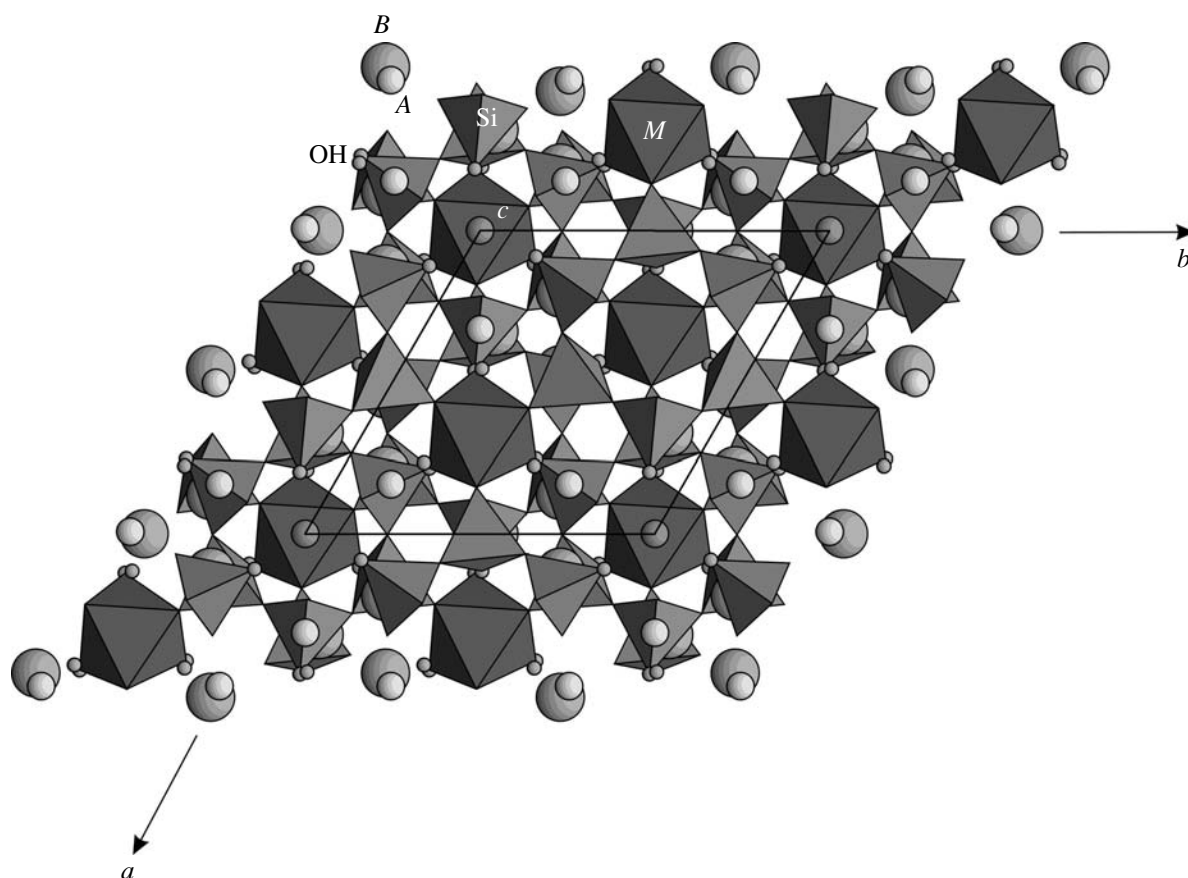


Fig. 2. Crystal structure of lovozerite projected onto the xy plane.

to 2.11 Å; the average is 2.06 Å) (Fig. 2). The M cations (predominantly Zr) in the model of lovozerite proposed earlier [1] and in the refined structure are located in the lattice sites of the pseudotrigonal (monoclinic) and trigonal unit cells, respectively. In the monoclinic cell, the M positions are located in the centers of the basal faces of the C cell. The matrix of the transformation from the C unit cell to the double-centered hexagonal R cell is $1/2 -1/2 1; 0 1 0; -1 0 1$. The refined lovozerite structure differs from the earlier model primarily in that in the former, the cationic C position is statistically (by ~60%) filled with Ca, Na, and Mn atoms (the C -O distances vary from 2.19 to 2.89 Å; the average is 2.54 Å). The C -octahedra share the oxygen faces with the M -octahedra and also contribute to strengthening of the crystal structure.

It should be noted that the C position was also found in the structure of a new representative of the lovozerite group, Na,Zr-silicate litvinskite $(\text{Na}, \text{H}_2\text{O}, \square)_3 (\square, \text{Na}, \text{Mn}^{2+})\text{Zr}[\text{Si}_6\text{O}_{12}(\text{OH})_3(\text{OH}, \text{O})_3]$ ($a = 10.589$ Å, $b = 10.217$ Å, $c = 7.355$ Å, $\beta = 92.91^\circ$, sp. gr. Cm , $Z = 2$) [7, 8] discovered in ultra-agpaitic pegmatites from the Lovozero massif (the Kola Peninsula). However, these positions in two minerals are filled differently. Thus, the C position in lovozerite is occupied predominantly

by Ca and Na cations by about 60%, whereas this position in litvinskite is occupied by 33% and predominantly by Na and Mn cations. Similar to litvinskite, this position in lovozerite is the only one that does not obey the center of inversion, i.e., violating the centrosymmetric structure. The Na cations in the lovozerite structure are located in the framework cavities and statistically occupy (by ~80%) the A position (in the monoclinic space group, this position is split into two independent positions). The A -O distances in the eight-vertex A -polyhedra vary from 2.38 to 2.87 Å (the average is 2.61 Å). In the study of the litvinskite structure [8], the possibility of the higher (trigonal) symmetry of the mineral has been examined; however, the results of the structure refinement within the trigonal unit cell turned out to be inadequate.

In the refined lovozerite structure, there is an additional B position statistically (by ~30%) filled with H_2O molecules. This position was not detected either in the initial lovozerite model [1] or in litvinskite [8].

The comparison of the refined lovozerite structure with the structure of zirsinalite having the similar composition $\text{Na}_6(\text{Ca}_{0.5}\square_{0.5})_2\text{Zr}[\text{Si}_6\text{O}_{18}]$ ($a = 10.29$ Å, $c = 26.31$ Å, sp. gr. $R\bar{3}c$, $Z = 6$) [9] after the transformation of the atomic coordinates of the latter [9] from the trig-

onal R unit cell to the double-centered hexagonal cell showed that these structures are virtually identical (the matrix of the transformation from the hexagonal R cell of zirsinalite to the analogous unit cell of lovozerite is $0 -1 0; 1 1 0; 0 0 1/2$). The only difference reduces to that the A position in the cubic prototype cell of the lovozerite structure (Fig. 1) is occupied by Na atoms and the B position is statistically (by ~30%) occupied by H_2O molecules, whereas both these positions (A and B) in the zirsinalite structure characterized by the substantially higher Na content are filled with Na atoms alone. The Ca atoms in the zirsinalite structure statistically (by ~50%) occupy both C positions with retention of the center of symmetry, whereas only one of two C positions in the lovozerite structure is occupied by Ca (Na, Mn) atoms (also statistically, by 60%), which excludes the presence of centers of inversion in the latter structure. In addition, doubling of the unit-cell parameter c of zirsinalite ($c = 26.31 \text{ \AA}$) in comparison with that of lovozerite ($c = 13.01 \text{ \AA}$) is explained by the presence of the coordinate planes c and the center of inversion in the holohedral sp. gr. $R\bar{3}c$ of zirsinalite, which are absent in the sp. gr. $R3$ of lovozerite. The structural similarity of lovozerite and zirsinalite is determined genetically. According to Khomyakov, lovozerite cannot be crystallized alone and, thus, can arise only as homoaxial pseudomorph after zirsinalite [10]. No facts inconsistent with this hypothesis have been found. Hence, the process of lovozerite generation from zirsinalite reduces to the loss of more than one-half of sodium atoms, with the deficiency of the positive charge being compensated by the replacement of the corresponding number of oxygen atoms by the OH groups. This process is also accompanied by incorporation of water molecules into one of the empty cavities. The number of cations located in the framework cavities drastically decreases upon the transformation of zirsinalite into lovozerite, which manifests itself in the density ($2.9\text{--}3.0 \text{ g/cm}^3$ for zirsinalite and $2.4\text{--}2.7 \text{ g/cm}^3$ for lovozerite) and in the refractive indices ($1.605\text{--}1.610$ and $1.53\text{--}1.57$ for zirsinalite and lovozerite, respectively). However, neither the cationic composition nor the configuration of the $\{Zr[Si_6(O, OH)_{18}]\}$ framework are changed in the transition from zirsinalite to lovozerite, which provides the close structural rela-

tionship between the prototype phase (zirsinalite) and the newly formed mineral (lovozerite).

To summarize, the refinement of the lovozerite structure confirmed the trigonal symmetry of the mineral proposed earlier by Kapustin *et al.* [2] and revealed the presence of two additional (C and B) positions statistically occupied by Ca and Na (and partly by Mn) cations and H_2O molecules, respectively. Thus, the idealized formula of lovozerite should be written as $Na_2CaZr[Si_6O_{12}(OH, O)_6] \cdot H_2O$.

ACKNOWLEDGMENTS

We are grateful to E.L. Belokoneva for her help in collection of X-ray diffraction data.

The study was supported by the Russian Foundation for Basic Research and by the National Science Foundation of China (NSFC), joint project no. 99-05-39019.

REFERENCES

1. V. V. Ilyukhin and N. V. Belov, Dokl. Akad. Nauk SSSR **131** (1), 176 (1960).
2. Yu. L. Kapustin, A. V. Bykova, and Z. V. Pudovkina, Izv. Akad. Nauk SSSR, Ser. Geol., No. 8, 106 (1973).
3. N. M. Chernitsova, Z. V. Pudovkina, A. A. Voronkov, *et al.*, Zap. Vses. Mineral. O-va **104** (1), 18 (1975).
4. R. A. Tamazyan and Yu. A. Malinovskii, Kristallografiya **35** (2), 398 (1990) [Sov. Phys. Crystallogr. **35**, 227 (1990)].
5. V. I. Andrianov, Kristallografiya **32** (1), 228 (1987) [Sov. Phys. Crystallogr. **32**, 130 (1987)].
6. Yu. A. Pyatenko, Kristallografiya **17** (4), 773 (1972) [Sov. Phys. Crystallogr. **17**, 677 (1972)].
7. I. V. Pekov, I. A. Ekimenkova, N. V. Chukanov, *et al.*, Zap. Vseross. Mineral. O-va **129** (1), 45 (2000).
8. N. A. Yamnova, Yu. K. Egorov-Tismenko, I. V. Pekov, and I. A. Ekimenkova, Kristallografiya **46** (2), 230 (2001) [Crystallogr. Rep. **46**, 190 (2001)].
9. Z. V. Pudovkina, N. M. Chernitsova, A. A. Voronkov, and Yu. A. Pyatenko, Dokl. Akad. Nauk SSSR **250** (4), 865 (1980) [Sov. Phys. Dokl. **25**, 69 (1980)].
10. A. P. Khomyakov, *Mineralogy of Ultra-Agpaitic Alkaline Rocks* (Nauka, Moscow, 1990).

Translated by T. Safonova

STRUCTURE
OF INORGANIC COMPOUNDS

Synthesis and Crystal Structures of Lithium Polyphosphates,
 LiPO_3 , $\text{Li}_4\text{H}(\text{PO}_3)_5$, and $\text{LiMn}(\text{PO}_3)_3$

E. V. Murashova and N. N. Chudinova

Kurnakov Institute of General and Inorganic Chemistry, Russian Academy of Sciences,
Leninskii pr. 31, Moscow, 117907 Russia

e-mail: murashova@ijic.ras.ru

Received December 29, 2000

Abstract—Polyphosphates of the compositions LiPO_3 , $\text{Li}_4\text{H}(\text{PO}_3)_5$, and $\text{LiMn}(\text{PO}_3)_3$ were prepared by the reactions of Li_2CO_3 and MnO_2 with melts of polyphosphoric acids at 240–350°C, and their crystal structures were established. The unit-cell parameters are $a = 13.074 \text{ \AA}$, $b = 5.4068 \text{ \AA}$, $c = 16.452 \text{ \AA}$, $\beta = 99.00^\circ$, sp. gr. $P2/n$; $a = 6.6434 \text{ \AA}$, $b = 7.253 \text{ \AA}$, $c = 11.399 \text{ \AA}$, $\alpha = 72.60^\circ$, $\beta = 83.36^\circ$, $\gamma = 85.32^\circ$, sp. gr. $P\bar{1}$; $a = 8.364 \text{ \AA}$, $b = 8.561 \text{ \AA}$, $c = 8.6600 \text{ \AA}$, sp. gr. $P2_12_12_1$, respectively. The influence of cations on the structures of the compounds is discussed. © 2001 MAIK “Nauka/Interperiodica”.

Continuing our studies of the effect of metal cations on the composition and structure of condensed phosphates formed in melts of polyphosphoric acids [1, 2], we examined the influence of metal cations on the

structure (including the configuration of polyphosphate chains) in a series of simple, acid, and double polyphosphates: LiPO_3 , $\text{Li}_4\text{H}(\text{PO}_3)_5$, and $\text{LiMn}(\text{PO}_3)_3$, respectively.

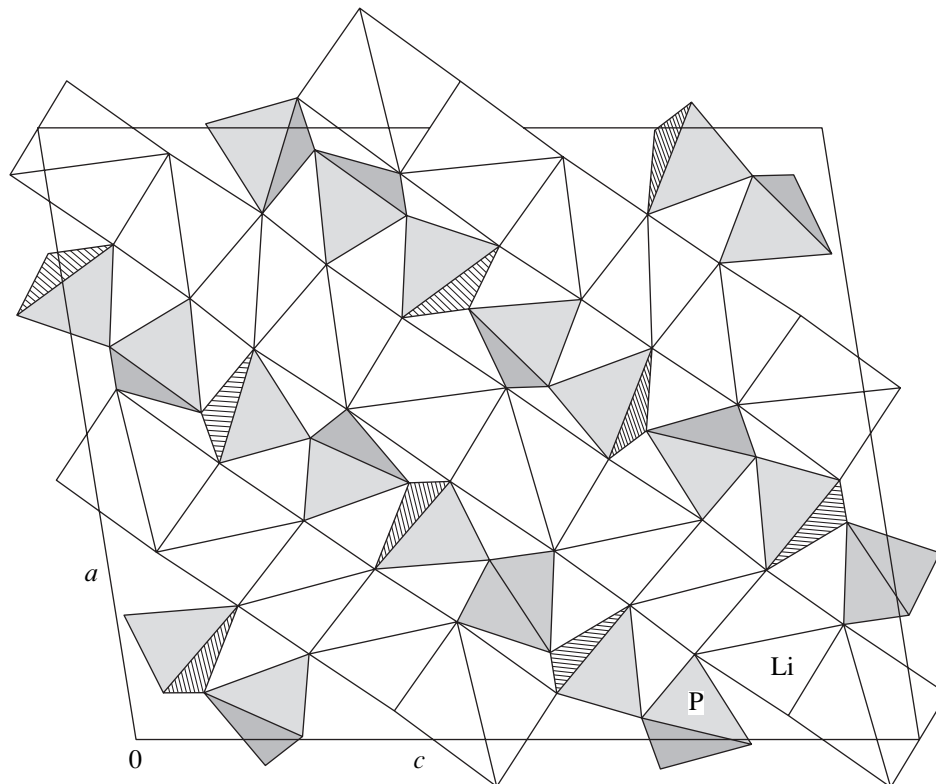


Fig. 1. The LiPO_3 crystal structure projected along the $[010]$ direction.

Table 1. Main crystallographic parameters, details of X-ray data collection, and characteristics of the refinement of the LiPO_3 , $\text{Li}_4\text{H}(\text{PO}_3)_5$, and $\text{LiMn}(\text{PO}_3)_3$ structures

Compound	LiPO_3	$\text{Li}_4\text{H}(\text{PO}_3)_5$	$\text{LiMn}(\text{PO}_3)_3$
System	Monoclinic	Triclinic	Orthorhombic
a , Å	13.074(2)	6.6434(8)	8.364(2)
b , Å	5.4068(8)	7.253(2)	8.561(2)
c , Å	16.452(2)	11.399(3)	8.6600(9)
α , deg	90	72.60(2)	90
β , deg	99.00(2)	83.36(2)	90
γ , deg	90	85.32(2)	90
Sp. gr.	$P2/n$	$P\bar{1}$	$P2_12_12_1$
Z	20	2	4
V , Å ³	1148.6(3)	520.0(2)	620.1(2)
ρ_{calcd} , g/cm ³	2.484	2.706	3.201
μ , mm ⁻¹	0.888	0.980	2.933
θ_{max} , deg	30	30	30
Diffractionmeter	Enraf Nonius CAD-4		
Scanning mode	$\omega/2\theta$		
Number of observed reflections	3121	3248	902
Number of crystallographically independent reflections	2772	3024	884
Number of crystallographically independent reflections with $I > 2\sigma(I)$	1872	1533	818
Number of parameters in the refinement	227	221	127
$R1/wR2$ ($I > 2\sigma(I)$)*	0.0379/0.0652	0.0319/0.0751	0.0350/0.0863
$R1/wR2$ (all data)	0.0828/0.0856	0.0463/0.0792	0.0386/0.0883
Gof	0.791	1.015	1.056

$$* R1 = \sum ||F_o| - |F_c|| / \sum |F_o|, wR2 = \{ \sum [w(F_o^2 - F_c^2)^2] / \sum [w(F_o^2)] \}^{1/2}.$$

EXPERIMENTAL

Simple, acid, and double lithium polyphosphates were synthesized starting from Li_2CO_3 , MnO_2 , In_2O_3 , and 85% phosphoric acid. Mixtures of the components taken in specified ratios were heated for 4–6 days in the temperature range of 240–350°C. The crystals formed were washed off from the melt with water and were studied by the X-ray phase and the X-ray structure analysis.

In the course of the synthesis in the $\text{Li}_2\text{O}-\text{MnO}_2-\text{P}_2\text{O}_5(\text{H}_2\text{O})$ system, Mn(IV) was reduced to Mn(III) and then to Mn(II). Heating of the mixture of the initial components taken in the atomic ratio Li : Mn : P = 5 : 1 : 15 in a platinum crucible for 4 days at 350°C provided the formation of the precipitate consisting of three phases: $\text{Mn}(\text{PO}_3)_3$ (its structure has been established earlier [3]), $\text{LiMn}(\text{PO}_3)_3$, and $\text{Li}_4\text{H}(\text{PO}_3)_5$. These

phases were ruby-red, pale lilac, and colorless, respectively.

We failed to obtain double lithium–indium phosphates in the $\text{Li}_2\text{O}-\text{In}_2\text{O}_3-\text{P}_2\text{O}_5(\text{H}_2\text{O})$ system. Heating of the mixture of the components taken in the atomic ratio Li : In : P = 5 : 1 : 15 in a glassy-carbon crucible for 6 days at 240°C resulted in synthesis of LiPO_3 crystals and trace amounts of an unidentified phase.

Earlier [4], LiPO_3 was studied by X-ray diffraction analysis, with the refinement being performed within the sp. gr. Pn . Based on analysis of the interatomic distances, we assumed that the centrosymmetric space group $P2/n$ is highly probable. Generally, polyphosphates containing the cations of only one kind have two types of P–O bonds—two short bonds involving the terminal atoms (~1.48 Å) and two long bonds with the participation of the bridging oxygen atoms (~1.60 Å). The unusual P–O bond lengths were reported in [4],

Table 2. Atomic coordinates and thermal parameters for the LiPO_3 , $\text{Li}_4\text{H}(\text{PO}_3)_5$, and $\text{LiMn}(\text{PO}_3)_3$ structures

Atom	x/a	y/b	z/c	$U_{\text{eq}}, \text{\AA}^2$
LiPO_3				
P(1)	0.45202(4)	0.67317(10)	0.31660(4)	0.00988(14)
P(2)	0.35155(4)	0.33960(10)	0.41668(4)	0.00839(14)
P(3)	0.23891(4)	0.68754(10)	0.50907(3)	0.00686(14)
P(4)	0.12646(4)	0.34525(9)	0.60220(4)	0.00885(14)
P(5)	0.03325(4)	0.68770(9)	0.70608(4)	0.00712(13)
O(1)	0.35939(12)	0.7562(4)	0.26052(11)	0.0239(4)
O(2)	0.54125(12)	0.8437(3)	0.33857(10)	0.0160(4)
O(3)	0.49433(14)	0.4164(3)	0.28561(11)	0.0210(4)
O(4)	0.42169(11)	0.5774(3)	0.40225(9)	0.0124(3)
O(5)	0.42300(12)	0.1449(3)	0.45414(11)	0.0179(4)
O(6)	0.27989(12)	0.2827(3)	0.34116(10)	0.0194(4)
O(7)	0.29515(13)	0.4356(3)	0.48838(11)	0.0229(4)
O(8)	0.31014(12)	0.8193(3)	0.57299(10)	0.0207(4)
O(9)	0.19359(12)	0.8258(3)	0.43501(10)	0.0167(4)
O(10)	0.14279(12)	0.5835(3)	0.54694(11)	0.0165(3)
O(11)	0.07563(12)	0.1497(3)	0.54779(10)	0.0150(4)
O(12)	0.22132(10)	0.2962(3)	0.65918(9)	0.0108(3)
O(13)	0.03568(12)	0.4449(3)	0.65069(9)	0.0160(4)
O(14)	0.13940(11)	0.7790(3)	0.73133(10)	0.0189(4)
O(15)	-0.04738(12)	0.8588(3)	0.66343(10)	0.0172(4)
Li(1)	0.1835(3)	-0.0095(7)	0.3246(2)	0.0150(8)
Li(2)	0.3233(3)	0.0214(7)	0.6735(3)	0.0197(8)
Li(3)	-0.0610(2)	0.9991(7)	0.5579(2)	0.0113(8)
Li(4)	0.5576(3)	0.0200(11)	0.4421(3)	0.0333(12)
Li(5)	1/4	0.5044(11)	1/4	0.0245(13)
Li(6)	1/4	0.5352(10)	3/4	0.0134(11)
$\text{Li}_4\text{H}(\text{PO}_3)_5$				
P(1)	0.28979(6)	0.87563(6)	0.95103(4)	0.00721(10)
P(2)	0.07194(6)	0.65685(6)	0.82848(4)	0.00665(10)
P(3)	0.14250(6)	0.72131(6)	0.56137(4)	0.00679(10)
P(4)	0.39016(6)	0.97605(6)	0.35973(4)	0.00714(10)
P(5)	0.20270(6)	0.76137(6)	0.22529(4)	0.00704(10)
O(1)	0.46199(18)	0.73138(19)	0.95362(12)	0.0126(2)
O(2)	0.16727(18)	0.83777(17)	0.08478(11)	0.0107(2)
O(3)	0.11915(18)	0.83093(17)	0.87748(12)	0.0116(2)
O(4)	0.3211(2)	0.08564(17)	0.90403(12)	0.0135(3)
O(5)	0.07094(18)	0.77204(17)	0.68435(11)	0.0102(2)
O(6)	0.23971(18)	0.50518(17)	0.84361(11)	0.0107(2)
O(7)	-0.13782(19)	0.60381(18)	0.88000(12)	0.0128(2)
O(8)	0.22013(18)	0.92178(17)	0.47568(11)	0.0108(2)
O(9)	0.30418(18)	0.56532(17)	0.57153(11)	0.0104(2)
O(10)	-0.05311(19)	0.69025(19)	0.51301(12)	0.0118(2)
O(11)	0.56411(19)	0.83264(18)	0.38250(11)	0.0115(2)
O(12)	0.42119(19)	0.18435(17)	0.33283(11)	0.0108(2)
O(13)	0.26927(19)	0.95091(17)	0.25159(11)	0.0110(2)
O(14)	0.36635(18)	0.60719(18)	0.25417(12)	0.0118(2)
O(15)	-0.00401(19)	0.71555(19)	0.29045(11)	0.0129(2)

Table 2. (Contd.)

Atom	x/a	y/b	z/c	$U_{eq}, \text{\AA}^2$
$\text{Li}_4\text{H}(\text{PO}_3)_5$				
Li(1)	0.7225(5)	0.7127(5)	0.0122(3)	0.0171(6)
Li(2)	0.3817(5)	0.3621(5)	0.4457(3)	0.0228(7)
Li(3)	0.6846(5)	0.6865(5)	0.2632(3)	0.0181(6)
Li(4)	0.4266(5)	0.3977(5)	0.1757(3)	0.0184(7)
H(1)	-0.049(4)	0.704(4)	0.441(3)	0.034(8)*
$\text{LiMn}(\text{PO}_3)_3$				
Mn(1)	0.12897(11)	0.85641(11)	0.15864(11)	0.0075(2)
P(1)	0.20179(19)	0.80733(19)	0.55968(18)	0.0086(3)
P(2)	0.31298(18)	0.52094(18)	0.68931(18)	0.0079(3)
P(3)	0.02851(17)	0.32069(19)	0.68323(17)	0.0081(3)
O(1)	0.1589(5)	0.8612(6)	0.4031(5)	0.0144(10)
O(2)	0.3103(5)	0.9063(5)	0.6546(5)	0.0108(9)
O(3)	0.2744(5)	0.6350(5)	0.5476(5)	0.0086(8)
O(4)	0.0411(5)	0.7731(5)	0.6534(5)	0.0123(9)
O(5)	0.3775(5)	0.6155(5)	0.8194(5)	0.0116(9)
O(6)	0.1383(5)	0.4637(5)	0.7358(5)	0.0117(9)
O(7)	0.5905(5)	0.8874(5)	0.8660(5)	0.0128(10)
O(8)	-0.1041(5)	0.3744(6)	0.5819(5)	0.0118(9)
O(9)	0.1305(5)	0.1918(6)	0.6221(5)	0.0137(9)
Li(1)	0.3464(13)	0.8649(16)	0.8842(14)	0.019(3)

* For the H(1) atom, the U_{iso} value is given.

e.g., 1.48, 1.48, 1.56, and 1.66 Å for the bond lengths involving P(1) and 1.44, 1.48, 1.49, and 1.60 Å for P(2). Taking into account all the above facts, we performed the refinement of the LiPO_3 crystal structure within the centrosymmetric space group $P2/n$.

The crystallographic parameters and the details of X-ray data collection and structure refinement of the compounds synthesized are given in Table 1. The crystal structures were solved by direct methods using the SHELXS97 program package [5]. The atomic coordinates and thermal parameters were refined using the SHELXL97 program package [6], and their refined values are listed in Table 2.

Lithium polyphosphate LiPO_3 consists of infinite polyphosphate chains aligned along the [101] direction with the periodic repetition of ten PO_4 -tetrahedra. Each PO_4 -tetrahedron contains two bridging oxygen atoms involved in the P–O–P bonds (1.57–1.62 Å) and two terminal oxygen atoms (P–O lengths range within 1.47–1.49 Å). The lithium atoms are located between the chains, so that the adjacent LiO_4 tetrahedra (the Li–O distances vary from 1.91 to 2.04 Å) share their edges to form infinite chains (Fig. 1) parallel to the polyphosphate chains.

In the structure of acid lithium polyphosphate $\text{Li}_4\text{H}(\text{PO}_3)_5$, the chains consisting of the PO_4 -tetrahedra (the repetition period equals five) are aligned along the

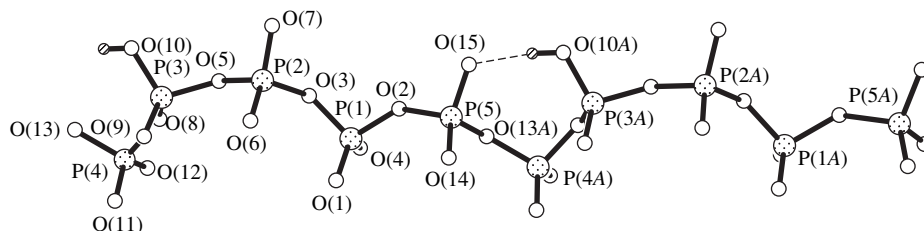


Fig. 2. The polyphosphate chain in the $\text{Li}_4\text{H}(\text{PO}_3)_5$ structure.

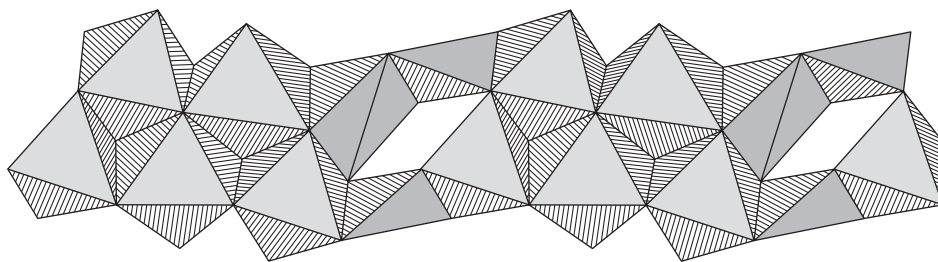


Fig. 3. Double chains of Li-polyhedra in the $\text{Li}_4\text{H}(\text{PO}_3)_5$ structure.

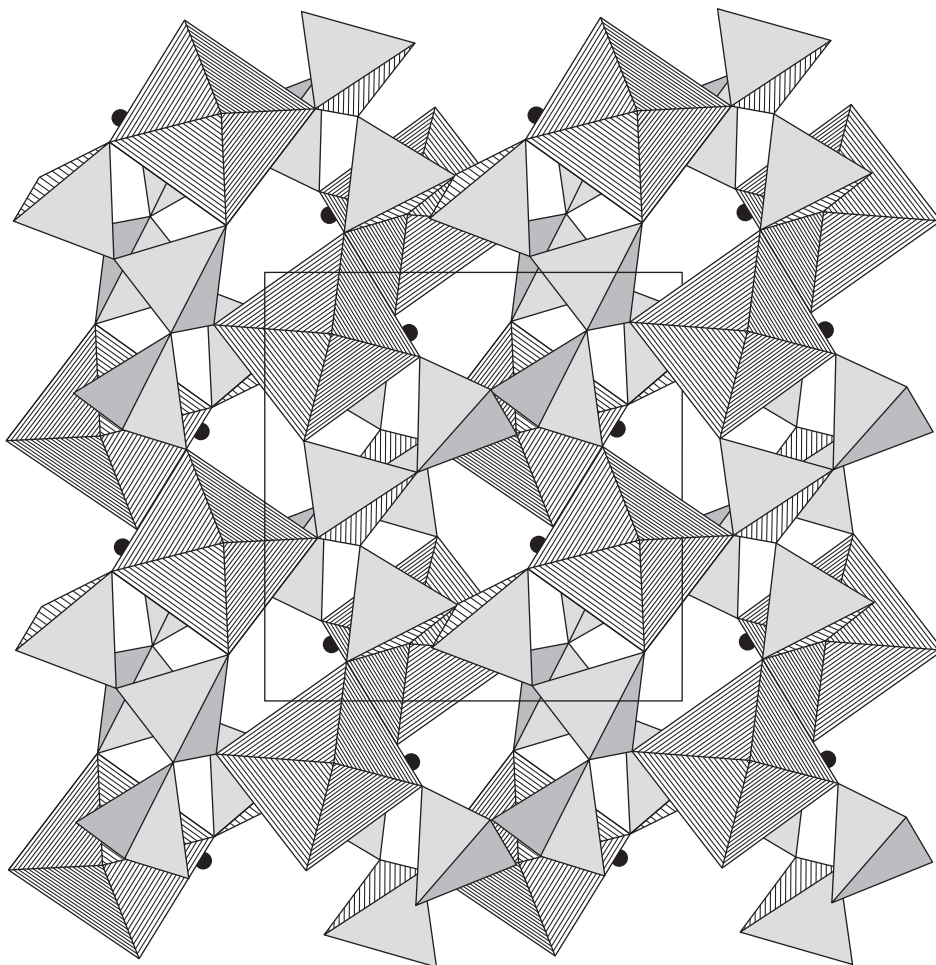


Fig. 4. The $\text{LiMn}(\text{PO}_3)_3$ crystal structure projected along the $[001]$ direction; Mn-octahedra and PO_4 -tetrahedra are shown; Li atoms are represented by circles.

$[001]$ direction. The P–O distances with the participation of the bridging and terminal oxygen atoms are range within 1.57–1.61 and 1.48–1.49 Å, respectively. The O(10) atom in the $\text{P}(3)\text{O}_4$ -tetrahedron is bound to the hydrogen atom involved in hydrogen bonding $\text{O}(10)\cdots\text{O}(15) \{x, y, z - 1\}$ is 2.473(2) Å; $\text{O}(10)\text{--H}(1)$ is 0.79(3) Å; $\text{H}(1)\cdots\text{O}(15)$ is 1.69(3) Å, the $\text{O}(10)\text{H}(1)\text{O}(15)$ angle equals $171(3)^\circ$, with the O(15) atom belonging to the $\text{P}(5)\text{O}_4$ tetrahedron of the same

chain (Fig. 2). Four independent lithium atoms are located in the coordination polyhedra of three types. Thus, the coordination environment of the Li(1) atom is a distorted tetrahedron (Li–O are 1.91–2.01 Å), the Li(2) and Li(3) atoms are in an octahedral environment (Li–O are 2.02–2.37 Å), and the Li(4) atom has a tetragonal-pyramidal environment (Li–O are 1.97–2.34 Å). The Li-polyhedra share edges to form infinite double ribbons (Fig. 3) extended, like the polyphosphate chains, along the $[001]$ direction.

Double lithium–manganese polyphosphate $\text{LiMn}(\text{PO}_3)_3$ is built by polyphosphate chains with the repetition period of six PO_4 tetrahedra and the Mn-octahedra. The P–O distances involving the bridging and the terminal oxygen atoms vary from 1.58 to 1.60 Å and from 1.48 to 1.49 Å, respectively. The Mn–O distances range within 2.08–2.13 Å. The polyphosphate chains and the Mn-octahedra form a framework with the cavities being occupied by lithium atoms. The nearest environment of the Li atoms consists of six oxygen atoms (Fig. 4).

RESULTS AND DISCUSSION

In addition to the crystal structures described in this study, a number of other double polyphosphates were reported. These are double polyphosphates $\text{LiM}^{\text{II}}(\text{PO}_3)_3$ ($M^{\text{II}} = \text{Cu}$ [7] or Fe [8]) isostructural to $\text{LiMn}(\text{PO}_3)_3$ and two series of isostructural double polyphosphates of lithium and trivalent metals $\text{LiM}^{\text{III}}(\text{PO}_3)_3$ ($M^{\text{III}} = \text{Al}$, Ga , Fe , or Cr) [9] and $\text{LiLn}(\text{PO}_3)_4$ ($\text{Ln} = \text{La–Lu}$) [10] prepared in our previous study. The structures of $\text{LiAl}(\text{PO}_3)_3$ [11], $\text{LiGa}(\text{PO}_3)_3$ [12], $\text{LiNd}(\text{PO}_3)_4$ [13], and $\text{LiEr}(\text{PO}_3)_4$ [14] were established. The structures of double polyphosphates of the composition $\text{LiM}^{\text{III}}(\text{PO}_3)_4$ are based on bent polyphosphate chains, $M^{\text{III}}\text{O}_6$ -octahedra, and LiO_4 -tetrahedra. Sharing edges octahedra and tetrahedra are linked in pairs and are located between the chains. In polyphosphates of the composition $\text{LiLn}(\text{PO}_3)_4$, the bent polyphosphate chains are linked by eight-vertex neodymium-polyhedra and lithium-tetrahedra into the framework. A comparison of the structural data for the LiPO_3 , $\text{Li}_4\text{H}(\text{PO}_3)_5$, $\text{LiM}^{\text{II}}(\text{PO}_3)_3$, $\text{LiM}^{\text{III}}(\text{PO}_3)_3$, and $\text{LiLn}(\text{PO}_3)_4$ series demonstrates that the cationic component produces a considerable effect on the configuration of the polyphosphate chains in the compounds under consideration. Thus, in LiPO_3 and $\text{Li}_4\text{H}(\text{PO}_3)_5$, these chains are linear, whereas in the structures of double polyphosphates, the chains are bent and are characterized by the repetition of six PO_4 -tetrahedra in $\text{LiM}^{\text{II}}(\text{PO}_3)_3$ to four tetrahedra in double phosphates with trivalent cations.

It is noteworthy that only polyphosphates can be crystallized from melts of polyphosphoric acids containing lithium cations and various cations of di- and trivalent metals, whereas double salts containing cyclic or branched anions cannot be formed. At the same time, double cyclophosphates, in which the ring size correlates with the size of the alkali metal cation, were obtained along with polyphosphates of other alkali metal cations: cyclopenta- $\text{Na}_2\text{MnP}_5\text{O}_{15}$, cycloocta- $\text{K}_2\text{M}_2^{\text{III}}\text{P}_8\text{O}_{24}$, cyclododecaphosphates $\text{Cs}_3\text{M}_{\text{III}}^3\text{P}_{12}\text{O}_{36}$,

and ultraphosphates $\text{Na}_3\text{M}^{\text{III}}\text{P}_8\text{O}_{23}$ with isolated cage-like anions [15].

The absence of lithium-containing cyclophosphates is explained by the fact that the cationic-environment geometry plays an important role in the formation of structures with “rigid” cyclic cations. Apparently, a small lithium cation can not satisfy these requirements. On the contrary, polyphosphate chains can change their configuration because of high flexibility of the constituent fragments. Thus, they can readily meet any geometric and coordination requirements set by metal cations. This situation is really observed in the series of the polyphosphates under consideration.

ACKNOWLEDGMENTS

This study was supported by the Russian Foundation for Basic Research, project no. 98-03-32695.

REFERENCES

1. N. N. Chudinova, E. V. Murashova, and B. S. Zakharova, *Zh. Neorg. Khim.* **43** (6), 885 (1998).
2. E. V. Murashova and N. N. Chudinova, *Neorg. Mater.* **36** (12), 1507 (2000); **36** (12), 1512 (2000).
3. M. Bagieu-Beucher, *Acta Crystallogr., Sect. B: Struct. Crystallogr. Cryst. Chem.* **B34**, 1443 (1978).
4. J. C. Guintel and I. Tordjman, *Acta Crystallogr., Sect. B: Struct. Crystallogr. Cryst. Chem.* **B32**, 2960 (1976).
5. G. M. Sheldrick, *SHELXS97: Program for the Solution of Crystal Structures* (Univ. of Göttingen, Göttingen, 1997).
6. G. M. Sheldrick, *SHELXL97: Program for the Refinement of Crystal Structures* (Univ. of Göttingen, Göttingen, 1997).
7. M. Laugt, I. Tordjman, J. C. Guintel, and M. Roudaut, *Acta Crystallogr., Sect. B: Struct. Crystallogr. Cryst. Chem.* **B28**, 2352 (1972).
8. E. A. Genkina, B. A. Maksimov, Yu. K. Kabalov, and O. K. Mel'nikov, *Dokl. Akad. Nauk SSSR* **270** (6), 1113 (1983) [*Sov. Phys. Dokl.* **28**, 426 (1983)].
9. I. Grunze, N. N. Chudinova, and H. Grunze, *Izv. Akad. Nauk SSSR, Neorg. Mater.* **25** (6), 886 (1989).
10. N. N. Chudinova and N. V. Vinogradova, *Izv. Akad. Nauk SSSR, Neorg. Mater.* **15** (12), 2171 (1979).
11. B. Bruehne and M. Jansen, *Z. Anorg. Allg. Chem.* **620**, 1409 (1994).
12. K. K. Palkina, S. I. Maksimova, and N. T. Chibiskova, *Izv. Akad. Nauk SSSR, Neorg. Mater.* **17** (1), 95 (1981).
13. H.-Y.-P. Hong, *Mater. Res. Bull.* **10**, 635 (1975).
14. J.-C. Liu and D.-Y. Li, *Acta Phys. Sin.* **32**, 786 (1983).
15. E. V. Murashova and N. N. Chudinova, *Neorg. Mater.* **36** (12), 1512 (2000).

Translated by T. Safonova

STRUCTURE
OF COORDINATION COMPOUNDS

Crystal and Molecular Structures
of 1,1'-Di-*tert*-Butylnickelocene ($\eta^5\text{-C}_5\text{H}_4\text{C}_4\text{H}_9^t$)₂Ni
in the Temperature Range 143–243 K: Thermal Motion
in the Crystal

I. E. Zanin* and M. Yu. Antipin**

* Voronezh State University, Universitetskaya pl. 1, Voronezh, 394893 Russia
e-mail: zie@main.vsu.ru

** Nesmeyanov Institute of Organoelement Compounds, Russian Academy of Sciences,
ul. Vavilova 28, 117813 Russia

Received June 9, 2000

Abstract—The crystal structure of 1,1'-di-*tert*-butylnickelocene is studied by the X-ray diffraction technique in the temperature range 143–243 K. The crystals are monoclinic, space group $P2_1/n$, $Z = 2$. The molecule is centrosymmetric. The cyclic ligands are parallel and adopt a staggered conformation. At 143 K, the mean bond lengths are as follows: Ni–C, 2.194(6); C–C (in the ring), 1.421(6); and C–C (*Me*), 1.538(2) Å. Analysis of the thermal motion of the molecule is performed within the single-parameter model, which allows for the independent motion of the cyclopentadienyl ring with the *tert*-butyl group as a whole and the motion of the *tert*-butyl group. It is shown that the molecule is structurally nonrigid and the *tert*-butyl group executes librational motion. The B_5 heights of the rotation barriers are estimated from the rms libration amplitudes: $\langle\phi^2\rangle$ are equal to 40(5) and 34(4) kJ/mol at 143 and 243 K, respectively. © 2001 MAIK “Nauka/Interperiodica”.

INTRODUCTION

Compound 1,1'-di-*tert*-butylnickelocene (**I**) belongs to the series of metallocene (sandwich π -complex) derivatives Cp^*M , where Cp^* is a substituted cyclopentadienyl ligand and M is 3d, 4d, or 5d transition metal. Our earlier systematic studies of the thermal intramolecular motion in crystals of metallocene derivatives [1–5] revealed a high rotational mobility of the ligands. It was also noted that the size of the substituents virtually does not affect the root-mean-square (rms) libration amplitude of the ligands. In molecule **I**, unlike the earlier-studied compounds, the ligand is asymmetrically substituted. It was of interest to elucidate how this substituent affects the mobility of the Cp^* ligand and the molecule as a whole in the crystal. For this purpose, we performed the X-ray structure analysis of ($\eta^5\text{-C}_5\text{H}_4\text{C}_4\text{H}_9^t$)₂Ni (**I**) in the temperature range 143–243 K, determined the crystal and molecular structures, and obtained the parameters of thermal motion of the molecule in the crystal. The compound reported here continues the series of metallocenes characterized in the same aspect.

EXPERIMENTAL

The crystal structure of **I** was studied by the X-ray diffraction technique at 143, 183, and 243 K with the same prismatic single crystal $0.4 \times 0.3 \times 0.3$ mm in size. The diffraction data were collected on a Siemens P3/PC

four-circle automated diffractometer ($\lambda\text{MoK}\alpha$, graphite monochromator, $\theta/2\theta$ scan mode, $\theta \leq 30^\circ$), which was equipped with an LT-2 low-temperature attachment. Crystals **I** are monoclinic; space group $P2_1/nac$ and $Z = 2$ are retained in the temperature range studied. The unit cell parameters at 243 and 143 K, respectively, have the following values: $a = 6.140(2)$ and $6.093(2)$ Å, $b = 11.158(3)$ and $11.086(2)$ Å, $c = 11.649(3)$ and $11.629(2)$ Å, $\beta = 95.21(2)^\circ$ and $95.56(2)^\circ$, and $V = 794.8$ and 781.8 Å³. The structure was solved by the heavy-atom method and refined by the least-squares procedure in the full-matrix anisotropic (isotropic for H atoms) approximation. The hydrogen atoms were located from the difference Fourier synthesis. In order to improve the accuracy in the determination of the atomic thermal parameters, the final refinement was performed using the procedure of quasi-high-angle refinement [6], which consisted in overestimating the statistic weights of the high-angle reflections by the choice of a proper weighting scheme. In this procedure, the thermal and positional parameters of the H atoms, which were preliminarily refined, were fixed. The results of the refinement are presented in Table 1. The coordinates of the non-hydrogen atoms at 143 and 243 K are listed in Table 2. All the calculations were performed with the SHELXTL programs [7] on an IBM personal computer. (The parameters of the anisotropic atomic displacements are available from the authors.)

RESULTS AND DISCUSSION

Molecular Geometry

A general view of molecule **I** with the atomic numbering is shown in Fig. 1. The projection of the molecule onto the plane of the substituted cyclopentadienyl ($\eta^5\text{-C}_5\text{H}_4\text{C}_4\text{H}_9^t$) ring (Cp^*), in which the atoms are represented as probability ($p = 50\%$) ellipsoids of thermal displacements at 143 and 243 K, is displayed in Fig. 2. The main geometric characteristics of molecule **I** at 243 and 143 K are given in Table 3.

Molecule **I** is centrosymmetric. The Cp^* ligands are strictly parallel and adopt a staggered conformation. The cyclopentadienyl rings are planar (the deviations of the C atoms from the rms plane are within 0.002 Å in the temperature range studied). The C(6) atom of the *tert*-butyl group deviates from the plane of the ring by 0.083(2) Å in the direction opposite to the Ni atom. The C(1)–C(5)–C(6)–C(7), C(1)–C(5)–C(6)–C(9), and C(1)–C(5)–C(6)–C(8) torsion angles, which characterize the orientation of the *tert*-butyl substituent, are equal to 85.4°, –154.8°, and –34.0° at 143 K and 84.8°, –155.5°, and –34.2° at 243 K, respectively. The bond lengths at 243 K have the following values: Ni–C, 2.180–2.204 Å [mean, 2.191(7) Å]; C–C (in the ring), 1.391–1.426 Å [mean, 1.414(10) Å]; and C–C(*Me*), 1.523–1.536 Å [mean, 1.529(5) Å]. As was expected, upon cooling to 143 K, the bond lengths slightly increase (due to the decrease in the amplitudes of thermal vibrations), whereas the spread in bond lengths and errors in their determination decrease: Ni–C, 2.187–2.208 Å [mean, 2.194(6) Å]; C–C, 1.410–1.429 Å [mean, 1.421(6) Å]; and C–C(*Me*), 1.536–1.540 Å [mean, 1.538(2) Å].

Correction for thermal motion [8] resulted in the lengthening of the Ni–C bonds, on average, by 0.005 Å; the C–C bonds, by 0.005–0.008 Å; and the C–C(*Me*) bonds, by 0.006–0.01 Å (Table 3).

Note that the noticeable spread in the Ni–C bond lengths (± 0.006 Å at 143 K) is due to the displacement of the Ni atom by 0.05 Å from the fivefold axis in the five-membered ring and not to the insufficient accuracy in their estimation (esd is 0.003 Å). The centers of two Cp^* rings are shifted relative to each other by 0.05 Å toward the *tert*-butyl groups, and the angle between the line connecting the centers of the Cp^* rings and the normal to the plane of the ring is 0.8°. A similar shift of the Cp ligands was observed in the monoclinic modification of nickelocene (space group $P2_1/a$, $Z = 2$): at 293 K, the shift is equal to 0.104 Å (the corresponding angle is 1.64°) [9].

In molecule **I**, the bond lengths are slightly longer than those in the unsubstituted nickelocene at 101 K (Ni–C, 2.185 Å and C–C, 1.423 Å) and are close to the bond lengths Cp_2Ni , which were determined by the electron diffraction technique in a gaseous phase (Ni–C, 2.196 Å and C–C, 1.430 Å [10]).

Table 1. Results of the refinement of structure **I**

<i>T</i> , K	143	183	243
Number of reflections measured	1896	2004	1794
$F > 8\sigma(F)$	1123	1092	1011
<i>R</i> , %	2.60	2.78	3.31
<i>R</i> _w , %	2.99	3.17	3.41
<i>GOF</i>	0.90	0.93	1.08

Table 2. Coordinates of the non-hydrogen atoms ($\times 10^4$) in crystal **I** at 243 K (the upper row) and 143 K (the lower row)

Atom	<i>x</i>	<i>y</i>	<i>z</i>
Ni	0	0	0
	0	0	0
C(1)	2610(8)	–1016(3)	–724(3)
	2634(4)	–1020(2)	–720(2)
C(2)	1416(9)	–1794(4)	–58(4)
	1426(5)	–1813(2)	–45(2)
C(3)	–726(9)	–1831(4)	–560(5)
	–765(5)	–1849(2)	–560(2)
C(4)	–895(8)	–1076(4)	–1542(4)
	–926(4)	–1089(2)	–1544(2)
C(5)	1188(7)	–558(4)	–1657(3)
	1190(4)	–575(2)	–1654(2)
C(6)	1830(7)	244(3)	–2620(3)
	1822(4)	237(2)	–2624(2)
C(7)	2666(12)	–554(6)	–3560(5)
	2630(6)	–566(3)	–3573(3)
C(8)	–130(11)	971(6)	–3136(5)
	–156(5)	982(3)	–3146(3)
C(9)	3652(9)	1098(4)	–2178(5)
	3681(5)	1109(3)	–2180(3)

It should be emphasized that, on the whole, the *tert*-butyl group does not substantially affect the geometry of the ($\eta^5\text{-C}_5\text{H}_4$) fragment of **I** (as compared to Cp_2Ni). However, in the case when the molecules of pentamethylruthenocene and pentamethylferrocene contain five methyl substituents, the Ru–C and Fe–C bonds shorten by 0.020 and 0.010 Å, respectively, and the C–C bonds in the rings lengthen by 0.013 and 0.010 Å, respectively, in comparison with the bond lengths in the compounds with unsubstituted ligands [1–3].

Analysis of Thermal Motion

Thermal motion in crystal **I** was studied within the framework of the LTS rigid-body model [11, 12] and its modification, the single-parametric Dunitz–White

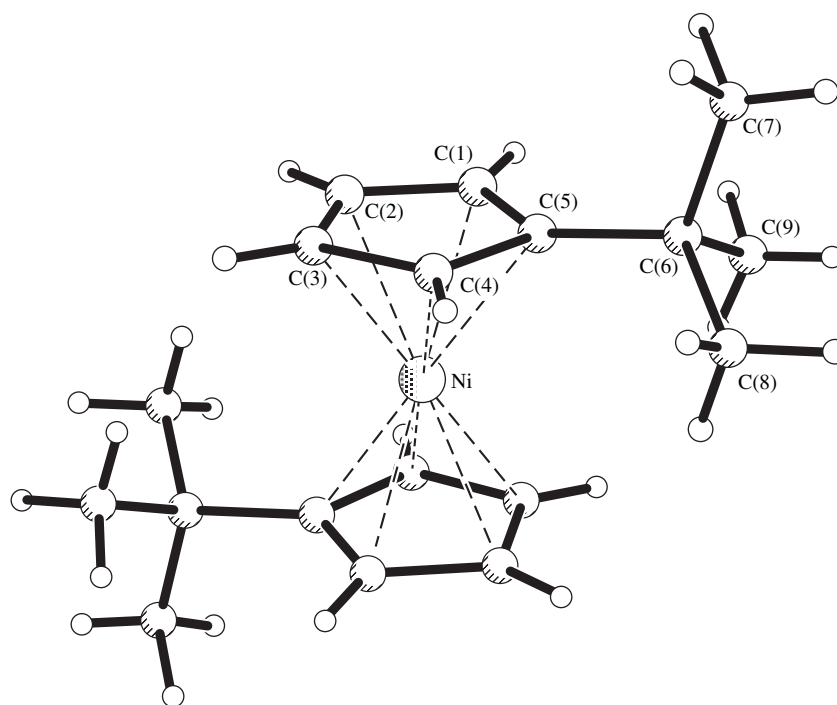


Fig. 1. A general view of molecule I and the atomic numbering.

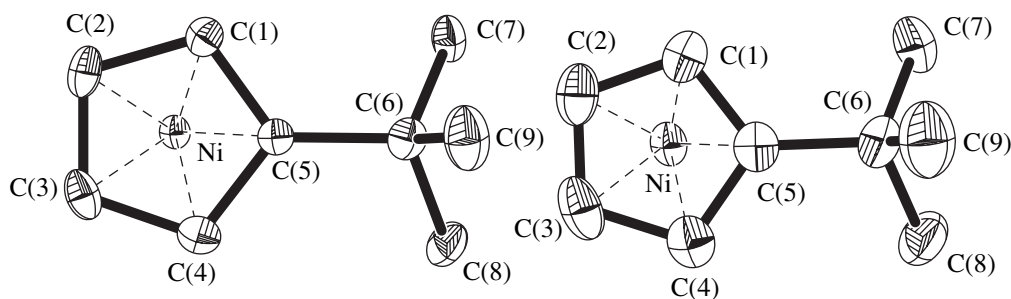


Fig. 2. Projection of molecule I onto the plane of the Cp^* ring. The atoms are represented by probability ellipsoids of thermal displacements ($p = 50\%$) at 143 K (left) and 243 K (right). The ligand related by the center of symmetry is omitted.

model, which allows for intramolecular librations of separate atomic groups in the molecule [8]. The calculations were performed with the THMA-11 program [13] according to the procedure proposed in [14, 15]. The coordinates and anisotropic thermal parameters of the non-hydrogen atoms, which were obtained in the refinement of the structure at each of the three temperatures, were used as the starting data. The results of the calculations are presented in Table 4.

The feature that distinguishes molecule I from the earlier-studied metallocenes [1–5] is the presence of the *tert*-butyl groups, which can execute librational vibrations about the C(5)–C(6) and C(5A)–C(6A) bonds in addition to the rotational vibrations together with the Cp^* rings. The possibility of occurring this type of intramolecular motion is indicated, in particular, by the

form of thermal ellipsoids of the atoms in the *tert*-butyl groups (Fig. 2).

This assumption is confirmed by the calculations within the single-parametric model (the motion of the molecule as a whole and the intramolecular libration of the *tert*-butyl group about the threefold axis). The agreement between the observed U_{ij} and the values calculated within this model was satisfactory in the entire temperature range [$R_u = 0.07\text{--}0.09$, $\langle\Delta U^2\rangle^{1/2} = 0.0011\text{--}0.0017 \text{ \AA}^2$, $\langle\Delta U^2\rangle^{1/2} = 0.0010\text{--}0.0016 \text{ \AA}^2$] and somewhat better than that in the case of the calculations performed with the usual LTS rigid-body model [$R_u = 0.10\text{--}0.11$, $\langle\Delta U^2\rangle^{1/2} = 0.0017\text{--}0.0019 \text{ \AA}^2$, $\langle\Delta U^2\rangle^{1/2} = 0.0015\text{--}0.0017 \text{ \AA}^2$]. Hereinafter, we present only the results obtained within the single-parametric model.

Table 3. Bond lengths (Å) [uncorrected (d) and corrected (d^*) for thermal motion] in molecule **I** at 243 K (the upper row) and 143 K (the lower row)

Bond	d	d^*	Bond	d	d^*
Ni–C(1)	2.193(4)	2.198	C(2)–C(3)	1.391(7)	1.410
	2.194(3)	2.197		1.410(4)	1.414
Ni–C(2)	2.187(5)	2.194	C(3)–C(4)	1.416(6)	1.423
	2.192(3)	2.195		1.417(4)	1.423
Ni–C(3)	2.180(4)	2.185	C(4)–C(5)	1.421(5)	1.427
	2.187(3)	2.191		1.426(4)	1.429
Ni–C(4)	2.189(4)	2.193	C(5)–C(6)	1.516(6)	1.523
	2.191(3)	2.194		1.522(4)	1.525
Ni–C(5)	2.204(4)	2.208	C(6)–C(7)	1.536(7)	1.543
	2.208(3)	2.211		1.537(4)	1.544
C(1)–C(2)	1.415(6)	1.420	C(6)–C(8)	1.529(7)	1.542
	1.429(4)	1.432		1.536(4)	1.544
C(1)–C(5)	1.426(6)	1.430	C(6)–C(9)	1.523(7)	1.535
	1.420(3)	1.425		1.540(4)	1.545
Mean Ni–C	2.191(7)	2.196(7)	Mean C–C(C_p)	1.414(10)	1.422(7)
	2.194(6)	2.198(6)		1.421(6)	1.425(6)
Mean C–C(Me)	1.529(5)	1.540(4)			
	1.538(2)	1.544(1)			

Table 4. Eigenvectors and eigenvalues of the L (deg²) and T ($\times 10^4$ Å²) tensors for molecule **I** in the Cartesian coordinate system

T , K	143	183	243
L_1	10.6 –0.639 0.110 0.762	13.9 0.559 –0.206 –0.803	18.6 0.581 –0.102 –0.807
L_2	2.4 0.753 0.294 0.589	3.2 –0.816 0.033 –0.576	5.1 –0.743 0.338 –0.578
L_3	1.2 –0.159 0.949 0.271	1.4 0.145 0.978 –0.150	1.5 0.332 0.935 0.121
T_1	0.0204 0.963 –0.083 0.258	0.0255 0.94 –0.116 0.317	0.0386 0.948 –0.131 0.288
T_2	0.0164 0.269 0.182 –0.964	0.0255 0.336 0.263 –0.904	0.0386 0.314 0.284 –0.905
T_3	0.0107 0.031 0.979 0.197	0.0134 0.022 0.958 0.286	0.0187 0.036 0.950 0.311

The rms libration amplitudes ($\langle \varphi^2 \rangle$) of the *tert*-butyl group are equal to 18(4), 20(5), and 29(6) deg² at 143, 183, and 243 K, respectively. The heights B_3 of the barrier of rotation about the threefold axis, which were calculated in the harmonic approximation, are equal to 46, 47, and 50 kJ/mol at 143, 183, and 243 K, respectively.

As could be expected from the results of the previous studies of the metallocene derivatives [1–5], the librational motion of molecule **I** as a whole in the crystal is anisotropic. The maximum amplitude is observed for the libration about the L_1 -axis (Table 4) close to the fivefold pseudoaxis. Upon heating from 143 to 243 K, the amplitude of the L_1 libration of the molecule as a whole increases from 10.6 to 18.6 deg².

Note that the eigenvalues of the L tensors calculated for **I** and Cp_2Ni differ significantly. The L_1 value for Cp_2Ni is considerably larger than that for **I**: it is equal

to 45.1 and 199.5 deg² at 101 and 293 K, respectively [9]. Thus, the *tert*-butyl substituent in the ligand of molecule **I** causes a significant decrease in the libration amplitude of this ligand. At the same time, the methyl substituents in the crystals of pentamethylruthenocene [1] and pentamethylferrocene [2] have only insignificant effect on the libration amplitudes of the corresponding ligands. Apparently, in the case of molecule **I**, the asymmetry of the ligand, rather than the size of its substituent, determines the L value. A similar result was obtained also for acetyl ruthenocene [16].

The translational molecular motion in crystal **I** is actually isotropic. Upon heating from 143 to 243 K, the amplitude of the translational motion increases approximately by a factor of two. The eigenvalues of the translation tensor for **I** at 143 and 243 K are close to those calculated for Cp_2Ni at 101 and 293 K, respectively.

The calculation of the Δ differences in the rms amplitudes of the "approaching" shifts for the pairs of carbon atoms in the direction of the chemical bond between them (the Hirshfeld rigid-bond test [17]) reveals that the Cp^* ring is structurally rigid in the temperature range studied; the mean Δ value for all the C–C bonds in the ring is 8×10^{-4} and $11 \times 10^{-4} \text{ \AA}^2$. At the same time, the rms Δ value for pairs of chemically non-bonded C atoms belonging to different ligands is 41×10^{-4} and $63 \times 10^{-4} \text{ \AA}^2$ at 143 and 243 K, respectively. This indicates that the ligands execute intramolecular librational vibrations. The calculated rms libration amplitudes of the Cp^* ligands in crystal **I** are equal to 9(1), 13(2), and 17(2) deg² at 143, 183, and 243 K, respectively.

The B_5 heights of the barriers of rotation about the fivefold axis for the ligands in molecule **I** in the crystal, which were calculated in the harmonic approximation using the $\langle \phi^2 \rangle$ data, are 40(5), 36(5), and 34(4) kJ/mol at 143, 183, and 243 K, respectively. These values are significantly larger than the B_5 rotation barriers for the Cp rings in the crystal of Cp_2Ni , which are equal to 7(1) and 5(1) kJ/mol at 101 and 293 K, respectively. This difference is explained by the steric hindrances in ligand reorientation, which are introduced by the *tert*-butyl group.

REFERENCES

1. I. E. Zanin, M. Yu. Antipin, and Yu. T. Struchkov, *Kristallografiya* **36** (2), 420 (1991) [*Sov. Phys. Crystallogr.* **36**, 225 (1991)].
2. I. E. Zanin, M. Yu. Antipin, and Yu. T. Struchkov, in *Abstracts of the XV International Congress of the International Union of Crystallography, Bordeaux, 1990*, p. C299.
3. I. E. Zanin, M. Yu. Antipin, Yu. T. Struchkov, *et al.*, *Metallorg. Khim.* **5** (3), 579 (1992).
4. I. E. Zanin, M. Yu. Antipin, and Yu. T. Struchkov, in *Abstracts of the XIII European Crystallographic Meeting, Trieste, 1991*, p. 207.
5. I. I. Vorontsov, K. A. Potekhin, M. Yu. Antipin, and I. E. Zanin, *Kristallografiya* **45** (2), 266 (2000) [*Crystallogr. Rep.* **45**, 234 (2000)].
6. C. P. Brock and J. D. Dunitz, *Acta Crystallogr., Sect. B: Struct. Sci.* **38** (10), 2218 (1982).
7. Siemens SHELXTL PLUS program (PC Version), 1997.
8. J. D. Dunitz and D. White, *Acta Crystallogr., Sect. A: Cryst. Phys., Diffr., Theor. Gen. Crystallogr.* **B29**, 93 (1973).
9. D. White and J. D. Dunitz, *Acta Crystallogr., Sect. B: Struct. Crystallogr. Cryst. Chem.* **B36** (10), 2255 (1980).
10. L. Hedberg and K. Hedberg, *J. Chem. Phys.* **53**, 1228 (1970).
11. V. Schomaker and K. N. Trueblood, *Acta Crystallogr., Sect. B: Struct. Crystallogr. Cryst. Chem.* **B24**, 63 (1968).
12. K. N. Trueblood, *Acta Crystallogr., Sect. A: Cryst. Phys., Diffr., Theor. Gen. Crystallogr.* **A34**, 950 (1978).
13. E. Maverick and K. N. Trueblood, Program THMA-11, Version January, 1987.
14. E. Maverick and J. D. Dunitz, *Mol. Phys.* **62** (2), 451 (1987).
15. J. D. Dunitz, V. Shomaker, and K. N. Trueblood, *J. Phys. Chem.* **92**, 856 (1988).
16. I. E. Zanin, Author's Abstract of Candidate's Dissertation in Physics and Mathematics (INÉOS RAN, Moscow, 1992).
17. F. L. Hirshfeld, *Acta Crystallogr., Sect. A: Cryst. Phys., Diffr., Theor. Gen. Crystallogr.* **A32** (3), 239 (1976).

Translated by I. Polyakova

STRUCTURE
OF ORGANIC COMPOUNDS

X-ray Diffraction Study of 2,2',4,4',6,8,8',10,10',12-Decamethylbicyclo[5.5.1]hexasiloxane and 2,2',4,4',6,8,8',10,10',12-Decamethylbicyclo[5.5.1]-9-Carbahexasiloxane

A. P. Polishchuk*, N. N. Makarova, T. V. Astapova**, and É. B. Rusanov*****

* *Institute of Physics, National Academy of Sciences of Ukraine, pr. Nauki 46, Kiev, 03650 Ukraine*

** *Nesmeyanov Institute of Organoelement Compounds, Russian Academy of Sciences, ul. Vavilova 28, Moscow, 117813 Russia*

*** *Institute of Organic Chemistry, National Academy of Sciences of Ukraine, Murmanskaya ul. 5, Kiev, 03094 Ukraine*

e-mail: nmakar@ineos.ac.ru

Received May 30, 2000

Abstract—The crystal structures of two organosilicon compounds are studied by X-ray diffraction at 200 K. Crystals of 2,2',4,4',6,8,8',10,10',12-decamethylbicyclo[5.5.1]hexasiloxane ($C_{10}H_{30}O_7Si_6$) are monoclinic, $a = 12.260(1)$ Å, $b = 11.716(1)$ Å, $c = 32.169(2)$ Å, $\beta = 92.802(2)^\circ$, space group $C2/c$, $Z = 8$, $wR2 = 0.132$, and $R1 = 0.053$ for 3989 reflections with $F > 4\sigma(F)$. Crystals of 2,2',4,4',6,8,8',10,10',12-decamethylbicyclo[5.5.1]-9-carbahexasiloxane ($C_{11}H_{32}O_6Si_6$) are triclinic, $a = 10.709(1)$ Å, $b = 11.046(1)$ Å, $c = 12.111(1)$ Å, $\alpha = 117.059(1)^\circ$, $\beta = 95.566(1)^\circ$, $\gamma = 108.088(1)^\circ$, space group $P\bar{1}$, $Z = 2$, $wR2 = 0.115$, and $R1 = 0.048$ for 3948 reflections with $F > 4\sigma(F)$. It is found that the substitution of the methylene group for the oxygen atom is accompanied by a minor conformational change in the bicyclic fragment and the SiCSi angle changes from the tetrahedral angle to $121.0(1)^\circ$. The high variability of the SiOSi bond angles is confirmed. © 2001 MAIK “Nauka/Interperiodica”.

INTRODUCTION

In recent years, cycloliner polyorganosiloxanes have attracted the particular attention of researchers owing to their liquid-crystal properties and application to Langmuir–Blodgett technologies. It was found that the properties of cycloliner polyorganosiloxanes are predominantly determined by the dimensions and conformations of the monomers and the nature of the substituents at the Si atoms [1]. The conformational potential of the monomers and, hence, the polymers depends on the limits of variation of the SiOSi angle. According to [2], the SiOSi angles vary from 142.2° in unsubstituted disiloxane to 180° in some disiloxanes that have bulky substituents without hydrogen bonding. In [1], it was assumed that the conformational flexibility of the monomers can be additionally affected by incorporation of the $(CH_2)_n$ fragments between the silicon atoms. Moreover, it is possible to control the hydrophilic–hydrophobic properties of macromolecules in organosilicon polymers based on the modified monomers by variation of the Si–O : Si–CH₂ ratio.

In the cyclic monomers that contain the SiCH₂Si groups, the conformation of the ring can differ from that in the purely oxygen analogues because of the difference in the electronic structure of the carbon and oxygen atoms. Possible conformational changes in the

monomers are primarily determined by the geometric parameters of the methylene group. In this connection, for the purpose of revealing the conformational changes, we carried out X-ray diffraction investigation of the crystal structures of two compounds, namely, 2,2',4,4',6,8,8',10,10',12-decamethylbicyclo[5.5.1]hexasiloxane (I) and 2,2',4,4',6,8,8',10,10',12-decamethylbicyclo[5.5.1]-9-carbahexasiloxane (II).

EXPERIMENTAL

According to the procedure described in [3], the reaction of 1,3-di-hydroxy-1,1,3,3-tetramethyldisiloxane with 1,1,7,7-tetra-chloro-1,3,3,5,5,7-hexamethyltetrasiloxane or bis(1,1-dichloro-1,3,3-trimethyldioxane)methylene resulted in the formation of 2,8-dichlorodecamethylcyclohexasiloxane or 2,8-dichloro-2,4,4,6,6,8,10,10,12-decamethylcyclo-9-carbahexasiloxane, respectively. These compounds underwent a partial hydrolysis. In turn, the products of partial hydrolysis were converted into compounds I and II due to the transannular interactions between the SiOH and SiCl groups.

Single crystals suitable for X-ray diffraction analysis were obtained by slow evaporation of benzene solutions. Main crystallographic parameters and experi-

Table 1. Crystallographic parameters and experimental data for structures **I** and **II**

Parameter	I	II
Empirical formula	C ₁₀ H ₃₀ O ₇ Si ₆	C ₁₁ H ₃₂ O ₆ Si ₆
<i>M_r</i>	430.88	428.91
Crystal system	Monoclinic	Triclinic
Space group	<i>C2/c</i>	<i>P</i> $\bar{1}$
<i>Z</i>	8	2
<i>a</i> , Å	12.260(1)	10.709(1)
<i>b</i> , Å	11.716(1)	11.046(1)
<i>c</i> , Å	32.169(2)	12.111(1)
α , deg	90	117.059(1)
β , deg	92.802(2)	95.566(1)
γ , deg	90	108.088(1)
<i>V</i> , Å ³	4615.2(6)	1163.7(1)
<i>D</i> _{calcd} , g/cm ³	1.240	1.224
μ , mm ⁻¹	0.385	0.378
<i>F</i> (000)	1840	460
Diffractometer	Smart 1000 CCD	Smart 1000 CCD
λ , Å	0.71073	0.71073
<i>T</i> , K	200(2)	200(2)
θ _{max} , deg	28.98	30.04
Total number of reflections	5600	6641
Number of reflections with <i>F</i> > 4 σ (<i>F</i>)	3989	3948
Refinement on	<i>F</i> ²	<i>F</i> ²
<i>R</i> 1	0.053	0.048
<i>wR</i> 2	0.132	0.115
<i>S</i>	0.961	0.870

Table 2. Coordinates ($\times 10^4$) and isotropic thermal parameters ($\text{Å}^2 \times 10^3$) of the non-hydrogen atoms in structure **I**

Atom	<i>x</i>	<i>y</i>	<i>z</i>	<i>U</i> _{eq}
Si(1)	2527(1)	5766(1)	1053(1)	32(1)
Si(2)	435(1)	7149(1)	799(1)	32(1)
Si(3)	1182(1)	3482(1)	983(1)	39(1)
Si(4)	-916(1)	4869(1)	739(1)	37(1)
Si(5)	2380(1)	6580(1)	1964(1)	39(1)
Si(6)	313(1)	8079(1)	1697(1)	38(1)
O(1)	1645(1)	6594(1)	814(1)	38(1)
O(2)	2003(2)	4525(1)	1110(1)	52(1)
O(3)	-454(1)	6142(1)	827(1)	50(1)
O(4)	2844(1)	6276(2)	1509(1)	46(1)
O(5)	1307(2)	7350(2)	1904(1)	77(1)
O(6)	318(1)	7991(1)	1194(1)	44(1)
O(7)	104(1)	3982(1)	733(1)	44(1)
C(1)	3758(2)	5708(3)	755(1)	50(1)
C(2)	216(3)	7960(3)	317(1)	54(1)
C(3)	1860(3)	2496(3)	637(1)	68(1)
C(4)	797(4)	2785(4)	1465(1)	70(1)
C(5)	-1821(3)	4508(3)	1160(1)	66(1)
C(6)	-1638(3)	4813(4)	224(1)	67(1)
C(7)	2038(6)	5264(4)	2236(1)	84(1)
C(8)	3450(4)	7372(5)	2256(1)	84(1)
C(9)	490(3)	9591(3)	1841(1)	65(1)
C(10)	-988(4)	7531(5)	1877(2)	76(1)

mental data at 200 K are summarized in Table 1. The processing of the experimental data and further calculations were performed with the SAINT [4] and SHELXTL97 [5] programs on an IBM AT personal computer. Both structures were solved by the direct method and refined by the full-matrix procedure in the anisotropic approximation for the non-hydrogen atoms. All hydrogen atoms in the structures studied were located from the difference Fourier syntheses and included in further refinement in the isotropic approximation. The coordinates and equivalent isotropic thermal parameters of the non-hydrogen atoms are listed in Tables 2 and 3. The bond lengths, bond angles, and torsion angles are listed in Tables 4–6, respectively.

RESULTS AND DISCUSSION

A distinctive feature of molecules **I** and **II** is the presence of the endocyclic bridging O(1) oxygen atom (Figs. 1, 2). This results in the formation of the bicyclic

systems in which the molecules are folded along the Si(1)–Si(2) segment. The Si atoms in both rings of the bicyclic fragments are coplanar (Table 7), and the angles between their planes are 106.9° and 106.5° in **I** and **II**, respectively. In an analogue of compound **I**, namely, *cis*-1,7-diphenyl-3,3,5,5,9,9,11,11-octamethylbicycloheptasiloxane [6, 7], the bicyclic fragment is less planar and the planar fragments are not distinguished: the atomic deviations from the planes passing through the Si atoms of the bicyclic fragments are approximately 0.27 Å and the dihedral angle between these planes is 125.9° [7]. Unlike *cis*-1,7-diphenyl-3,3,5,5,9,9,11,11-octamethylbicycloheptasiloxane, in which the SiOSi angles have close values and their mean is 144.2° [6], the SiOSi bond angles in the structures studied vary over wide ranges: 144.6°–162.6° in **I** and 139.2°–163.6° in **II** (Table 5).

Substitution of the CH₂ group in molecule **II** for the oxygen atom in **I** is accompanied by an insignificant

Table 3. Coordinates ($\times 10^4$) and isotropic thermal parameters ($\text{\AA}^2 \times 10^3$) of the non-hydrogen atoms in structure **II**

Atom	<i>x</i>	<i>y</i>	<i>z</i>	<i>U</i> _{eq}
Si(1)	4419(1)	5426(1)	2199(1)	32(1)
Si(2)	3472(1)	6380(1)	4639(1)	31(1)
Si(3)	3444(1)	7551(1)	1554(1)	36(1)
Si(4)	2321(1)	8367(1)	4073(1)	36(1)
Si(5)	2057(1)	2254(1)	722(1)	34(1)
Si(6)	1021(1)	3244(1)	3189(1)	35(1)
O(1)	4437(2)	5952(2)	3691(1)	39(1)
O(2)	3730(2)	6281(2)	1752(2)	53(1)
O(3)	3219(2)	7779(2)	4725(1)	38(1)
O(4)	3513(2)	3671(2)	1319(2)	47(1)
O(5)	1124(2)	2594(2)	1713(2)	46(1)
O(6)	2005(2)	4998(2)	4043(2)	43(1)
C(1)	6160(3)	5763(3)	2041(3)	50(1)
C(2)	4334(3)	6849(4)	6245(3)	48(1)
C(3)	4906(4)	8480(4)	1121(4)	62(1)
C(4)	1873(3)	6602(4)	214(3)	56(1)
C(5)	587(3)	6884(4)	3130(3)	57(1)
C(6)	2207(5)	9997(4)	5435(3)	65(1)
C(7)	1144(3)	1928(4)	-817(3)	57(1)
C(8)	2390(3)	639(3)	517(3)	50(1)
C(9)	1583(4)	2283(4)	3915(3)	58(1)
C(10)	-755(3)	3027(4)	3152(3)	52(1)
C(11)	3251(3)	8940(3)	3061(2)	41(1)

Table 4. Bond lengths (\AA) in structures **I** and **II**

I		II	
Bonds	<i>d</i>	Bonds	<i>d</i>
Si(1)–O(2)	1.604(2)	Si(1)–O(2)	1.598(2)
Si(1)–O(4)	1.614(2)	Si(1)–O(4)	1.608(2)
Si(1)–O(1)	1.619(2)	Si(1)–O(1)	1.624(2)
Si(1)–C(1)	1.829(3)	Si(1)–C(1)	1.831(3)
Si(2)–O(3)	1.612(2)	Si(2)–O(3)	1.610(1)
Si(2)–O(1)	1.617(2)	Si(2)–O(6)	1.615(2)
Si(2)–O(6)	1.620(2)	Si(2)–O(1)	1.626(2)
Si(2)–C(2)	1.828(3)	Si(2)–C(2)	1.828(3)
Si(3)–O(7)	1.622(2)	Si(3)–O(2)	1.636(2)
Si(3)–O(2)	1.622(2)	Si(3)–C(4)	1.842(3)
Si(3)–C(3)	1.831(3)	Si(3)–C(3)	1.852(3)
Si(3)–C(4)	1.834(3)	Si(3)–C(11)	1.858(2)
Si(4)–O(3)	1.616(2)	Si(4)–O(3)	1.636(2)
Si(4)–O(7)	1.627(2)	Si(4)–C(5)	1.853(3)
Si(4)–C(6)	1.841(3)	Si(4)–C(6)	1.857(3)
Si(4)–C(5)	1.842(3)	Si(4)–C(11)	1.856(3)
Si(5)–O(5)	1.599(2)	Si(5)–O(5)	1.623(2)
Si(5)–O(4)	1.634(2)	Si(5)–O(4)	1.625(2)
Si(5)–C(7)	1.830(4)	Si(5)–C(7)	1.838(3)
Si(5)–C(8)	1.830(4)	Si(5)–C(8)	1.839(3)
Si(6)–O(5)	1.605(2)	Si(6)–O(6)	1.623(2)
Si(6)–O(6)	1.624(2)	Si(6)–O(5)	1.627(2)
Si(6)–C(10)	1.839(4)	Si(6)–C(10)	1.835(3)
Si(6)–C(9)	1.841(3)	Si(6)–C(9)	1.845(3)

conformational change in the bicyclic fragment (Table 7). This is associated, to some extent with the value of the SiCSi angle. In structure **I**, the

Si(3)O(7)Si(4) bond angle is $146.4(1)^\circ$, and in structure **II**, the Si(3)C(11)Si(4) angle is $121.0(1)^\circ$. The latter angle essentially differs from the tetrahedral angle but

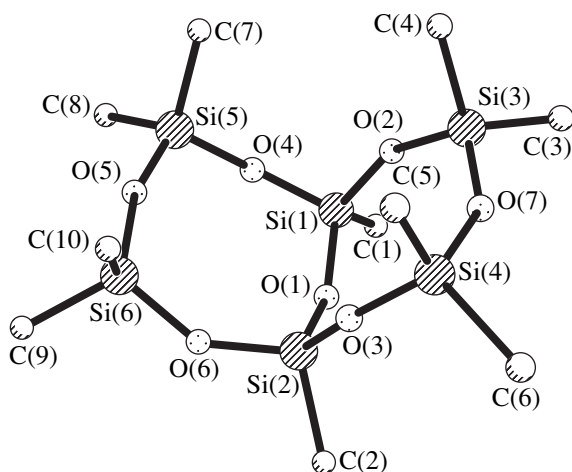
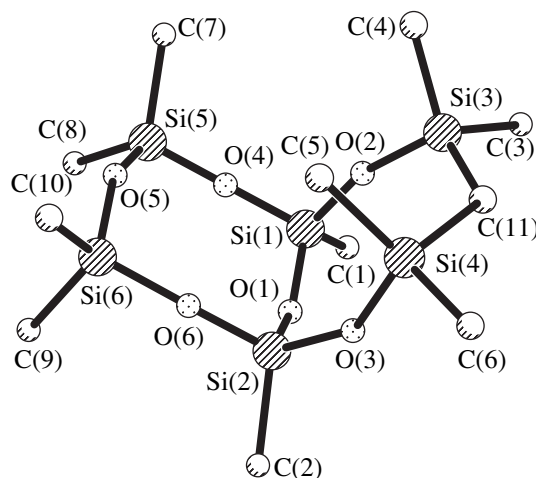
**Fig. 1.** Structure of molecule **I**.**Fig. 2.** Structure of molecule **II**.

Table 5. Bond angles (deg) in structures **I** and **II**

I		I		II		II	
Angles	ω	Angles	ω	Angles	ω	Angles	ω
O(2)–Si(1)–O(4)	108.2(1)	O(7)–Si(4)–C(5)	110.7(1)	O(2)–Si(1)–O(4)	109.2(1)	C(5)–Si(4)–C(11)	112.4(1)
O(2)–Si(1)–O(1)	109.6(1)	C(6)–Si(4)–C(5)	112.0(2)	O(2)–Si(1)–O(1)	108.4(1)	C(6)–Si(4)–C(11)	110.0(2)
O(4)–Si(1)–O(1)	109.6(1)	O(5)–Si(5)–O(4)	109.5(1)	O(4)–Si(1)–O(1)	108.7(1)	O(5)–Si(5)–O(4)	109.7(1)
O(2)–Si(1)–C(1)	111.8(1)	O(5)–Si(5)–C(7)	109.1(2)	O(2)–Si(1)–C(1)	112.6(1)	O(5)–Si(5)–C(7)	108.5(1)
O(4)–Si(1)–C(1)	108.9(1)	O(4)–Si(5)–C(7)	110.0(2)	O(4)–Si(1)–C(1)	107.9(1)	O(4)–Si(5)–C(7)	109.4(1)
O(1)–Si(1)–C(1)	108.8(1)	O(5)–Si(5)–C(8)	109.9(2)	O(1)–Si(1)–C(1)	109.9(1)	O(5)–Si(5)–C(8)	108.9(1)
O(3)–Si(2)–O(1)	109.0(1)	O(4)–Si(5)–C(8)	107.3(2)	O(3)–Si(2)–O(6)	108.0(1)	O(4)–Si(5)–C(8)	108.5(1)
O(3)–Si(2)–O(6)	108.4(1)	C(7)–Si(5)–C(8)	110.9(3)	O(3)–Si(2)–O(1)	109.6(1)	C(7)–Si(5)–C(8)	111.8(2)
O(1)–Si(2)–O(6)	109.7(1)	O(5)–Si(6)–O(6)	109.8(1)	O(6)–Si(2)–O(1)	109.3(1)	O(6)–Si(6)–O(5)	109.2(1)
O(3)–Si(2)–C(2)	110.9(1)	O(5)–Si(6)–C(10)	109.7(2)	O(3)–Si(2)–C(2)	109.7(1)	O(6)–Si(6)–C(10)	108.5(1)
O(1)–Si(2)–C(2)	109.3(1)	O(6)–Si(6)–C(10)	109.7(2)	O(6)–Si(2)–C(2)	111.3(1)	O(5)–Si(6)–C(10)	107.8(1)
O(6)–Si(2)–C(2)	109.5(1)	O(5)–Si(6)–C(9)	109.3(2)	O(1)–Si(2)–C(2)	108.8(1)	O(6)–Si(6)–C(9)	108.6(1)
O(7)–Si(3)–O(2)	109.5(1)	O(6)–Si(6)–C(9)	107.8(1)	O(2)–Si(3)–C(4)	107.4(1)	O(5)–Si(6)–C(9)	110.6(1)
O(7)–Si(3)–C(3)	108.0(1)	C(10)–Si(6)–C(9)	110.5(2)	O(2)–Si(3)–C(3)	108.7(1)	C(10)–Si(6)–C(9)	112.1(2)
O(2)–Si(3)–C(3)	109.5(2)	Si(2)–O(1)–Si(1)	147.7(1)	C(4)–Si(3)–C(3)	109.6(2)	Si(1)–O(1)–Si(2)	139.2(1)
O(7)–Si(3)–C(4)	110.0(2)	Si(1)–O(2)–Si(3)	154.3(1)	O(2)–Si(3)–C(11)	110.5(1)	Si(1)–O(2)–Si(3)	163.6(1)
O(2)–Si(3)–C(4)	107.8(2)	Si(2)–O(3)–Si(4)	153.9(1)	C(4)–Si(3)–C(11)	110.9(1)	Si(2)–O(3)–Si(4)	147.1(1)
C(3)–Si(3)–C(4)	112.1(2)	Si(1)–O(4)–Si(5)	144.6(1)	C(3)–Si(3)–C(11)	109.7(1)	Si(1)–O(4)–Si(5)	150.8(1)
O(3)–Si(4)–O(7)	109.2(1)	Si(5)–O(5)–Si(6)	162.6(1)	O(3)–Si(4)–C(5)	109.4(1)	Si(5)–O(5)–Si(6)	148.4(1)
O(3)–Si(4)–C(6)	109.9(2)	Si(2)–O(6)–Si(6)	145.6(1)	O(3)–Si(4)–C(6)	106.2(1)	Si(2)–O(6)–Si(6)	152.7(1)
O(7)–Si(4)–C(6)	107.6(1)	Si(3)–O(7)–Si(4)	146.4(1)	C(5)–Si(4)–C(6)	110.1(2)	Si(4)–O(11)–Si(3)	121.0(1)
O(3)–Si(4)–C(5)	107.5(2)			O(3)–Si(4)–C(11)	108.5(1)		

the Si(3)–C(11) [1.858(2) Å] and Si(4)–C(11) [1.856(3) Å] bond lengths are close to the normal values [7]. A similar difference between the SiCSi angle and the standard value was found also in the linear monomer of bis(hydroxydimethylsilyl)methane [8], in which the Si atoms have the classic tetrahedral coordination, the SiCSi angle is 118.1(3)°, and the Si–C bond lengths are 1.853(5) and 1.875(7) Å. Note that, in the oxygen analogue of bis(hydroxydimethylsilyl)methane, namely, 1,3-dioxy-1,1,3,3-tetramethyldisiloxane, the bond angle at the oxygen atom is 140.1(1)° [9].

At the same time, in the cyclic monomer 1,3-dihydroxy-1,3-dimethyl-1,3-disilacyclobutane, which contains two independent molecules with very close geometric parameters [10], the SiCSi angle is equal to 88.2(2)° and the Si–C bond length is 1.875(4) Å (the data cited refer to the independent molecule A). The Si atoms in the structure of 1,3-dihydroxy-1,3-dimethyl-

1,3-disilacyclobutane have a distorted tetrahedral coordination with the endocyclic angle decreased to 91.2(2)°. This angle is close to the corresponding angle in 1,3-diphenyl-1,3-dimethyl-1,3-disilacyclobutane (92.8°), in which the SiCSi angle is 86.6° [11]. Note that the above angles (close to 90°) are characteristic of strained 1,3-disilacyclobutane systems [12–18].

Thus, the structural studies of the bicyclic molecules **I** and **II** confirmed the high variability of the SiOSi bond angles, which is characteristic of organosilicon compounds. We emphasize that, for dioxydisiloxanes, this variability is one of the main factors that favor the formation of the mesophase with columnar H-associates [9, 19–22]. The conformational flexibility associated with the variation in the SiOSi angles is undoubtedly important for the liquid-crystal properties of cycloliner polyorganosiloxanes.

Table 6. Torsion angles (deg) in structures **I** and **II**

I		II	
Angles	ω	Angles	ω
O(3)–Si(2)–O(1)–Si(1)	–53.2(2)	O(2)–Si(1)–O(1)–Si(2)	37.9(2)
O(6)–Si(2)–O(1)–Si(1)	65.3(2)	O(4)–Si(1)–O(1)–Si(2)	–80.7(2)
C(2)–Si(2)–O(1)–Si(1)	–174.6(2)	C(1)–Si(1)–O(1)–Si(2)	161.4(2)
O(2)–Si(1)–O(1)–Si(2)	55.2(2)	O(3)–Si(2)–O(1)–Si(1)	–60.5(2)
O(4)–Si(1)–O(1)–Si(2)	–63.4(2)	O(6)–Si(2)–O(1)–Si(1)	57.7(2)
C(1)–Si(1)–O(1)–Si(2)	177.7(2)	C(2)–Si(2)–O(1)–Si(1)	179.5(2)
O(4)–Si(1)–O(2)–Si(3)	147.0(3)	O(4)–Si(1)–O(2)–Si(3)	–167.4(4)
O(1)–Si(1)–O(2)–Si(3)	27.6(4)	O(1)–Si(1)–O(2)–Si(3)	74.4(4)
C(1)–Si(1)–O(2)–Si(3)	–93.2(3)	C(1)–Si(1)–O(2)–Si(3)	–47.5(5)
O(7)–Si(3)–O(2)–Si(1)	–27.5(4)	C(4)–Si(3)–O(2)–Si(1)	168.1(4)
C(3)–Si(3)–O(2)–Si(1)	90.8(3)	C(3)–Si(3)–O(2)–Si(1)	49.7(5)
C(4)–Si(3)–O(2)–Si(1)	–147.1(3)	C(11)–Si(3)–O(2)–Si(1)	–70.8(4)
O(1)–Si(2)–O(3)–Si(4)	–33.9(3)	O(6)–Si(2)–O(3)–Si(4)	–35.3(2)
O(6)–Si(2)–O(3)–Si(4)	–153.3(3)	O(1)–Si(2)–O(3)–Si(4)	83.7(2)
C(2)–Si(2)–O(3)–Si(4)	86.5(3)	C(2)–Si(2)–O(3)–Si(4)	–156.8(2)
O(7)–Si(4)–O(3)–Si(2)	32.5(3)	C(5)–Si(4)–O(3)–Si(2)	27.4(2)
C(6)–Si(4)–O(3)–Si(2)	–85.4(3)	C(6)–Si(4)–O(3)–Si(2)	146.2(2)
C(5)–Si(4)–O(3)–Si(2)	152.6(3)	C(11)–Si(4)–O(3)–Si(2)	–95.5(2)
O(2)–Si(1)–O(4)–Si(5)	–54.7(2)	O(2)–Si(1)–O(5)–Si(5)	–54.2(3)
O(1)–Si(1)–O(4)–Si(5)	64.7(2)	O(1)–Si(1)–O(5)–Si(5)	63.9(3)
C(1)–Si(1)–O(4)–Si(5)	–176.4(2)	C(1)–Si(1)–O(5)–Si(5)	–176.9(3)
O(5)–Si(5)–O(4)–Si(1)	–52.3(2)	O(5)–Si(5)–O(4)–Si(1)	–29.4(3)
C(7)–Si(5)–O(4)–Si(1)	67.7(3)	C(7)–Si(5)–O(4)–Si(1)	89.5(3)
C(8)–Si(5)–O(4)–Si(1)	–171.6(3)	C(8)–Si(5)–O(4)–Si(1)	–148.3(3)
O(4)–Si(5)–O(5)–Si(6)	–0.5(7)	O(4)–Si(5)–O(5)–Si(6)	–44.0(2)
C(7)–Si(5)–O(5)–Si(6)	–121.0(7)	C(7)–Si(5)–O(5)–Si(6)	–163.4(2)
C(8)–Si(5)–O(5)–Si(6)	117.1(7)	C(8)–Si(5)–O(5)–Si(6)	74.7(2)
O(6)–Si(6)–O(5)–Si(5)	4.8(7)	O(6)–Si(6)–O(5)–Si(5)	62.5(2)
C(10)–Si(6)–O(5)–Si(5)	125.4(7)	C(10)–Si(6)–O(5)–Si(5)	–179.9(2)
C(9)–Si(6)–O(5)–Si(5)	–113.3(7)	C(9)–Si(6)–O(5)–Si(5)	–57.0(3)
O(3)–Si(2)–O(6)–Si(6)	55.3(2)	O(3)–Si(2)–O(6)–Si(6)	146.9(2)
O(1)–Si(2)–O(6)–Si(6)	–63.7(2)	O(1)–Si(2)–O(6)–Si(6)	27.8(3)
C(2)–Si(2)–O(6)–Si(6)	176.3(2)	C(2)–Si(2)–O(6)–Si(6)	–92.5(3)
O(5)–Si(6)–O(6)–Si(2)	45.1(3)	O(5)–Si(6)–O(6)–Si(2)	–58.3(3)
C(10)–Si(6)–O(6)–Si(2)	–75.6(3)	C(10)–Si(6)–O(6)–Si(2)	–175.6(3)
C(9)–Si(6)–O(6)–Si(2)	164.1(2)	C(9)–Si(6)–O(6)–Si(2)	62.4(3)
O(2)–Si(3)–O(7)–Si(4)	–55.7(2)	O(3)–Si(4)–O(11)–Si(3)	68.2(2)
C(3)–Si(3)–O(7)–Si(4)	–174.9(2)	C(5)–Si(4)–O(11)–Si(3)	–52.8(2)
C(4)–Si(3)–O(7)–Si(4)	62.5(3)	C(6)–Si(4)–O(11)–Si(3)	–175.9(2)
O(3)–Si(4)–O(7)–Si(3)	55.3(2)	O(2)–Si(3)–O(11)–Si(4)	–39.2(2)
C(6)–Si(4)–O(7)–Si(3)	174.5(3)	C(4)–Si(3)–O(11)–Si(4)	79.8(2)
C(5)–Si(4)–O(7)–Si(3)	–62.9(3)	C(3)–Si(3)–O(11)–Si(4)	–159.0(2)

Table 7. Planar fragments in molecules **I** and **II**

Plane	Mean atomic deviation from the plane, Å	Atoms and their deviations from the plane, Å
Molecule I		
Si(1), Si(2), Si(4), Si(3)	0.008	O(1) -0.389; O(2) 0.233; O(3) 0.262; O(7) -0.410
Si(1), Si(2), Si(6), Si(5)	0.034	O(1) 0.329; O(4) -0.378; O(5) -0.065; O(6) 0.344
Molecule II		
Si(1), Si(2), Si(4), Si(3)	0.040	O(1) 0.384; O(2) -0.232; O(3) 0.421; C(11) 0.654
Si(1), Si(2), Si(6), Si(5)	0.020	O(1) -0.508; O(4) -0.265; O(5) 0.338; O(6) 0.264

It was found that substitution of the methylene group for the oxygen atom results in no fundamental conformational changes in the bicyclic fragment, but the SiCSi angle changes from the tetrahedral angle to 121.0(1)°. Taking into account that these angles in 1,3-disilacyclobutanes are close to 90° [10–18], we suppose that the SiCSi angles in organosilicon compounds can vary over a wide range (~90°–120°).

ACKNOWLEDGMENTS

This study was supported by the INTAS European Program, project no. 97-0485.

We are grateful to F.M. Dolgushin for his aid in data collection.

REFERENCES

- N. N. Makarova and Yu. K. Godovsky, *Prog. Polym. Sci.* **22**, 1001 (1997).
- V. E. Shklover, Yu. T. Struchkov, I. V. Karpova, *et al.*, *Zh. Strukt. Khim.* **26**, 125 (1985).
- N. N. Makarova, B. D. Lavrukhin, T. V. Timofeeva, and V. N. Zelencheva, *Izv. Akad. Nauk SSSR, Ser. Khim.*, No. 5, 1114 (1985).
- SMART Version 5.051 and SAINT Version 5.00. Area Detector Control and Integration Software* (Bruker AXS Inc., Madison, WI-53719, 1998).
- G. M. Sheldrick, *SHELXTL97, Version 5.10* (Bruker AXS Inc., Madison, WI-53719, 1997).
- V. E. Shklover, Yu. T. Struchkov, N. N. Makarova, and A. A. Zhdanov, *Cryst. Struct. Commun.* **9**, 1 (1980).
- V. E. Shklover, Yu. T. Struchkov, N. N. Makarova, and A. A. Zhdanov, *Zh. Strukt. Khim.* **22** (4), 103 (1981).
- K. Yu. Suponitsky, K. A. Lyssenko, T. V. Astapova, *et al.*, *Liq. Cryst.* **25**, 179 (1998).
- A. P. Polishchuk, T. V. Timofeeva, N. N. Makarova, *et al.*, *Liq. Cryst.* **9**, 433 (1991).
- K. A. Lyssenko, T. V. Astapova, M. Yu. Antipin, and N. N. Makarova, *Mendeleev Commun.*, No. 3, 87 (1998).
- K. Hayakawa, M. Tachikawa, T. Suzuki, *et al.*, *Tetrahedron Lett.* **36**, 3181 (1995).
- C. Eaborn, J. D. Smith, P. B. Hitchcock, and S. E. Sozzerli, *J. Chem. Res.*, 566 (1998).
- N. Wiberg, C. M. M. Finger, T. Passler, *et al.*, *Z. Naturforsch. B* **51**, 1744 (1996).
- N. Auner, W. Ziche, and E. Herdtweck, *J. Organomet. Chem.* **426** (1), 1 (1992).
- K. M. Baines, A. G. Brook, P. D. Lickiss, and J. F. Sawyer, *Organometallics* **8**, 709 (1989).
- C. Krempner, H. Reinke, and H. Oehme, *Angew. Chem. Int. Ed. Engl.* **33**, 1615 (1994).
- J. Braddock-Wilking, M. Y. Chiang, and P. P. Gaspar, *Organometallics* **12**, 197 (1993).
- K. Schmohl, M. Blach, H. Reinke, *et al.*, *Eur. J. Inorg. Chem.*, No. 11, 1667 (1998).
- A. P. Polishchuk, N. N. Makarova, M. Yu. Antipin, *et al.*, *Kristallografiya* **35** (2), 446 (1990) [*Sov. Phys. Crystallogr.* **35**, 258 (1990)].
- A. P. Polishchuk, N. N. Makarova, T. V. Timofeeva, *et al.*, *Kristallografiya* **35** (2), 452 (1990) [*Sov. Phys. Crystallogr.* **35**, 261 (1990)].
- A. P. Polishchuk, M. Yu. Antipin, T. V. Timofeeva, *et al.*, *Kristallografiya* **36** (1), 92 (1991) [*Sov. Phys. Crystallogr.* **36**, 50 (1991)].
- A. P. Polishchuk, T. V. Timofeeva, M. Yu. Antipin, *et al.*, *Metalloorgan. Khim.* **4**, 147 (1991).

Translated by I. Polyakova

STRUCTURE OF ORGANIC COMPOUNDS

X-ray Structure Investigation of 1-Acetoxy-1-Cyano-2-Naphthylethylene and 1,1-Dicyano-2-Naphthylethylene

V. N. Nesterov, L. N. Kuleshova, and M. Yu. Antipin

Nesmeyanov Institute of Organoelement Compounds, Russian Academy of Sciences,
ul. Vavilova 28, Moscow, 117813 Russia

Received June 30, 2000

Abstract—The crystal structures of 1-acetoxy-1-cyano-2-naphthylethylene (**I**) and 1,1-dicyano-2-naphthylethylene (**II**) are determined by X-ray structure analysis. Crystals **I** are monoclinic; at 25°C, the unit cell parameters are as follows: $a = 17.308(6)$ Å, $b = 4.507(1)$ Å, $c = 17.845(5)$ Å, $\beta = 107.90(2)^\circ$, $V = 1324.7(7)$ Å³, $d_{\text{calcd}} = 1.260$ g/cm³, $Z = 4$, and space group $P2_1/n$. Crystals **II** are monoclinic; at 25°C, the unit cell parameters are $a = 3.827(1)$ Å, $b = 15.784(4)$ Å, $c = 17.226(2)$ Å, $\beta = 91.22(2)^\circ$, $V = 1040.3(4)$ Å³, $d_{\text{calcd}} = 1.304$ g/cm³, $Z = 4$, and space group $P2_1/n$. It is revealed that, in crystal structures of **I** and **II**, the molecular stacks characteristic of compounds of this series are formed through stacking contacts along the direction of the smallest lattice parameter. © 2001 MAIK “Nauka/Interperiodica”.

INTRODUCTION

This study continues a series of investigations into the factors responsible for the formation of crystal structures of cyanovinylbenzene derivatives. We performed X-ray structure analysis of 1-acetoxy-1-cyano-2-naphthylethylene (**I**) and 1,1-dicyano-2-naphthylethylene (**II**).

EXPERIMENTAL

Synthesis. Compounds **I** and **II** were synthesized according to the Knoevenagel reaction through the condensation of aromatic aldehydes with ethyl cyanoacetic ester in alcohol in the presence of an organic base (morpholine) in catalytic amounts. The yields of the reaction products were 80 and 85%, respectively.

Colorless crystals **I** and **II** were obtained by slow isothermal evaporation of ethanol solutions for three days.

X-ray structure analysis. Crystals **I** are monoclinic; at 25°C, the unit cell parameters are as follows: $a = 17.308(6)$ Å, $b = 4.507(1)$ Å, $c = 17.845(5)$ Å, $\beta = 107.90(2)^\circ$, $V = 1324.7(7)$ Å³, $d_{\text{calcd}} = 1.260$ g/cm³, $Z = 4$, and space group $P2_1/n$.

Crystals **II** are monoclinic; at 25°C, the unit cell parameters are as follows: $a = 3.827(1)$ Å, $b = 15.784(4)$ Å, $c = 17.226(2)$ Å, $\beta = 91.22(2)^\circ$, $V = 1040.3(4)$ Å³, $d_{\text{calcd}} = 1.304$ g/cm³, $Z = 4$, and space group $P2_1/n$.

The unit cell parameters and the intensities of 2581 and 2310 reflections (for structures **I** and **II**, respectively) were measured on a Siemens P3/PC four-circle automated diffractometer ($\lambda\text{MoK}\alpha$, graphite monochromator, $\theta/2\theta$ scan mode, $\theta_{\text{max}} = 27^\circ$). The structures were

solved by the direct method for all the non-hydrogen atoms. The refinement was performed according to the full-matrix least-squares procedure in the anisotropic approximation for the non-hydrogen atoms by using 1058 and 1304 unique reflections. The hydrogen atoms in molecule **II** were located independently from difference Fourier syntheses and then were refined in the iso-

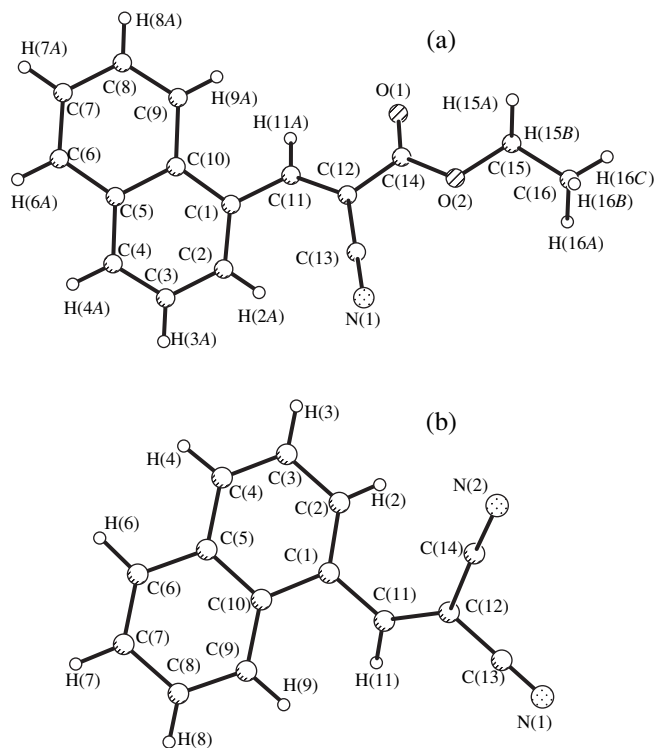


Fig. 1. A general view of molecules (a) **I** and (b) **II** and the atomic numbering.

Table 1. Coordinates ($\times 10^4$) and isotropic equivalent thermal parameters ($\times 10^3$) of non-hydrogen atoms in structure **I**

Atom	<i>x</i>	<i>y</i>	<i>z</i>	$U_{\text{eq}}, \text{\AA}$	Atom	<i>x</i>	<i>y</i>	<i>z</i>	$U_{\text{eq}}, \text{\AA}$
O(1)	6639(2)	948(7)	2771(2)	86(1)	C(8)	3953(3)	10082(11)	1260(3)	97(2)
O(2)	7632(2)	2603(6)	3817(2)	77(1)	C(9)	4490(3)	8524(9)	1850(2)	77(1)
N(1)	6962(2)	7571(10)	4873(2)	96(1)	C(10)	4421(2)	8564(8)	2621(2)	60(1)
C(1)	4959(2)	6985(8)	3260(2)	59(1)	C(11)	5580(2)	5061(8)	3132(2)	63(1)
C(2)	4854(2)	7166(9)	3990(2)	68(1)	C(12)	6344(2)	4580(8)	3601(2)	59(1)
C(3)	4239(3)	8871(10)	4119(2)	79(1)	C(13)	6680(2)	6204(10)	4316(3)	68(1)
C(4)	3725(2)	10417(10)	3526(3)	76(1)	C(14)	6868(3)	2515(10)	3343(3)	67(1)
C(5)	3798(2)	10300(9)	2757(2)	69(1)	C(15)	8200(3)	633(11)	3620(3)	91(1)
C(6)	3269(2)	11912(11)	2136(3)	88(1)	C(16)	8959(3)	583(15)	4270(3)	131(2)
C(7)	3336(3)	11723(12)	1400(3)	102(2)					

Table 2. Atomic coordinates ($\times 10^4$) and isotropic equivalent (isotropic for H atoms) thermal parameters ($\times 10^3$) for structure **II**

Atom	<i>x</i>	<i>y</i>	<i>z</i>	$U_{\text{eq}}/U_{\text{iso}}, \text{\AA}^2$	Atom	<i>x</i>	<i>y</i>	<i>z</i>	$U_{\text{eq}}/U_{\text{iso}}, \text{\AA}^2$
N(1)	-1779(6)	7821(1)	5435(1)	67(1)	C(11)	2007(5)	6031(1)	6324(1)	43(1)
N(2)	3291(6)	5715(1)	4345(1)	73(1)	C(12)	1442(5)	6407(1)	5627(1)	43(1)
C(1)	1296(5)	6399(1)	7075(1)	39(1)	C(13)	-311(6)	7205(1)	5531(1)	48(1)
C(2)	1912(6)	7245(1)	7215(1)	46(1)	C(14)	2472(6)	6013(1)	4915(1)	52(1)
C(3)	1320(6)	7610(1)	7940(1)	51(1)	H(2)	2780(60)	7592(14)	6860(14)	58(7)
C(4)	116(6)	7121(1)	8526(1)	51(1)	H(3)	1840(60)	8213(16)	8013(13)	72(7)
C(5)	-536(5)	6245(1)	8425(1)	43(1)	H(4)	-350(50)	7348(13)	9027(14)	51(6)
C(6)	-1769(6)	5736(2)	9037(1)	54(1)	H(6)	-2100(60)	6020(15)	9550(15)	72(7)
C(7)	-2372(6)	4901(2)	8934(1)	57(1)	H(7)	-3160(60)	4524(16)	9352(15)	75(7)
C(8)	-1836(6)	4528(2)	8206(1)	55(1)	H(8)	-2280(60)	3957(16)	8135(13)	61(7)
C(9)	-683(5)	4997(1)	7597(1)	46(1)	H(9)	-410(50)	4750(13)	7074(13)	52(6)
C(10)	62(4)	5868(1)	7688(1)	37(1)	H(11)	3060(60)	5449(15)	6307(13)	61(6)

Table 3. Basic parameters characterizing the conformation of molecules **I** and **II**

Parameter	Molecule	
	I	II
Root-mean-square plane (1) of the naphtho group δ^* , \AA	0.007	0.005
Root-mean-square plane (2) C(11)–C(12)–C(13)–C(14), δ^* , \AA	0.013	0.005
Dihedral angle 1–2, deg	41.6	41.3
Torsion angle C(2)–C(1)–C(11)–C(12), deg	-40.8	-38.3
Torsion angle C(10)–C(1)–C(11)–C(12), deg	143.1	144.1
Torsion angle C(1)–C(11)–C(12)–C(13), deg	-4.8	-6.8
Torsion angle C(1)–C(11)–C(12)–C(14), deg	-179.8	175.4

* Mean atomic deviation from the plane.

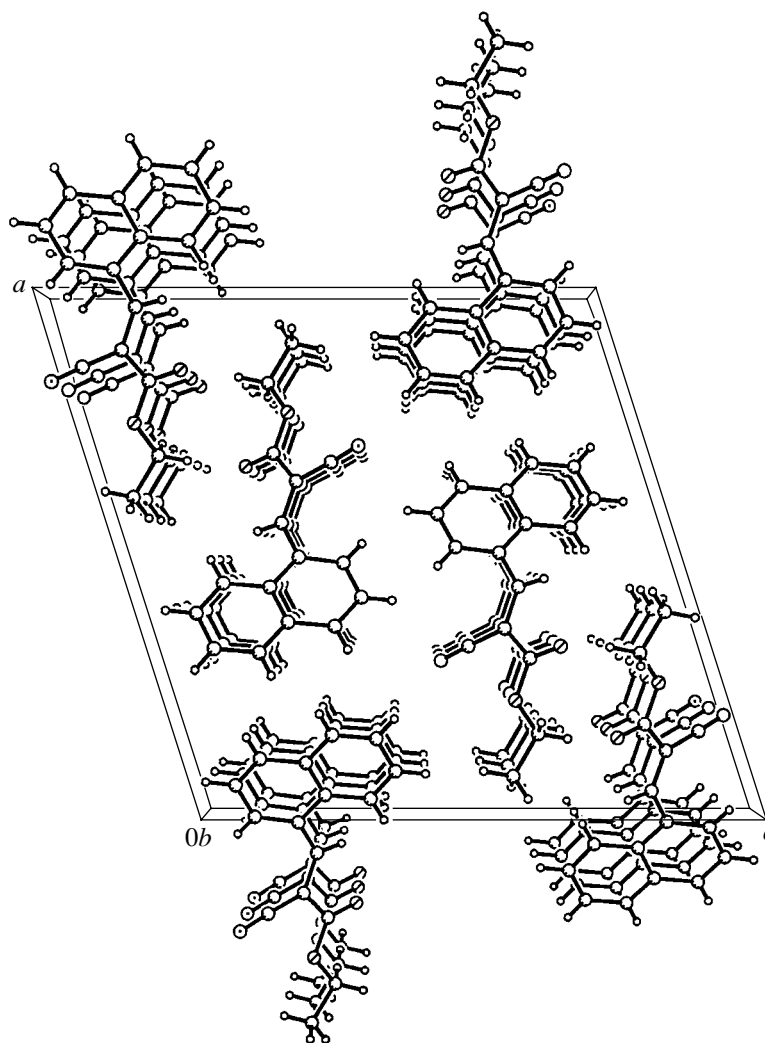


Fig. 2. Molecular packing in crystal I.

tropic approximation. In molecule **I**, the positions of hydrogen atoms were calculated geometrically and included in the refinement within the riding-atom model. The final discrepancy factors were as follows: $R_1 = 0.090$ for 1058 unique reflections with $I > 2\sigma$ and $wR_2 = 0.164$ for 2058 reflections for structure **I** (the large value of R_1 can be explained by the rather poor

quality of the crystals) and $R_1 = 0.055$ for 1304 unique reflections with $I > 2\sigma$ and $wR_2 = 0.143$ for 2006 reflections for structure **II**. All the calculations were performed using the SHELXTL97 software package [1]. The atomic coordinates and isotropic equivalent (isotropic for H atoms) thermal parameters for structures **I** and **II** are presented in Tables 1 and 2, respectively.

Table 4. Selected bond lengths (Å) in the studied molecules

Molecule	R_{nh}^*	$R_{min}-R_{max}^{**}$	C(1)–C(11)	C(11)–C(12)	C(12)–C(13)	C(12)–C(14)
I	1.390(2)	1.355–1.421(2)	1.452(2)	1.347(2)	1.430(3)	1.469(2)
II	1.396(4)	1.359–1.436(4)	1.449(4)	1.353(4)	1.436(4)	1.438(3)

* Mean bond length in the naphtho group.

** Range of bond lengths in the naphtho group.

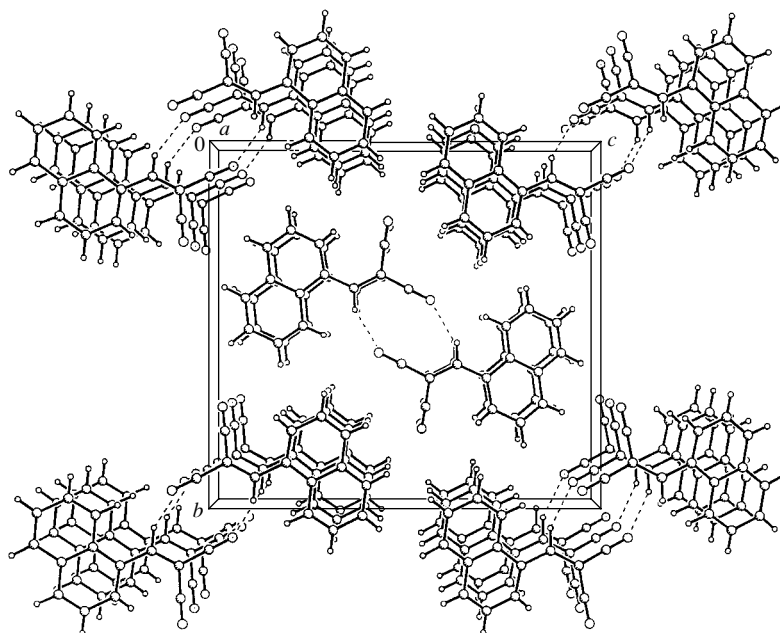


Fig. 3. Molecular packing in crystal **II**.

RESULTS AND DISCUSSION

Figure 1 shows a general view of molecules. Both molecules are nonplanar. The torsion angles and other parameters that characterize the molecular conformation are listed in Table 3. The molecules consist of two planar fragments, namely, the naphtho and cyanovinyl groups. The dihedral angles between the planar molecular fragments in compounds **I** and **II** are equal to 41.6° and 41.3° , respectively. However, the bond lengths (Table 4) indicate the electron conjugation in the $R-C(1)-C(11)-C(12)$ chain. The difference between the lengths of the formally single bond $C(1)-C(11)$ and the formally double bond $C(11)-C(12)$ is equal to 0.105 \AA in **I** and 0.096 \AA in **II**. In both molecules, the $C(1)-C(10)$ bond lengths are maximum in the naphtho group. The remaining bond lengths and bond angles have standard values [2, 3]. The short intramolecular contacts $H(2)\cdots C(13)$, which were revealed earlier in 3,4-dimethoxy, 3,4,5-trimethoxy, and 4-fluoro derivatives of benzylidenecyanoacetic acid [4], are absent in molecules **I** and **II** due to their nonplanar molecular structure.

The intermolecular stacking contacts, which are typical of crystal packings in cyanovinylbenzene derivatives, are also formed in crystals **I** and **II**. In both cases, these contacts are parallel ($\uparrow\uparrow$) stacking contacts that are responsible for the formation of molecular stacks in the crystals (Figs. 2, 3). The distances between the corresponding planar molecular fragments in stacks are equal to 3.56 \AA in **I** and 3.58 \AA in **II**. These values correspond to the sums of the van der Waals radii for carbon atoms [5]. Moreover, in crystals **II**, molecules of

the adjacent stacks are linked by the $H(11a)\cdots N(2)$ contacts (2.579 \AA) into dimers of the $D\bar{1}$ type (Fig. 3). As a result, the centrosymmetric space group $P2_1/n$ is realized in these crystals. In molecules of crystal **I**, the replacement of the second cyano group by the ester group prevents the formation of the $D\bar{1}$ centrosymmetric dimer. The structure of this crystal is built up of antiparallel stacks with the $P2_1/n$ symmetry.

ACKNOWLEDGMENTS

This work was supported by the Russian Foundation for Basic Research, project no. 00-03-32840a.

REFERENCES

1. G. M. Sheldrick, *SHELXTL97: An Integrated System for Solving, Refining, and Displaying Crystal Structures from Diffraction Data, Versions 5.10* (Bruker AXS, Madison, 1997).
2. F. H. Allen, O. Kennard, D. G. Watson, *et al.*, *J. Chem. Soc., Perkin Trans. 2*, S1 (1987).
3. A. G. Orpen, L. Brammer, F. H. Allen, *et al.*, *J. Chem. Soc., Dalton Trans.* **1**, S1 (1989).
4. V. N. Nesterov, L. N. Kuleshova, and M. Yu. Antipin, *Kristallografiya* **46** (3), 452 (2001) [*Crystallogr. Rep.* **46** (3), 402 (2001)].
5. R. S. Rowland and R. Taylor, *J. Phys. Chem.* **100**, 7384 (1996).

Translated by O. Borovik-Romanova

STRUCTURE OF ORGANIC COMPOUNDS

Crystal Structure of Cholest-4-ene-3,6-Dione: A Steroid*

Rajnikant^{1, **}, V. K. Gupta², E. H. Khan², S. Shafi², S. Hashmi², Shafiullah²,
B. Varghese³, and Dinesh¹

¹ X-ray Crystallography Laboratory, Post-Graduate Department of Physics,
University of Jammu, Jammu Tawi, 180006 India

² Steroid Research Laboratory, Department of Chemistry, Aligarh Muslim University, Aligarh, 202002 India

³ Regional Sophisticated Instrumentation Center, Indian Institute of Technology, Chennai, 600036 India
e-mail: rajni_kant_verma@hotmail.com

Received July 27, 2000; in final form, December 7, 2000

Abstract—The crystal structure of cholest-4-ene-3,6-dione (C₂₇H₄₄O₂) has been determined by X-ray diffraction methods. The compound crystallizes in the monoclinic crystal system (space group *P*2₁) with the unit cell parameters *a* = 10.503(4) Å, *b* = 8.059(1) Å, *c* = 14.649(1) Å, β = 105.4(2)°, and *Z* = 2. The structure has been refined to an *R* value of 0.035 for 2252 observed reflections. Ring *A* of the steroid nucleus exists in a sofa conformation, while rings *B* and *C* adopt a chair conformation. The five-membered ring *D* exhibits a half-chair conformation. The molecules in the unit cell are linked together by the C–H···O hydrogen bonds. © 2001 MAIK “Nauka/Interperiodica”.

INTRODUCTION

Steroids are known to have multifaceted biological properties [1–3]. The present work is a part of our systematic research on the synthesis and structure analysis of a variety of steroidal molecules [4–13].

EXPERIMENTAL

The title compound was synthesized by the reaction shown in Fig. 1.

Pyridinium dichromate (44 g) was added to a solution of cholesterol (10 g) and *N,N*-dimethylformamide (220 ml), and the reaction mixture was stirred at room temperature for 4 h. The reaction was monitored with the help of thin-layer chromatography. After completion of the reaction, water was added and the reaction mixture was treated with ether. The ether layer was washed with water, dilute HCl, and sodium bicarbonate (5%) and then was dried over anhydrous sodium sulfate. Slow evaporation of the solvent yielded a yellow solid, which was crystallized from methanol.

Rectangular platelike crystals of cholest-4-ene-3,6-dione (the melting point is 397 K) were grown from methanol by slow evaporation at room temperature. Three-dimensional intensity data were collected on an Enraf–Nonius CAD4 diffractometer (CuK_α radiation, λ = 1.5418 Å, ω/2θ scan mode). The unit cell parameters were refined from accurately determined 25 reflections in the range 14.5° < θ < 26.5°. A total of 2568 reflections were measured, of which 2433 reflections were found to be unique (0 ≤ *h* ≤ 12, 0 ≤ *k* ≤ 9, –17 ≤ *l* ≤ 17) and 2252 reflections were treated as observed [*F*_o > 4σ(*F*_o)]. Two standard reflections (13 $\bar{5}$ and 03 $\bar{4}$) measured every 100 reflections showed no significant variation in the intensity data. The reflection data were corrected for Lorentz and polarization effects. No absorption and extinction corrections were applied. The crystallographic data are listed in Table 1.

The structure was solved by the direct method using SHELXS86 program [14]. All the non-hydrogen atoms of the molecule were located from the *E*-map. The *R*-factor based on *E*-values converged to *R*_{*E*} = 0.209. Refinement of the structure was carried out by the full-matrix least-squares method using SHELXL93 pro-

* This article was submitted by the authors in English.

** Author for correspondence.

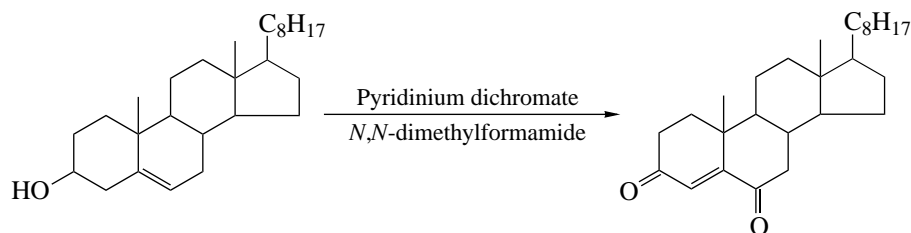


Fig. 1.

Table 1. Crystal data and experimental details

Crystal habit	Rectangular plates
Empirical formula	C ₂₇ H ₄₄ O ₂
Molecular weight	398.63
Unit cell volume	1195.4(5) Å ³
Unit cell parameters	$a = 10.503(4)$ Å, $b = 8.059(1)$ Å, $c = 14.649(1)$ Å, $\beta = 105.4(2)^\circ$
Crystal system, space group	Monoclinic, $P2_1$
Density (calcd)	1.1076 mg/m ³
No. of molecules per unit cell	2
Linear absorption coefficient (μ)	0.513 mm ⁻¹
$F(000)$	440
Crystal size	0.3 × 0.2 × 0.1 mm
θ range for data collection	3.13° ≤ θ ≤ 69.92°
Data/restraints/parameters	2429/1/431
Final R -factors	$R_1 = 0.035$, $wR_2 = 0.136$
Absolute structure parameter	0.4(5)
Extinction coefficient	0.005(1)
Final residual electron density	-0.11 < $\Delta\rho$ < 0.19 e Å ⁻³
Maximum ratio Δ/σ	0.955 for H (221)

Table 2. Atomic coordinates and equivalent isotropic thermal parameters (Å²) (e.s.d.'s are given in parentheses) for the non-hydrogen atoms

Atom	x	y	z	U_{eq}^*	Atom	x	y	z	U_{eq}^*
O(1)	0.8958(4)	0.2605(6)	-0.1805(2)	0.134(2)	C(14)	0.5198(2)	0.1625(3)	0.2032(2)	0.048(1)
O(2)	0.7537(3)	-0.1592(3)	0.0180(2)	0.092(1)	C(15)	0.4769(4)	0.0187(3)	0.2568(2)	0.067(1)
C(1)	0.7983(4)	0.4387(4)	0.0175(3)	0.076(1)	C(16)	0.3811(4)	0.1020(4)	0.3065(2)	0.069(1)
C(2)	0.8920(4)	0.4206(5)	-0.0465(3)	0.086(1)	C(17)	0.3932(2)	0.2927(3)	0.2950(2)	0.052(1)
C(3)	0.8659(3)	0.2702(6)	-0.1065(2)	0.081(1)	C(18)	0.6430(3)	0.3011(4)	0.3593(2)	0.064(1)
C(4)	0.8070(3)	0.1282(4)	-0.0698(2)	0.065(1)	C(19)	0.9177(3)	0.2621(5)	0.1572(2)	0.072(1)
C(5)	0.7753(2)	0.1310(3)	0.0130(2)	0.051(1)	C(20)	0.3703(3)	0.3889(4)	0.3803(2)	0.059(1)
C(6)	0.7219(3)	-0.0257(3)	0.0432(2)	0.057(1)	C(21)	0.3912(4)	0.5766(5)	0.3752(3)	0.075(1)
C(7)	0.6232(3)	-0.0106(3)	0.1001(2)	0.057(1)	C(22)	0.2302(3)	0.3550(5)	0.3901(2)	0.066(1)
C(8)	0.6424(2)	0.1394(3)	0.1670(2)	0.045(1)	C(23)	0.2157(3)	0.3816(5)	0.4896(2)	0.065(1)
C(9)	0.6648(2)	0.2960(3)	0.1141(2)	0.044(1)	C(24)	0.0763(3)	0.3548(4)	0.4984(2)	0.057(1)
C(10)	0.7900(2)	0.2835(3)	0.0757(2)	0.050(1)	C(25)	0.0559(3)	0.3879(3)	0.5965(2)	0.056(1)
C(11)	0.6641(3)	0.4536(3)	0.1727(2)	0.057(1)	C(26)	0.1368(4)	0.2719(6)	0.6716(2)	0.078(1)
C(12)	0.5429(3)	0.4671(3)	0.2129(2)	0.052(1)	C(27)	-0.0893(3)	0.3755(5)	0.5931(3)	0.075(1)
C(13)	0.5277(2)	0.3133(3)	0.2699(1)	0.047(1)					

$$* U_{eq} = (1/3) \sum_i \sum_j U_{ij} a_i^* a_j^* (\mathbf{a}_i \mathbf{a}_j).$$

gram [15]. The positional and thermal parameters of non-hydrogen atoms were refined isotropically with the residual index $R = 0.129$. Further refinement with anisotropic thermal parameters resulted in the final reli-

ability index $R = 0.035$ with weighted $R (F_2) = 0.136$. All the hydrogen atoms were located from the difference Fourier map. Their positional and isotropic temperature factors were refined.

Table 3. Endocyclic torsion angles (deg) (e.s.d.'s are given in parentheses)

C(2)–C(1)–C(10)–C(5)	–45.5(4)	C(14)–C(8)–C(9)–C(11)	51.1(3)
C(10)–C(1)–C(2)–C(3)	51.3(4)	C(8)–C(9)–C(10)–C(5)	56.4(3)
C(1)–C(2)–C(3)–C(4)	–27.7(5)	C(8)–C(9)–C(11)–C(12)	–50.7(3)
C(2)–C(3)–C(4)–C(5)	1.0(5)	C(9)–C(11)–C(12)–C(13)	–54.3(3)
C(3)–C(4)–C(5)–C(10)	3.3(5)	C(11)–C(12)–C(13)–C(14)	56.5(2)
C(4)–C(5)–C(10)–C(1)	19.4(4)	C(12)–C(13)–C(14)–C(8)	–60.7(2)
C(6)–C(5)–C(10)–C(9)	–41.4(3)	C(14)–C(13)–C(17)–C(16)	39.6(2)
C(10)–C(5)–C(6)–C(7)	31.6(4)	C(17)–C(13)–C(14)–C(15)	47.2(2)
C(5)–C(6)–C(7)–C(8)	–33.1(3)	C(13)–C(14)–C(15)–C(16)	36.0(3)
C(6)–C(7)–C(8)–C(9)	47.0(3)	C(14)–C(15)–C(16)–C(17)	–10.3(3)
C(7)–C(8)–C(9)–C(10)	–60.3(3)	C(15)–C(16)–C(17)–C(13)	–18.6(3)
C(9)–C(8)–C(14)–C(13)	–58.4(3)		

RESULTS AND DISCUSSION

The final positional and equivalent isotropic displacement parameters for all the non-hydrogen atoms are listed in Table 2. The endocyclic torsion angles are presented in Table 3. A general view of the molecule with the atomic numbering scheme (thermal ellipsoids are drawn at a 50% probability) is shown in Fig. 2 [16]. The geometric calculations were performed using PARST program [17].

Bond distances and bond angles are in good agreement with some analogous steroids [4–6, 18]. The

mean bond lengths [$C(sp^3)–C(sp^3)$, 1.537(4) Å; $C(sp^3)–C(sp^2)$, 1.498(5) Å; and $C(sp^2)–C(sp^2)$, 1.435(3) Å] are also quite close to their theoretical values [19, 20]. In ring A, the C(2)–C(3) bond length [1.479(6) Å] is slightly shorter than its theoretical value [19]. The shortening of the C(2)–C(3) bond in the structure under investigation can be due to the location of the ketone group at the C(3) atom. The endocyclic bond angles in the steroid nucleus fall in the range from 106.7(2)° to 123.4(2)° [the average value is 113.9(2)°] for the six-

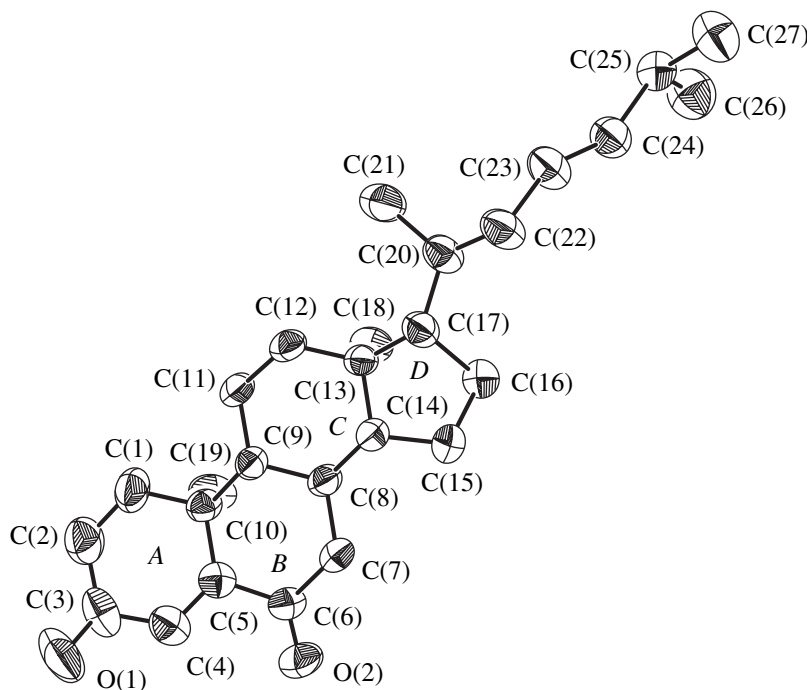
**Fig. 2.** A general view of the molecule and the atomic numbering.

Table 4. Geometry of intramolecular and intermolecular C–H...O hydrogen bonds (e.s.d.'s are given in parentheses)

C–H...O	H...O(Å)	C...O(Å)	C–H...O(deg)
C4–H41...O2	2.44(6)	2.776(4)	99(4)
C1–H12...O2 ⁽ⁱ⁾	2.57(6)	3.274(4)	122(4)
C27–H271...O1 ⁽ⁱⁱ⁾	2.66(5)	3.487(6)	144(3)

Note: Symmetry codes: (i) $x, y + 1, z$ and (ii) $x - 1, y, z + 1$.

membered rings and from $99.5(2)^\circ$ to $107.2(2)^\circ$ [the average value is $103.6(4)^\circ$] for the five-membered ring.

Ring *A* adopts a sofa conformation with an asymmetry parameter $\Delta C_s = 6.01$ [21]. The average value of torsion angles in this ring is $24.7(4)^\circ$. Ring *B* exists in a distorted chair conformation [$\Delta C_2 = 8.88$ and $\Delta C_s = 4.01$]. The average value of torsion angles in this ring is $45.0(3)^\circ$. Ring *C* also exists in a chair conformation [$\Delta C_2 = 2.67$ and $\Delta C_s = 3.38$]. The average value of torsion angles in this ring is $55.3(3)^\circ$. The five-membered ring *D* occurs in a half-chair conformation [$\Delta C_2 = 6.38$], the phase angle of pseudorotation is $\Delta = -3.8^\circ$, and the maximum torsion angle $\phi_m = -47.2^\circ$ [22]. The average value of torsion angles in this ring is $30.4(3)^\circ$. There exists one intramolecular and two intermolecular C–H...O hydrogen bonds (see Table 4), which contribute to the stability of the crystal structure.

ACKNOWLEDGMENTS

Rajnikant acknowledges the support of the University Grant Commission, New Delhi, Government of India for research funding under the DSA Research Program, project no. F 530/1/DSA/95(SAP-I).

REFERENCES

- W. L. Duax, C. M. Weeks, and D. C. Rohrer, in *Topics in Stereochemistry*, Ed. by N. L. Allinger and E. L. Eliel (Wiley, New York, 1976), Vol. 9, p. 271.
- E. V. Jensen and E. R. Desombre, *Annu. Rev. Biochem.* **41**, 203 (1972).
- H. G. Williams-Ashman and A. H. Reddi, *Annu. Rev. Physiol.* **33**, 31 (1971).
- V. K. Gupta, Rajnikant, K. N. Goswami, and K. K. Bhutani, *Cryst. Res. Technol.* **29**, 77 (1994).
- V. K. Gupta, K. N. Goswami, K. K. Bhutani, and R. M. Vaid, *Mol. Mater.* **4**, 303 (1994).
- V. K. Gupta, Rajnikant, K. N. Goswami, *et al.*, *Acta Crystallogr., Sect. C: Cryst. Struct. Commun.* **50**, 798 (1994).
- A. Singh, V. K. Gupta, Rajnikant, and K. N. Goswami, *Cryst. Res. Technol.* **29**, 837 (1994).
- A. Singh, V. K. Gupta, Rajnikant, *et al.*, *Mol. Mater.* **4**, 295 (1994).
- A. Singh, V. K. Gupta, K. N. Goswami, *et al.*, *Mol. Mater.* **6**, 53 (1996).
- Rajnikant, V. K. Gupta, J. Firoz, *et al.*, *Kristallografiya* **46**, 465 (2001) [*Crystallogr. Rep.* **46**, 415 (2001)].
- Rajnikant, V. K. Gupta, J. Firoz, *et al.*, *Kristallografiya* **45**, 857 (2000) [*Crystallogr. Rep.* **45**, 785 (2000)].
- Rajnikant, V. K. Gupta, J. Firoz, *et al.*, *Cryst. Res. Technol.* (in press).
- Rajnikant, V. K. Gupta, J. Firoz, *et al.*, *Cryst. Res. Technol.* (in press).
- G. M. Sheldrick, *SHELXS86: Program for the Solution of Crystal Structures* (Univ. of Göttingen, Göttingen, 1986).
- G. M. Sheldrick, *SHELXL93: Program for the Refinement of Crystal Structures* (Univ. of Göttingen, Göttingen, 1993).
- C. K. Johnson, *ORTEP-II: A Fortran Thermal Ellipsoid Plot Program for Crystal Structure Illustrations*, ORNL-5138 (Oak Ridge National Laboratory, Tennessee, 1976).
- M. Nardelli, *Comput. Chem.* **7**, 95 (1993).
- R. Radhakrishnan, M. A. Viswamitra, K. K. Bhutani, and R. M. Vaid, *Acta Crystallogr., Sect. C: Cryst. Struct. Commun.* **44**, 1820 (1988).
- L. E. Sutton, *Tables of Interatomic Distances and Configuration in Molecules and Ions* (The Chemical Society, London, 1965), Spec. Publ. Chem. Soc., No. 18.
- L. S. Bartell and R. A. Bonhan, *J. Chem. Phys.* **32**, 824 (1960).
- W. L. Duax and D. A. Norton, *Atlas of Steroid Structure* (Plenum, New York, 1975), Vol. 1.
- C. Altona, H. J. Geise, and C. Romers, *Tetrahedron* **24**, 13 (1968).

STRUCTURE
OF ORGANIC COMPOUNDS

The Electronic Nature of the Substituents and the Structure
of 4,4'-Dipyridilium Dications. The Crystal Structure
of *N,N'*-Di(carbomethoxymethyl)-4,4'-Dipyridilium Dipерchlorate

A. Yu. Vishnyakov, A. P. Polishchuk, and I. Yu. Polishchuk

Institute of Physics, National Academy of Sciences of Ukraine, pr. Nauki 46, Kiev, 03650 Ukraine

Received December 5, 2000

Abstract—The crystal structure of *N,N'*-di(carbomethoxymethyl)-4,4'-dipyridilium dipерchlorate (**I**) $C_{18}H_{22}Cl_2N_2O_{12}$ at 293 K is determined by the X-ray diffraction technique. The crystals are monoclinic, $a = 5.501(1)$ Å, $b = 26.460(5)$ Å, $c = 8.140(2)$ Å, $\beta = 100.63(3)^\circ$, space group $P2_1/n$, $Z = 2$, 2271 reflections measured (2052 reflections unique), $R_1 = 0.062$, and $wR2 = 0.141$ for 1161 reflections with $F \geq 4\sigma(F)$. The interaction between the lone-electron pair of the carbonyl oxygen atom of the electron-withdrawing ester group and the π system of the dication manifests itself as the intramolecular O(1)···N contact (2.780 Å). In the absence of charge transfer from the counterion to the dication, this interaction contributes to the stabilization of a planar structure of the dication fragment of the molecule despite the electron-withdrawing nature of the ester groups.
© 2001 MAIK "Nauka/Interperiodica".

INTRODUCTION

The quaternary salts of 4,4'-dipyridyl (viologens) have found wide practical use owing to the large variety of properties. In our previous papers [1–4], we gave the detailed description of viologens as promising light-sensitive materials for data imaging and storage. Polymers are certainly among these materials. The viologen polymers, like viologens themselves, are characterized by electrical conductivity [5, 6], photochromism [7, 8], electrochromism [9], thermochromism [10], and their ability to undergo photomechanical transformations [8]. The synthesis of liquid-crystal viologens makes it possible to expand the field of application of viologens. Liquid-crystal viologens were first described in [11]. It was found that the thermotropic mesophase of *N,N'*-di(3,6,9-trioxatridecyl)-4,4'-dipyridilium diiodide exhibits electrochromic properties. The preparation of liquid-crystal viologen polymers has been reported recently in [12, 13]. These compounds show promise for new applications. In particular, they can be used for the preparation of various coatings, films, and multifunctional composite materials [14].

It is known that the change in color in viologens is associated with the generation of radical cations under ultraviolet irradiation or in response to the electric field applied to the cell at a field strength corresponding to the electrochemical potential of the material [15]. We used the colored state of the radical cations for preparation of a new photorefractive material through addition of the viologens to lyotropic ionic liquid crystals. The holographic grating for liquid-crystal media of this type was first recorded in [16].

It is generally believed that the molecular shape and its related anisotropy of polarizability are of consider-

able importance in the formation of mesophases [17]. The molecular shape of the viologens used as photochromic and electrochromic additives to a liquid-crystal matrix is also an important factor. In this respect, detailed investigation of the structure of viologens containing substituents of different electronic nature is currently of interest.

Earlier [1–3], we studied the effect of the electron-donating properties of the anions on the structure of the dipyridilium nucleus of the

$R-N \begin{array}{c} \text{+} \\ \text{+} \end{array} - \begin{array}{c} \text{+} \\ \text{+} \end{array} N-R \ 2A^-$ cations. The electronic effect of the substituents containing lone-electron pairs on the structure of this nucleus in the absence of charge transfer in viologens was analyzed in [4]. In particular, it was found that the planar structure of the dication fragment in *N,N'*-di(2-hydroxyethyl)-4,4'-dipyridilium dipерchlorate [$HOEtD^{2+}2ClO_4^-$, $R = (CH_2)_2OH$, $A = ClO_4^-$] results to a large extent from the conjugation between the lone-electron pairs of the electron-donating hydroxyl groups and the π system of the dication.

The purpose of this work was to elucidate the effect of the electron-withdrawing ester groups in the tails of the molecule on the structure of the dipyridilium skeleton of the dication. In this connection, we performed the X-ray diffraction study of *N,N'*-di(carbomethoxymethyl)-4,4'-dipyridilium dipерchlorate (**I**) ($R = CH_2COOC_2H_5$, $A = ClO_4^-$), which is characterized by the lack of the charge-transfer interaction and contains the COO electron-withdrawing group.

Table 1. Crystallographic and data-collection parameters for structure **I**

Parameter	I
Empirical formula	C ₁₈ H ₂₂ Cl ₂ N ₂ O ₁₂
<i>M_r</i>	529.28
Crystal system	Monoclinic
Space group	<i>P</i> 2 ₁ / <i>n</i>
<i>Z</i>	2
<i>a</i> , Å	5.501(1)
<i>b</i> , Å	26.460(5)
<i>c</i> , Å	8.140(2)
α, deg	90
β, deg	100.63(3)
γ, deg	90
<i>V</i> , Å ³	1164.5(4)
<i>D</i> _{calcd} , g/cm ³	1.509
μ, mm ⁻¹	0.345
<i>F</i> (000)	548
Diffractometer	Enraf-Nonius CAD-4
λ, Å	0.71073
<i>T</i> , K	293
θ _{max} , deg	25
Number of reflections measured	2271
Number of reflections with <i>F</i> ≥ 4σ(<i>F</i>)	1161
Refinement on	<i>F</i> ²
<i>R</i> 1	0.062
<i>wR</i> 2	0.141
<i>S</i>	1.055

EXPERIMENTAL

Compound **I** was prepared from *N,N'*-di(carbetoxyethyl)-4,4'-dipyridilium dichloride (*R* = CH₂COOC₂H₅, *A* = Cl) (the synthesis of this compound was reported in [3]) according to the ion-exchange procedure described in [2]. Single crystals were grown by slow evaporation of a solution in isopropyl alcohol. Transparent plate-like single crystals were obtained in the course of crystallization. The X-ray experiment was carried out at room temperature on an Enraf-Nonius CAD4 automated four-circle diffractometer (graphite monochromator, ω/2θ scan mode).

The structure was solved by the direct method and refined in the full-matrix anisotropic approximation for the non-hydrogen atoms. In the course of structure refinement, we revealed that, as in the crystal of HOEtD²⁺2ClO₄⁻ [4], all the four oxygen atoms of the ClO₄⁻ anion are disordered over three positions, each with the occupancy *G* = 0.33. All the hydrogen atoms in the studied structure were located from the difference Fourier synthesis and refined within the riding-atom model at fixed parameters *U*_{iso} = 0.08 Å². The calculations were performed on an IBM AT personal computer using the SHELXS86 [18] and SHELXL93 [19] program packages. The main crystal data and data-collection parameters at room temperature are summarized in Table 1. The atomic coordinates and selected torsion angles are listed in Tables 2 and 3, respectively.

RESULTS AND DISCUSSION

In crystal **I**, the dication occupies a special position at the center of symmetry and its dipyrilidium nucleus is exactly planar. The rotation of the *N*-substituent with respect to the nucleus [the angle between the planes of the C(1)C(2)C(3)N(4)C(4)C(5) pyridine ring and the

Table 2. Coordinates (×10⁴) and equivalent isotropic thermal parameters (Å² × 10³) of the non-hydrogen atoms in structure **I**

Atom	<i>x</i>	<i>y</i>	<i>z</i>	<i>U</i> _{eq}	Atom	<i>x</i>	<i>y</i>	<i>z</i>	<i>U</i> _{eq}
Cl	-1239(2)	981(1)	2973(2)	77(1)	O(5B)	-3398(32)	709(10)	3098(37)	115(12)
O(1)	-3361(6)	6717(1)	7355(4)	70(1)	O(6B)	880(35)	673(9)	3467(28)	210(19)
O(2)	-900(6)	7261(1)	8971(4)	72(1)	N	447(6)	6011(1)	7796(4)	48(1)
O(3)	-3729(24)	851(12)	3041(26)	75(7)	C(1)	119(7)	5213(1)	5602(4)	42(1)
O(4)	-876(41)	1496(3)	3413(19)	75(5)	C(2)	1705(7)	5606(2)	5515(5)	54(1)
O(5)	-829(35)	884(10)	1348(15)	112(9)	C(3)	1859(8)	6000(2)	6619(6)	56(1)
O(6)	-357(37)	685(6)	4152(25)	114(9)	C(4)	-1113(9)	5633(2)	7912(6)	64(1)
O(3A)	-810(32)	509(6)	2245(36)	155(10)	C(5)	-1283(8)	5233(2)	6860(5)	60(1)
O(4A)	-3826(17)	1052(10)	2788(34)	165(15)	C(6)	555(8)	6450(2)	8907(5)	56(1)
O(5A)	-181(34)	965(13)	4683(11)	174(13)	C(7)	-1510(8)	6817(2)	8292(5)	51(1)
O(6A)	-143(45)	1357(10)	2140(41)	290(19)	C(8)	-2633(12)	7684(2)	8544(8)	91(2)
O(3B)	-1007(33)	1413(5)	4022(20)	68(5)	C(9)	-4291(12)	7699(2)	9704(8)	108(2)
O(4B)	-1264(41)	1142(6)	1309(12)	90(6)					

C(7)O(1)O(2) ester group is 76.3 Å; Fig. 1 and Table 3] predetermines the formation of the intramolecular O(1)⋯N contact (2.780 Å). This indicates that the π - π conjugation between the ester groups and the pyridine rings of the dication is minimum. At the same time, the O(1)⋯N contact, whose length is close to the sum of the van der Waals radii of the N (1.50 Å [20]) and O (1.29 Å [21]) atoms, suggests that the lone-electron pair of the carbonyl O(1) oxygen is able to interact with the π -system of the pyridine ring, which is far more electron-deficient than the ester group. It can be assumed that, in this case, the ester group in **I** acts as a donor with respect to the pyridine fragment.

It is remarkable that similar intermolecular contacts between the N and O atoms of the electron-donating hydroxyl group are observed in *N,N'*-di(2-hydroxyethyl)-4,4'-dipyridilium dichloride [HOEtD²⁺2Cl⁻, *R* = (CH₂)₂OH, *A* = Cl⁻] [12] and HOEtD²⁺2ClO₄⁻ [*R* = (CH₂)₂OH, *A* = ClO₄⁻] [4] (2.966 Å for HOEtD²⁺2Cl⁻ and 2.847 Å for HOEtD²⁺2ClO₄⁻), which differ only in the nature of the counterions and, hence, are characterized by the presence or absence of charge transfer. Moreover, the charge-transfer complexes containing carboxyl groups, namely *N,N'*-di(carboxymethyl)-4,4'-dipyridilium dichloride, dibromide, and diiodide (COMD²⁺2A⁻; *R* = CH₂COOH; *A* = Cl⁻, Br⁻, or I⁻) [3], are also characterized by similar intramolecular O⋯N contacts (2.739, 2.743, and 2.711 Å, respectively). As was noted in [4], this interaction contributes to the stabilization of the planar structure of the central dipyridilium skeleton of the molecule in the absence of charge

Table 3. Selected torsion angles (deg) in structure **I**

Angle	ω
C(3)–N–C(6)–C(7)	96.9
C(4)–N–C(6)–C(7)	–80.6
N–C(6)–C(7)–O(1)	20.2
N–C(6)–C(7)–O(2)	–159.8
C(8)–O(2)–C(7)–C(6)	179.5
C(7)–O(2)–C(8)–C(9)	90.0

transfer and can serve as an additional factor enhancing this stabilization for charge-transfer viologens.

In [1, 22, 23], it was emphasized that the packing effects in the crystals are able to stabilize the conformationally unfavorable planar form of the dipyridilium skeleton of molecules through the π - π' interactions between the molecules in the stacks. Actually, the short period in structure **I** (*a* = 5.501 Å) is most likely predetermined by the packing type characterized by the stacking of the dication that are related by the translation along this period (Fig. 2). For this type of packing, the maximum interaction between the molecules in stacks is observed when the planes of the pyridine rings are perpendicular to the [100] crystallographic direction. In the structure studied, however, this angle is 128°; i.e., the efficiency of overlapping the π orbitals of the dication in the stacks is not maximum.

The absence of charge transfer from the counterion to the dication in crystal **I** indicates that the electronic effect of the ClO₄⁻ anions on the flattening of the dipyridilium nucleus of the dication is minor. Note once

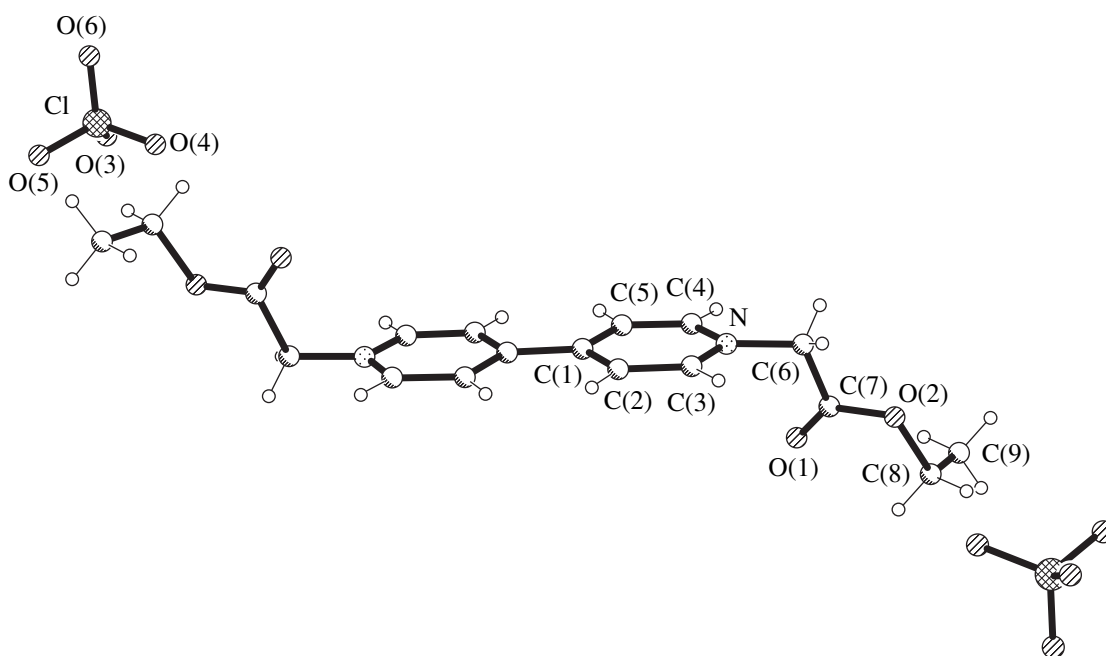


Fig. 1. Structure of molecule **I** and the atomic numbering.

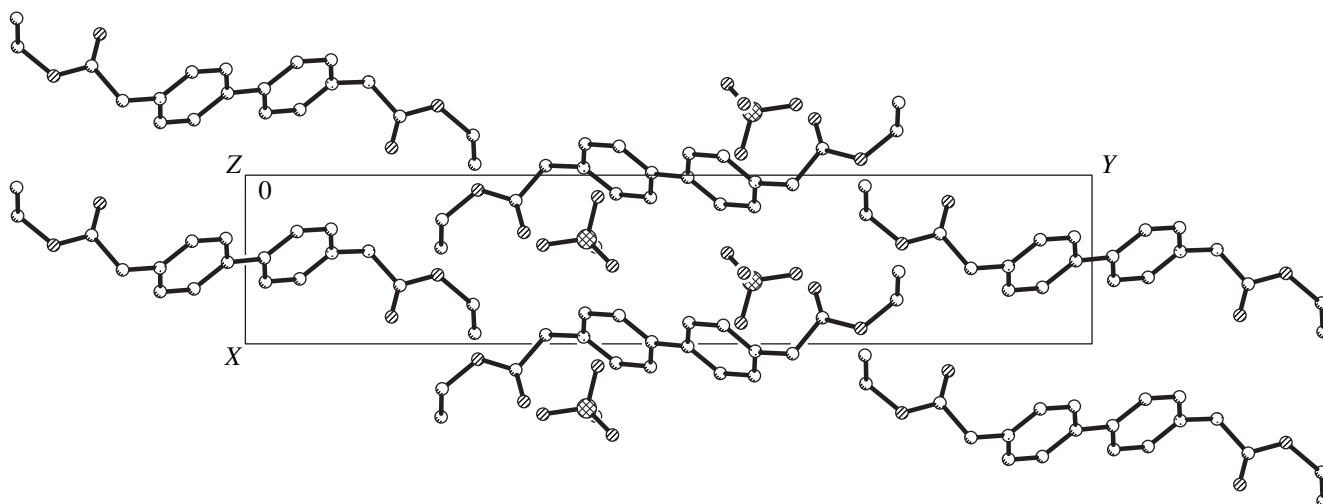


Fig. 2. Stacking of molecules **I** along the *a* period.

again that, in addition to the packing effects, the electronic effects due to the interaction of the lone-electron pairs of the O(1) atoms of the ester groups with the electron-deficient π -system of the pyridine rings also contribute to the stabilization of the planar structure of the dipyrilidium fragment in **I**. As a consequence, the electron density shifts from the O(1) atoms to the electron-deficient dication and then redistributes over the whole π -system. This redistribution most efficiently proceeds through the maximum π - π' conjugation between the pyridine rings, which is accompanied by the flattening of the molecules.

Thus, the X-ray structure analysis of compounds **I** and $\text{HOEtD}^{2+}2\text{ClO}_4^-$ [4], in which the charge transfer is absent, has demonstrated that the planar structure of the dipyrilidium nucleus is attended by short intramolecular O \cdots N contacts. The occurrence of these contacts suggests that the interaction between the π -system of the dication and the lone-electron pairs of the oxygen atoms of both electron-donating and electron-withdrawing groups is responsible to a large extent for the stabilization of the planar structure of the dipyrilidium nucleus of the molecules.

REFERENCES

- I. Yu. Polishchuk, L. G. Grineva, A. P. Polishchuk, and A. N. Chernega, *Zh. Obshch. Khim.* **66** (9), 1530 (1996).
- I. Yu. Polishchuk, L. G. Grineva, A. P. Polishchuk, and A. N. Chernega, *Zh. Obshch. Khim.* **67** (11), 1893 (1997).
- I. Yu. Polishchuk, L. G. Grineva, A. P. Polishchuk, and A. N. Chernega, *Zh. Obshch. Khim.* **68** (4), 647 (1998).
- A. Yu. Vishnyakov, A. P. Polishchuk, I. Yu. Polishchuk, and L. G. Grineva, *Kristallografiya* (2001) (in press).
- A. Rembaum, A. M. Hermann, F. E. Stevart, and F. Gutmann, *J. Phys. Chem.* **73**, 513 (1969).
- A. Merz and S. Reitmeir, *Angew. Chem. Int. Ed. Engl.* **28** (6), 807 (1989).
- M. S. Simon and P. T. Moore, *J. Polym. Sci., Polym. Chem. Ed.* **13**, 1 (1975).
- T. Hashimoto, S. Kohjiya, S. Yamashita, and M. Irie, *J. Polym. Sci., Polym. Chem. Ed.* **29**, 651 (1991).
- H. Sato and T. Tamamura, *J. Appl. Polym. Sci.* **24**, 2075 (1979).
- J. S. Moore and S. I. Stupp, *Macromolecules* **19**, 1815 (1986).
- I. Tabushi, K. Yamamura, and K. Kominami, *J. Am. Chem. Soc.* **108**, 6409 (1986).
- P. K. Bhowmik and H. Han, *J. Polym. Sci., Part A: Polym. Chem.* **33**, 1745 (1995).
- P. K. Bhowmik, S. Akhter, and H. Han, *J. Polym. Sci., Part A: Polym. Chem.* **33**, 1927 (1995).
- W. Hatke, H.-W. Schmidt, and W. Heitz, *J. Polym. Sci., Part A: Polym. Chem.* **29**, 1387 (1991).
- A. V. Vannikov and A. D. Grishina, *Photochemistry of Polymeric Donor-Acceptor Complexes* (Nauka, Moscow, 1984).
- A. G. Iljin, G. V. Klimusheva, L. P. Yatsenko, *et al.*, *Proc. SPIE* **3488**, 16 (1998).
- G. W. Gray, *Molecular Structure and Properties of Liquid Crystals* (Academic, New York, 1962).
- G. M. Sheldrick, *SHELXS86: Program for the Solution of Crystal Structures* (Univ. of Göttingen, Göttingen, 1986).
- G. M. Sheldrick, *SHELXL93: Program for the Refinement of Crystal Structures* (Univ. of Göttingen, Göttingen, 1993).
- L. Pauling, *The Nature of the Chemical Bond and the Structure of Molecules and Crystals* (Cornell Univ. Press, London, 1960, 3rd ed.).
- Yu. V. Zefirov and P. M. Zorky, *Zh. Strukt. Khim.* **15** (1), 118 (1974).
- I. Yu. Grineva, I. P. Kraïnov, A. P. Polishchuk, *et al.*, *Kristallografiya* **37** (6), 1485 (1992) [*Sov. Phys. Crystallogr.* **37**, 805 (1992)].
- I. Grineva, I. Krainov, A. Polishchuk, and A. Tolmachev, *Mol. Cryst. Liq. Cryst.* **211** (5), 397 (1992).

Translated by I. Polyakova

STRUCTURE
OF ORGANIC COMPOUNDS

Molecular and Crystal Structures
of 3-Methyl-3-[1,7-Dicarba-*closo*-dodecaborane(12)-
1-oyl-peroxy]-but-1-yne

A. S. Lyakhov*, L. S. Ivashkevich*, A. P. Yuvchenko**, T. D. Zvereva**,
A. A. Govorova*, and Yu. I. Petrushevich*

* Research Institute of Physicochemical Problems, Belarussian State University,
Leningradskaya ul. 14, Minsk, 220080 Belarus

** Institute of Chemistry of New Materials, National Academy of Sciences of Belarus,
ul. Kuprevicha 16, Minsk, 220141 Belarus

e-mail: iva@fhp.bsu.unibel.by

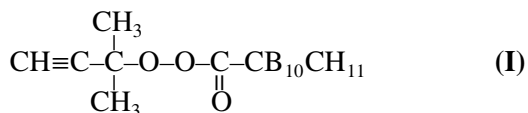
Received October 5, 2000

Abstract—The crystal and molecular structures of 3-methyl-3-[1,7-dicarba-*closo*-dodecaborane(12)-1-oyl-peroxy]-but-1-yne (**I**) are determined by X-ray diffraction analysis (Nicolet R3m automated diffractometer, MoK α radiation, $\theta/2\theta$ scan mode). It is found that the compound crystallizes in the orthorhombic crystal system, space group $P2_12_12_1$. The unit cell parameters are as follows: $a = 7.355(2)$ Å, $b = 9.773(3)$ Å, $c = 21.938(7)$ Å, and $Z = 4$. The structure is solved by the direct method and refined to $R = 0.0658$. The structural features of the molecule and the C–H...O contacts in the structure are discussed. © 2001 MAIK “Nauka/Interperiodica”.

INTRODUCTION

Over the past few decades, carborane-containing peroxides have attracted the particular attention of many researchers owing to a number of their specific chemical properties. It is known [1–5] that certain of these compounds initiate the polymerization of olefins and serve as cross-linking agents of polyolefins. As a consequence, the polymers thus prepared acquire increased resistance to UV and γ -radiation and thermooxidative destruction. The determination of the molecular structure of carborane-containing peroxides is of considerable importance in elucidating their reactivity and choosing the optimum conditions for their efficient use.

The purpose of the present work was to reveal the structural features of 3-methyl-3-[1,7-dicarba-*closo*-dodecaborane(12)-1-oyl-peroxy]-but-1-yne (**I**):



EXPERIMENTAL

Compound **I** was synthesized by the reaction of 3-methyl-3-hydroperoxy-but-1-yne with 1,7-dicarba-*closo*-dodecaborane(12)-1-carboxyl chloride according to the procedure described in [6]. Crystals suitable for X-ray structure investigation were obtained by crystallization from a 70% aqueous solution of ethanol. A crystal $0.5 \times 0.22 \times 0.12$ mm in size was chosen for the

Atomic coordinates ($\times 10^4$) and equivalent isotropic thermal parameters ($\text{Å}^2 \times 10^3$) in structure **I**

Atom	<i>x/a</i>	<i>y/b</i>	<i>z/c</i>	U_{eq}
C(1)	3130(6)	889(4)	3880(2)	45(1)
B(2)	3132(9)	2586(6)	4050(3)	61(2)
B(3)	2692(8)	1986(6)	3301(2)	62(2)
B(4)	4010(9)	501(6)	3181(3)	65(2)
B(5)	5248(8)	168(7)	3863(3)	69(2)
B(6)	4709(8)	1453(7)	4384(2)	67(2)
C(7)	5357(8)	2928(6)	4056(2)	72(2)
B(8)	4200(9)	3354(6)	3418(3)	69(2)
B(9)	4745(9)	2072(7)	2884(2)	69(2)
B(10)	6334(9)	942(7)	3231(3)	71(2)
B(11)	6723(8)	1531(8)	3973(3)	77(2)
B(12)	6435(9)	2717(6)	3365(3)	68(2)
C(13)	1602(6)	62(5)	4164(2)	51(1)
C(14)	−67(7)	−3019(5)	3873(2)	56(1)
C(15)	1500(8)	−3343(5)	4257(2)	61(1)
C(16)	2733(9)	−3636(6)	4570(3)	83(2)
C(17)	309(8)	−3301(6)	3209(2)	81(2)
C(18)	−1786(8)	−3728(6)	4100(3)	80(2)
O(1)	921(4)	−770(3)	3727(1)	59(1)
O(2)	−572(4)	−1583(3)	3970(1)	59(1)
O(3)	1100(5)	141(4)	4678(1)	70(1)

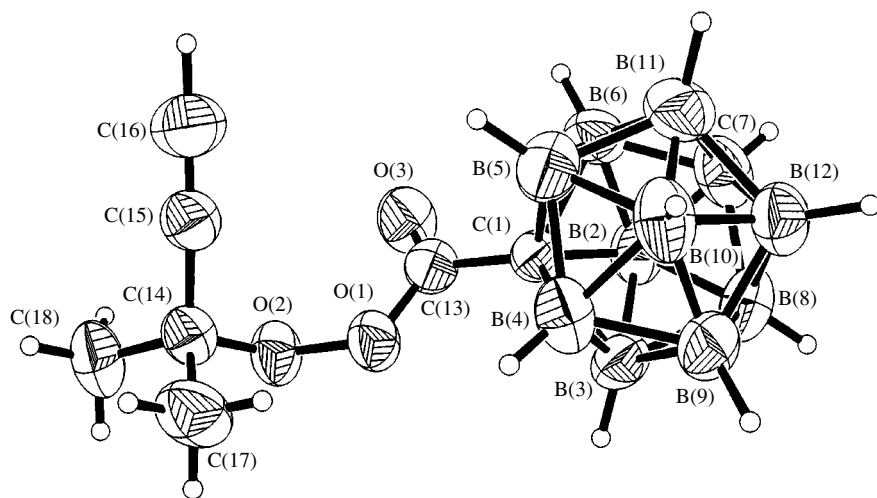


Fig. 1. Molecular structure and the atomic numbering.

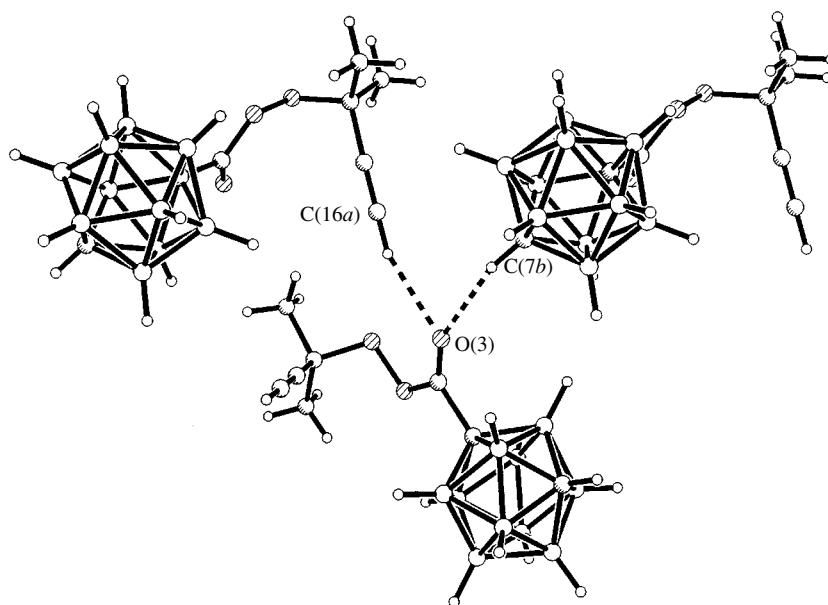


Fig. 2. A structural fragment with the C–H...O intermolecular contacts (indicated by dashed lines).

X-ray diffraction analysis. A three-dimensional set of X-ray diffraction data was collected on a Nicolet *R3m* automated four-circle diffractometer (MoK α radiation, graphite monochromator, $\theta/2\theta$ scan mode, $2\theta_{\max} = 55^\circ$). A total of 2182 reflections was measured, of which 2113 reflections were unique ($R_{\text{int}} = 0.0061$). It was found that compound **I** crystallizes in the orthorhombic crystal system, space group $P2_12_12_1$. The unit cell parameters are as follows: $a = 7.355(2)$ Å, $b = 9.773(3)$ Å, $c = 21.938(7)$ Å, $V = 1576.9(8)$ Å³, $Z = 4$, $d_{\text{X-ray}} = 1.139$ g/cm³, and $\mu = 0.68$ cm⁻¹. The structure was solved by the direct method (SIR97 [7]). The hydrogen atom of the ethynyl group was located from the difference Fourier synthesis. The positions of the remaining

hydrogen atoms were calculated geometrically. The refinement was performed by the full-matrix least-squares method with allowance made for the anisotropic thermal vibrations of non-hydrogen atoms (SHELX97 [8]). The hydrogen atom of the ethynyl group was refined in the isotropic approximation, and the remaining hydrogen atoms were refined using a riding model. The discrepancy factors are as follows: $R1 = 0.0658$ and $wR2 = 0.1558$ for the reflections with $I > 2\sigma(I)$, $R1 = 0.1064$ and $wR2 = 0.2036$ for all the reflections, and $GOOF = 1.065$. The figures were drawn using the ORTEP III program package [9]. The atomic coordinates and equivalent isotropic thermal parameters are listed in the table.

RESULTS AND DISCUSSION

Figure 1 shows the molecular structure of compound **I** and the atomic numbering. The C–B bond lengths lie in the range 1.671(9)–1.722(8) Å. Note that the C(7)–B(2) and C(7)–B(12) bonds are the shortest and longest bonds, respectively. The B–B bond lengths fall in the range from 1.73(1) Å [for the B(5)–B(11) bond] to 1.780(9) Å [for the B(4)–B(5) bond]. These parameters and the bond angles in the $\text{CB}_{10}\text{CH}_{11}$ icosahedral fragment are close to those observed for other similar compounds [10]. The length of the C(1)–C(13) bridging bond is equal to 1.518(6) Å. In the other fragments of molecule **I**, the bond lengths and angles has normal values [10].

The classical hydrogen bonds are absent in structure **I**. However, it should be noted that structure **I** involves the C–H...O-type intermolecular contacts [11] between the O(3) oxygen atom of the carbonyl group and two hydrogen atoms, namely, the H(16) atom of the acetylene group and the H(7) atom [bonded to the C(7) atom] of the carborane fragment. These contacts are depicted in Fig. 2 and have the following geometric parameters. In the D–H...A chain, the D–H, H...A, and D...A distances are equal to 1.00(5), 2.36(4), and 3.320(7) Å for the C(16)–H(16)...O(3) contact and 0.99(4), 2.48(3), and 3.406(6) Å for the C(7)–H(7)...O(3) contact, respectively. The C(16)–H(16)...O(3) and C(7)–H(7)...O(3) angles are equal to 162(2)° and 154(3)°, respectively. The interaction between the oxygen atom of the carbonyl group and the hydrogen atom of the ethynyl group is confirmed by the IR absorption spectra of compound **I** [6]. According to the IR data, the frequencies of the stretching vibrations of these groups in the crystal are substantially shifted toward the low-frequency range as compared to those in solutions. The aforementioned contacts, together with the van der Waals interactions, are responsible for the molecular packing in the crystal.

ACKNOWLEDGMENTS

We acknowledge the support of the Russian Foundation for Basic Research (project no. 99-07-90133) in the payment of the license to use the Cambridge Structural Database in analyzing the results obtained in this work.

REFERENCES

1. Yu. A. Ol'dekop, S. F. Naumova, L. A. Churkina, *et al.*, USSR Inventor's Certificate No. 681068 (1977), Byull. Izobret., No. 31 (1979).
2. L. A. Churkina, S. F. Naumova, T. D. Zvereva, *et al.*, Vestsi Akad. Navuk BSSR, Ser. Khim. Navuk, No. 3, 125 (1981).
3. L. A. Churkina, S. F. Naumova, T. D. Zvereva, *et al.*, Vestsi Akad. Navuk BSSR, Ser. Khim. Navuk, No. 3, 108 (1982).
4. A. P. Yuvchenko, A. Ya. Markina, N. R. Prokopchuk, *et al.*, Zh. Prikl. Khim. (St. Petersburg) **71** (3), 472 (1998).
5. R. Grimes, *Carboranes* (Academic, New York, 1970; Mir, Moscow, 1974).
6. T. D. Zvereva, A. P. Yuvchenko, and N. A. Zhukovskaya, Zh. Obshch. Khim. **62** (4), 855 (1992).
7. A. Altomare, M. C. Burla, M. Camalli, *et al.*, J. Appl. Crystallogr. **32**, 115 (1999).
8. G. M. Sheldrick, *SHELX97: Program for the Solution and Refinement of Crystal Structures* (Univ. of Göttingen, Göttingen, Germany, 1997).
9. L. J. Farrugia, J. Appl. Crystallogr. **30**, 565 (1997).
10. F. H. Allen and O. Kennard, Chem. Des. Autom. News **8** (1), 31 (1993).
11. G. R. Desiraju and T. Steiner, *The Weak Hydrogen Bond in Structural Chemistry and Biology* (Oxford Univ. Press, Oxford, 1999).

Translated by O. Borovik-Romanova

STRUCTURE
OF ORGANIC COMPOUNDS

Crystal Structures of $[\text{N}(\text{CH}_3)_4](\text{HSeO}_4)$
at 298, 363, and 380 K

M. A. Zakharov*, S. I. Troyanov*, V. B. Rybakov*,
L. A. Aslanov*, and E. Kemnitz**

* Chemistry Faculty, Moscow State University, Vorob'evy gory, Moscow, 119899 Russia

e-mail: karpova@inorg.chem.msu.ru

** Institut für Chemie, Humboldt Universität, Berlin, 10115 Germany

Received October 4, 2000

Abstract—Three crystalline $[\text{N}(\text{CH}_3)_4](\text{HSeO}_4)$ modifications are studied by X-ray diffraction method at 298, 363, and 380 K. The high-temperature phases are characterized by disordering of HSeO_4 -tetrahedra. The systems of hydrogen bonds and the mechanism of the phase transitions are considered. © 2001 MAIK "Nauka/Interperiodica".

INTRODUCTION

The compounds described by the general formula MHXO_4 , where $M = \text{Rb}, \text{Cs}, \text{NH}_4, \text{N}(\text{CH}_3)_4$ and $X = \text{S}, \text{Se}$, have intensely been studied since the discovery of phase transitions into the state with high protonic conductivity [1]. High protonic conductivity in the tetramethylammonium hydrogen sulfate (TMSO) above 175°C [2] indicates a possible existence of the superionic phase also in tetramethylammonium hydrogen selenate. Tetramethylammonium hydrogen sulfate has three crystalline modifications which were studied at room temperature and at 215 and 175 K [3].

Below we present the results of the X-ray diffraction study of the three modifications of the tetramethylammonium hydrogen selenate (two high-temperature ones and the modification existing at room temperature).

EXPERIMENTAL

The tetramethylammonium hydrogen selenate $[\text{N}(\text{CH}_3)_4]\text{HSeO}_4$ (TMSeO) was synthesized by the reaction of the 20% aqueous solution of tetramethylammonium hydroxide with 25% excess of 70% selenic acid. Prismatic rhombic crystals were grown by slow evaporation of water. The differential thermal analysis (DTA) on a Netzsch STA-429 thermal analyzer in the temperature range 25–200°C revealed three peaks of endothermic effects at 81, 98, and 124°C (Fig. 1). The latter peak corresponds to the unidentified phase transition. The pronounced endothermic effect at $98 \pm 1^\circ\text{C}$ was shown to be reversible and is characterized by a small hysteresis of the reverse phase transition at $94 \pm 1^\circ\text{C}$ (Fig. 1a). A very weak endothermic effect observed during heating at $81 \pm 1^\circ\text{C}$ showed no corresponding exothermic effect during cooling. Thus, the sequence of phase transitions can be represented by the following scheme: III $\xrightleftharpoons{81^\circ}$ II $\xrightleftharpoons[94^\circ]{98^\circ}$ I $\xrightarrow{124^\circ}$ unidentified phase

(phases), where III is the TMSeO phase at room temperature.

The X-ray diffraction experiment on TMSeO crystals (phase III) was performed on an Enraf-Nonius CAD-4 diffractometer at room temperature and on crystals of phases II and I on a Stoe IPDS diffractometer at temperatures of 90 ± 3 and $107 \pm 3^\circ\text{C}$, respectively. In the latter case, the specimens were heated by an Enraf-Nonius FR-559 high-temperature attachment. The absorption correction for phase III was introduced using the results of the ψ -scanning of five reflections. The diffraction data for phases II and I were corrected by the numerical absorption method based on real crystal shape.

All the structures were solved by direct methods using the SHELXL97 program [4]. The positions of non-hydrogen atoms were refined in the anisotropic approximation by the SHELXS97 program [5]. All the hydrogen atoms in phase III and only the hydrogen atom in the HSeO_4 group in phase II were refined in the isotropic approximation. Hydrogen atoms of the methyl groups in phases I and II were considered with due regard for the geometry of the CH_3 groups. It was found that hydrogen atoms in one of the tetramethylammonium groups in phase I are disordered over two positions.

The choice of the space group from two possible— $C2$ and $C2/m$ —is rather difficult. In particular, the statistical criterion based on $|E^2 - 1|$ indicated the absence of the center of inversion. The sp. gr. $C2/m$ was chosen for phase II for following reasons: the R -factor was lower despite the fact that the number of the parameters to be refined was twice as low; the geometry of disordered HSeO_4 groups was closer to tetrahedral; the anisotropy of thermal vibrations of oxygen atoms seemed to be more reasonable (in the sp. gr. $C2$, some oxygen atoms showed pronounced anisotropy of ther-

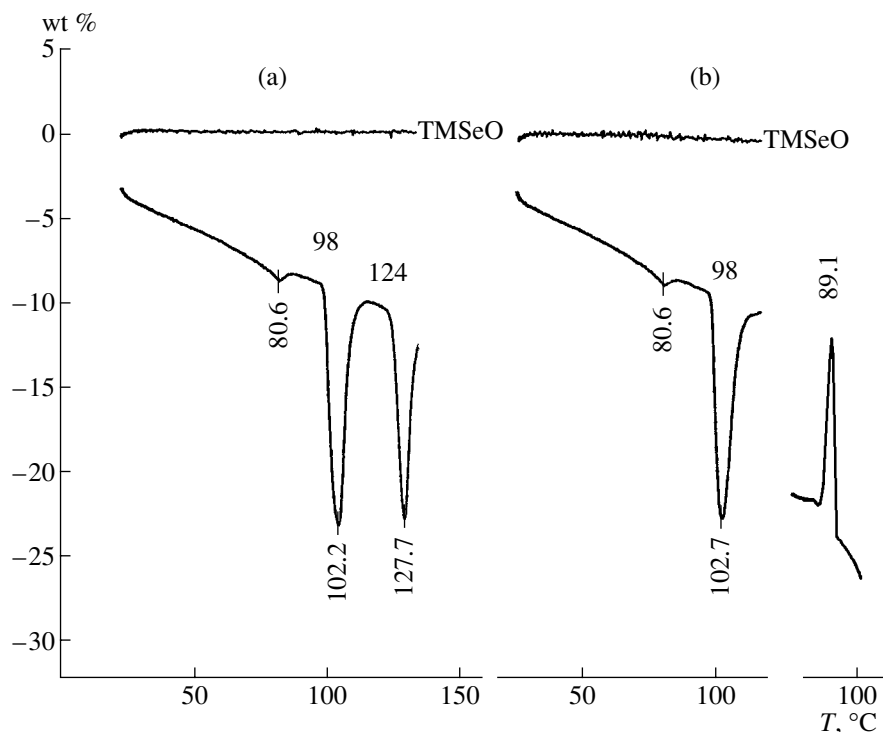


Fig. 1. DTA and thermogravimetric data for TMSeO: (a) three peaks of endothermic effect under heating at 81 (III \rightarrow II), 98 (II \rightarrow I), and 124°C (phase transition) and (b) two points of the endothermic effect under heating up to 115°C and a portion of the DTA curve obtained during specimen cooling. The temperatures of the beginning of the manifestation of the thermal effect are considered to be the temperatures of the phase transitions. The maximum temperatures of thermal effects are also indicated.

mal vibrations); and HSeO_4 -tetrahedra in the calculations within the sp. gr. $C2$ statistically occupied two positions with almost equal occupancies.

The crystallographic characteristics of all the three modifications and the corresponding parameters of the X-ray diffraction experiments are listed in table. The atomic positional and thermal parameters for the structures of the three TMSeO modifications are deposited in the Cambridge Structural Database (CCDC 157 404, CCDC 157 405, and CCDC 157 406 for modifications I, II, and III, respectively).

RESULTS AND DISCUSSION

Structure of phase III. Crystal structure of phase III consists of tetrahedral tetramethylammonium cations and HSeO_4 -tetrahedra (anions). One Se–O distance, is longer by ~ 0.1 Å (Se–O(4) 1.725(3) Å) than all the other Se–O distances (1.603–1.614 Å), which is explained by the participation of the O(4) atom as a donor in hydrogen bonding. Hydrogen bonds O(4)–H(1)···O(1) 2.673(5) Å connect HSeO_4 -tetrahedra into closed centrosymmetric dimers (Fig. 2) similar to those in the NaHSeO_4 [6] and KHSeO_4 [7] structures. The latter compound, unlike III and NaHSeO_4 , in addition to closed dimers, also has chains of the HSeO_4 tetrahedra. The structure of phase III of TMSeO considerably differs from the orthorhombic TMSO (sp. gr. $Pna2_1$) crys-

tallized at room temperature [3] because HSO_4 -tetrahedra are disordered over two positions and are linked by hydrogen bonds into infinite chains along b -axis. One more characteristic feature of the room temperature TMSeO phase is its stability in air, whereas TMSO phase is highly hygroscopic [3].

Structure of phase II. When studying phase II, we also considered the sp. gr. $C2$. Similar to phase III, the structure of phase II consists of the $[\text{N}(\text{CH}_3)_4]^+$ and HSeO_4^- -tetrahedra. The N-atom occupies the $4h$ position on the axis 2. The oxygen atoms of the HSeO_4 -tetrahedron are disordered over two positions with the occupancy 0.5. Two HSeO_4 tetrahedra are related by the mirror plane (Fig. 3). It is interesting that the H atom at the selenate ion, localized from difference Fourier maps, lies, in fact, in this plane (i.e., is almost ordered), while the O(4) atom, the hydrogen donor, is located at a very small distance (about 0.1 Å) outside this plane. The Se–O distances in the tetrahedron are different, which is explained by pronounced thermal vibrations of O and Se atoms. Two too short Se–O(1) and Se–O(3) distances (1.523 and 1.557 Å) were corrected for libration by the method described in [8] to yield 1.556 to 1.596 Å, respectively. Of two remaining distances, only the Se–O(4) 1.683 Å distance it approximately corresponds to the distance for an oxygen atom involved in hydrogen bonding as a donor and, thus, requires no considerable correction. The correc-

Crystallographic characteristics and parameters of X-ray diffraction experiment for phases I–III

	III	II	I
Temperature, K	293(2)	363(3)	380(3)
Crystal system	Monoclinic	Monoclinic	Tetragonal
Sp. gr.	$P2_1/c$	$C2/m$	$I\bar{4}2m$
a , Å	5.601(3)	10.918(3)	11.460(3)
b , Å	13.663(2)	13.669(3)	
c , Å	10.760(2)	5.665(2)	13.635(3)
β , deg	90.83(3)	90.92(3)	90
V , Å ³ ; Z	823.3(5); 4	845.3(4); 4	1790.7(8); 8
ρ_{calc} , g/cm ³	1.760	1.746	1.618
μ (MoK α), mm ⁻¹	4.525	4.408	4.161
Crystal dimensions, mm	0.2 × 0.2 × 1.0	0.15 × 0.3 × 0.4	0.15 × 0.3 × 0.4
Range of angles θ , deg	2–32	2–26	2–26
The number of the reflections (measured/crystallographically nonequivalent)	2972/2844	3952/848	4211/938
The number of reflections with $I > 2\sigma(I)$	1632	676	567
Absorption correction	ψ -scanning	By crystal shape	By crystal shape
The number of reflections/parameters used in the least-squares procedure	2034/144	734/72	775/82
Extinction correction	0.008(3)	0.014(3)	0.008(2)
$GOF(F^2)$	1.036	1.093	1.029
R_1	0.0415	0.0246	0.0402
wR_2	0.0985	0.0588	0.0960
Residual electron density (max; min), e Å ⁻³	1.144; -1.215	0.232; -0.488	0.401; -0.399

tion for libration yields 1.711 Å, i.e., makes this distance even closer to the values 1.69–1.72 Å characteristic of the Se–OH distances in the ordered structures with the weak atomic vibrations [9]. The Se–O(2) distance equal to 1.754 Å seems to be overestimated. The amplitudes of the Se vibrations parallel to the Se–O bonds are approximately equal to 0.2 Å for the bonds with O(1), O(3), and O(4) atoms, while the amplitude for the bond with the O(2) atom is by 0.1 Å larger. Most likely that the Se–O(2) distance must be shorter by the same value, i.e., to be about 1.65 Å. The tetrahedra form disordered closed dimers via the hydrogen O(4)–H···O(3)' 2.711(8) Å and O(4)–H···O(3)" 2.665(7) Å (Fig. 3).

The structure of phase I. The structure of phase I is built by $[N(CH_3)_4]^+$ tetrahedra and highly disordered tetrahedral selenate anions. Two symmetrically independent nitrogen atoms, N(1) and N(2) occupy the $4e$ and $4d$ positions with the symmetries $2mm$ and $\bar{4}$, respectively. Similar to most oxygen atoms (except O(11) and O(21) in the general positions), selenium atoms occupy the $8i$ positions, i.e., the positions in the diagonal m planes. The $HSeO_4$ -tetrahedra are disordered

over two positions with the occupancy 0.5. Because of pronounced thermal vibrations, the Se–O distances show considerable scatter. Correction for libration introduced according to [8] “improves” these distances. Thus, the distances Se–O(11) 1.56(1) Å and Se–O(21) 1.51(2) Å become equal to 1.67 and 1.68 Å, respectively. This elongation is quite clear if one takes into account the participation of the O(11) and O(21) atoms in hydrogen bonding. The Se–O distances for O(13) and O(23) atoms not participating in hydrogen bonding are much shorter, 1.58 and 1.62 Å, respectively (with the allowance for libration). A somewhat larger Se–O(12) distance (1.70 Å) can be explained by anisotropy of thermal vibrations of the Se atom, as was made earlier for the phase II.

It is worth noting that we revealed some additional electron-density peaks at the distances of 1.5–1.6 Å around Se atoms on electron-density maps. All these peaks corresponded to the occupancies of O atoms not exceeding several percent and, therefore, were ignored. We believe that the presence of these peaks reflects a more complex character of the disorder of $HSeO_4$ tetrahedra, than their location over two positions.

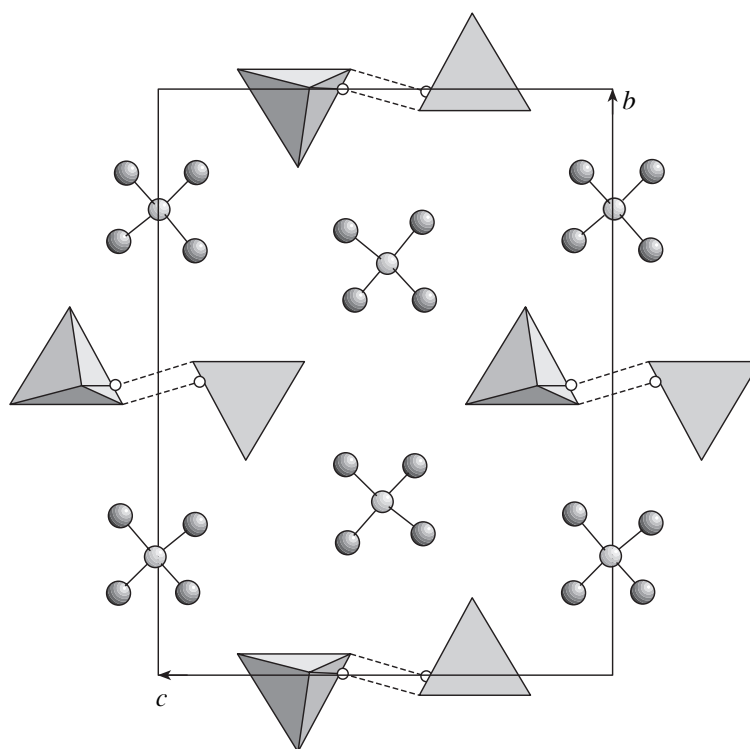


Fig. 2. Structure of TMSeO at room temperature. The ordered HSeO₄-tetrahedra form closed dimers.

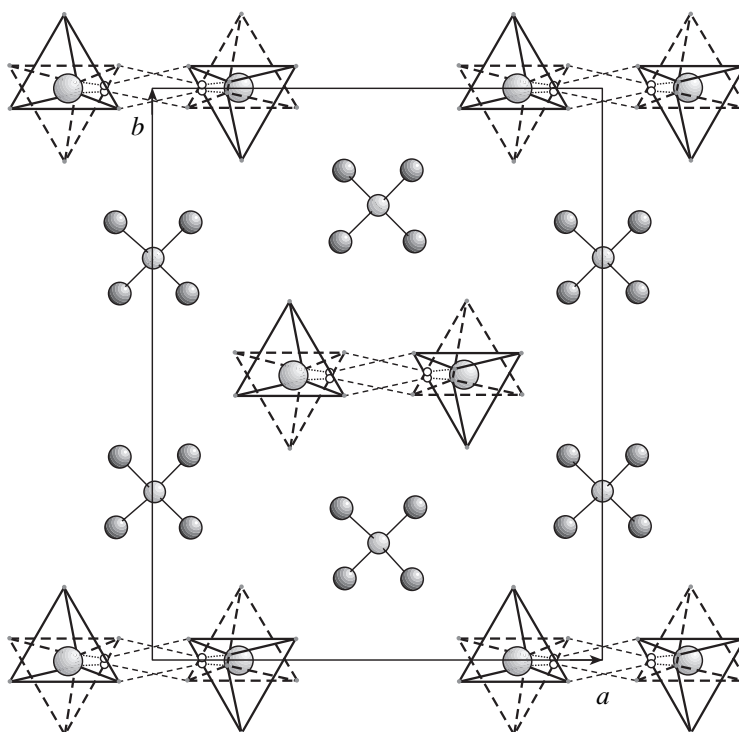


Fig. 3. Projection of the TMSeO-II structure onto the *xy*0 plane; HSeO₄-tetrahedra are disordered over two positions; the closed dimers are preserved.

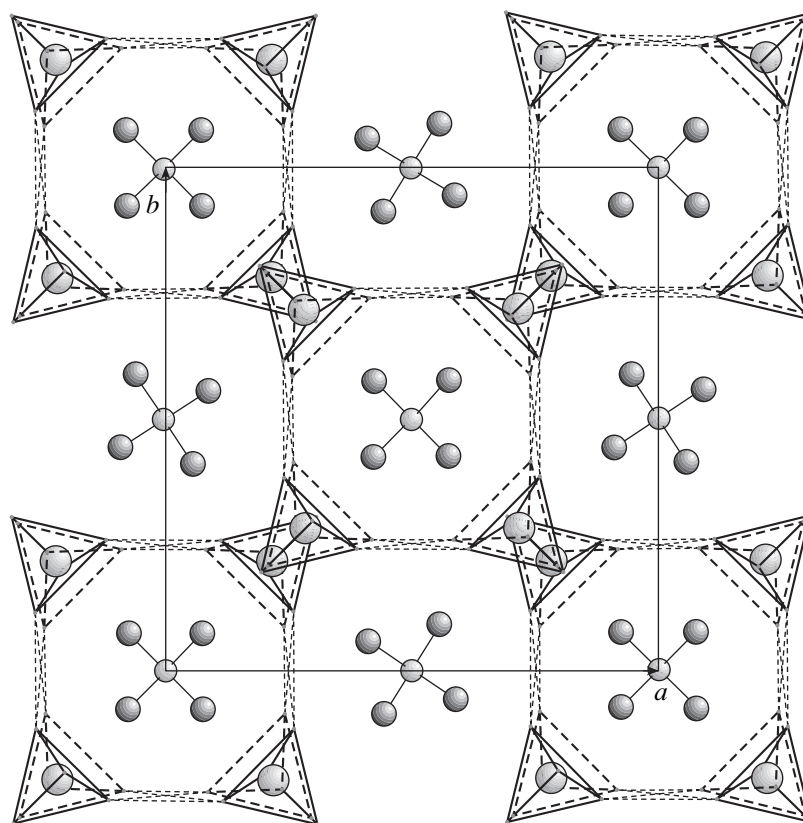


Fig. 4. Projection of the TMSeO-I structure onto the $xy0$ plane; HSeO_4 -tetrahedra are disordered over two positions and form cyclic tetramers with the $\bar{4}2m$ symmetry.

The probable system of hydrogen bonds is built by cyclic tetramers with the symmetry $\bar{4}2m$ (Fig. 4). The following hydrogen bonds are possible: $\text{O}(11)\cdots\text{O}(11)'$ 2.51(3) Å, two $\text{O}(11)\cdots\text{O}(21)$ 2.35(3) Å, and $\text{O}(21)\cdots\text{O}(21)'$ 2.67(7) Å. It seems that the hydrogen atom should be statistically distributed over four positions.

Phase transition III \rightarrow II. This phase transformation does not change the unit cell volume. The primitive unit cell is transformed into the base-centered one (or side-centered one, *A*, in the coordinate system of phase III). In the transition to phase II, the $(\text{HSeO}_4)_2$ -dimers become disordered over two positions. These two positions are also present in structure III but are occupied by different dimers and are related by the 2_1 -axis (or the *c* plane). Presumably, the III–II transformation requires the overcoming of the activation barrier for the group transition from one position to another. The disordering process gives rise to the appearance of the (010) mirror plane (or the twofold axis along [010]) with the centering of the *A* face in phase III. The displacements of Se, N, and C atoms, necessary for the III–II transition do not exceed 0.1 Å which is consistent with a weak thermal effect in this phase transformation.

Phase transition II \rightarrow I. This transition is accompanied by doubling of the unit cell volume and disappearance of the center of inversion. The transition matrix was obtained from the matrices of crystal orientation prior to and upon the transformation:

$$\begin{pmatrix} 0 & 0 & -2 \\ -1 & 0 & 0 \\ 0 & 1 & 0 \end{pmatrix}.$$

The II–I transition is characterized by considerably more pronounced atomic displacements than the III–II transition, which is also reflected in the much higher value of the thermal effect. Thus, the displacement of selenium atoms along some directions amounts to about 1 Å. The distance between selenium atoms of the neighboring dimers in structure II (5.66 Å) increases to 6.59 Å, which corresponds to the distance between the Se atoms of the neighboring tetramers in phase I. The maximum displacement of N atoms is even greater—1.3 Å. Structure I loses the center of inversion since the Se atoms are displaced from the *m* plane, where they are located in structure II. Also, in this case the $\text{SeO}_{8/2}$ polyhedra (the tetrahedra disordered over two posi-

tions) are slightly rotated so that the neighboring polyhedra are tilted in opposite directions (Fig. 4).

It is important to indicate that the II–I transition is somewhat similar to the phase transition of CsHXO_4 ($X = \text{S}$ [10] or Se [11]) into the superprotonic state. Both transitions are characterized by atomic displacements and disordering of oxygen atoms having high values of thermal parameters. This, in turn, leads to disordering of hydrogen atoms over several positions. In both cases, the transition is accompanied by the transformation of the monoclinic unit cell into the tetragonal body-centered cell. All the above facts suggest a high protonic conductivity of the TMSO-I phase. The structures of the high-temperature phases of the compounds are slightly different. The structure of phase I of CsHXO_4 has a system of hydrogen bonds providing the formation of infinite layers of tetrahedra perpendicular to the c -axis, whereas the structure of phase I of $[\text{N}(\text{CH}_3)_4](\text{HSeO}_4)$ is characterized by the presence of closed tetramers. The rigorous localization of hydrogen atoms in the high-temperature phase I of tetramethylammonium hydrogen selenate requires the neutron diffraction study. To verify our assumption about high protonic conductivity of the latter phase, a number of physical measurements on single crystal specimens are planned in the near future.

ACKNOWLEDGMENTS

The authors are grateful to Dr. M. Feist for performing the DTA measurements.

REFERENCES

1. A. I. Baranov, L. A. Shuvalov, and N. M. Shchagina, *Pis'ma Zh. Éksp. Teor. Fiz.* **36**, 381 (1982) [*JETP Lett.* **36**, 459 (1982)].
2. R. Blinc, G. Lahajnar, I. Zupančič, and H. Arend, *Solid State Commun.* **51**, 751 (1984).
3. N. L. Speziali and G. Chapuis, *Acta Crystallogr., Sect. B: Struct. Sci.* **47**, 757 (1991).
4. G. M. Sheldrick, *SHELXS97: The Program for the Crystal Structure Solution* (Univ. of Göttingen, Göttingen, 1997).
5. G. M. Sheldrick, *SHELXL97: The Program for the Crystal Structure Refinement* (Univ. of Göttingen, Göttingen, 1997).
6. M. A. Zakharov, S. I. Troyanov, V. B. Rybakov, *et al.*, *Kristallografiya* **44** (3), 448 (1999) [*Crystallogr. Rep.* **44**, 408 (1999)].
7. J. Baran and T. Lis, *Acta Crystallogr., Sect. C: Cryst. Struct. Commun.* **42**, 270 (1986).
8. V. Schomaker and K. N. Trueblood, *Acta Crystallogr., Sect. B: Struct. Crystallogr. Cryst. Chem.* **B24**, 63 (1968).
9. E. Kemnitz and S. I. Troyanov, in *Advances in Molecular Structure Research* (JAI Press, Greenwich, 1998), Vol. 4, p. 79.
10. A. V. Belushkin, W. I. F. David, R. M. Ibberson, and L. A. Shuvalov, *Acta Crystallogr., Sect. B: Struct. Sci.* **47**, 166 (1991).
11. M. A. Zakharov, S. I. Troyanov, and E. Kemnitz, *Z. Kristallogr.* **216**, 172 (2001).

Translated by A. Zolot'ko

STRUCTURE
OF ORGANIC COMPOUNDS

Molecular and Crystal Structures of Chiral
2-(4-Phenylbenzylidene)-3-Methyl-6-Isopropylcyclohexanone
6-Bromo Derivative

A. S. Tolochko*, V. I. Kulishov*, L. A. Kutulya**,
V. P. Kuznetsov**, and V. V. Vashchenko**

* Institute of Physics, National Academy of Sciences of Ukraine, pr. Nauki 46, Kiev, 03039 Ukraine

** Institute for Single Crystals, National Academy of Sciences of Ukraine, pr. Lenina 60, Kharkov, 61001 Ukraine

e-mail: tolochko@iop.kiev.ua

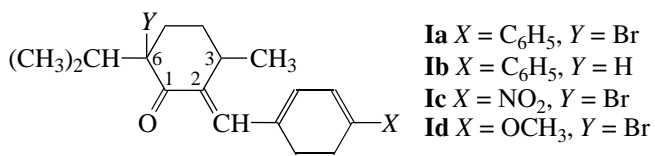
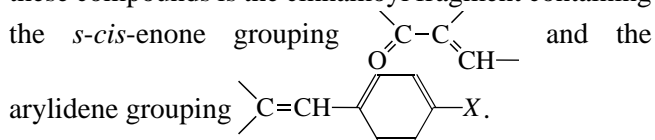
Received June 6, 2000; in final form, May 16, 2001

Abstract—The molecular and crystal structures of chiral 3*R*,6*S*-2-(4-phenylbenzylidene)-3-methyl-6-bromo-6-isopropylcyclohexanone C₂₃H₂₅BrO (**Ia**) are determined by X-ray diffraction. Crystals **Ia** are monoclinic, $a = 11.005(4)$ Å, $b = 12.229(4)$ Å, $c = 14.376(5)$ Å, $\beta = 91.37(1)^\circ$, $Z = 4$, and space group $P2_1$. The geometric parameters of two crystallographically independent molecules are close to each other in magnitude. The cyclohexanone ring adopts a chair-type conformation with an equatorial isopropyl substituent and an axial orientation of the methyl group and the C–Br bond. The 3,6-alkyl groups are in the *cis* position with respect to the cyclohexanone ring. It is demonstrated that, in the series of 6-bromo substituted compounds, as in their analogues unsubstituted for bromine in the 6-position, the maximum flattening of the cinnamoyl fragment O=C=C–C₆H₄X is observed in the structure with X = C₆H₅. © 2001 MAIK “Nauka/Interperiodica”.

INTRODUCTION

2-Arylidene derivatives of 3-methyl-6-isopropylcyclohexanone (1*R*,4*R*-*cis*-2-arylidene-*p*-menthan-3-ones) (**I**) have attracted the particular attention of researchers, because they can serve as efficient chiral dopants to liquid-crystal systems with induced helical ordering [1–3]. This has lent impetus to the investigation into their molecular and crystal structures [4–8].

The most important structural unit in molecules of these compounds is the cinnamoyl fragment containing the *s-cis*-enone grouping



According to X-ray structure analysis [7], the geometry of the cinnamoyl fragment in molecules **I** (primarily, the degree of nonplanarity of its particular groupings) is determined, to a large measure, by the intramolecular electron interaction of the electron-acceptor carbonyl group and the substituent X. For the compound with a strong electron-donor dimethylamino group [X =

N(CH₃)₂, Y = H], the twisting of the enone and arylidene fragments is relatively small (the torsion angles are equal to 20.2° and 23.2°, respectively) [7]. In structures with the electron-acceptor substituents, the torsion angles are substantially larger and are equal, respectively, to 38.5° and 42.7° in the chloro substituted compound [4] and 42.0° and 42.4° in the compound with X = NO₂ [7]. In this case, the torsion angles are virtually independent of the electron-acceptor power of substituent X [4, 7]. Correspondingly, the conformation of the cyclohexanone ring changes from the half-chair type for the compound with X = N(CH₃)₂ to the chair type for structures with electron-acceptor substituents X.

The unexpected feature was revealed in the structure of the compound with X = C₆H₅ [8]. Although the phenyl group is not a strong electron-donor substituent, the enone and benzylidene groupings in this structure exhibit a substantial flattening (the torsion angles are equal to 13.0° and 4.9°, respectively) as compared to that in the dimethylamino substituted compound. In [8], it was assumed that the observed effect is associated with the intermolecular π -electron interaction in the crystal. In this respect, it was of interest to examine the structures of other compounds of this class with the biphenyl fragment.

The main purpose of the present work was to investigate the molecular and crystal structures of compound **Ia** containing the biphenyl grouping (X = C₆H₅) and the

bulky substituent $Y = \text{Br}$ in the 6-position of the cyclohexanone fragment and to compare the spatial structures of compound **1a** and its analogues **1b–1d**, which were studied earlier in [5, 8].

EXPERIMENTAL

Compound **1a** was synthesized according to the procedure described in [9]. Single crystals suitable for X-ray diffraction analysis were grown from acetonitrile. Crystals **1a** were obtained in the form of yellow prisms. A single crystal $0.3 \times 0.4 \times 0.6$ mm in size was chosen for X-ray structure analysis. The crystals are monoclinic, $a = 11.005(4)$ Å, $b = 12.229(4)$ Å, $c = 14.376(5)$ Å, $\beta = 91.37(1)^\circ$, $V = 1934.2(11)$ Å³, $M = 397.3$ (C₂₃H₂₅BrO), space group $P2_1$, $Z = 4$, $d_{\text{calcd}} = 1.365$ g/cm³, and $\mu(\text{MoK}\alpha) = 2.133$ mm⁻¹.

The X-ray diffraction data were collected on a Siemens P3/PC automated diffractometer (MoK α radiation, graphite monochromator, $\theta/2\theta$ scan mode, $2\theta_{\text{max}} = 50^\circ$).

The intensities of 1744 reflections were measured in the hkl index ranges $0 < h < 11$, $0 < k < 13$, $-15 < l < 16$. After averaging of equivalent reflections, the final data set included 1641 independent reflections ($R_{\text{int}} = 0.0241$), which were used in further calculations. No absorption correction was introduced.

The structure was solved by the direct method. The hydrogen atoms were located from successive electron-density difference syntheses. The absolute configuration was determined from the known R configuration of the C(3) chiral center.

The refinement of the structure was performed by the full-matrix least-squares method in the anisotropic approximation for the non-hydrogen atoms (the coordinates of hydrogen atoms were refined using a riding-atom model with the fixed thermal parameters $U_{\text{iso}} = 0.08$ Å²). The isotropic extinction coefficient g was equal to 0.00013(6). The absolute structure parameter was $\chi = 0.87(7)$. The final discrepancy factors were as follows: $R1 = 0.0517$, $wR2 = 0.0512$, and $GOOF = 1.95$.

Table 1. Coordinates of non-hydrogen atoms ($\times 10^4$) and equivalent isotropic thermal parameters B_{eq} (Å²) for structure **1a** (independent molecules are designated as M and M')

Atom	M				M'			
	x/a	y/b	z/c	$B_{\text{eq}}, \text{Å}^2$	x/a	y/b	z/c	$B_{\text{eq}}, \text{Å}^2$
Br(1)	-1399(1)	8343(2)	9418(1)	5.5(1)	-11220(2)	11037(2)	5567(1)	7.3(1)
O(1)	-1478(9)	8466(9)	10166(6)	6.8(4)	-8455(9)	11080(10)	4824(8)	8.2(5)
C(1)	-961(13)	7810(12)	9646(9)	4.6(5)	-8867(12)	10405(11)	5327(10)	4.5(5)
C(2)	-1476(11)	7516(11)	8724(8)	3.5(5)	-8287(11)	10112(11)	6266(8)	3.6(5)
C(3)	-1139(10)	6411(9)	8317(9)	3.1(4)	-8646(11)	9064(11)	6723(8)	3.9(5)
C(4)	-157(12)	6108(14)	8598(9)	5.0(5)	-9984(12)	8833(11)	6600(8)	4.5(5)
C(5)	-449(12)	6165(12)	9625(8)	4.6(5)	-10398(12)	8837(11)	5572(8)	4.6(5)
C(6)	-263(12)	7295(10)	10027(10)	4.8(5)	-10106(11)	9861(10)	5053(7)	3.3(4)
C(7)	-2247(10)	8222(12)	8338(8)	3.8(4)	-7457(12)	10818(10)	6597(8)	3.8(5)
C(8)	-2920(10)	8249(11)	7451(9)	3.5(4)	-6716(10)	10817(10)	7449(9)	3.1(5)
C(9)	-3091(12)	7355(10)	6842(9)	4.0(5)	-6493(13)	9927(12)	7984(12)	5.2(6)
C(10)	-3721(12)	7462(10)	6036(9)	3.5(5)	-5821(12)	9985(10)	8812(10)	4.0(5)
C(11)	-4248(11)	8415(13)	5733(9)	4.5(5)	-5446(10)	10999(13)	9155(9)	4.2(5)
C(12)	-4135(12)	9287(13)	6315(10)	4.7(6)	-5683(14)	11943(14)	8589(10)	6.0(6)
C(13)	-3457(13)	9219(10)	7152(8)	4.0(5)	-6308(12)	11818(12)	7742(10)	4.9(5)
C(14)	-2017(13)	5555(11)	8678(10)	5.3(5)	-7884(14)	8119(14)	6382(12)	7.2(7)
C(15)	-434(13)	7395(13)	11090(9)	5.3(5)	-10290(12)	9831(11)	4024(8)	4.2(5)
C(16)	-534(15)	6729(15)	11548(11)	7.9(7)	-9404(17)	9108(14)	3576(10)	7.7(7)
C(17)	-1654(15)	7035(15)	11388(10)	6.8(7)	-11570(17)	9449(15)	3712(12)	8.6(8)
C(18)	-4931(11)	8550(15)	4796(9)	5.2(6)	-4795(11)	11073(10)	10054(9)	3.4(4)
C(19)	-4875(13)	9485(12)	4297(10)	5.0(6)	-4985(12)	11921(10)	10667(9)	4.0(5)
C(20)	-5462(14)	9503(14)	3432(13)	6.4(7)	-4450(15)	11960(13)	11537(11)	6.1(6)
C(21)	-6067(13)	8632(12)	3052(10)	5.2(6)	-3632(12)	11101(14)	11767(9)	4.6(5)
C(22)	-6169(12)	7713(11)	3622(10)	4.5(5)	-3435(14)	10274(12)	11221(12)	5.4(6)
C(23)	-5557(8)	7660(14)	4488(12)	6.2(7)	-3995(13)	10242(11)	10371(10)	4.9(6)

The structural calculations were performed using the SHELXTL PLUS/PC software package [10]. The coordinates of non-hydrogen atoms are listed in Table 1.

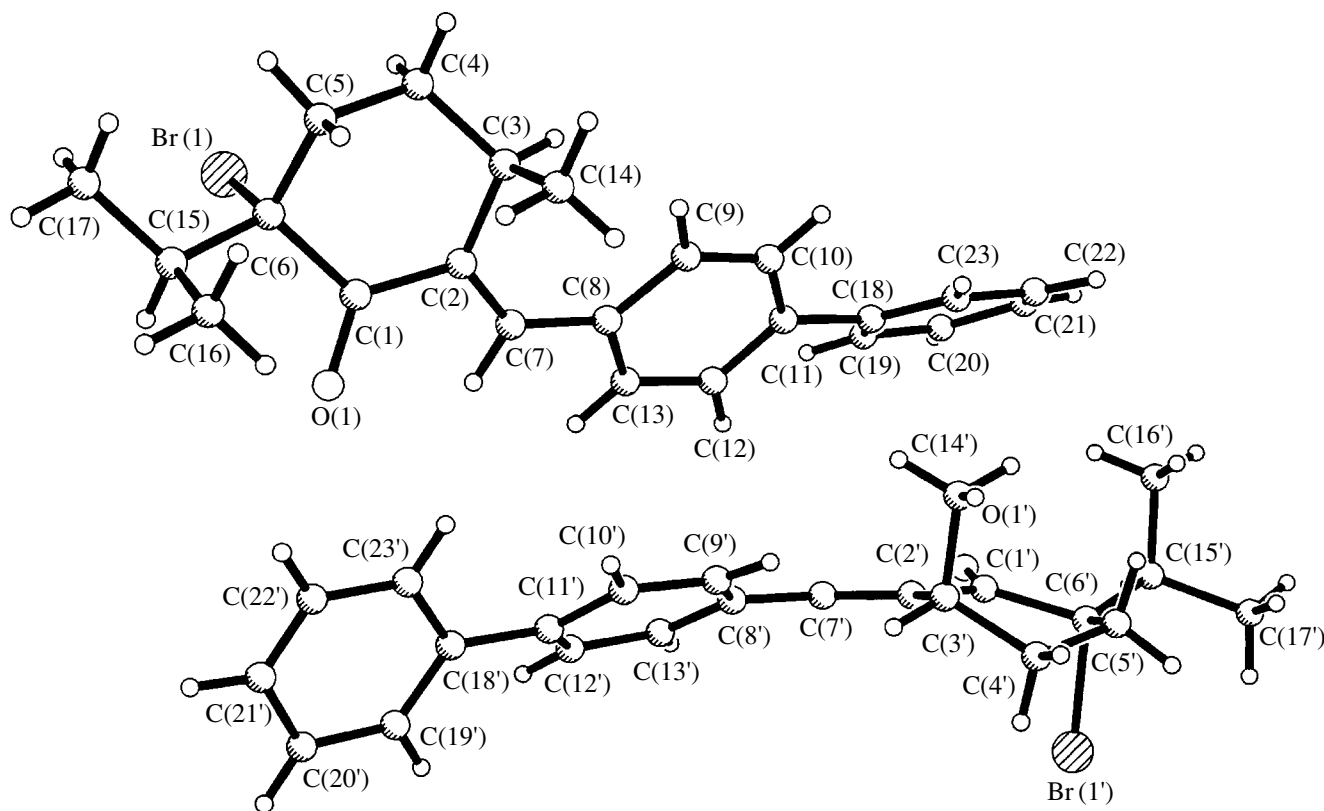
RESULTS AND DISCUSSION

In structure **Ia**, the unit cell involves two crystallographically independent molecules *M* and *M'* with about the same geometric parameters.

As in the earlier-studied structures **Ib–Id** [5, 8], both crystallographically independent molecules of compound **Ia** are characterized by the *cis* orientation of the alkyl groups with respect to the cyclohexanone ring: the deviations of the C(14) and C(15) atoms (see figure) in the same direction from the root-mean-square planes passing through pairs of the C(2)–C(3) and C(5)–C(6) (the P_1 plane) [C(1)–C(6) and C(3)–C(4) (the P_2 plane)] opposite bonds in the cyclohexanone ring are equal, respectively, to 1.39 and 0.73 Å (1.53 and 0.80 Å) in molecule *M* and 1.42 and 0.81 Å (1.57 and 0.88 Å) in molecule *M'* (the error is ± 0.02 Å). These deviations indicate that the methyl group has an axial orientation and the isopropyl group position equatorial occupies the (see also the ϕ_1 – ϕ_4 torsion angles in Table 2).

The C–Br bond has an axial orientation (see the ϕ_5 and ϕ_6 torsion angles) and is in the *trans* position with respect to the methyl group in the cyclohexanone ring as judged from the deviations of the C(14) and Br atoms in opposite directions from the root-mean-square planes P_1 and P_2 in both independent molecules in the unit cell. For the Br atom, the magnitudes of these deviations are equal to 1.96 (1.94) ± 0.02 Å and 1.88 (1.93) ± 0.02 Å, respectively.

Note that compounds **Ia**, **Ic**, and **Id** were synthesized by bromination of the relevant substituted 3*R*,6*R*-2-(4-*X*-benzylidene)-3-methyl-6-isopropylcyclohexanones [9], during which the *R* configuration of the C(3) chiral center distant from the carbonyl group remains unchanged. This makes it possible to determine the absolute configuration of the molecule under investigation. The above X-ray diffraction data indicate the *cis* orientation of the alkyl substituents in the 3- and 6-positions. However, according to the Kahn–Ingold–Prelog rules [11], the configuration of the C(6) chiral center formally changes as a result of the substitution of the bromine atom for the hydrogen atom at this center. Consequently, the chiral compound **Ia** is 3*R*,6*S*-2-(4-phenylbenzylidene)-3-methyl-6-bromo-6-isopropylcyclohexanone. Its analogues **Ic** and **Id**, which were studied earlier in [5], also belong to the same series.

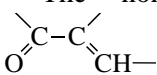


Structure of two crystallographically independent molecules of compound **Ia**.

Table 2. Selected bond angles (ω , deg), torsion angles (φ_i , deg), and puckering parameters in structures **Ia–Id**

Parameter	Structure			
	Ia *	Ib [8]	Ic [5]	Id [5]
Bond angles, ω				
ω_α ; C(3)C(2)C(7)	125.3(11); 125.6(11)	126.1(2)	127.7(7)	127.2(6)
ω_β ; C(2)C(7)C(8)	133.5(13); 131.6(12)	134.1(3)	129.6(7)	129.9(6)
ω_γ ; C(7)C(8)C(9)	125.6(12); 124.8(12)	127.3(2)	124.8(7)	125.9(5)
Torsion angles, φ_i				
φ_1 ; C(14)C(3)C(2)C(1)	86.3(2); 86.1(2)	92.5	76.1	81.1
φ_2 ; C(14)C(3)C(4)C(5)	-67.5(2); -70.0(2)	-70.0	-69.0	-68.7
φ_3 ; C(15)C(6)C(1)C(2)	-160.9(2); -155.7(2)	-159.4	-170.8	-167.7
φ_4 ; C(15)C(6)C(5)C(4)	174.8(1); 169.5(1)	177.1	174.7	176.8
φ_5 ; BrC(6)C(1)C(2)	85.0(2); 91.5(1)	-	78.2	81.7
φ_6 ; BrC(6)C(5)C(4)	-62.3(2); -70.4(1)	-	-65.7	-63.9
φ_7 ; O(1)C(1)C(2)C(7)	22.7(2); 14.9(2)	13.0	42.0	37.8
φ_8 ; C(2)C(7)C(8)C(9)	14.5(3); 18.5(3)	4.9	35.4	35.6
φ_9 ; C(10)C(11)C(18)C(23)	34.8(2); 33.4(2)	-40.2	-	-
φ_{10} ; C(12)C(11)C(18)C(19)	35.5(2); 39.8(2)	-43.0	-	-
φ_{11} ; C(1)C(2)C(3)C(4)	-34.3(2); -39.2(2)	-32.7	-44.6	-42.9
φ_{12} ; C(2)C(3)C(4)C(5)	52.3(2); 54.9(2)	53.4	51.9	53.1
φ_{13} ; C(3)C(4)C(5)C(6)	-59.7(2); -55.2(2)	-61.1	-52.3	-54.9
φ_{14} ; C(4)C(5)C(6)C(1)	43.8(2); 36.5(2)	46.2	43.2	42.9
φ_{15} ; C(5)C(6)C(1)C(2)	-28.6(2); -20.1(2)	-27.2	-37.1	-30.5
φ_{16} ; C(6)C(1)C(2)C(3)	24.9(2); 21.9(2)	20.8	39.3	32.3
Puckering parameters for the cyclohexanone ring				
θ , deg	16.38; 19.52	19.00	6.89	11.64
Ψ , deg	16.53; 3.41	19.66	5.55	0.10
S	0.88; 0.84	0.88	0.94	0.91

* Parameters are given for two independent molecules M and M' , respectively.

The nonplanarity of the enone grouping  in two independent molecules of the studied compound in the crystal differs significantly (see the φ_7 torsion angles in Table 2). The degree of nonplanarity in molecule M' is comparatively small and virtually does not differ from that in structure **Ib**. In molecule M , the nonplanarity of this fragment is more pronounced. The arylidene fragment in molecules M and M' of structure **Ia** is characterized by a substantial twisting (see the φ_8 torsion angles in Table 2), whereas this fragment in structure **Ib** is nearly planar. At the same time, the degree of nonplanarity (twisting) of the enone and arylidene fragments in both crystallographically independent molecules of structure **Ia** is appreciably less than that in structures **Ic** and **Id**: these fragments are intermediate in the degree of nonplanarity between the latter structures (**Ic** and **Id**) and structure **Ib**. Therefore, as in the earlier-studied compounds with

$Y = \text{H}$ [4, 7, 8], the $\text{O}=\text{C}-\text{C}=\text{C}-\text{C}_6\text{H}_4\text{X}$ cinnamoyl grouping in the series of their 6-bromo substituted analogues **Ia**, **Ic**, and **Id** shows a maximum flattening in the case of $X = \text{C}_6\text{H}_5$, i.e., in the structure involving the biphenyl fragment.

As regards the structure of the biphenyl grouping in the studied compound **Ia**, the degree of nonplanarity of its two benzene rings differs insignificantly for the crystallographically independent molecules M and M' and is only slightly smaller than that in structure **Ib** (see the φ_9 and φ_{10} torsion angles in Table 2).

It follows from the endocyclic torsion angles $\varphi_{11}-\varphi_{16}$ that the cyclohexanone ring in structure **Ia** adopts a chair conformation, which is substantially distorted, especially in molecule M' , as judged from the considerably decreased values of the φ_{15} and φ_{16} torsion angles. As in structure **Ib** [8], the conformation of the cyclohexanone ring is best described as a chair-1,4 [the C(2), C(3), C(5), and C(6) atoms in molecules M' and

Table 3. Selected intramolecular contacts (d , Å) in structures **Ia** and **Ib**

Contact	Structure		
	Ia		Ib [8]
	molecule M	molecule M'	
H(3)⋯H(9)	1.92	1.91	1.93
H(3)⋯C(9)	2.60	2.53	2.65
H(9)⋯C(3)	2.57	2.52	2.66
C(3)⋯C(9)	3.20(2)	3.13(2)	3.28
H(3)⋯C(7)	2.66	2.61	2.68
H(3)⋯C(8)	2.91	2.83	2.95
H(9)⋯H(14)	2.43	2.27	–
H(9)⋯C(14)	2.85	2.71	2.90
C(7)⋯C(14)	3.31(2)	3.35(2)	3.26
H(7)⋯H(13)	2.34	2.28	2.10
H(7)⋯O(1)	2.33	2.35	2.33

Note: The sums of the van der Waals radii are as follows [15]: H⋯H, 2.32 Å; H⋯C, 2.87 Å; H⋯O, 2.46 Å; and C⋯C, 3.42 Å.

M are coplanar to within 0.01 and 0.03 Å, respectively]. The tendency toward flattening of the C(3)C(2)C(1)C(6) fragment in the cyclohexanone ring (these atoms are coplanar to within 0.08 Å in molecules M and M') suggests that the conformation of the ring as a whole is intermediate between a chair-1,4 and a half-chair. This is also confirmed by the calculated puckering parameters [12, 13], which, at the same time, indicate that the cyclohexanone rings in molecules M and M' of structure **Ia** considerably differ in shape from each other (Table 2): the conformation of the cyclohexanone ring in molecule M is closely similar to that observed in structure **Ib**, whereas its conformation in molecule M' is noticeably different.

As in the case of structure **Ib** [8] and the other earlier-studied structures of 2-arylidene derivatives of cyclohexanone [14] and its chiral 3-methyl-6-isopropyl substituted compounds [4–7], the characteristic feature of structure **Ia** is a substantial distortion of the bond angles at the sp^2 carbon atoms in the $-C(3)HCH_3C(2)=C(7)HC_6H_4-$ fragment: the bond angles C(3)C(2)C(7) (ω_α), C(2)C(7)C(8) (ω_β), and C(7)C(8)C(9) (ω_γ) considerably exceed 120° (Table 2). The degree of distortion of the bond angles is virtually identical in molecules M and M' . It should be noted that there is a certain tendency to a weaker distortion of these bond angles in structure **Ia** as compared to that in structure **Ib**. For all the structures studied, the ω_β angle has a maximum value. The ω_β angle in compounds **Ia** and **Ib** is substantially larger than that in compounds **Ic** and **Id**, as well as in the other 2-arylidene-3-methyl-6-isopropylcyclohexanones investigated earlier in [4, 6, 7]. The data obtained are in close agreement with the infer-

ence made in [7] that the maximum distortion of the ω_β bond angle is observed in structures with a noticeably flattened arylidene grouping.

It is worth noting that the distortions of the above bond angles in structures **Ia**, **Ib** and **Ic**, **Id** differ in character (Table 2). In structures **Ia** and **Ib** (in which the arylidene fragment is substantially flattened and the conformation of the cyclohexanone ring is intermediate between a chair and a half-chair), the ω_β angle is maximum, whereas the distortion of the ω_α and ω_γ bond angles is appreciably less and virtually identical. In structures **Ic** and **Id**, the distortion of the ω_β angle is less pronounced compared to that in structures **Ia** and **Ib**, whereas the ω_α bond angle tends to increase. This can be associated with substantially different conformations of the cyclohexanone ring in these compounds [7]. Thus, the degree of nonplanarity of the enone and arylidene groupings, the conformation of the cyclohexanone ring, and the distortion of the bond angles at the sp^2 carbon atoms are interrelated in compounds of the structure type under investigation.

The steric strain of molecules **Ia** and **Ib** also manifests itself in the occurrence of intramolecular contacts between the atoms of the $>C(3)HCH_3$ fragment and the nearest benzene ring (Table 3), which can be considered shortened contacts [15].

CONCLUSION

It was demonstrated that structures **Ia** and **Ib** with the biphenyl fragments exhibit common features, namely, the similarity in both the structure of the cinnamoyl fragment and the conformation of the cyclohexanone ring in compounds **Ia** and **Ib** and other compounds of this class with strong electron-donor substituents (even though the biphenyl group does not belong to this type substituents). It was assumed that these features of the studied compounds are associated with the intermolecular interactions and the molecular packing in the crystal, which is characterized by the stacks formed by crystallographically independent molecules M and M' .

ACKNOWLEDGMENTS

This work was supported by the International Association of Assistance for the promotion of co-operation with scientists from the New Independent States of the former Soviet Union, project no. INTAS-1997-1730.

REFERENCES

1. L. A. Kutulya, I. B. Nemchenok, and T. V. Khandri-maïlova, *Kristallografiya* **35**, 1234 (1990) [*Sov. Phys. Crystallogr.* **35**, 724 (1990)].
2. L. A. Kutulya, I. B. Nemchenok, and S. S. Oleïnik, *Kristallografiya* **35**, 1242 (1990) [*Sov. Phys. Crystallogr.* **35**, 729 (1990)].

3. L. A. Kutulya, Proc. SPIE **3488**, 84 (1998).
4. V. I. Kulishov, L. A. Kutulya, V. E. Kuz'min, *et al.*, Zh. Obshch. Khim. **61** (1), 155 (1991).
5. L. A. Kutulya, V. P. Kuznetsov, E. E. Lakin, *et al.*, Kristallografiya **38**, 86 (1993) [Crystallogr. Rep. **38**, 630 (1993)].
6. L. A. Kutulya, V. V. Vashchenko, V. P. Kuznetsov, *et al.*, Kristallografiya **40**, 1015 (1995) [Crystallogr. Rep. **40**, 941 (1995)].
7. L. A. Kutulya, V. P. Kuznetsov, V. I. Kulishov, *et al.*, Kristallografiya **44**, 475 (1999) [Crystallogr. Rep. **44**, 435 (1999)].
8. A. S. Tolochko, V. I. Kulishov, L. A. Kutulya, *et al.*, Kristallografiya **46**, 254 (2001) [Crystallogr. Rep. **46**, 214 (2001)].
9. V. V. Vashchenko, V. V. Yurkova, L. A. Kutulya, and G. P. Semenkova, Ukraine Patent 17347A (1997).
10. G. M. Sheldrick, *SHELXTL PLUS, PC Version: A System of Computer Programs for the Determination of Crystal Structures from X-ray Diffraction Data, Rev. 4.2* (1992).
11. M. Nogradi, *Stereochemistry: Basic Concepts and Applications* (Akademiai Kiado, Budapest, 1981; Mir, Moscow, 1984).
12. N. S. Zefirov and V. I. Palyulin, Dokl. Akad. Nauk SSSR **252** (1), 111 (1980).
13. N. S. Zefirov, V. A. Palyulin, and E. E. Dashevskaya, J. Phys. Org. Chem. **3**, 147 (1990).
14. V. P. Kuznetsov, V. I. Kulishov, L. A. Kutulya, *et al.*, Kristallografiya **44**, 229 (1999) [Crystallogr. Rep. **44**, 196 (1999)].
15. Yu. V. Zefirov and P. M. Zorkii, Usp. Khim. **64**, 446 (1995).

Translated by O. Borovik-Romanova

STRUCTURE
OF ORGANIC COMPOUNDS

**X-ray Mapping in Heterocyclic Design:
V. Diffractometric Study of the Crystal Structure
of 2-Hydroxy-3-Trifluoroacetylimidazo[1,2-*a*]pyridine
Hydrochloride at 180 K**

V. B. Rybakov, S. I. Troyanov, E. V. Babaev, O. S. Mazina, and L. A. Aslanov

Chemistry Department, Moscow State University, Vorob'evy gory, Moscow, 119899 Russia

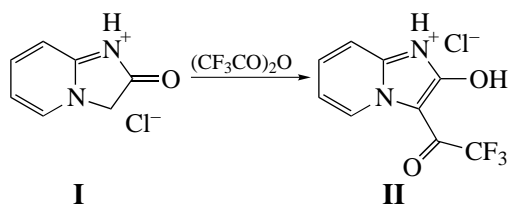
e-mail: rybakov@biocryst.phys.msu.su

Received November 23, 2000

Abstract—The crystal structure of 2-hydroxy-3-trifluoroacetylimidazo[1,2-*a*]pyridine hydrochloride $C_9H_6F_3ClN_2O_2$ is determined by X-ray diffraction at 180 K. The structure is solved by the direct method and refined by the least-squares procedure to $R = 0.0296$. The alternation of bond lengths in the six-membered fragment of the molecule is observed. One of the specific features of the crystal structure is the formation of a system of the $N-H\cdots Cl^-$ ($N\cdots Cl$, 3.09 Å; $N-H$, 0.83 Å; $H\cdots Cl$, 2.33 Å; and $N-H\cdots Cl$, 153°) and $O-H\cdots Cl^-$ ($O\cdots Cl$, 2.87 Å; $O-H$, 0.95 Å; $H\cdots Cl$, 1.92 Å; and $O-H\cdots Cl$, 178°) hydrogen bonds in which the chlorine atoms are related to the reference atom by different symmetry transformations. © 2001 MAIK "Nauka/Interperiodica".

INTRODUCTION

This work continues the series of our investigations of heterocyclic compounds that are able to enter into the reactions of cyclization and ring transformation [1–8]. Earlier [6], we described the structure of 2-oxo-2,3-dihydroimidazo[1,2-*a*]pyridine hydrochloride $C_7H_7ClN_2O$ (**I**). This salt was used as a starting substance for preparation of 2-hydroxy-3-trifluoroacetylimidazo[1,2-*a*]pyridine hydrochloride $C_9H_6F_3ClN_2O_2$ (**II**). Compound **II** was prepared by the reaction between **I** and trifluoroacetic anhydride



Colorless crystals of the prismatic habit precipitated in the reaction vessel. The crystals removed from the mother liquor cracked within 30 s. Because of the high volatility of trifluoroacetic anhydride, the X-ray-quality crystals were chosen under the flow of cooled nitrogen with a binocular microscope in polarized light.

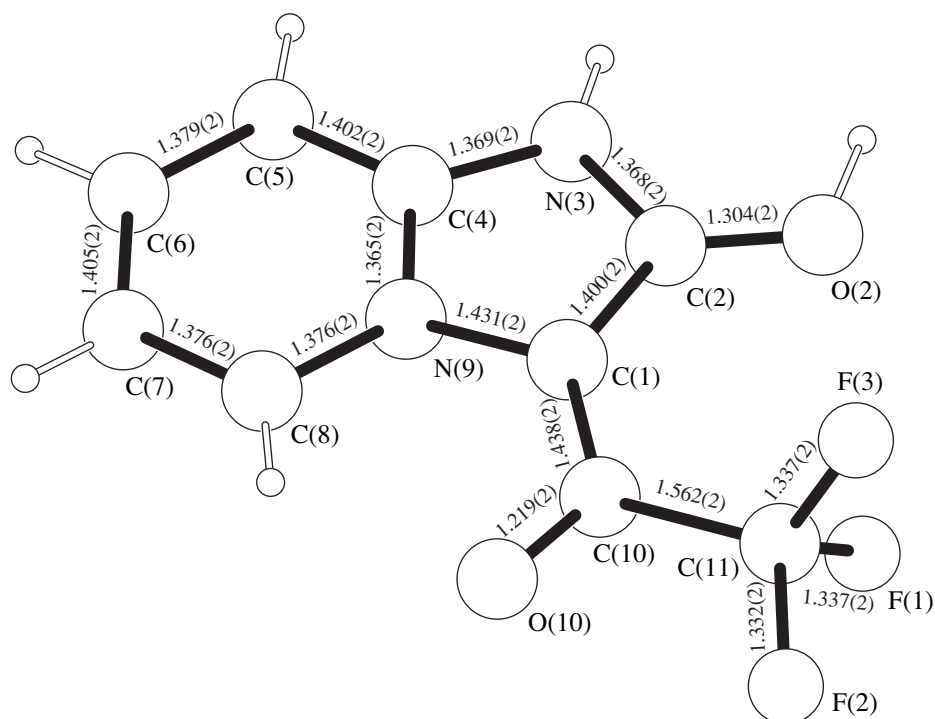
According to the data of the Cambridge Structural Database [9], the X-ray structure analysis of **II** has not been performed.

EXPERIMENTAL

Crystals of compound **II** are monoclinic. The unit cell parameters were determined and refined at

Coordinates ($\times 10^4$) and equivalent isotropic thermal parameters U_{eq}/U_{iso} ($\text{Å}^2 \times 10^3$) for molecule **II**

Atom	<i>x</i>	<i>y</i>	<i>z</i>	U_{eq}/U_{iso}
Cl	4755(1)	1286(1)	1458(1)	31(1)
C(1)	3540(1)	4336(3)	2447(1)	20(1)
C(2)	3885(1)	6417(3)	2227(1)	20(1)
O(2)	3887(1)	7359(2)	1538(1)	25(1)
N(3)	4231(1)	7391(2)	2873(1)	21(1)
C(4)	4123(1)	6006(3)	3505(1)	21(1)
C(5)	4354(1)	6330(3)	4286(1)	26(1)
C(6)	4148(1)	4654(3)	4803(1)	30(1)
C(7)	3721(1)	2694(3)	4548(1)	31(1)
C(8)	3501(1)	2434(3)	3778(1)	26(1)
N(9)	3704(1)	4117(2)	3262(1)	20(1)
C(10)	3099(1)	2626(3)	2024(1)	22(1)
O(10)	2867(1)	733(2)	2301(1)	31(1)
C(11)	2904(1)	3220(3)	1149(1)	26(1)
F(1)	2773(1)	5869(2)	1006(1)	34(1)
F(2)	2434(1)	1766(2)	885(1)	45(1)
F(3)	3305(1)	2518(2)	743(1)	35(1)
H(2)	4186(9)	8630(40)	1523(12)	49(5)
H(3)	4488(8)	8570(40)	2893(10)	37(5)
H(5)	4635(7)	7800(40)	4407(10)	31(4)
H(6)	4300(7)	4780(40)	5344(10)	36(4)
H(7)	3585(8)	1560(40)	4901(11)	37(4)
H(8)	3208(7)	1230(30)	3562(9)	29(4)

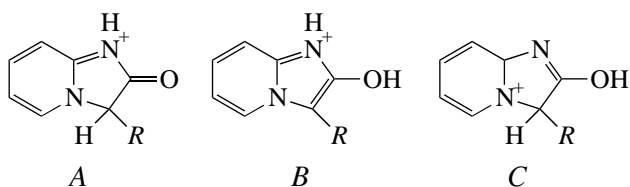
Structure of heterocyclic cation **II**.

180(2) K on an IPDS automated diffractometer using 1097 reflections in the θ range 5° – 25° (λ MoK α , graphite monochromator). The crystal data are $a = 23.761(5)$ Å, $b = 4.856(1)$ Å, $c = 17.713(4)$ Å, $\beta = 100.41(3)^\circ$, $V = 2010.1(7)$ Å³, $Z = 8$, space group $C2/c$, $d_{\text{calcd}} = 1.762$ g/cm³, and $\mu(\lambda\text{Mo}) = 0.415$ mm⁻¹. A set of 4505 reflections with $I \geq 2\sigma(I)$ was collected on the same diffractometer and at the same temperature by the ω -scan technique in the θ range 3.16° – 26.19° . The diffraction data measured were processed with the X-RED-107 program package. The non-hydrogen atoms were located by the direct method and refined in the anisotropic approximation by the least-squares procedure according to the SHELX97 program package [10]. All the hydrogen atoms were located from the difference Fourier syntheses of electron density. The structure was refined by the least-squares procedure in the anisotropic approximation (isotropic, for H atoms) to $R1 = 0.0296$ ($wR2 = 0.0642$). The atomic coordinates and isotropic thermal parameters that are equivalent to the corresponding anisotropic parameters are listed in the table. The residual (maximum and minimum) electron densities are $\Delta\rho_{\text{max}} = 0.240$ and $\Delta\rho_{\text{min}} = -0.184$ e/Å³. The drawing of the cation with the atomic numbering (see figure) was obtained with the PLUTON96 program [11].

RESULTS AND DISCUSSION

The chloride ion serves as a counterion in compound **II**. The heterocyclic cation is planar: the largest

atomic deviation from the plane of the bicyclic fragment is $0.015(1)$ Å. The cations of salts **I** and **II** can be represented by one of the three structures ($R = \text{H}$ or COCF_3):

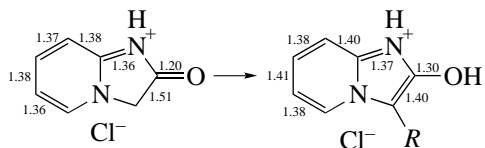


In our earlier work [6], we found that the structure of salt **I** is of the A type. The localization of the protons at the N(3) and O(2) atoms and the absence of a proton at the C(1) atom suggest that the structure of salt **II** (which is prepared by acylation of **I**) should be unambiguously assigned to the B-type structure rather than to the C type.

It is of interest to reveal the structural changes upon the **I** \rightarrow **II** acylation. A comparison of the bond lengths in the cations studied shows that the quasi-diene character of the C(5)C(6)C(7)C(8) moiety of the six-membered heterocycle in **II** is pronounced more than that in **I**. Protonation of the exocyclic O atom results in a redistribution of the bond lengths in the five-membered ring.

In particular, the C(2)–O(2) bond lengthens and the C(1)–C(2) bond shortens. This is consistent with the expected bond-length distribution in the ketonic compound **I** and the enolic compound **II**. We conclude that

the attachment of the COCF_3 group to the C(1) atom in the ketonic *A* form increases the acidity of the remaining proton and stabilizes the enolic *B* form. Since the C(1)–C(10) bond (heterocycle–acyl) is rather long (1.44 Å), the COCF_3 group in **II** is apparently weakly conjugated with the enolic fragment.

**I** (the *A* form)**II** (the *B* form; $R = \text{COCF}_3$)

Another specific structural feature of **II** is the formation of the hydrogen-bond system. The N(3)–H(3)···Cl[−] hydrogen bond, in which the chlorine atom is related to the reference atom by the $(1 - x, 1 + y, 1/2 - z)$ symmetry transformation, is characterized by the following parameters: N(3)···Cl[−], 3.09 Å; N(3)–H(3), 0.83 Å; H(3)···Cl[−], 2.33 Å; and N(3)–H(3)···Cl[−], 153°. In the O(2)–H(2)···Cl[−] hydrogen bond [O(2)···Cl[−], 2.87 Å; O(2)–H(2), 0.95 Å; H(2)···Cl[−], 1.92 Å; and O(2)–H(2)···Cl[−], 178°], the chlorine atom is related to the reference atom by the $(x, 1 + y, z)$ symmetry transformation.

ACKNOWLEDGMENTS

We are grateful to Professor E. Kemnitz (Institut für Chemie, Humboldt Universität, Berlin), who kindly allowed us to perform the diffractometric experiment. The synthetic part of this study was supported by the Russian Foundation for Basic Research, project no. 99-03-33076. We also acknowledge the support of this Foundation in the payment of the license to use the

Cambridge Structural Database, project no. 99-07-90133.

REFERENCES

1. E. V. Babaev, A. V. Efimov, S. G. Zhukov, and V. B. Rybakov, *Khim. Geterotsykl. Soedin.*, No. 7, 983 (1998).
2. E. V. Babaev, S. V. Bozhenko, D. A. Maiboroda, *et al.*, *Bull. Soc. Chim. Belg.* **106** (11), 631 (1997).
3. S. G. Zhukov, V. B. Rybakov, E. V. Babaev, *et al.*, *Acta Crystallogr., Sect. C: Cryst. Struct. Commun.* **53**, 1909 (1997).
4. E. V. Babaev, S. V. Bozhenko, S. G. Zhukov, and V. B. Rybakov, *Khim. Geterotsykl. Soedin.*, No. 8, 1105 (1997).
5. V. B. Rybakov, S. G. Zhukov, E. V. Babaev, *et al.*, *Kristallografiya* **44** (6), 1067 (1999) [*Crystallogr. Rep.* **44**, 997 (1999)].
6. V. B. Rybakov, S. G. Zhukov, E. V. Babaev, *et al.*, *Kristallografiya* **45** (1), 108 (2000) [*Crystallogr. Rep.* **45**, 103 (2000)].
7. V. B. Rybakov, S. G. Zhukov, E. V. Babaev, *et al.*, *Kristallografiya* **45** (2), 292 (2000) [*Crystallogr. Rep.* **45**, 261 (2000)].
8. V. B. Rybakov, S. G. Zhukov, E. V. Babaev, and E. J. Sonneveld, *Kristallografiya* **46** (3), 435 (2001) [*Crystallogr. Rep.* **46**, 385 (2001)].
9. F. H. Allen and O. Kennard, *Chem. Des. Autom. News* **8**, 31 (1993).
10. G. M. Sheldrick, *SHELX97: Programs for the Solution and Refinement of Crystal Structures*, Göttingen: Univ. of Göttingen, 1997.
11. A. L. Spek, *PLUTON96: Molecular Graphics Program*, Utrecht: Univ. of Utrecht, 1996.

Translated by I. Polyakova

Comparative Characterization of Defects Formed by Di- and Trivalent Metal Dopants in KDP Crystals and the Structural Mechanism of Influence of Impurities on Face Morphology

T. A. Eremina*, V. A. Kuznetsov*, N. N. Eremin**, T. M. Okhrimenko*,
N. G. Furmanova*, E. P. Efremova*, and V. S. Urusov**

* Shubnikov Institute of Crystallography, Russian Academy of Sciences, Leninskii pr. 59, Moscow, 117333 Russia

e-mail: furm@ns.crys.ras.ru

** Faculty of Geology, Moscow State University, Vorob'evy gory, Moscow, 119899 Russia

Received October 31, 2000

Abstract—The structure of KDP crystals doped with trivalent (Al^{3+} , Fe^{3+} , Mn^{3+} , V^{3+} , and La^{3+}) and divalent (Ni^{2+} , Co^{2+} , Fe^{2+} , Mn^{2+} , Ca^{2+} , Sr^{2+} , and Ba^{2+}) cations was simulated by minimizing the energy of atomic interactions. Three types of defects were revealed: isolated defect centers formed by M^{3+} and Ni^{2+} ions, cluster chain centers formed by M^{2+} ions with ionic radii exceeding 0.9 Å, and complex centers formed via the replacement of potassium ions by large Ba^{2+} dopants with the simultaneous replacement of some of the phosphorus atoms by silicon ones. The corresponding energies of defect formation are calculated. The surface morphology of the crystal faces is studied. The changes in morphology in the presence of M^{3+} dopants are caused by their adsorption, whereas for M^{2+} dopants, these changes are caused mainly by their incorporation into the crystal structure.
© 2001 MAIK "Nauka/Interperiodica".

INTRODUCTION

Two competitive processes—adsorption of impurity ions on the face surface and their incorporation into the surface layer of the crystal—are responsible for the effect of impurities on the grown kinetics and morphology of crystals. The effect of interstitial ions is provided mainly by two factors—the longer lifetime of the impurity within the surface layer (compared to the adsorbed state) [1] and the local stresses caused by deformation of the crystal structure by impurity particles [2]. The stresses increase the chemical potential of the compound in deformed surface regions and, thus, reduce the actual supersaturation there. Hence, the effect of impurities incorporated into the surface layer is determined not only by the impurity particles proper, which are the stoppers for growth layers (e.g., in the case of impurities adsorbed on the surface), but also by the degree of deformation of the adjacent crystal region whose dimensions cannot be less than the dimensions of the first coordination sphere of the impurity ion (the structural mechanism of impurity influence).

In our earlier publications [3–5], we demonstrated by computer simulation and crystallochemical analysis that di- and trivalent iron dopants are incorporated into the potassium dihydrophosphate (KDP) structure by two different mechanisms. Thus, although Fe^{3+} and Fe^{2+} dopants occupy the same interstitial position in the structure, $M1$, the Fe^{3+} ions form isolated monoatomic

defect centers, whereas, in accordance with the principle of charge compensation, the Fe^{2+} ions are forced to occupy several adjacent $M1$ positions and to form impurity chains. The preliminary estimates showed that an analogous mechanism of dopant incorporation should also exist for other M^{2+} and M^{3+} ions with the radii close to those of Fe^{2+} and Fe^{3+} , respectively. The comparison of the energies of Fe^{3+} and Fe^{2+} defect formation and the analysis of the displacements of the atoms of the matrix in the vicinity of the dopant ions showed that the KDP structure the incorporation of M^{2+} ions deforms the structure more pronouncedly than the incorporation of M^{3+} ions. Correspondingly, the stresses in the crystal structure in the former case are also more pronounced, which accounts for the different effect of the Co^{2+} and Ni^{2+} ions, on the one hand, and the Fe^{3+} and Cr^{3+} ions, on the other hand, on the growth kinetics of the faces of KDP crystals [6].

The present paper continues our studies in this field and is dedicated to the comprehensive analysis of the mechanism of incorporation of di- and trivalent cations with a wide range of ionic radii r into the KDP structure (r varies from 0.66 to 1.2 Å for Al^{3+} , Fe^{3+} , Mn^{3+} , V^{3+} , and La^{3+} and from 0.83 to 1.50 Å for Ni^{2+} , Co^{2+} , Fe^{2+} , Mn^{2+} , Ca^{2+} , Sr^{2+} , and Ba^{2+}). We also study the effect of the above cations on the surface morphology and the structure of KDP crystals.

Table 1. Parameters of the potentials of the M –O atomic interactions

M	$B (M-O)$	$\rho (M-O)$
Al	1005.77	0.3118
Mn ³⁺	1134.83	0.3214
Fe ³⁺	1102.41	0.3239*
Y	1213.51	0.3588
La	1215.31	0.3651
Ni	1582.5	0.2882
Co	1491.7	0.2951
Fe ²⁺	1207.6	0.3084
Mn ²⁺	1007.4	0.3262
Ca	1090.4	0.3437
Sr	959.1	0.3721
Ba	905.7	0.3976

* Data [3].

COMPARATIVE CHARACTERIZATION OF DEFECTS FORMED BY DI- AND TRIVALENT METALS

Defect centers were simulated by minimizing the energy of atomic interactions by the GULP (General Utility Lattice Program) program package [7]. As in our previous studies [4, 5], the effective charges of the ions were taken to be equal to 2.7 and 1.9 e for M^{3+} and M^{2+} , respectively. The parameters of the pair potentials of M –O atomic interactions with due regard for the change in the effective ion charge were taken from [8] (Table 1). In the discussion, we used the absolute ionic radii [9].

As in our previous studies [4, 5], we examined various modes of incorporation of ions into the KDP structure, namely, into the $M1$ (0.25, 0.35, 0.125), $M2$ (0.75, 0.22, 0.125), and potassium positions. In the course of optimization, the M^{2+} ions were displaced from the $M2$ into the $M1$ position. Therefore, the $M2$ position is not considered as an alternative position for divalent cations. The results obtained for incorporation of impurity cations into the potassium positions are only qualitative, because it was shown [5] that the calculations within the framework of the model used provide the correct evaluation of the energy of defect formation in the K^+ cavity only for large cations whose size is comparable with the size of a potassium ion, which ensures the formation of typical M –O distances. Of all the trivalent cations considered, only La^{3+} cation meets this requirement. The adequate description of incorporation of smaller cations into the potassium position, the potential of the M –O interaction should involve the Morse potential taking into account the degree of the bond covalence. The contribution of the Morse potential is negligible of an ion is incorporated into the void with the commensurate size, but it increases with a decrease of the radius of the interstitial ion. Hence, the energies of defect formation in the K^+ position (except for Ba^{2+}) given below are underestimated. Nevertheless, even this qualitative estimate for trivalent cations proved to be sufficient for determining the most probable positions for their incorporation into the structure.

The results of our calculations are summarized in Table 2, which shows that the minimum energies of defect formation for trivalent cations correspond to the $M1$ position. This position is most favorable for incorporation of all the M^{3+} cations. The underestimated energies of defects for the replacement of K^+ cations

Table 2. Energies of defect formation (eV)

Ion		Ionic radius	$M1$	$M2$	Potassium position	Chain calculated per atom
M^{2+}	Ni	0.83	0.76*	–	–	0.85
	Co	0.88	1.10*	–	–	1.25
	Fe	0.92	1.44	–	–	1.41*
	Mn	0.97	2.13	–	–	2.01*
	Ca	1.14	3.62	–	–	3.29*
	Sr	1.27	5.24	–	–	4.93*
	Ba	1.50	6.98*	–	7.75	7.48
M^{3+}	Al	0.53	–6.90	–5.15	–2.33	–
	Fe	0.55	–4.79	–2.86	–1.24	–
	Mn	0.58	–5.05	–3.13	–1.31	–
	Y	0.90	–1.22	0.88	1.32	–
	Ce	1.01	1.63	3.66	3.61	–
	La	1.03	1.23	2.89	2.99	–

* The most favorable variant of defect formation for M^{2+} .

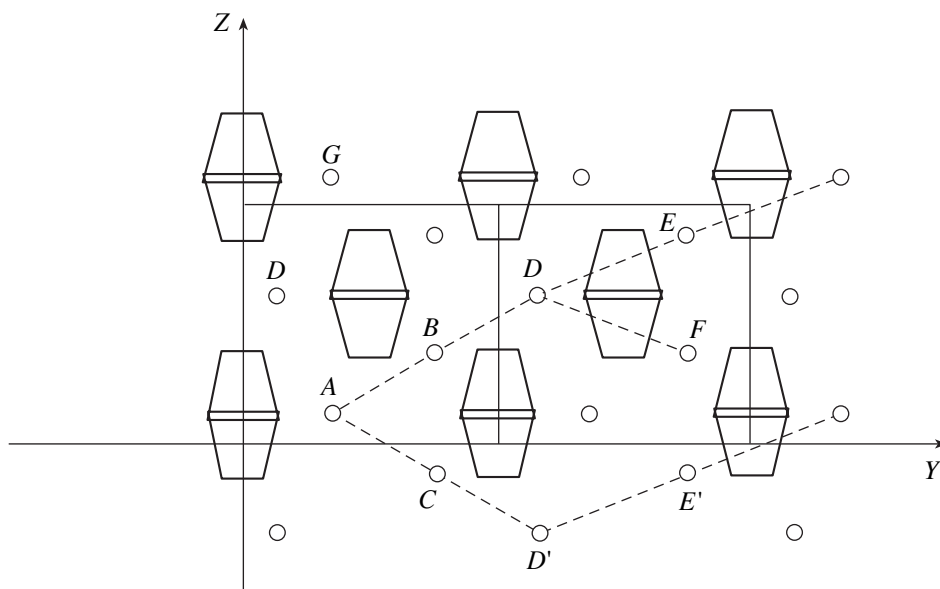


Fig. 1. Schematic view of the KDP structure projected onto the (100) plane (overlapping phosphorus–oxygen tetrahedra and the $M1$ positions); the orientations of the impurity chains are shown by dashed lines.

are substantially higher than the corresponding values for the $M1$ position. With the introduction of the Morse potential this difference increases.

Thus the main defects in the KDP structure doped with trivalent cations in the wide range of ionic radii are isolated regions with the dopant coordinates (0.25, 0.35, 0.125). The energy of defect formation increases with an increase of the ionic radius of the dopant, which indicates that the incorporation of larger cations is more difficult because it requires more pronounced structure deformation. Since the $M1$ positions are in the $\{100\}$ plane [3], their partial occupancy by M^{3+} ions provides the formation of loose “impurity networks” parallel to the $\{100\}$ plane. Intersections of these networks create channels along the Z -axis of the crystal, which are filled with impurity ions (the A and G positions; Fig. 1).

The situation for divalent cations is more complex. Unlike M^{3+} , divalent cations form different defect centers depending on their ionic radii. Calculations show (Table 2) that the $M1$ positions are characterized by the minimum energies of defect formation; i.e., the $M1$ positions are still the most probable positions for incorporation of the M^{2+} ions as well (the case of Ba^{2+} is discussed below). However, only Ni^{2+} of all the M^{2+} ions form isolated defect centers analogous to M^{3+} ions. Similar to M^{3+} these centers are located in channels along the $[001]$ direction (Fig. 2). For larger M^{2+} cations ($r > 0.9 \text{ \AA}$), the incorporation into the adjacent $M1$ positions is more favorable with the formation of $A-B-D-E\dots$ or $A-B-D-F\dots$ impurity chains in the (100) planes (Fig. 1). The linear chains ($ABDE\dots$) are tilted by an angle of $\sim 60^\circ$ to the Z -axis of the crystal, whereas the average angles characterizing the orientation of different types of “broken” chains ($ABDF\dots$) can be equal to

75° or even somewhat larger. In the crystals, the systems of such chains form second-type dopant networks occupied by M^{2+} ions with the radii exceeding 0.9 \AA . Because of the intermediate position of the Co^{2+} and Fe^{2+} cations ($r(Co^{2+}) = 0.88 \text{ \AA}$ and $r(Fe^{2+}) = 0.92 \text{ \AA}$) they are statistically distributed over both types of networks.

For large divalent Ba^{2+} cations ($r = 1.50 \text{ \AA}$) whose the ionic radius is comparable with that of K^+ ($r = 1.56 \text{ \AA}$), the $M1$ positions are characterized by the very high energy of defect formation (Table 2). Thus, the incorporation of barium ions into KDP structure is very difficult. On the other hand, it is known that Ba^{2+} ions in natural minerals readily replace potassium ions by

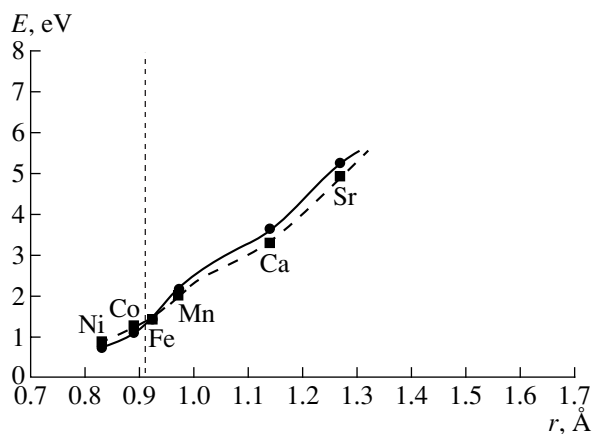


Fig. 2. Energies of defect formation (E) depending on the absolute ionic radii (r) of divalent metal ions occupying the $M1$ position. The solid line indicates the energies of formation of single defects; dashed line indicates the energies of cluster formation.

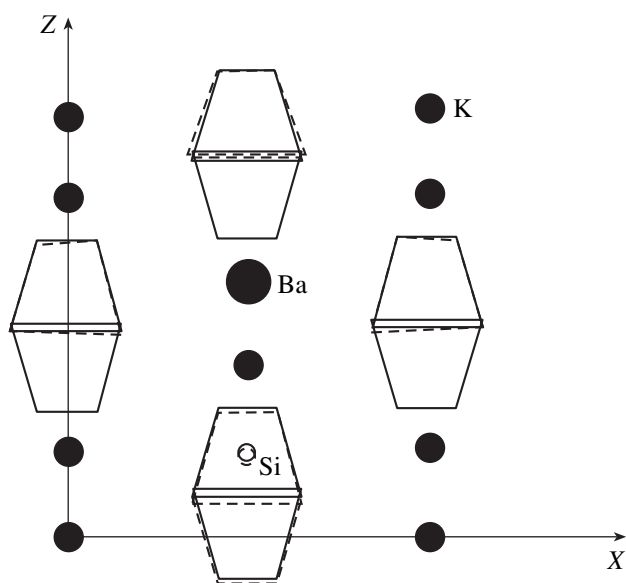


Fig. 3. Structure of a complex defect center $K^+ + P^{5+} = Ba^{2+} + Si^{4+}$; the solid line shows the positions of phosphorus–oxygen tetrahedra in the ideal and the deformed structures, respectively.

the mechanism of heterovalent isomorphism. According to [10, 11] and our estimates (see below), the distribution coefficients of barium ions in KDP crystals considerably exceed unity. These facts indicate that Ba^{2+} ions can readily be incorporated into the KDP structure. We analyzed the model of a complex double defect center with the simultaneous replacement of potassium by barium and phosphorus by silicon. The validity of this model is confirmed by the fact that mother liquors of KDP necessarily contain noticeable amounts of silicon. The calculations demonstrated that the energy of formation of this double defect center (4.77 eV) is almost 1.5 times lower than the corresponding value for the $M1$ position. Therefore, the formation of a complex defect center of the third type in the KDP structure by the mechanism of heterovalent isomorphism is more probable for large Ba^{2+} cations (Fig. 3). The analysis of possible incorporation of other large cations (Ca^{2+} and Sr^{2+}), whose radii are essentially different from the radius of a K cation in comparison with that of Ba^{2+} , requires the allowance for the Morse potential in the consideration of the $M-O$ interactions. The results of such an analysis will be presented in the next publication.

The calculations (Table 2) demonstrated that the energies of defect formation are much higher for the M^{2+} than for the M^{3+} ions. This fact and the analysis of local distortions of the KDP crystals doped with various ions [4, 5] indicate that the M^{3+} ions cause weaker deformations of the KDP structure than the M^{2+} ions, and, thus, lower local stresses. Although the Ni^{2+} ions give rise to the formation of defect centers analogous to

the M^{3+} centers, they cause higher local stresses. Higher stresses also arise because the formation of impurity chains of M^{2+} ions. Finally, the maximum deformations are observed in the case of heterovalent isomorphism $K^+ + P^{5+} = Ba^{2+} + Si^{4+}$, however, the condition of charge compensation does not require the formation of additional vacancies. As a result, distortions are observed in a narrower region of the occurrence of replacement. Thus, this situation is most favorable energetically for Ba^{2+} cations.

Thus, the dopants of di- and trivalent metals provide the formation of three types of defect centers in the KDP structure:

- (1) isolated defect centers forming chains along the Z -axis of the crystal (M^{3+} and Ni^{2+} cations);
- (2) dense impurity chains of the “cluster” type oriented at angles from 60° to 75° to the Z -axis of the crystal (M^{2+} cations with $r > \sim 0.9 \text{ \AA}$);
- (3) complex double impurity centers generated by the mechanism of heterovalent isomorphism (Ba^{2+}).

INFLUENCE OF M^{3+} AND M^{2+} DOPANTS ON SURFACE MORPHOLOGY AND CRYSTAL STRUCTURE

We studied crystals grown in the kinetic and diffusion (isothermal evaporation at room temperature) modes in the presence of Cr^{3+} , Fe^{3+} , Ni^{2+} , Co^{2+} , or Ba^{2+} dopants. For both modes, the general characteristics of dopant-induced changes of the $\{100\}$ surface relief were identical, but some effects are more pronounced in the diffusion mode. Surface morphology was studied using a Neophot microscope. The dopant concentrations in the crystals and in the initial solutions were determined by chemical analysis and were used to calculate the effective distribution coefficients of impurity elements. It was found that at low concentrations of the impurities in the initial solutions ($1.0\text{--}1.4 \times 10^{-6}$ mole of an impurity per mole of KDP for Cr^{3+} , Fe^{3+} , and Ba^{2+} and $1\text{--}7 \times 10^{-8}$ mol/mol for Ni^{2+} and Co^{2+}), the effective coefficients of chromium, iron, nickel, and cobalt incorporation are 0.2, 1.7, 0.6, and 1.5, respectively, whereas $k_{Ba^{2+}}$ is equal to 13 and shows a pronounced tendency to a further increase with an increase of Ba^{2+} concentration in solutions in the range $5 \times 10^{-7}\text{--}5 \times 10^{-6}$ mol/mol.

The changes in the surface relief of KDP faces induced by dopants is associated with the valence of the latter and the type of defect centers formed. The relief of the $\{100\}$ faces of KDP in nominally pure solutions consists of large vicinal formations [12–15]. The smooth slopes of these formations show numerous rounded or elongated dislocation hillocks. Growth steps generated by those hillocks merge together and form macrosteps visible under an optical microscope.

The addition of small amounts of trivalent chromium or iron ions ($\sim 10^{-6}$ mol/mol) to the initial solution only weakly affects the surface morphology of the $\{100\}$ faces; thin growth layers become somewhat more “dissected,” and sometimes acquire the saw-toothed or dendrite-like shape. Along with small (of the order of 10^{-2} mm) elongated hillocks with sharp tops there are also flat-top formations consisting of closed low-height macrosteps. The orientation of the macrosteps on the $\{100\}$ surface is arbitrary, but, often, their long axis is oriented at an angle of not less than 60° to the Z -axis of the crystal. With an increase of Cr^{3+} and Fe^{3+} concentrations, the growth steps of the neighboring hillocks merge into a single front moving along the $[001]$ direction (Fig. 4a). Apparently, this stage corresponds to the onset of tapering on the $\{100\}$ faces, a phenomenon well-known for KDP crystals [16–17], although the tapering angle is still very small. With the further increase of impurity concentration, the tapering angle increases and the surface of the $\{100\}$ faces acquires a stepped relief, with the step rises being divided into isolated rectilinear fragments (Fig. 4b).

A different pattern of relief evolution of the $\{100\}$ faces is observed for Co^{2+} and Ni^{2+} dopants. These dopants only slightly affect tapering on the prism faces. Thus, the tapering angle does not exceed $\sim 1^\circ$ for Co^{2+} and 1.5° – 2.5° for Ni^{2+} even at the maximum concentrations ($\sim 10^{-2}$ mol/mol). The characteristic elements of the $\{100\}$ surface relief now (Figs. 5a, 5b), are larger elongated growth hillocks become with their density being the higher, the higher the dopant concentration (Fig. 5b). Apparently, these elements are generated by more powerful dislocation sources and are also promoted by more pronounced deformations of the KDP structure by Ni^{2+} and Co^{2+} ions than in the case of M^{3+} ions. Hillocks are often located (particularly, in the presence of nickel) one above the other and form columns along the $[001]$ direction. On the $\{100\}$ surface, hillocks are always arranged so that their long axes are tilted to the Z -axis of the crystal (in most cases by angles ranging from 65° to 75°). The angle tends to decrease for more smooth hillocks consisting of thinner steps.

Far from the centers of the growth hillocks, thin steps merge together and form macrosteps, which then are grouped to form step echelons with broad terraces. Initially, the orientation of their fronts repeats the orientation of the hillocks; however with an increase of the step thickness, the direction of the front movement approaches the $[001]$ direction. In the case of Ni^{2+} , these directions coincide at the dopant concentration of $\sim 10^{-4}$ mol/mol. This seems to be also promoted by weak but noticeable tapering of the prism faces. The formation of step echelons with rounded edges is more characteristic of Co^{2+} . The tilt of the fronts with respect to the $[001]$ direction is preserved even at higher Co^{2+} concentrations. Only close to crystal edges, where the

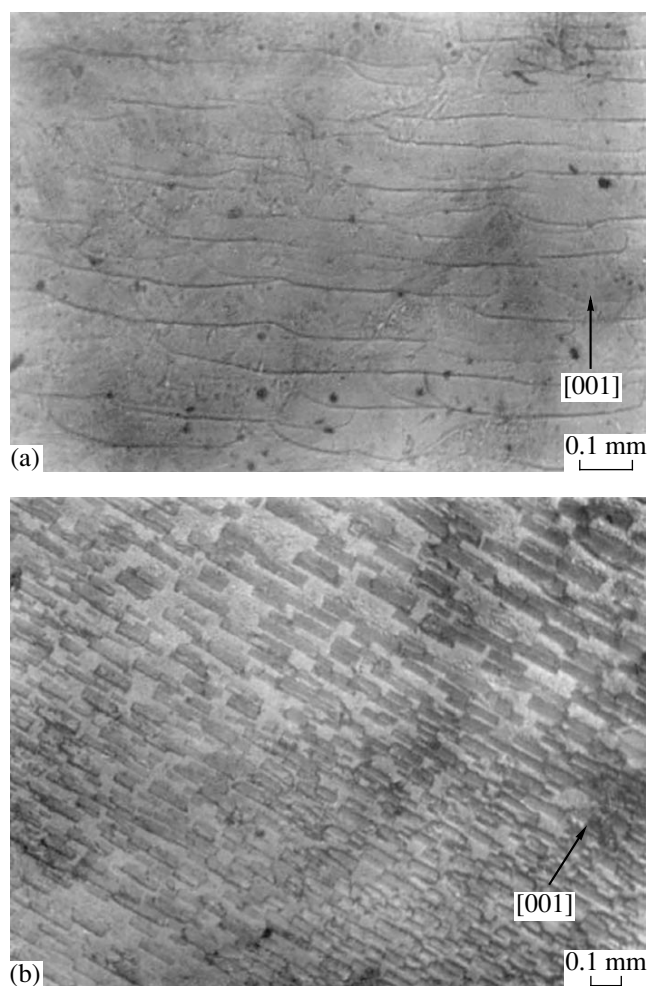


Fig. 4. Surface of the $\{100\}$ faces of a KDP crystal grown in the presence of Cr^{3+} ions: (a) $c_{\text{Cr}^{3+}} = 10^{-6}$ mol/mol and (b) $c_{\text{Cr}^{3+}} = 9.3 \times 10^{-6}$ mol/mol.

most powerful step echelons are formed, the fronts become parallel to the crystal edges.

At the maximum Ni^{2+} and Co^{2+} concentrations in solutions ($>10^{-2}$ mol/mol), numerous large rounded macrohillocks consisting of high macrosteps are formed on the (100) -type faces because of precipitation of poorly soluble nickel and cobalt phosphates promoting heterogeneous nucleation. According to [18], this should lead to acceleration of face growth (we really observed such acceleration for KDP : Co^{2+} [6]).

The characteristic feature of the relief of the $\{100\}$ faces in the presence of Ni^{2+} or Co^{2+} dopants is the formation of the surface columnar “texture” (Fig. 5c). The step echelons are sliced into narrow bands parallel to the Z -axis of the crystal. Weak manifestations of the surface texture are noticeable even at low Ni^{2+} and Co^{2+} concentrations ($\sim 10^{-5}$ mol/mol). At higher dopant concentrations, the surface texture becomes more pronounced. The brightest manifestation of this phenome-

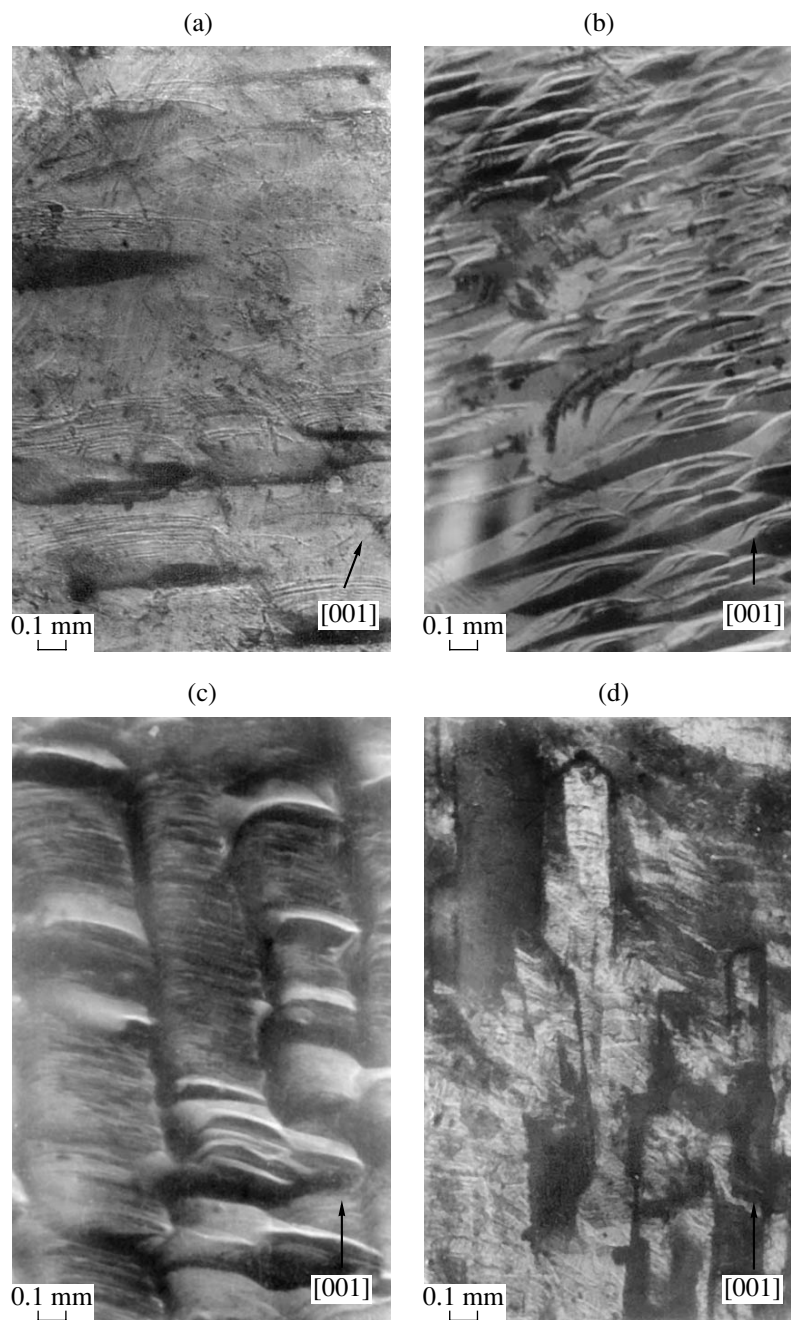


Fig. 5. Surface of the {100} faces of a KDP crystal grown in the presence of Co^{2+} and Ni^{2+} ions: (a) $c_{\text{Co}^{2+}} = 10^{-7}$ mol/mol; (b) $c_{\text{Co}^{2+}} = 4 \times 10^{-6}$ mol/mol; (c) $c_{\text{Co}^{2+}} = 10^{-2}$ mol/mol; (d) $c_{\text{Ni}^{2+}} = 2 \times 10^{-2}$ mol/mol.

non is the formation of a rough surface relief in the presence of Ni^{2+} (Fig. 5d) and some other characteristic formations in the crystal. The crystal can even disintegrate into (1.0–1.5)-mm-thick columnar individuals. The analogous situation was also observed for KDP crystals grown in the diffusion mode at the Ni^{2+} concentrations in the solutions exceeding $>10^{-2}$ mol/mol.

Unlike Ni^{2+} and Co^{2+} , divalent Ba^{2+} ions exert the most substantial effect on the morphology of the {101}

faces and on the growth pyramids on these faces. Even at low Ba^{2+} concentrations ($\sim 10^{-6}$ mol/mol), the {101} surface is noticeably roughened and looks hilly in the reflected light. With an increase of the barium concentration in the solution, roughness of the {101} faces becomes more pronounced and high macrosteps appear. Beginning with concentration c_{Ba} of 5×10^{-5} mol/mol, visible milk-white interlayers occur in the {101} growth pyramids. These interlayers are parallel to the

{101} faces of the bipyramid and consist mainly of minute inclusions of the mother liquor.

RESULTS AND DISCUSSION

Our study demonstrated that the incorporation of di- and trivalent cations into the KDP lattice proceeds by different mechanisms. We revealed the formation of different types of defect centers and established the specific effect of these ions on the face morphology and crystal structure. Although we simulated the positions of dopants ions in the crystal bulk, the main features of defect-center formation are also the same for the surface layers of the crystal. The differently oriented columns of dopants and chains formed by M^{3+} and M^{2+} ions act as barriers for motion of growth layers, and their decelerating effect becomes more pronounced because of local stresses in the structure. Below, we analyze the results obtained in this context.

According to the commonly accepted views, the effect of an trivalent cations is explained mainly by their adsorption. This conclusion is additionally supported by the observed "catalytic" effect of the Cr^{3+} and Fe^{3+} dopants caused by a decrease in the "edge" energy of steps because of ion adsorption [6]. Apparently, the effect of the M^{3+} ions located in the surface layer is still rather weak, because the stresses induced by these ions in the structure are insignificant.

A different situation arises for cobalt and nickel dopants, which cause more substantial deformations of the crystal lattice. In these cases, the effects associated with impurity adsorption (tapering on prism faces, the catalytic effect) are very weak or absent, but noticeable deceleration of growth of the {100} faces is retained [6] (comparable with effect with that of Cr^{3+} and Fe^{3+}). One also observes the change in the {100} surface relief typical only of Ni^{2+} and Co^{2+} dopants. All the above-mentioned facts allow the conclusion that cobalt and nickel ions incorporated into the surface layer of the crystal play a dominant role, whereas the contribution of the same ions adsorbed on the surface to the total effect is rather small. It is reasonable to attribute the formation of the surface columnar texture to deceleration of growth layers by the defect centers located in the channels parallel to the [001] direction. High density of these centers in the crystal bulk, and the accompanying high stresses can stimulate the development of block boundaries along the {100} planes and appearance of some formations in the crystal. For Co^{2+} ions, this effect is less noticeable due to the ability of Co^{2+} to form defect centers of the second type (chains), which allows its low concentration in channels.

The specific orientation of growth hillocks on the {100} faces can be explained by the decelerating effect of the ABD chains of dopants. Earlier, an analogous orientation of hillocks was observed in the KDP crystals grown from solutions without doping [13–15]. The angle between the long axis of a hillock and the Z -axis

of the crystal equals 67° [13], which is consistent with our results. This hillock orientation cannot be related to the KDP structure, e.g., with the directions of the chains of strong bonds [15]. At the same time, taking into account that dopant can considerably influence crystallization even at the concentrations of ~ 0.3 bbm [13] (which is by one to two orders of magnitude lower than their concentrations in nominally pure KDP solutions), this effect can be explained by the influence of "background" impurities. The dynamics of the change in the shape of growth hillocks with an increasing supersaturation is characteristic. At low supersaturations, growth hillocks are almost rounded [13, 15], which is explained by adsorption of background impurities [15]. With an increase of supersaturation, the barrier of the latter background impurities is overcome, the rate of step motion increases, and the shape of growth hillocks is changed from round to ellipsoidal in the jumpwise manner. Evidently, the growth steps more readily propagate along the impurity chains, whereas their motion in the perpendicular direction is hindered by these chains. This mechanism explains the fact that the predominant orientation of the long axis of ellipsoidal growth hillocks (tilted by an angle of 65° – 77° to the Z -axis of the crystal) coincides with the orientation of the ABD chains of dopants (60° – 75°). We did not find any growth hillocks whose axes were inclined to the Z -axis by an angle smaller than 60° . The dependence of the orientation of the hillocks on the slope steepness and height of macrosteps reflects the fact that high macrosteps overcome dopant barrier more readily and the crystal structure has a more substantial effect on the orientation.

The strong influence of the barium dopant on the morphology of the {101} faces and the "defect" nature of the growth pyramids on these faces is adequately explained by the structure of {101}. In the KDP structure, the layers of potassium ions alternate with phosphorus–oxygen layers along the [101] direction [3], with the {101} surface always consisting of potassium layers [19]. This facilitates the replacement of K^+ by Ba^{2+} ions with the simultaneous replacement of $[PO_4]^{3-}$ -ions located in the next layer by $[SiO_4]^{4-}$ -ions. The resulting strong deformations of the structure are favorable for incorporation of microinclusions from the solution and formation of "defect interlayers" parallel to the {101} faces.

Thus, our study confirmed once again the fact that the dopants incorporated into surface layers and the induced stresses play an important role in the mechanism of effect of dopants on the growth kinetics and the "defect" crystal structure. At the same time, our data disprove the opinion [20] that divalent cation dopants produce insignificant effect on KDP crystallization. The results obtained indicate that the influence of M^{2+} ions is comparable or even more pronounced than the influence of M^{3+} ions.

ACKNOWLEDGMENTS

We are grateful to N.A. Sizova and N.A. Skvortsova for their help in the optical measurements.

This study was supported by the Russian Foundation for Basic Research, project no. 99-03-32557.

REFERENCES

1. V. V. Voronkov, *Kristallografiya* **19**, 475 (1974) [*Sov. Phys. Crystallogr.* **19**, 296 (1974)].
2. N. T. Barret, G. M. Hamble, K. J. Roberts, and J. M. Sherwood, *J. Cryst. Growth* **94**, 689 (1989).
3. T. A. Eremina, V. A. Kuznetsov, T. M. Okhrimenko, and N. G. Furmanova, *Kristallografiya* **41** (4), 717 (1996) [*Crystallogr. Rep.* **41**, 680 (1996)].
4. T. A. Eremina, V. A. Kuznetsov, T. M. Okhrimenko, *et al.*, *Kristallografiya* **43**, 906 (1998) [*Crystallogr. Rep.* **43**, 852 (1998)].
5. T. A. Eremina, N. N. Eremin, N. G. Furmanova, *et al.*, *Kristallografiya* **46**, 82 (2001) [*Crystallogr. Rep.* **46**, 75 (2001)].
6. V. A. Kuznetsov, T. A. Eremina, N. N. Eremin, *et al.*, *Kristallografiya* **45**, 1120 (2000) [*Crystallogr. Rep.* **45**, 1035 (2000)].
7. J. D. Gale, *GULP: User Manual* (Royal Institution and Imperial College, London, 1992–1994).
8. G. V. Lewis and C. R. A. Catlow, *J. Phys. C* **18**, 1149 (1985).
9. R. D. Shannon and C. T. Prewitt, *Acta Crystallogr., Sect. B: Struct. Crystallogr. Cryst. Chem.* **B25**, 925 (1969); **B26**, 1046 (1970).
10. C. Belouet, E. Dunia, and J. F. Petroff, *J. Cryst. Growth* **23**, 243 (1974).
11. H. V. Alexandru, A. C. Otea, and G. Hlevca, *Rev. Roum. Phys.* **30** (6), 525 (1985).
12. V. Bredikhin, G. L. Galushkina, and S. P. Kuznetsov, in *Abstracts of the XII International Conference on Crystal Growth, Jerusalem, 1998*.
13. A. A. Chernov and L. N. Rashkovich, Preprint No. 01/1986, IK AN SSSR (Inst. of Crystallography, USSR Academy of Sciences, Moscow, 1986), p. 9.
14. L. N. Rashkovich, A. A. Mkrtychyan, and A. A. Chernov, *Kristallografiya* **30**, 380 (1985) [*Sov. Phys. Crystallogr.* **30**, 219 (1985)].
15. J. W. Noor and B. Dam, *J. Cryst. Growth* **76**, 243 (1986).
16. I. Owczarek and K. Sangwal, *J. Cryst. Growth* **102**, 574 (1990).
17. I. Owczarek and K. Sangwal, *J. Cryst. Growth* **99**, 827 (1990).
18. X. Y. Lin, K. Maiwa, and K. Tsukamoto, *J. Chem. Phys.* **106** (5), 1870 (1997).
19. S. A. De Vries, P. Goettkindt, S. H. Bennett, *et al.*, *Phys. Rev. Lett.* **80**, 2229 (1998).
20. M. H. J. Hottenhuis and C. B. Lucasius, *J. Cryst. Growth* **78**, 379 (1986).

Translated by T. Safonova

On Temperature Variation of Oxygen Parameter for Magnetite Nanoparticles

V. I. Nikolaev*, A. M. Shipilin**, and I. N. Zakharova**

* Moscow State University, Vorob'evy gory, Moscow, 119899 Russia

e-mail: vnik@cs.msu.su

** Yaroslavl Polytechnical Institute, Moskovskii pr. 88, Yaroslavl, 150053 Russia

Received October 30, 2000

Abstract—The Mössbauer spectra of ^{57}Fe nuclei for magnetite nanoparticles have been studied. It is established that the oxygen parameter u changes by a value of about 0.002 with the temperature increase in the range 100–300 K. The u values are obtained from the shifts of partial spectra corresponding to the Fe^{3+} ions in both tetrahedral and octahedral positions. The “covalence effects” are calculated by the molecular orbitals method. © 2001 MAIK “Nauka/Interperiodica”.

As is known, the determination of the free parameters of the regular crystal structure is a rather difficult problem. Prior to the discovery of the Mössbauer effect, these parameters were determined by the X-ray and neutron diffraction methods, but they proved to be inefficient in the case of nanoparticles.

The advent and development of methods based on the nuclear gamma-resonance opened new vistas in studying the local structure of the solid state. In particular, it turns out that the Mössbauer spectroscopy not only complements the conventional methods, but can also be a more efficient and even unique method for solving such problems. Thus, the Mössbauer method can be applied to the iron-containing systems and yield the quantitative information about the effect produced by different factors (such as temperature, pressure, magnetic or electric field) on the nanoparticle structure.

Below, we describe the results of Mössbauer study of magnetite (Fe_3O_4) nanoparticles. Our purpose was to study of the influence of temperature in the system of ultrafine magnetite particles crystallizing in the spinel structure (sp. gr. $Fd\bar{3}m$) on the value of oxygen parameter u . It was assumed that the changes caused by temperature can be measured because anharmonicity of atomic vibrations of “peripheral” atoms (which comprise a considerable fraction of the total number of atoms in a particle) considerably change the average interatomic distances.

The method for determining the values of the free structural parameter u from the data on the initial experimental spectrum of the ^{57}Fe nuclei of iron atoms in the Fe_3O_4 particles used in this study is based on the fact that the difference $\Delta\delta^{AB}(a, u) \equiv \delta_I^B(\text{Fe}^{3+}) - \delta_I^A(\text{Fe}^{3+})$ in

the isomer shifts of partial Mössbauer spectra corresponding to trivalent iron atoms in the tetrahedral (A) and the octahedral (B) positions of the spinel structure is uniquely determined by the value of the oxygen parameter u (if the unit cell parameter a is known) [1]. This difference is caused by so-called “covalence effects” and can be calculated using the formalism of the method of molecular orbitals [2, 3].

In our experiments, we used a finely dispersed magnetite powder obtained by the conventional chemical condensation. According to the electron microscopy data, the average size of the magnetite particles was $d = (7.5 \pm 0.5)$ nm. The Mössbauer spectra were recorded in the absorption geometry. The specimen density was about 0.15 mg/cm^2 (with respect to ^{57}Fe) and corresponded to the approximation of a thin specimen, which allowed the application of the superposition principle to the partial spectra. The ^{57}Co isotope in the chromium matrix served as a source of gamma-radiation. Since the Verwey temperature of fine magnetite particles (<9 nm) is higher than room temperature [4], the model processing of the spectra obtained in the temperature range 100–300 K was made under the assumption on the existence of three sextets (one corresponding to Fe^{3+} ions in the A -positions, and two other, to Fe^{2+} and Fe^{3+} ions in the B -positions).

Figure 1 shows two initial experimental spectra obtained at considerably different temperatures. It is seen that the character of the spectra are unchanged within the whole temperature range studied, even at the Verwey temperature $T_V = 119$ K for “bulk” magnetite particles (which qualitatively agrees with [4]).

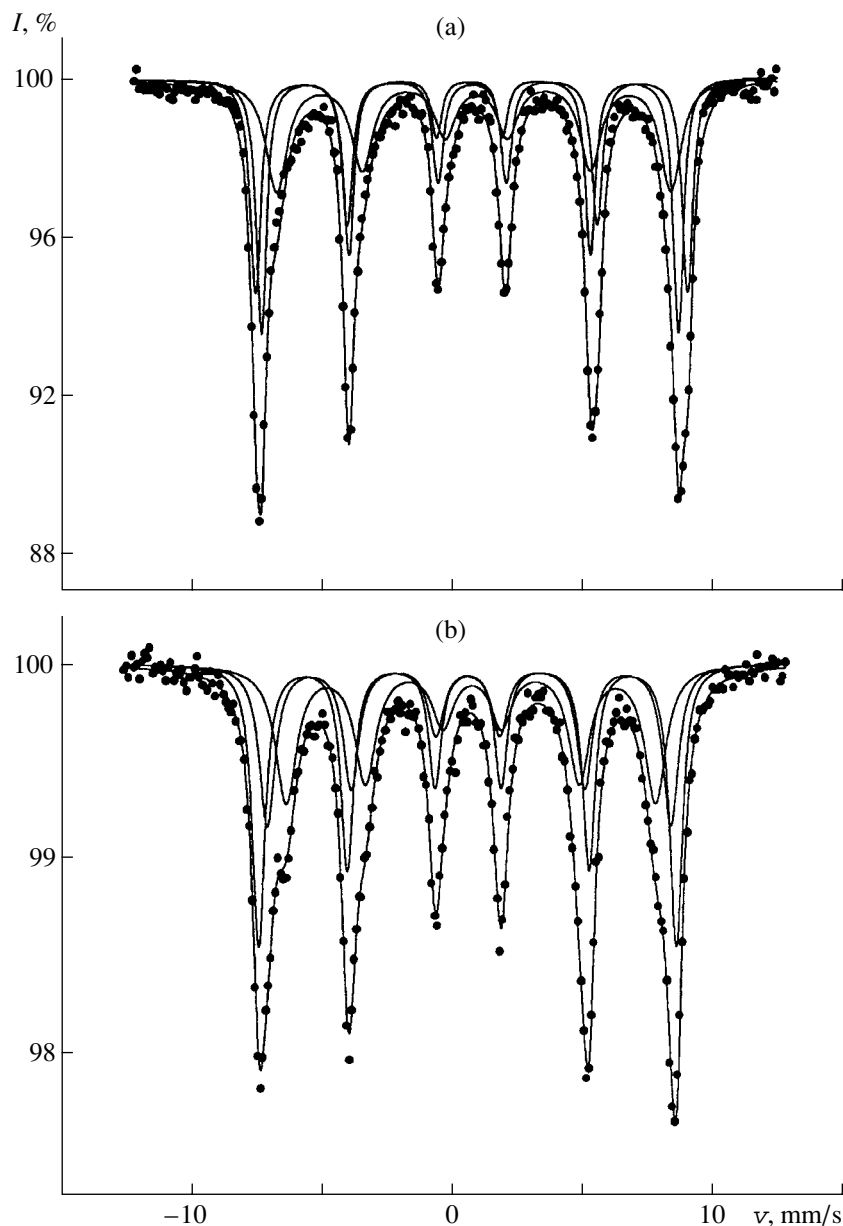


Fig. 1. Mössbauer spectra of ^{57}Fe nuclei in Fe_3O_4 nanoparticles at (a) 100 and (b) 300 K.

The basic results obtained are illustrated in Figs. 2 and 3. According to the data on the temperature dependence of the shifts in partial spectra corresponding to the Fe^{3+} ions in the A- and B-positions, the oxygen parameter u noticeably changes with the temperature. This is evident from pronounced temperature changes of the “gap” between $\delta^A(T)$ and $\delta^B(T)$ curves for the Fe^{3+} ions. Subtracting one dependence from another (the difference $\Delta\delta^{BA}$ as a function of temperature), we can exclude not only the relativistic correction δ_T for a total shift $\delta \equiv \delta_I + \delta_T$, but, partly, also the change of the isomer shift δ_I associated with thermal expansion [1] (Fig. 2 and the inset there). It is this difference that was

used to obtain the sought $u(T)$ dependence. As is seen from Fig. 3, for magnetite nanoparticles, the change in the temperature gives rise to significant changes in the free structural parameter u . For comparison, the analogous temperature changes in the u parameter observed earlier for bulk ferrite spinels particles of the compositions $\text{Li}_{0.5}\text{Fe}_{2.5}\text{O}_4$ [6], NiFe_2O_4 [7], and CuFe_2O_4 [8] were considerably lower.

The oxygen parameter u for magnetite nanoparticles in the whole temperature range studied, including room temperature had much higher values than for “bulk” Fe_3O_4 particles ($u = 0.379$ at 300 K) [9]. Since the u parameter for nanoparticles increases with temperature,

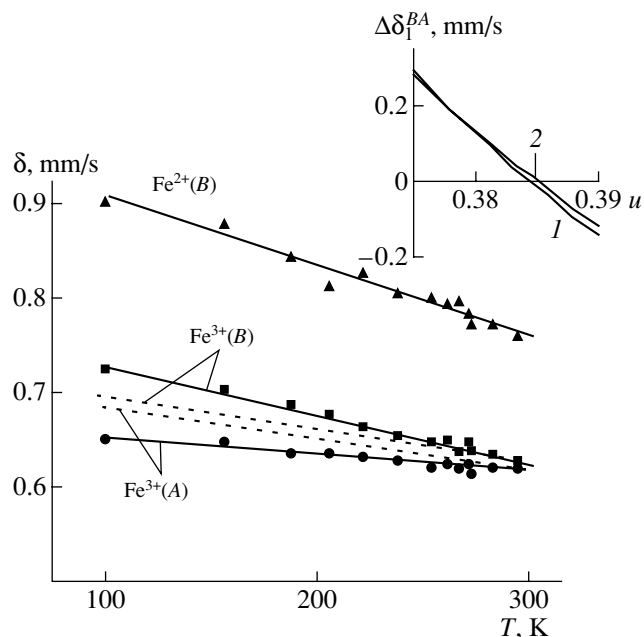


Fig. 2. Temperature dependence of shifts in partial Mössbauer spectra (with respect to the sodium nitroprusside line) for Fe^{3+} and Fe^{2+} ions in Fe_3O_4 nanoparticles. Dashed lines show the temperature dependences of shift calculated for the $\text{Fe}^{3+}(\text{A})$ and $\text{Fe}^{3+}(\text{B})$ cations at $u = \text{const} = 0.384$.

In the inset: parametric dependences $\Delta\delta_1^{A,B}(a, u)$ calculated by the molecular orbital method at two constant a values: (1) 8.30 and (2) 8.50 Å.

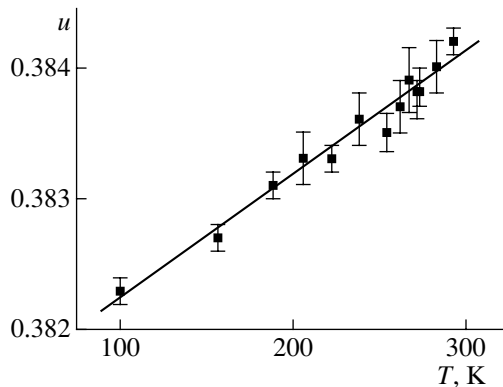


Fig. 3. Temperature dependence of the oxygen parameter u for Fe_3O_4 nanoparticles.

the common physical factor giving rise to the changes of the u parameter (both associated with the transition from “bulk” particles to ultrafine ones and with the temperature variations in the case of ultrafine particles) is the anharmonism of atomic thermal vibrations of “surface” atoms, whose number becomes comparable with the total number of atoms in a particle.

REFERENCES

1. V. I. Nikolaev and V. S. Rusakov, *Mössbauer Research of Ferrites* (Mosk. Gos. Univ., Moscow, 1985).
2. G. A. Sawatzky, C. Boekema, and F. van der Woude, in *Proceedings of the International Conference on Magnetism, Dresden, 1971*, p. 239.
3. F. van der Woude and G. A. Sawatzky, in *Proceedings of the International Conference on Magnetism, Dresden, 1971*, p. 335.
4. Yu. F. Krupyanskiĭ and I. P. Suzdalev, *Zh. Éksp. Teor. Fiz.* **67**, 736 (1974) [*Sov. Phys. JETP* **40**, 364 (1974)].
5. S. Krupička, *Physik der Ferrite und der verwandten magnetischen Oxide* (Academia, Prague, 1973; Mir, Moscow, 1976), Vol. 1.
6. V. I. Nikolaev, N. N. Oleĭnikov, V. S. Rusakov, and A. M. Shipilin, *Vestn. Mosk. Univ., Ser. 3: Fiz., Astron.* **28**, 96 (1987).
7. V. I. Nikolaev, N. N. Oleĭnikov, V. S. Rusakov, and A. M. Shipilin, *Kristallografiya* **33** (2), 518 (1988) [*Sov. Phys. Crystallogr.* **33**, 306 (1988)].
8. V. I. Nikolaev, V. S. Rusakov, and A. M. Shipilin, *Vestn. Mosk. Univ., Ser. 3: Fiz., Astron.* **27**, 65 (1986).
9. G. Blasse, *Crystal Chemistry and Some Magnetic Properties of Mixed Metal Oxides with Spinel Structure* (Philips Research Laboratories, Eindhoven, 1964; Metallurgiya, Moscow, 1968); *Philips Res. Rep., Suppl.*, No. 3, 1 (1964).

Translated by T. Dmitrieva